

Nonlinear models for flows by rotating disk



By

Sumaira Qayyum

**A THESIS SUBMITTED IN THE PARTIAL FULFILLMENT OF THE REQUIREMENT FOR
THE DEGREE OF
DOCTOR OF PHILOSOPHY
IN
MATHEMATICS**

**Supervised By
Prof. Dr. Tasawar Hayat**

**Department of Mathematics
Quaid-I-Azam University
Islamabad, Pakistan
2019**

Author's Declaration

I, Sumaira Qayyum, hereby state that my PhD thesis titled *Nonlinear models for flows by rotating disk* is my own work and has not been submitted previously by me for taking any degree from Quaid-I-Azam University Islamabad, Pakistan or anywhere else in country/world.

At any time, if my statement is found to be incorrect even after my graduation the university has the right to withdraw my PhD degree.

Name of student: Sumaira Qayyum

Dated: 20-12-2019

Plagiarism Undertaking

I solemnly declare that research work presented in the thesis titled “**Nonlinear models for flows by rotating disk**” is solely my research work with no significant contribution from any other person. Small contribution/help wherever taken has been duly acknowledged and that complete thesis has been written by me.

I understand the zero tolerance policy of the HEC and **Quaid-I-Azam University** towards plagiarism. Therefore, I as an Author of the above titled thesis declare that no portion of my thesis has been plagiarized and any material used as reference is properly referred/cited.

I undertake that if I am found guilty of any formal plagiarism in the above titled thesis even afterward of PhD degree, the University reserves the rights to withdraw/revoke my PhD degree and that HEC and the University has the right to publish my name on the HEC/University Website on which names of students are placed who submitted plagiarized thesis.

Student/Author Signature

Name: Sumaira Qayyum

Nonlinear models for flows by rotating disk

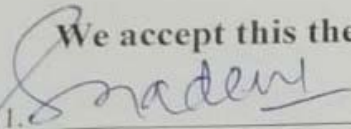
By

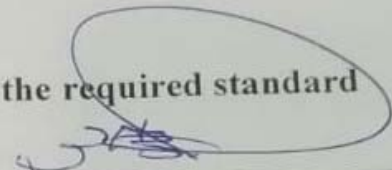
Sumaira Qayyum

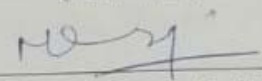
CERTIFICATE

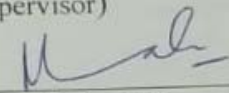
A THESIS SUBMITTED IN THE PARTIAL FULFILLMENT OF THE
REQUIREMENTS FOR THE DEGREE OF THE DOCTOR OF
PHILOSOPHY

We accept this thesis as conforming to the required standard

1. 
Prof. Dr. Sohail Nadeem
(Chairman)

2. 
Prof. Dr. Tasawar Hayat
(Supervisor)

3. 
Dr. Meraj Mustafa Hashmi
Associate Professor
School of Natural Sciences SNS,
National University of Sciences &
Technology (NUST), Islamabad.
(External Examiner)

4. 
Dr. Nasir Ali
Associate Professor
Department of Mathematics &
Statistics, International Islamic
University, Islamabad.
(External Examiner)

**Department of Mathematics
Quaid-I-Azam University
Islamabad, Pakistan
2019**

Certificate of Approval

This is to certify that the research work presented in this thesis entitled Nonlinear models for flows by rotating disk was conducted by Ms. Sumaira Qayyum under the kind supervision of Prof. Dr. Tasawar Hayat. No part of this thesis has been submitted anywhere else for any other degree. This thesis is submitted to the Department of Mathematics, Quaid-i-Azam University, Islamabad in partial fulfillment of the requirements for the degree of Doctor of Philosophy in field of Mathematics from Department of Mathematics, Quaid-I-Azam University Islamabad, Pakistan.

Student Name: Sumaira Qayyum

Signature: Sumaira

External committee:

a) External Examiner 1:

Name: **Dr. Nasir Ali**

Designation: Associate Professor

Office Address: Department of Mathematics & Statistics, International Islamic University Islamabad, H-10 Islamabad.

Signature: Nasir Ali

b) External Examiner 2:

Name: **Dr. Meraj Mustafa Hashmi**

Designation: Associate Professor

Office Address: School of Natural Sciences (SNS), National University of Sciences & Technology, Islamabad.

Signature: Meraj

c) Internal Examiner

Name: **Prof. Dr. Tasawar Hayat**

Designation: Professor

Office Address: Department of Mathematics, QAU Islamabad.

Signature: Tasawar Hayat

Supervisor Name:

Prof. Dr. Tasawar Hayat

Signature: Tasawar Hayat

Name of Dean/ HOD

Prof. Dr. Sohail Nadeem

Signature: Sohail Nadeem

Dedicated to my aabi, ammi and my family whose constant love, support and encouragement have put me where I am now. And special thanks to dadi aman for her constant prayers throughout my studying period of 21 years.

Preface

Flow due to rotating surfaces has been extensively investigated by many researchers. It is because of their applications in aeronautical science and other industrial and engineering branches. Rotating disks have applications in marine, vehicle industries, rotating heat exchanger, gas turbine, semiconductor manufacturing, magnetic storage drives, electronic gadgets having rotational parts, disk reactor for production of bio-fluids and rotating heat exchanger. Heat transport phenomenon by a stretching disk is still being given remarkable consideration by the engineers and scientists. It is in view of their applications in power generating, computer storage devices, medical equipment, crystal growth processes, electronic devices and air cleaning machines. Viscous as well as non-Newtonian liquids like Williamson model, Jeffrey model and second grade etc., are viewed supportive in above mechanical, biological and computer sciences applications. Therefore, the Williamson, Jeffrey, second grade and viscous fluid models are adopted in the mathematical modeling of this thesis. Fluid flow is examined by a stretched rotating disk or between rotating disks. Main stress is given to the flow by a rotating surface. Boundary layer concept for stretched surface is implemented. Concept of second law of thermodynamics is also used for the calculation of entropy generation. This thesis is designed as: Chapter one contains the basic concept about flow by a rotating disk, nanofluid, ferrofluid, magnetohydrodynamics boundary layer, viscous and non-Newtonian fluids, homogeneous and heterogeneous reactions and activation energy. Conservation laws and tensor form for viscous fluid, Williamson, Jeffrey and second grade fluids are presented. Solution procedure is discussed.

Chapter two reports the heat, mass and motile microorganism transfer rates in radiated flow of nanomaterial by a rotating disk. The flow is discussed over a variable thicked surface of disk. Concept of microorganisms suspended nanoparticles is stabilized via bio-convection in the presence of buoyancy forces and magnetic field. Homotopy analysis method is used for convergent solution. The data of this chapter is published in **Chinese Journal of Physics, 56 (2018) 2404-2423.**

Chapter three reports the mixed convective fluid flow (with silver and copper nanomaterials) by a rotating stretched disk. Energy expression is mathematically modeled subject to radiative flux, viscous dissipation and Ohmic heating. The flow under consideration is of nonlinear stretching attributes of disk. Concept of thermodynamics second law is implemented for the entropy rate. Nonlinear formulation based upon conservation laws is made. Attention is particularly given to the entropy generation and convergence analysis. Research of this chapter is reported in **Colloids and Surfaces A: Physicochemical and Engineering Aspects, 539 (2018) 335-346.**

Chapter four is generalized version of chapter two in view of five different types of nanoparticles and partial slip. The concept of motile microorganisms is dropped in this chapter. Silver, Copper, Copper oxide, Aluminum oxide and Titanium oxide are used as nanoparticles and water as continuous phase fluid. The data of this research is published in **Physica B: Condensed Matter, 534 (2018) 173-183.**

Chapter five presents the flow of magnetic nanofluid or ferrofluid between two coaxially rotating stretchable disks. Both disks have different rotating and stretching velocities. Water based fluid comprising magnetite Fe_3O_4 nanomaterials is addressed. Furthermore the velocity and temperature jump at the solid-liquid interface are accounted. Series solutions are developed using

homotopy analysis method (HAM). The data of this research is printed in **Journal of Magnetism and Magnetic Materials, 413 (2016) 39-48.**

Chapter six provides us the mathematical modeling of statistical declaration and probable error about skin friction coefficients and Nusselt numbers for flow between two coaxially rotating stretchable disks. Furthermore the homogeneous and heterogeneous reactions are considered. Thermo-physical characteristics of nanofluids are scrutinized through Silver and Copper nanoparticles. Main consideration is given to the statistical declaration and probable error for the coefficients of skin friction and Nusselt numbers. HAM is used for the series solution developments. The research of this chapter is reported in **International Journal of Hydrogen Energy, 42 (2017) 29107-29120.**

Chapter seven deals with entropy optimization and heat transport in 3D unsteady flow between two coaxially stretched disks. Energy equation is developed via Ohmic heating, heat source/sink and dissipation. Thermo-diffusion effect is further considered. The flow is conducting for time dependent MHD fluid. Thermal and velocity slip conditions at both the surface are implemented. Flow problem is modeled by using Navier-Stokes equations with entropy generation. Transformations (Von-Karman) are utilized to convert the nonlinear flow expressions into ordinary ones and then tackled for series solutions employing HAM. The contents of this chapter are accepted for publication in **International Journal of Numerical Methods for Heat and Fluid Flow (2019).**

In chapter eight, the contents of chapter seven is generalized in view of thermo-diffusion and diffusion-thermo effects, nonlinear radiative flux, porous medium and Joule heating. The data of this research is published in **Journal of Molecular Liquid, 262 (2018) 261-274.**

Chapter nine is extension of chapter eight in view of Jeffrey fluid model, thermal stratification and homogeneous and heterogeneous reactions. The findings of this chapter are reported in **Results in Physics, 7 (2017) 2557-2567.**

In chapter ten, the data of chapter nine is generalized by considering second grade fluid and heat generation/absorption. In this chapter radiative heat flux is dropped. The results of this chapter is published in **Results in Physics, 8 (2018) 223-230.**

Chapter eleven communicates the flow of Williamson fluid between two-coaxially stretchable rotating disks with entropy generation. MHD Williamson liquid is considered. Through second law of thermodynamics the entropy rate is obtained. Viscous dissipation, radiative heat flux and heat source/sink effects are considered for the modeling of energy equation. Transformation procedure converts the nonlinear flow expressions into ordinary differential equations. HAM is used for the development of convergent series solutions. The results of this research is published in **International Journal of Heat and Mass Transfer, 127 (2019) 933-942.**

Chapter twelve is the extension of chapter eleven for Soret and Dufour effects and stratification in flow between two rotating disks with entropy generation. The observations data of this chapter are reported for publication in **Scientia Iranica, (2019).**

Nomenclature	
B_0	Applied magnetic field strength
$\hat{T}_w, \hat{T}_\infty$	Surface and ambient temperatures
b, W_c, ζ	chemotaxis constant, maximum speed of swimming cell and the disk thickness index
a^*	the thickness coefficient of disk which is very small
k^*	mean absorption coefficient
$\hat{C}_w, \hat{C}_\infty$	surface and ambient concentration
$\hat{N}_w, \hat{N}_\infty$	surface and ambient density of gyrotactic microorganism
σ^*	Stefan-Boltzman constant
R_0	feature radius
D_N	diffusivity of microorganisms
D_B, D_T	Brownian and thermophoretic diffusion coefficient respectively
$\hat{u}, \hat{v}, \hat{w}$	velocity field
r, ϑ, z	cylindrical coordinates
\tilde{H}, \tilde{F}, G	self similar axial, radial, tangential velocities
$\tilde{\theta}, \tilde{C}, \tilde{N}$	temperature, concentration and density profile,

	disk thickness coefficient
ε^*	is a dimensionless constant
Pr	Prandtl number
Re	Reynolds number
M	magnetic parameter
A	scaled stretching parameters
r^*	the dimensionless radius
Nt, q_w, q_r	thermophoresis parameter, heat flux and radiative heat flux
Pe, ξ	bioconvection Peclet number, independent variable
R, Nb	radiation parameter, Brownian motion parameter
$\tilde{h}, \tilde{f}, \tilde{g}, \tilde{\theta}, \tilde{\chi}$	axial, radial, tangential velocities, temperature, concentration and density profile
Le and Lb	Lewis and bioconvection Lewis number
Ω, μ_{nf}, μ_f	angular velocity, dynamic viscosity of nanofluid and base fluid
$\sigma_{nf}, \sigma_f, \sigma_s$	electrical conductivity of nanofluid, base fluid, nanoparticles respectively
ν_{nf}, ν_f	kinematic viscosity of nanofluid and base fluid

$(\rho c_p)_{nf}$, $(\rho c_p)_f$ and $(\rho c_p)_p$	heat capacity of nanofluid, base fluid, nanoparticles
$\rho_{nf}, \rho_s, \rho_f$	density of nanofluid, base fluid, nanoparticles
$(\beta\rho)_{nf}$	volumetric thermal expansion coefficient of nanofluid
$(\beta\rho)_f, (\beta\rho)_s$	volumetric thermal expansion coefficient of base fluid, nanoparticles
N_G , Be	entropy generation rate, Bejan number
Br	Brinkman number
k_{nf}, k_f, k_s	thermal conductivity of nanofluid, base fluid, nanoparticles
λ, φ	mixed convection parameter,, nanoparticles volume fraction
Ec	Eckert number
\hat{T}_1 and \hat{T}_2	lower and upper disk temperatures
a_1, a_2	Stretching rate of lower and upper disk
Ω_1, Ω_2	angular velocity lower and upper disk
A_1, A_2	scaled stretching parameters of lower and upper disks
ε	pressure parameter

$\xi, \gamma_1, \gamma_2, \gamma_3$	independent variable, slip and thermal slip parameters
h	distance between disks
λ_1 and λ_2, λ_3	velocity slip coefficients, thermal slip coefficient
k_c and k_s	rate constants
C and D, c and d	chemical species, concentrations
Sc, δ	Schmidt number, ratio of diffusion coefficient
k_1 and k_2	homogeneous and heterogeneous reactions parameters
$\hat{\psi}_1$	solutal concentration of lower disk
$\hat{\psi}_2$	solutal concentration of upper disk
$\hat{p}, \alpha_1, \alpha_2$	fluid pressure, temperature and concentration difference parameter
(D_T) and A^*	thermophoretic diffusion coefficient and dimensionless parameter
L	diffusive parameter
K	chemical reaction coefficient
$(D_{CT}), (D_{TC})$	nanoparticles volume fraction, are Soret and Dufour diffusivities ,
D_s	solutal diffusivity

c^*	unsteadiness parameter
A^0	unsteadiness parameter
$\hat{T}_m, \hat{\psi}_m$	mean temperature, mean concentration
Ld	modified Soret parameter
Q^*	heat generation/absorption parameter
Nd	modified Dufour parameter
K^*	porosity rate
D	coefficient of molecular diffusion
K_T	ratio of thermal diffusion
C_s	concentration susceptibility
K	rate of chemical reaction
W_0	suction/injection rate
β^*	porosity parameter
Du, Sr, Q^*	Dufour/Soret number and heat generation/absorption parameter
Sc, R^*, W_s	Suction/injection parameter
λ_1^*, λ_2^*	ratio of relaxation to retardation times , retardation time
β	Deborah number

α_1^*	material parameter of second grade fluid
We	Weissenberg number
(D_m)	the effective diffusivity rate of mass
(T_m)	mean temperature of fluid
(E_α)	activation energy
(E_1)	dimensionless activation energy
$(S_1), (S_2)$	thermal and solutal stratification parameter,

Contents

1	Background and basic laws	7
1.1	Background	7
1.2	Concept of entropy	12
1.2.1	Definition	12
1.2.2	Examples of entropy	12
1.2.3	Types of processes	13
1.2.4	Proof that entropy always increases	14
1.3	Fundamental laws	14
1.3.1	Mass conservation law	14
1.3.2	Momentum conservation law	14
1.3.3	Conservation law of energy	16
1.3.4	Conservation law of concentration	17
1.4	Solution procedure	18
2	Rotating disk flow of nanomaterial with gyrotactic microorganism and variable thickness	19
2.1	Formulation	19
2.2	Methodology	23
2.2.1	Zeroth-order formulations	24
2.2.2	m^{th} order problems	25
2.3	Convergence analysis	27
2.4	Discussion	31

2.4.1	Axial, radial and tangential velocity components	32
2.4.2	Temperature	35
2.4.3	Concentration	37
2.4.4	Density	39
2.4.5	Surface drag force	42
2.4.6	Nusselt number	42
2.5	Conclusions	43
3	Rotating disk flow of nanomaterial with mixed convection and entropy generation	44
3.1	Problem formulation	45
3.2	Quantities of engineers interest	48
3.2.1	Surface drag force	48
3.2.2	Heat transfer rate	49
3.3	Exploration of entropy generation	49
3.4	Homotopy procedure	51
3.5	Convergence analysis	51
3.6	Discussion	53
3.7	Entropy analysis	64
3.8	Conclusions	68
4	Slip and Joule heating effects in rotating disk flow with nanoparticles	70
4.1	Modeling	70
4.2	Solutions expressions	75
4.3	Convergence analysis	75
4.4	Discussion	80
4.4.1	Axial, radial and tangential velocity components	80
4.4.2	Temperature	88
4.4.3	Surface drag force	91
4.4.4	Nusselt number	92
4.5	Conclusions	94

5	Flow of magnetite-Fe_3O_4 nanoparticles in presence of partial slip conditions	95
5.1	Problem formulation	95
5.2	Solutions	99
5.3	Convergence analysis	100
5.4	Discussion	102
5.4.1	Radial and axial velocities	102
5.4.2	Tangential velocity	105
5.4.3	Dimensionless temperature	108
5.4.4	Skin friction coefficient	109
5.4.5	Nusselt number	110
5.5	Conclusions	111
6	Computations of probable error and statistical declaration for radiated reactive flow	112
6.1	Physical model and mathematical formulation	113
6.2	Solution technique	118
6.3	Convergence region	118
6.3.1	Surface drag force	122
6.3.2	Nusselt number	123
6.3.3	Statistical approach	124
6.3.4	Probable error (P.E)	126
6.3.5	Statistical declaration about parameters	127
6.4	Graphical illustration	128
6.4.1	Radial and axial velocity components	129
6.4.2	Tangential velocity	132
6.4.3	Temperature	134
6.4.4	Concentration	137
6.5	Final remarks	139
7	Entropy optimized unsteady reactive flow between two rotating disks with thermo-diffusion effects	140

7.1	Modeling	140
7.2	Entropy modeling	145
7.3	Technique Procedure	147
7.4	Convergence analysis	147
7.5	Discussion	149
7.5.1	Velocity and temperature	149
7.5.2	Solutal ($\tilde{\chi}(\xi)$) and nanoparticles ($\tilde{\phi}(\xi)$) concentration profiles	154
7.5.3	Entropy generation	158
7.5.4	Skin friction	164
7.5.5	Nusselt number	165
7.5.6	Sherwood number	165
7.6	Conclusions	166
8	Nonlinear radiative flow by rotating disks with entropy generation and Soret and Dufour effects	168
8.1	Formulation	169
8.1.1	Physical quantities	171
8.2	Solutions technique	172
8.3	Entropy generation minimization	173
8.4	Convergence analysis	174
8.5	Physical results	177
8.5.1	Velocity components	177
8.5.2	Temperature	180
8.5.3	Concentration profile	183
8.5.4	Entropy generation	185
8.5.5	Physical quantities	189
8.6	Conclusions	191
9	Nonlinear radiated flow of Jeffrey fluid with heat source/sink and thermal stratification	192
9.1	Modeling	193

9.2	Solutions methodology and convergence	198
9.3	Discussion	199
9.3.1	Axial, radial and tangential velocity components	200
9.3.2	Temperature	207
9.3.3	Concentration	209
9.3.4	Surface drag force	211
9.3.5	Nusselt number	213
9.4	Closing remarks	213
10	Second grade fluid flow by rotating disk with heat generation/absorption and homogeneous/heterogeneous reactions	215
10.1	Modeling	216
10.2	Solutions methodology and convergence	220
10.3	Discussion	221
10.3.1	Axial, radial and tangential velocity components	222
10.3.2	Temperature	225
10.3.3	Concentration	227
10.3.4	Surface drag force	230
10.3.5	Nusselt number	231
10.4	Closing remarks	232
11	Dissipative flow of Williamson fluid with entropy generation	234
11.1	Constitutive equations	234
11.1.1	Physical quantities	238
11.2	Solution technique	238
11.3	Determination of entropy generation	239
11.4	Convergence analysis	240
11.5	Physical results	241
11.5.1	Velocity components	242
11.5.2	Temperature	247
11.5.3	Bejan number and entropy generation	249

11.5.4 Skin friction and Nusselt number	254
11.6 Conclusions	254
12 Novel aspects of Soret and Dufour in entropy generation minimization for Williamson fluid flow	256
12.1 Formulation	256
12.2 Solution technique	261
12.3 Convergence	262
12.4 Entropy	263
12.5 Discussion	264
12.5.1 Temperature	267
12.5.2 Concentration	269
12.5.3 Entropy generation minimization	272
12.5.4 Skin friction and Nusselt and Sherwood numbers	277
12.6 Conclusions	279
13 Thesis Conclusion	281

Chapter 1

Background and basic laws

First chapter focuses on the literature review for rotating disk, nanofluid, ferrofluid, magneto-hydrodynamics, non-Newtonian fluids, heterogeneous-homogeneous reactions, activation energy and entropy generation and basic laws for nanofluid flow.

1.1 Background

The flow created by an infinite rotating disk is known as Von Karman [1], swirling flow named after the scientist Theodore Von Karman who introduced the problem in 1921. Application of this problem is found in centrifugal compressors. This is a steady state flow in which vorticity produced at a solid surface is not allowed to diffuse far away by convection, some of the other examples includes the Blasius boundary layer with suction, etc. This problem finds its application in many fields, including rotating machines, filtering systems, heat transfer and mass transfer applications, geophysical applications etc. Flow investigation by stretchable rotating disk has significance in different mechanical and industrial engineering process like food processing technology, medical equipment, spin coating, manufacturing, air cleaning machine, centrifugal pumps, electric power generating system, at high melting point liquid metals pumping, turbo-machinery and gas turbines. Cochran [2] utilized the Von-Karman transformations to analyze the rotating flow. Stewartson [3] was pioneer in discussing the flow between two disks. Mellor et al. [5] and Chapple and Stokes [4] studied flow between two disks. Arora and Stokes [6] considered fluid flow and heat transport between two rotating disks. Kumar et al.

[7] examined liquid flow between two porous solid rotating disks. Hayat et al. [8] investigated effect of thermally stratification on fluid flow between rotating stretchable disks. Convective radiative flow of carbon nanotube is scrutinized by Imtiaz et al. [9]. Investigation of entropy generation in MHD radiative flow with Ohmic heating and dissipation is done by Hayat et al [10]. Some significant attempts for rotating disk are presented in refs. [11-15].

Nanofluid is termed as a material having nano sized particles in the traditional liquid. These particles are named as nanoparticles. Because of its variety of applications many scientists and engineers are working on this topic. Pioneering work on nanofluid was done by Choi [16]. Such materials of fluids are basically the combination of nanoparticles in a suspension of base fluid. Aforesaid small particles are usually made up of oxides, carbon nanotubes, carbides and metals. Frequently used base fluids are oil, water and glycol. Nanomaterials has some properties which helps it in several applications like fuel chambers, mining and boiler gas outlet, local refrigerator, caloric controlling, in crushing process, cooling engine automobile, hybrid electric engines, pharmacological methods, temperature control and microelectronics. These fluids have high thermal conductivity heat transport capability when compared with base fluid. They have special characteristics that make them suitable for ultrasonic applications. Additional influence includes shear transformation of an instant compression ray and this property becomes more operative when concentration enhances. Information of rheological implementation of nanofluids is said to be more influential in view of their stability for convection applications. In an alternative way, model containing two components are also taken. This phenomenon attained much attention of the scientists due to such prospective applications. Another term used to describe the suspension of nano sized particles is nanolubricants. Mainly oil is used as a base fluid, they are used for engine and machine lubricants. It used to enhance the property of anti-wear of base oils. The important nanofluids are ferrofluid which are the suspension of magnetic nanoparticles. Magnetic nanoparticles have both the magnetic and liquid characteristics. Nanofluids behave like normal fluids in the absence of magnetic field. Ferrofluids are produced by mixture of non-conducting fluids with colloidal suspension of magnetic particles. Magneto nanofluids help the particles to move through the blood towards the tumor as nanofluids have adhesion properties with tumor cells. In cancer therapy these particles have more absorption power than micro particles. Usage of magnetic nanofluids includes hyperthermia, drug deliv-

ery, magnetic cell separation, contrast augmentation in magnetic resonance imaging etc. Some recent literature for nanofluid flow is presented in Refs. [17-30].

Non-Newtonian fluids have extensive applications in technological and industrial sectors. Formulation of equations for these types of fluids is complex in comparison to the usual Naviers Stokes equation. It is due to extra rheological parameters in the constitutive relations of such materials. Applications related to geophysics, biological sciences and chemical processes involve non-Newtonian materials. Materials such as foams, pastes, ketchup, lubricant, certain oils, sugar solution, apple sauce, colloidal and suspension solutions, drilling muds, clay coating and soaps are the non-Newtonian fluids. Tangent hyperbolic nanofluid radiative flow is presented by Hayat et al. [31]. Turkyilmazoglu [32] worked on micropolar fluid bounded due to heated sheet. Effect of non-Fourier heat flux on viscoelastic material (Jeffrey fluid) flow is presented by Hayat et al. [33]. Rahman et al. [34] examined effect of slip on flow of Jeffrey nanofluid through tapered artery with mild stenosis. Some more recent works on non-Newtonian fluids can be seen through refs. [35-45].

The minimum amount of energy which is necessary for the atoms or molecules in any chemical reaction through which reaction initiate is known as activation energy. This concept was initiated by Svante Arrhenius (Swedish scientist) in 1889. Symbol for activation energy is E_a in a chemical reaction and its unit is kcal/mol. The activation energy of some elements and compounds which react with one another is zero. The threshold value of activation energy is required for the atoms or molecules to react. It is measured as barrier between two energy states. To start a reaction processes the threshold of barrier must be crossed. For continuation of chemical reaction there is some certain range of molecules and atoms which are required having translational energy which should be greater than or equal to activation energy. Maxwell distribution is applied, and the molecules which have energy greater than the energy of barrier will cross the threshold. Therefore the highest energy of barrier is the activation energy. The effect of tunneling is ignored in this case and the barrier's shape as well which shows the particles which have energy greater than activation energy. However the number of particles with enough energy that start the reaction totally depends on the energy, which is why a concept of pre-exponential factor function is included of the temperature. This concept is usually utilized in calculating rates and estimating cross sections. Some more investigations on this regards can

be witnessed from refs. [46-55].

Several chemical reacting systems consist of heterogeneous-homogeneous reactions. Except in the presence of catalyst some of the reactions does not work or may proceed very slow. Correlation between homogeneous-heterogeneous reactions is very complex. Ceramics, fog dispersion, food processing, crops damage via freezing, fog formation and polymer production, hydrometallurgical industry are applications of chemical reaction. Various scientists now are engaged in the discussion of flows with homogeneous-heterogeneous reactions via different aspects [56-70].

Surface with varying thickness has many applications especially in marine, architectural, civil, aeronautical processes and in mechanical engineering. By the help of variable thickness of sheet the structural material becomes light and enhance the usage of material. Fluid flow by variable thickness of sheet with non-Fourier heat flux and variable thermal conductivity is presented by Hayat et al. [71]. Fluid flow of non-Newtonian liquid near stagnation point with variable thicked surface is analyzed by Ramesh et al. [72]. Ostwald-de Waele fluid flow by a rotating disk with variable thickness and decreasing index is illustrated by Xun et al. [73]. Effect of stagnation point flow and carbon nanotubes with variable thicked surface is explored by Hayat et al. [74]. Fang et al. [75] worked on flow over a variable thicked stretching sheet.

At present the method of thermodynamic optimization of real devices and entropy generation minimization (EGM) are rapidly growing. Principle of thermodynamics method also called "thermodynamic design", "thermodynamic optimization" and "finite time thermodynamics". Basic rules of thermodynamics such as fluid mechanics and heat transfer are merged through EGM. These type of principles are applied by EGM on schemes that are made by limited time constraint, these processes are restricted by irreversibilities of mass, fluid flow and heat transfer. Recent progress in this constraint includes heat exchanger design, storage optimization by melting and solidification, the various functions of refrigerators, power from hot-dry-rock deposits and power plants having the heat exchangers that are fouled. Newton's second law of motion and laws of thermodynamics are the important principles on the basis of which heat transfer and flow studies are based. First law of thermodynamics gives basic knowledge about energy of system. Second law of thermodynamics shows that entire actuality developments are irreversible and it is a significant apparatus to study the generation of entropy to assess the irreversibility in the system. Entropy generation optimization governs the irreversibility associated to the natural

developments for example a counter current flow of gas and gas in heat exchange. At present the entropy generation optimization is a topic of different interests in few territories similar to rotating disk reactors, porous media, propulsion ducts ,electromagnetic materials processing, turbo machinery, electric cooling, heat transferring devices and combustions. Few current utilizations of entropy analysis are solar heat exchangers in pseudo-optimization process, fuel rods cooling nuclear industry, slurry systems, electromagnetic propulsion used in nuclear industry, cooling of modern electronic systems, loss of heat from steam pipes and solar energy collectors etc. The investigation of entropy generation optimization with MHD in which the flow study is done due to rotating disk has gained significant consideration due to consistently developing applications i.e., accelerators, power plant, micropumps, flow meters, filtration , MHD generators, nuclear reactors, and geothermal systems etc. Initially Bejan [76] showed how the entropy production rate can be decreased in simple components for heat transport like heat exchanges with prescribed heat flux distribution, counter flow gas to gas heat exchangers and sensible heat units for energy storage. Ijaz et al. [77] studied entropy generation in flow of Sisko liquid subject to heat generation/absorption. Flow is investigated over a stretched surface. Nonlinear flow expressions are solved for series solutions via homotopy method. The obtained outcomes predict that velocity field diminishes for higher material variable while thermal field increases for larger radiation parameter and Biot number. Vatanmakan et al. [78] explored steam flow in turbine blades with entropy generation and volumetric heating. Numerical simulation is conducted through two phase Eulerian description for steam flow. Khan et al. [79] worked on chemically reactive flow of Casson liquid with activation energy and entropy generation. Gul et al. [80] studied Poiseuille flow of nanofluid with entropy generation. Xie and Jian [81] discussed MHD two-layer electroosmotic flow with entropy generation through micro-parallel channels. Ijaz et al. [82] scrutinized forced convection flow of viscous nanofluid for entropy generation. Huminić and Huminić [83] analyzed heat transfer performances of hybrid nanomaterials with entropy generation in a flattened tube. Farooq et al. [84] examined radiative flow of carbon nanotubes with mixed convection. Kiyasatfar et al. [85] explored entropy production in flow of power law fluid considering slip conditions.

1.2 Concept of entropy

1.2.1 Definition

Randomness in the system or molecular disorder is called entropy.

1.2.2 Examples of entropy

1. Fig. 1 shows that for a substance of high temperature the entropy enhances (see link [https://chem.libretexts.org/Bookshelves/General_Chemistry/Book%3A_Chemistry_\(Averill_and_Eldredge\)](https://chem.libretexts.org/Bookshelves/General_Chemistry/Book%3A_Chemistry_(Averill_and_Eldredge))

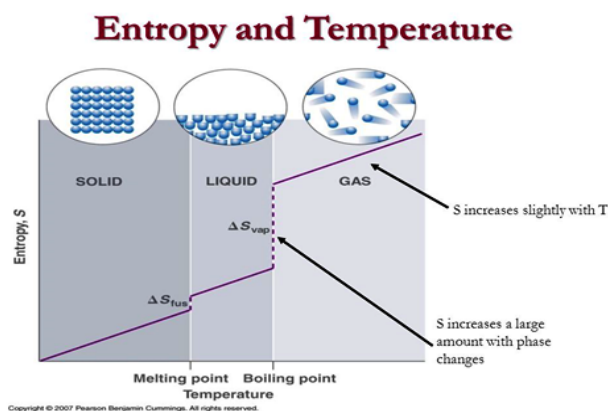


Fig. 1.1: Entropy increases via temperature.

2. Fig. 2 tells that there is large entropy for larger molecules when compared with smaller molecules (see link <https://www.google.com/url?sa=i&url=http%3A%2F%2Fwww.chemhume.co.uk%2FA2CH.htm&psig=AOvVaw1X5LbZWSVGyWh9W-OVA8T-&ust=1574487855725000&source=images&cd=vfe&v>)

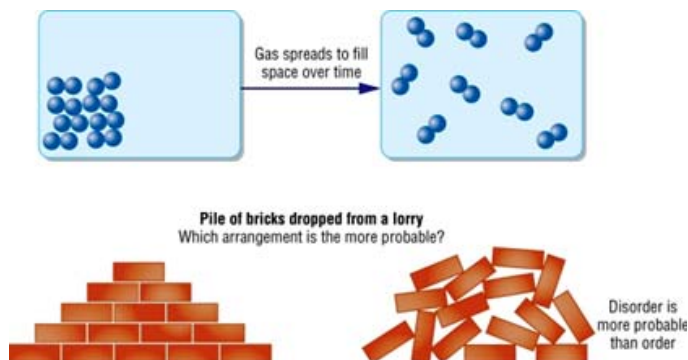


Fig. 1.2: Entropy via amount of molecules.

3. Solids have lesser entropy than gas and liquid (See Fig. 1.3 and link https://www.google.com/url?sa=i&u=1574487259982000&source=images&cd=vfe&ved=0CAIQjRxqFwoTCPCer8WO_eUCFQAAAAAdAA)

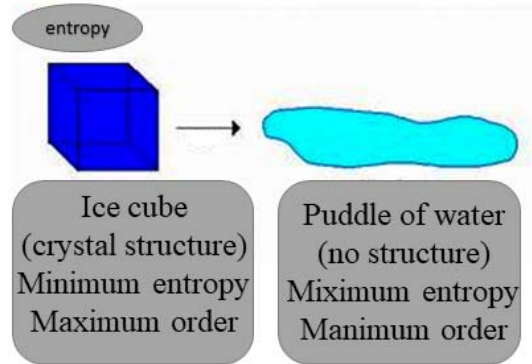


Fig. 1.3: Entropy for solid, gas and liquid.

1.2.3 Types of processes

Reversible process

A process in which surrounding or system can take its original position from the final form without changing the properties in thermodynamics of the universe is known as reversible process (see Fig. 1.4).

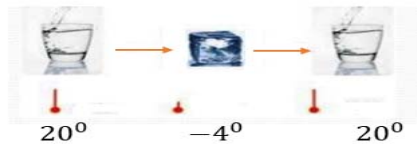


Fig. 1.4: Reversible processes.

Irreversible process

A process that is not reversible is irreversible. Factors causes process irreversible are friction, mixing of two gases, plastic deformation and chemical reaction.

1.2.4 Proof that entropy always increases

In all natural process the entropy increase so entropy cannot conserved. Suppose a body at temperature T_1 radiates always a small heat dQ . A cold body B at temperature T_2 receives that heat. If dQ be so small that T_1 and T_2 are not altered then entropy of A decrease by $-\frac{dQ}{T_1}$ and entropy of B increased by $\frac{dQ}{T_2}$. Further

$$dS = S_2 - S_1 = \frac{dQ}{T_2} - \frac{dQ}{T_1}, \quad (1.1)$$

$$T_1 > T_2 \text{ So } \frac{1}{T_1} < \frac{1}{T_2}, \quad (1.2)$$

$$dS = dQ \left(\frac{1}{T_2} - \frac{1}{T_1} \right), \quad (1.3)$$

$$dS > 0. \quad (1.4)$$

1.3 Fundamental laws

1.3.1 Mass conservation law

Equation of continuity without any source or sink is expressed as

$$\nabla \cdot (\rho \mathbf{V}) + \frac{\partial \rho}{\partial t} = 0. \quad (1.5)$$

Here ρ , t and \mathbf{V} are density, time and velocity. When liquid is considered incompressible then Eq. (1.5) becomes

$$\nabla \cdot \mathbf{V} = 0. \quad (1.6)$$

1.3.2 Momentum conservation law

Equation of motion is

$$\rho \frac{d\mathbf{V}}{dt} = \nabla \cdot \boldsymbol{\tau} + \rho \mathbf{b}, \quad (1.7)$$

and for two phase nanofluid model we have

$$\rho_{nf} \frac{d\mathbf{V}}{dt} = -\nabla \cdot \boldsymbol{\tau} + \rho_{nf} \mathbf{b}. \quad (1.8)$$

In above expressions right hand side depicts the surface and body forces and left hand side denotes an inertial force. Here mathematical expression for effective nanofluid density ρ_{nf} is

$$\rho_{nf} = \rho_f(1 - \phi) + \rho_s\phi, \quad (1.9)$$

Viscous fluid

For viscous fluid model the Cauchy stress tensor τ has the form

$$\tau = -\hat{p}\mathbf{I} + \mu\mathbf{A}_1, \quad (1.10)$$

here \hat{p} , I , b , \mathbf{A}_1 and d/dt are pressure, identity tensor, body force, first Rivlin-Erickson tensor.

Mathematically, \mathbf{A}_1 is defined as

$$\mathbf{A}_1 = \nabla\mathbf{V} + (\nabla\mathbf{V})^t, \quad (1.11)$$

where

$$\nabla\mathbf{V} = \begin{bmatrix} \frac{\partial \hat{u}}{\partial r} & -\frac{\hat{v}}{r} + \frac{1}{r} \frac{\partial \hat{u}}{\partial \vartheta} & \frac{\partial \hat{u}}{\partial z} \\ \frac{\partial \hat{v}}{\partial r} & -\frac{\hat{u}}{r} + \frac{1}{r} \frac{\partial \hat{v}}{\partial \vartheta} & \frac{\partial \hat{v}}{\partial z} \\ \frac{\partial \hat{w}}{\partial r} & \frac{1}{r} \frac{\partial \hat{w}}{\partial \vartheta} & \frac{\partial \hat{w}}{\partial z} \end{bmatrix} \quad (1.12)$$

Here ϕ , f and s are nanoparticles volume fraction, subscripts for base fluid and nanoparticles respectively. Further incompressible character of liquid is considered.

Second grade fluid model

The Cauchy stress tensor for second grade is expressed as:

$$\tau = -\hat{p}\mathbf{I} + \mu\mathbf{A}_1 + \alpha_1^*\mathbf{A}_2 + \alpha_2^*\mathbf{A}_1^2, \quad (1.13)$$

where α_1^* and α_2^* are two material constants. Second Rivlin-Ericksen tensors is

$$\mathbf{A}_2 = \frac{d\mathbf{A}_1}{dt} + (\nabla\mathbf{V})^t \mathbf{A}_1 + \mathbf{A}_1 (\nabla\mathbf{V}), \quad (1.14)$$

For thermodynamics consistency, Clausius–Duhem inequality we have:

$$\mu \geq 0, \alpha_1^* \geq 0, \alpha_1^* + \alpha_2^* = 0, \quad (1.15)$$

Jeffrey fluid model

The Cauchy stress tensor for Jeffrey fluid model is expressed as:

$$\tau = -\hat{p}\mathbf{I} + \frac{\mu}{1 + \lambda_1^*} \left(\mathbf{A}_1 + \lambda_2^* \frac{d\mathbf{A}_1}{dt} \right), \quad (1.16)$$

where λ_2^* and λ_1^* are retardation time and ratio of relaxation to retardation times respectively.

Williamson fluid model

For Williamson fluid model τ is given by

$$\tau = -\hat{p}\mathbf{I} + \left[\mu_\infty + (\mu_0 - \mu_\infty) (1 - \Gamma\dot{\gamma})^{-1} \right] \dot{\gamma}, \quad (1.17)$$

in which Γ , μ_0 , μ_∞ denote time constant, zero and infinite shear rate viscosity respectively and $\dot{\gamma}$ is expressed as

$$\dot{\gamma} = \sqrt{\frac{1}{2} \text{trace}(A_1)^2}. \quad (1.18)$$

1.3.3 Conservation law of energy

Energy equation for nanofluid (Buongiorno model) can be written as

$$(\rho c_p) \frac{d\hat{T}}{dt} = -\nabla \cdot \vec{q} + h_p \nabla \cdot \vec{j}_p. \quad (1.19)$$

Here \hat{T} , c_p , h_p , \vec{q} , \vec{j}_p denote fluid temperature, specific heat, nanoparticles specific enthalpy, heat flux and mass flux for nanoparticles diffusion respectively. Mass flux for diffusion of

nanoparticles $\vec{\mathbf{j}}_p$ and heat flux \vec{q} are defined as

$$\vec{\mathbf{j}}_p = -\rho_s D_B \nabla \hat{C} - \rho_s D_T \frac{\nabla \hat{T}}{\hat{T}_\infty}, \quad (1.20)$$

$$\vec{q} = -k \nabla \hat{T} + h_p \vec{\mathbf{j}}_p, \quad (1.21)$$

in which ρ_s , D_B , k , D_T are nanoparticles density, Brownian diffusion coefficient, thermal conductivity and thermophoretic force respectively. Eq. (1.18) becomes

$$\rho c_p \frac{d\hat{T}}{dt} = k \nabla^2 \hat{T} + \rho_s c_p \left[D_T \frac{\nabla \hat{T} \cdot \nabla \hat{T}}{\hat{T}_\infty} + D_B \nabla \hat{C} \cdot \nabla \hat{T} \right], \quad (1.22)$$

which is the heat equation of nanofluid in Buongiorno model of nanofluid.

Energy equation for two phase model of nanofluid is written as

$$(\rho c_p)_{nf} \frac{d\hat{T}}{dt} = k_{nf} \nabla^2 \hat{T}, \quad (1.23)$$

where $(\rho c_p)_{nf}$, μ_{nf} and k_{nf} highlight effective heat capacity, dynamic viscosity and effective thermal conductivity. Note that nf stands for nanofluid. These quantities are defined as

$$(\rho c_p)_{nf} = (\rho c_p)_f (1 - \phi) + (\rho c_p)_s \phi. \quad (1.24)$$

$$\mu_{nf} = \frac{\mu_f}{(1 - \phi)^{2.5}}, \quad (1.25)$$

$$\frac{k_{nf}}{k_f} = \frac{k_s + 2k_f - 2\phi(k_f - k_s)}{k_s + 2k_f + \phi(k_f - k_s)}. \quad (1.26)$$

1.3.4 Conservation law of concentration

The concentration equation for nanofluids is

$$\frac{\partial \hat{C}}{\partial t} + \mathbf{V} \cdot \nabla \hat{C} = -\frac{1}{\rho_s} \nabla \cdot \vec{\mathbf{j}}_p, \quad (1.27)$$

After using Eq. (1.19), we get

$$\frac{\partial \hat{C}}{\partial t} + \mathbf{v} \cdot \nabla \hat{C} = D_B \nabla^2 \hat{C} + D_T \frac{\nabla^2 \hat{T}}{\hat{T}_\infty}. \quad (1.28)$$

1.4 Solution procedure

Governing equations for flow are mostly highly nonlinear. It is very complicated to find the exact solution for these equations. There are numerous techniques which are used to solve the nonlinear equations such as Adomian decomposition method, perturbation and homotopy perturbation methods etc. Note that there are some limitations in these methods that are dependent on large or small parameters in the equations and convergence. In this thesis the flow problems will be solved by using homotopy analysis method [86 – 100]. It has many advantages such as it is independent of small/large parameters. We can adjust or control the convergence of the problem by setting auxiliary parameter. We can freely choose the initial guesses and base functions for the problem.

Chapter 2

Rotating disk flow of nanomaterial with gyrotactic microorganism and variable thickness

Abstract: Here heat, concentration and motile microorganism transfer rates in magnetohydrodynamic (MHD) radiative flow of nanofluid are investigated. Variable thicked rotating disk is examined. Concept of microorganisms suspended nanoparticles is stabilized through bioconvection. This concept is induced by combined effects of magnetic field and buoyancy forces. Nonlinear differential systems are solved for series solutions. Velocity, temperature, concentration and motile density behaviors for different parameters are analyzed. Skin friction coefficient and Nusselt number are numerically discussed. Temperature and concentration have opposite behavior for larger Brownian motion parameter. Motile density reduces for bioconvection Peclet number and bioconvection Lewis number.

Keywords: Nanofluid; Rotating disk; Variable thickness; Thermal radiation; Motile microorganism

2.1 Formulation

MHD flow of nanomaterial past a stretchable rotating disk of variable thickness is considered. Applied magnetic field in z -direction has strength B_0 . Brownian motion and thermophoresis

are analyzed. Motile gyrotactic microorganism in nanofluid is accounted. Furthermore thermal radiation is considered. Disk is taken at $z = a^* \left(\frac{r}{R_0} + 1 \right)^{-\zeta}$. Disk is stretched with rate a_1 and rotate subject to angular velocity Ω_1 . \hat{T}_w and \hat{T}_∞ are surface and ambient temperatures respectively (see Fig. 1). By using the above assumptions the problems become

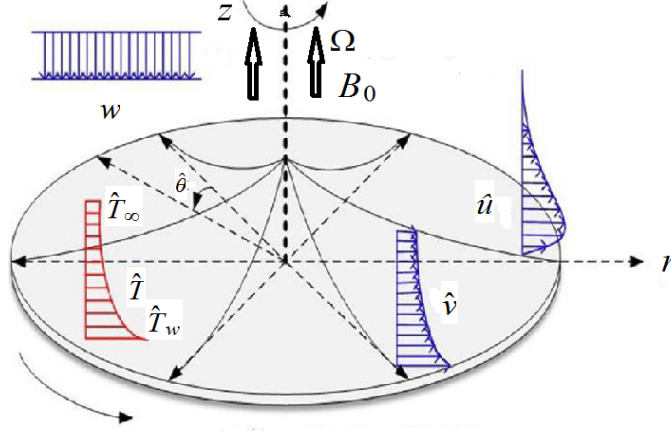


Fig. 2.1: Schematic diagram.

$$\frac{\partial \hat{u}}{\partial r} + \frac{\partial \hat{w}}{\partial z} + \frac{\hat{u}}{r} = 0, \quad (2.1)$$

$$\hat{u} \frac{\partial \hat{u}}{\partial r} - \frac{\hat{v}^2}{r} + \hat{w} \frac{\partial \hat{u}}{\partial z} = \nu \frac{\partial^2 \hat{u}}{\partial z^2} - \frac{\sigma}{\rho} B_0^2 \hat{u}, \quad (2.2)$$

$$\hat{u} \frac{\partial \hat{v}}{\partial r} + \frac{\hat{u} \hat{v}}{r} + \hat{w} \frac{\partial \hat{v}}{\partial z} = \nu \frac{\partial^2 \hat{v}}{\partial r^2} - \frac{\sigma}{\rho} B_0^2 \hat{v}, \quad (2.3)$$

$$(\rho c_p)_f \left(\hat{u} \frac{\partial \hat{T}}{\partial r} + \hat{w} \frac{\partial \hat{T}}{\partial z} \right) = \left(k + \frac{16\sigma^* \hat{T}_\infty^3}{3k^*} \right) \frac{\partial^2 \hat{T}}{\partial z^2} + (\rho c_p)_p \left[\frac{D_T}{T_\infty} \left(\frac{\partial T}{\partial z} \right)^2 + D_B \left(\frac{\partial T}{\partial z} \frac{\partial C}{\partial z} \right) \right], \quad (2.4)$$

$$\left(\hat{w} \frac{\partial \hat{C}}{\partial z} + \hat{u} \frac{\partial \hat{C}}{\partial r} \right) = D_B \frac{\partial^2 \hat{C}}{\partial z^2} + \frac{D_T}{T_\infty} \frac{\partial^2 \hat{T}}{\partial z^2}, \quad (2.5)$$

$$\left(\hat{w} \frac{\partial \hat{N}}{\partial z} + \hat{u} \frac{\partial \hat{N}}{\partial r} \right) = -\frac{bW_c}{\hat{C}_w - \hat{C}_\infty} \left[\frac{\partial}{\partial z} \left(\hat{N} \frac{\partial \hat{C}}{\partial z} \right) \right] + D_N \frac{\partial^2 \hat{N}}{\partial z^2}, \quad (2.6)$$

$$\left. \begin{aligned} \hat{u} = ra_1, \quad \hat{v} = r\Omega_1, \quad \hat{w} = 0, \quad \hat{T} = \hat{T}_w, \quad \hat{C} = \hat{C}_w, \quad \hat{N} = \hat{N}_w \text{ at } z = a^* \left(\frac{r}{R_0} + 1 \right)^{-\zeta}, \\ \hat{u} = 0, \quad \hat{v} = 0, \quad \hat{w} = 0, \quad \hat{T} = \hat{T}_\infty, \quad \hat{C} \rightarrow \hat{C}_\infty, \quad \hat{N} \rightarrow \hat{N}_\infty \text{ at } z \rightarrow \infty, \end{aligned} \right\}, \quad (2.7)$$

where σ electrical conductivity, ν kinematic viscosity, ρ density, $(\rho c_p)_f$ and $(\rho c_p)_p$ are base fluid specific heat and the effective heat capacity of the nanoparticles, \hat{C}_w and \hat{C}_∞ the surface and ambient concentrations, \hat{N}_w and \hat{N}_∞ the surface and ambient densities of gyrotactic microorganism, σ^* Stefan-Boltzman constant, R_0 feature radius, k thermal conductivity, k^* mean absorption coefficient, a^* the small thickness coefficient of disk, D_B and D_T the Brownian diffusion coefficient and thermophoretic diffusion coefficient respectively, D_N , b , W_c and ς the diffusivity of microorganisms, chemotaxis constant, maximum speed of swimming cell and the disk thickness index. Letting

$$\left. \begin{aligned} \hat{u} &= r^* R_0 \Omega \tilde{F}(\eta), \quad \hat{v} = r^* R_0 \Omega \tilde{G}(\eta), \quad \hat{w} = R_0 \Omega (1 + r^*)^{-\varsigma} \tilde{H}(\eta), \\ \tilde{\vartheta} &= \frac{\hat{T} - \hat{T}_\infty}{\hat{T}_w - \hat{T}_\infty}, \quad \tilde{\Phi} = \frac{\hat{C} - \hat{C}_\infty}{\hat{C}_w - \hat{C}_\infty}, \quad \tilde{\chi} = \frac{\hat{N} - \hat{N}_\infty}{\hat{N}_w - \hat{N}_\infty}, \quad \eta = \frac{z}{R_0} (1 + r^*)^\varsigma, \end{aligned} \right\} \quad (2.8)$$

the resulting problems are reduced in the form

$$2\tilde{F} + \tilde{H}' + \eta \epsilon^* \varsigma \tilde{F}' = 0, \quad (2.9)$$

$$\tilde{F}'' \frac{1}{\text{Re}} (1 + r^*)^{2\varsigma} - \tilde{F}^2 + \tilde{G}^2 - \tilde{H}\tilde{F}' - \tilde{F}\tilde{F}' \varsigma \eta \epsilon^* - M\tilde{F} = 0, \quad (2.10)$$

$$\tilde{G}'' \frac{1}{\text{Re}} (1 + r^*)^{2\varsigma} - 2\tilde{F}\tilde{G} - \tilde{H}\tilde{G}' - \tilde{F}\tilde{G}' \varsigma \eta \epsilon^* - M\tilde{G} = 0, \quad (2.11)$$

$$\frac{1}{\text{Pr}} (1 + R) \frac{1}{\text{Re}} (1 + r^*)^{2\varsigma} \tilde{\vartheta}'' - \tilde{F}\tilde{\vartheta}' \varsigma \eta \epsilon^* - \tilde{H}\tilde{\vartheta}' + \frac{1}{\text{Re}} (1 + r^*)^{2\varsigma} \left(Nb \tilde{\vartheta}' \tilde{\Phi}' + Nt \tilde{\vartheta}'^2 \right) = 0, \quad (2.12)$$

$$\frac{1}{\text{Pr}} \frac{1}{Le} \frac{1}{\text{Re}} (1 + r^*)^{2\varsigma} \tilde{\Phi}'' - \tilde{H}\tilde{\Phi}' - \varsigma \eta \epsilon^* \tilde{F}\tilde{\Phi}' + \frac{Nt}{Nb} \frac{1}{Le} \frac{1}{\text{Pr}} \frac{1}{\text{Re}} (1 + r^*)^{2\varsigma} \tilde{\vartheta}'' = 0, \quad (2.13)$$

$$\frac{1}{Lb} \frac{1}{\text{Re}} (1 + r^*)^{2\varsigma} \tilde{\chi}'' - \tilde{H}\tilde{\chi}' - \varsigma \eta \epsilon^* \tilde{F}\tilde{\chi}' - \frac{Pe}{Lb} \frac{1}{\text{Re}} (1 + r^*)^{2\varsigma} \left(\tilde{\Phi}' \tilde{\chi}' + \tilde{\chi} \tilde{\Phi}'' \right) = 0, \quad (2.14)$$

$$\left. \begin{aligned} \tilde{H}(\alpha) &= 0, \quad \tilde{F}(\alpha) = A_1, \quad \tilde{G}(\alpha) = 1, \quad \tilde{\vartheta}(\alpha) = 1, \quad \tilde{\Phi}(\alpha) = 1, \quad \tilde{\chi}(\alpha) = 1, \\ \tilde{F}(\infty) &= 0, \quad \tilde{G}(\infty) = 0, \quad \tilde{\vartheta}(\infty) = 0, \quad \tilde{\Phi}(\infty) = 0, \quad \tilde{\chi}(\infty) = 0, \end{aligned} \right\} \quad (2.15)$$

where

$$\begin{aligned}
\epsilon^* &= \frac{r^*}{R_0 + r^*}, \quad \text{Pr} = \frac{(\rho c_p)_p \nu}{k}, \quad \text{Re} = \frac{\Omega_1 R_0^2}{\nu}, \quad A_1 = \frac{a_1}{\Omega_1}, \quad R = \frac{16\sigma^* \hat{T}_\infty^3}{3kk^*}, \quad M = \frac{\sigma B_0^2}{\rho \Omega_1}, \\
Nt &= \frac{(\rho c_p)_p D_T (\hat{T}_w - \hat{T}_\infty)}{(\rho c_p)_f \nu T_\infty}, \quad Nb = \frac{(\rho c_p)_p D_B (\hat{C}_w - \hat{C}_\infty)}{(\rho c_p)_f \nu}, \quad Le = \frac{k}{(\rho c_p)_f D_B}, \\
Lb &= \frac{\nu}{D_N}, \quad Pe = \frac{bW_c}{D_N}, \quad \alpha = \frac{a^*}{R_0},
\end{aligned} \tag{2.16}$$

where ϵ^* is a dimensionless constant, Pr Prandtl number, Re Reynolds number, M magnetic parameter, A_1 scaled stretching parameters, r^* the dimensionless radius, Nt /thermophoresis parameter, Pe bioconvection Peclet number, R radiation parameter, Nb Brownian motion variable, Le and Lb respectively the Lewis and bioconvection Lewis number and α disk thickness coefficient.

Considering

$$\left. \begin{aligned}
\tilde{H} &= \tilde{h}(\eta - \alpha) = \tilde{h}(\xi), \quad \tilde{F} = \tilde{f}(\eta - \alpha) = \tilde{f}(\xi), \\
\tilde{G} &= \tilde{g}(\eta - \alpha) = \tilde{g}(\xi), \quad \tilde{\vartheta} = \tilde{\theta}(\eta - \alpha) = \tilde{\theta}(\xi), \\
\tilde{\varphi} &= \tilde{\phi}(\eta - \alpha) = \tilde{\phi}(\xi), \quad \tilde{\chi} = \tilde{\chi}(\eta - \alpha) = \tilde{\chi}(\xi),
\end{aligned} \right\} \tag{2.17}$$

expressions (2.9 – 2.15) are reduced as follows:

$$2\tilde{f} + \tilde{h}' + (\xi + \alpha)\epsilon^* \zeta \tilde{f}' = 0, \tag{2.18}$$

$$\tilde{f}'' \frac{1}{\text{Re}} (1 + r^*)^{2\zeta} - \tilde{f}^2 + \tilde{g}^2 - \tilde{h}\tilde{f}' - \tilde{f}\tilde{f}'\zeta(\xi + \alpha)\epsilon^* - M\tilde{f} = 0, \tag{2.19}$$

$$\tilde{g}'' \frac{1}{\text{Re}} (1 + r^*)^{2\zeta} - 2\tilde{f}\tilde{g} - \tilde{h}\tilde{g}' - \tilde{f}\tilde{g}'\zeta(\xi + \alpha)\epsilon^* - M\tilde{g} = 0, \tag{2.20}$$

$$\frac{1}{\text{Pr}}(1 + R) \frac{1}{\text{Re}} (1 + r^*)^{2\zeta} \tilde{\theta}'' - \tilde{f}\tilde{\theta}'\zeta(\xi + \alpha)\epsilon^* - \tilde{h}\tilde{\theta}' + \frac{1}{\text{Re}} (1 + r^*)^{2\zeta} \left(Nb\tilde{\theta}'\tilde{\phi}' + Nt\tilde{\theta}'' \right) = 0, \tag{2.21}$$

$$\frac{1}{\text{Pr}} \frac{1}{Le} \frac{1}{\text{Re}} (1 + r^*)^{2\zeta} \tilde{\phi}'' - \tilde{h}\tilde{\phi}' - \zeta\eta\epsilon^* \tilde{f}\tilde{\phi}' + \frac{Nt}{Nb} \frac{1}{Le} \frac{1}{\text{Pr}} \frac{1}{\text{Re}} (1 + r^*)^{2\zeta} \tilde{\theta}'' = 0, \tag{2.22}$$

$$\frac{1}{\text{Pr}} \frac{1}{Lb} \tilde{\chi}'' - \tilde{h}\tilde{\chi}' - \zeta\eta\epsilon^* \tilde{f}\tilde{\chi}' - Pe \frac{1}{\text{Re}} (1 + r^*)^{2\zeta} \left(\tilde{\phi}'\tilde{\chi}' + \tilde{\chi}\tilde{\phi}'' \right) = 0, \tag{2.23}$$

$$\left. \begin{aligned}
\tilde{h}(0) &= 0, \quad \tilde{f}(0) = A_1, \quad \tilde{g}(0) = 1, \quad \tilde{g}(\infty) = 0, \quad \tilde{\theta}(0) = 1, \quad \tilde{\phi}(0) = 1, \quad \tilde{\chi}(0) = 1, \\
\tilde{f}(\infty) &= 0, \quad \tilde{\theta}(\infty) = 0, \quad \tilde{\phi}(\infty) = 0, \quad \tilde{\chi}(\infty) = 0.
\end{aligned} \right\} \tag{2.24}$$

Shear stresses (radial and tangential) are mathematically defined as

$$\left. \begin{aligned} \tau_{zr} &= \mu \left. \frac{\partial \hat{u}}{\partial z} \right|_{z=0} = \frac{\mu r^* \Omega_1 R_0 (1+r^*)^\zeta \tilde{f}'(0)}{R_0}, \\ \tau_{z\theta} &= \mu \left. \frac{\partial \hat{v}}{\partial z} \right|_{z=0} = \frac{\mu r^* \Omega_1 R_0 (1+r^*)^\zeta \tilde{g}'(0)}{R_0}, \end{aligned} \right\} \quad (2.25)$$

and

$$\tau_w = \sqrt{\tau_{zr}^2 + \tau_{z\theta}^2}. \quad (2.26)$$

The mathematical form of (C_{fx}) is

$$C_{fx} \text{Re} = \frac{\tau_w|_{z=0}}{\rho(r\Omega_1)^2} = \frac{1}{r^*} (1+r^*)^\zeta [(\tilde{f}'(0))^2 + (\tilde{g}'(0))^2]^{1/2}. \quad (2.27)$$

The Nusselt number is

$$Nu_x = \left. \frac{R_0 q_w}{k(\hat{T}_w - \hat{T}_\infty)} \right|_{z=0}, \quad (2.28)$$

with heat flux q_w as

$$q_w|_{z=0} = -k \left. \frac{\partial \hat{T}}{\partial z} + q_r \right|_{z=0} = -k(\hat{T}_w - \hat{T}_\infty) (1+R) (1+r^*)^\zeta \tilde{\theta}'(0). \quad (2.29)$$

Final expression of Nusselt number is

$$Nu_x \text{Re}^{\frac{1}{n+1}} = -(1+R) (1+r^*)^\zeta \tilde{\theta}'(0). \quad (2.30)$$

2.2 Methodology

Initial approximations and linear operators are

$$\left. \begin{aligned} \tilde{h}_0(\xi) &= 0, \\ \tilde{f}_0(\xi) &= A_1 e^{-\xi}, \\ \tilde{g}_0(\xi) &= e^{-\xi}, \\ \tilde{\theta}_0(\xi) &= e^{-\xi}, \\ \tilde{\phi}_0(\xi) &= e^{-\xi}, \\ \tilde{\chi}_0(\xi) &= e^{-\xi}, \end{aligned} \right\} \quad (2.31)$$

$$\mathcal{L}_{\tilde{h}} = \tilde{h}', \quad \mathcal{L}_{\tilde{f}} = \tilde{f}'' - \tilde{f}, \quad \mathcal{L}_{\tilde{g}} = \tilde{g}'' - \tilde{g}', \quad \mathcal{L}_{\tilde{\theta}} = \tilde{\theta}'' - \tilde{\theta}, \quad \mathcal{L}_{\tilde{\phi}} = \tilde{\phi}'' - \tilde{\phi}, \quad \mathcal{L}_{\tilde{\chi}} = \tilde{\chi}'' - \tilde{\chi}, \quad (2.32)$$

with

$$\left. \begin{aligned} \mathcal{L}_{\tilde{h}}[\bar{B}_1] &= 0, \\ \mathcal{L}_{\tilde{f}}[\bar{B}_2e^\xi + \bar{B}_3e^{-\xi}] &= 0, \\ \mathcal{L}_{\tilde{g}}[\bar{B}_4e^\xi + \bar{B}_5e^{-\xi}] &= 0, \\ \mathcal{L}_{\tilde{\theta}}[\bar{B}_6e^\xi + \bar{B}_7e^{-\xi}] &= 0, \\ \mathcal{L}_{\tilde{\phi}}[\bar{B}_8e^\xi + \bar{B}_9e^{-\xi}] &= 0, \\ \mathcal{L}_{\tilde{\chi}}[\bar{B}_{10}e^\xi + \bar{B}_{11}e^{-\xi}] &= 0, \end{aligned} \right\} \quad (2.33)$$

where \bar{B}_i ($i = 1 - 11$) are the constants.

Letting $q \in [0, 1]$ denotes the embedding parameter and $(\hbar_{\tilde{h}}, \hbar_{\tilde{f}}, \hbar_{\tilde{g}}, \hbar_{\tilde{\theta}}, \hbar_{\tilde{\phi}}$ and $\hbar_{\tilde{\chi}})$ the auxiliary parameters.

2.2.1 Zeroth-order formulations

$$q\hbar_{\tilde{h}}\mathcal{N}_{\tilde{h}}[H(\xi, q), F(\xi, q)] = (1 - q)\mathcal{L}_{\tilde{h}}[H(\xi, q) - \tilde{h}_0(\xi)], \quad (2.34)$$

$$q\hbar_{\tilde{f}}\mathcal{N}_{\tilde{f}}[F(\xi, q), H(\xi, q), G(\xi, q)] = (1 - q)\mathcal{L}_{\tilde{f}}[F(\xi, q) - \tilde{f}_0(\xi)], \quad (2.35)$$

$$q\hbar_{\tilde{g}}\mathcal{N}_{\tilde{g}}[G(\xi, q), F(\xi, q), H(\xi, q)] = (1 - q)\mathcal{L}_{\tilde{g}}[G(\xi, q) - \tilde{g}_0(\xi)], \quad (2.36)$$

$$q\hbar_{\tilde{\theta}}\mathcal{N}_{\tilde{\theta}}[\vartheta(\xi, q), F(\xi, q), H(\xi, q), \Phi(\xi, q)] = (1 - q)\mathcal{L}_{\tilde{\theta}}[\vartheta(\xi, q) - \tilde{\theta}_0(\xi)], \quad (2.37)$$

$$q\hbar_{\tilde{\phi}}\mathcal{N}_{\tilde{\phi}}[\Phi(\xi, q), F(\xi, q), H(\xi, q), \vartheta(\xi, q)] = (1 - q)\mathcal{L}_{\tilde{\phi}}[\Phi(\xi, q) - \tilde{\phi}_0(\xi)], \quad (2.38)$$

$$q\hbar_{\tilde{\chi}}\mathcal{N}_{\tilde{\chi}}[\chi(\xi, q), \Phi(\xi, q), F(\xi, q), H(\xi, q), \vartheta(\xi, q)] = (1 - q)\mathcal{L}_{\tilde{\chi}}[\chi(\xi, q) - \tilde{\chi}_0(\xi)], \quad (2.39)$$

$$\begin{aligned} H(0, q) &= 0, \quad F(0, q) = A_1, \quad F(\infty, q) = 0, \quad G(0, q) = 1, \quad G(\infty, q) = 0, \quad \vartheta(0, q) = 1, \\ \vartheta(\infty, q) &= 0, \quad \Phi(0, q) = 1, \quad \Phi(\infty, q) = 0, \quad \chi(0, q) = 1, \quad \chi(\infty, q) = 0, \end{aligned} \quad (2.40)$$

where $\mathcal{N}_{\tilde{h}}, \mathcal{N}_{\tilde{f}}, \mathcal{N}_{\tilde{g}}, \mathcal{N}_{\tilde{\theta}}, \mathcal{N}_{\tilde{\phi}}$ and $\mathcal{N}_{\tilde{\chi}}$ are

$$\mathcal{N}_{\tilde{h}}[H(\xi, q), F(\xi, q)] = 2F + \frac{\partial H(\xi, q)}{\partial \xi} + (\xi + \alpha)\epsilon^* \varsigma \frac{\partial F(\xi, q)}{\partial \xi}, \quad (2.41)$$

$$\begin{aligned} \mathcal{N}_{\tilde{f}}[F(\xi, q), H(\xi, q), G(\xi, q)] &= \frac{\partial^2 F(\xi, q)}{\partial \xi^2} \frac{1}{\text{Re}} (1 + r^*)^{2\varsigma} - F^2 + G^2 \\ &\quad - H \frac{\partial F(\xi, q)}{\partial \xi} - F \frac{\partial F(\xi, q)}{\partial \xi} \varsigma (\xi + \alpha) \epsilon^* - MF, \end{aligned} \quad (2.42)$$

$$\begin{aligned} \mathcal{N}_{\tilde{g}}[G(\xi, q), F(\xi, q), H(\xi, q)] &= \frac{\partial^2 G(\xi, q)}{\partial \xi^2} \frac{1}{\text{Re}} (1 + r^*)^{2\varsigma} - 2FG \\ &\quad - H \frac{\partial G(\xi, q)}{\partial \xi} - F \frac{\partial G(\xi, q)}{\partial \xi} \varsigma (\xi + \alpha) \epsilon^* - MG, \end{aligned} \quad (2.43)$$

$$\begin{aligned} \mathcal{N}_{\tilde{\theta}}[\vartheta(\xi, q), F(\xi, q), H(\xi, q), \Phi(\xi, q)] &= \frac{1}{\text{Pr}} (1 + R) \frac{1}{\text{Re}} (1 + r^*)^{2\varsigma} \frac{\partial^2 \vartheta(\xi, q)}{\partial \xi^2} - F \frac{\partial \vartheta(\xi, q)}{\partial \xi} \varsigma (\xi + \alpha) \epsilon^* - H \frac{\partial \vartheta(\xi, q)}{\partial \xi} \\ &\quad + \frac{1}{\text{Re}} (1 + r^*)^{2\varsigma} \left(Nb \frac{\partial \vartheta(\xi, q)}{\partial \xi} \frac{\partial \Phi(\xi, q)}{\partial \xi} + Nt \left(\frac{\partial \vartheta(\xi, q)}{\partial \xi} \right)^2 \right), \end{aligned} \quad (2.44)$$

$$\begin{aligned} \mathcal{N}_{\tilde{\phi}}[\Phi(\xi, q), F(\xi, q), H(\xi, q), \vartheta(\xi, q)] &= \frac{1}{\text{Pr}} \frac{1}{Le} \frac{1}{\text{Re}} (1 + r^*)^{2\varsigma} \frac{\partial^2 \Phi(\xi, q)}{\partial \xi^2} - H \frac{\partial \Phi(\xi, q)}{\partial \xi} \\ &\quad - \varsigma \eta \epsilon^* F \frac{\partial \Phi(\xi, q)}{\partial \xi} + \frac{Nt}{Nb} \frac{1}{Le} \frac{1}{\text{Pr}} \frac{1}{\text{Re}} (1 + r^*)^{2\varsigma} \frac{\partial^2 \vartheta(\xi, q)}{\partial \xi^2}, \end{aligned} \quad (2.45)$$

$$\begin{aligned} \mathcal{N}_{\tilde{\chi}}[\chi(\xi, q), \Phi(\xi, q), F(\xi, q), H(\xi, q), \vartheta(\xi, q)] &= \frac{1}{\text{Pr}} \frac{1}{Lb} \frac{\partial^2 \chi(\xi, q)}{\partial \xi^2} - h \frac{\partial \chi(\xi, q)}{\partial \xi} - \varsigma \eta \epsilon^* f \frac{\partial \chi(\xi, q)}{\partial \xi} \\ &\quad - Pe \frac{1}{\text{Re}} (1 + r^*)^{2\varsigma} \left(\frac{\partial \Phi(\xi, q)}{\partial \xi} \frac{\partial \chi(\xi, q)}{\partial \xi} + \chi \frac{\partial^2 \Phi(\xi, q)}{\partial \xi^2} \right), \end{aligned} \quad (2.46)$$

2.2.2 m^{th} order problems

We can write

$$\left. \begin{aligned} \tilde{h}_{\tilde{h}} \mathcal{R}_{\tilde{h}, m}(\xi) &= \mathcal{L}_{\tilde{h}} \left[\tilde{h}_m(\xi) - \check{\chi}_m \tilde{h}_{m-1}(\xi) \right], \\ \tilde{h}_{\tilde{f}} \mathcal{R}_{\tilde{f}, m}(\xi) &= \mathcal{L}_{\tilde{f}} \left[\tilde{f}_m(\xi) - \check{\chi}_m \tilde{f}_{m-1}(\xi) \right], \\ \tilde{h}_{\tilde{g}} \mathcal{R}_{\tilde{g}, m}(\xi) &= \mathcal{L}_{\tilde{g}} \left[\tilde{g}_m(\xi) - \check{\chi}_m \tilde{g}_{m-1}(\xi) \right], \\ \tilde{h}_{\tilde{\theta}} \mathcal{R}_{\tilde{\theta}, m}(\xi) &= \mathcal{L}_{\tilde{\theta}} \left[\tilde{\theta}_m(\xi) - \check{\chi}_m \tilde{\theta}_{m-1}(\xi) \right], \\ \tilde{h}_{\tilde{\phi}} \mathcal{R}_{\tilde{\phi}, m}(\xi) &= \mathcal{L}_{\tilde{\phi}} \left[\tilde{\phi}_m(\xi) - \check{\chi}_m \tilde{\phi}_{m-1}(\xi) \right], \\ \tilde{h}_{\tilde{\chi}} \mathcal{R}_{\tilde{\chi}, m}(\xi) &= \mathcal{L}_{\tilde{\chi}} \left[\tilde{\chi}_m(\xi) - \check{\chi}_m \tilde{\chi}_{m-1}(\xi) \right], \end{aligned} \right\} \quad (2.47)$$

$$\begin{aligned}
\tilde{h}_m(0, q) &= \tilde{f}_m(0, q) = \tilde{f}_m(\infty, q) = \tilde{g}_m(0, q) = \tilde{g}_m(\infty, q) = \tilde{\theta}_m(0, q) = 0, \\
\tilde{\theta}_m(\infty, q) &= \tilde{\phi}_m(0, q) = \tilde{\phi}_m(\infty, q) = \tilde{\chi}_m(0, q) = \tilde{\chi}_m(\infty, q) = 0,
\end{aligned} \tag{2.48}$$

where $\mathcal{R}_{\tilde{h},m}(\xi)$, $\mathcal{R}_{\tilde{f},m}(\xi)$, $\mathcal{R}_{\tilde{g},m}(\xi)$, $\mathcal{R}_{\tilde{\theta},m}(\xi)$, $\mathcal{R}_{\tilde{\phi},m}(\xi)$ and $\mathcal{R}_{\tilde{\chi},m}(\xi)$ are

$$\mathcal{R}_{\tilde{h},m}(\xi) = 2\tilde{f}_{m-1} + \tilde{h}'_{m-1} + (\xi + \alpha)\epsilon\varsigma\tilde{f}'_{m-1}, \tag{2.49}$$

$$\begin{aligned}
\mathcal{R}_{\tilde{f},m}(\xi) &= \tilde{f}''_{m-1} \frac{1}{\text{Re}} (1+r^*)^{2\varsigma} - \sum_{k=0}^{m-1} \tilde{f}_{m-1-k} \tilde{f}'_k + \sum_{k=0}^{m-1} \tilde{g}_{m-1-k} \tilde{g}'_k - \sum_{k=0}^{m-1} \tilde{h}_{m-1-k} \tilde{f}'_k \\
&\quad - \sum_{k=0}^{m-1} \tilde{f}_{m-1-k} \tilde{f}'_k \varsigma (\xi + \alpha) \epsilon^* - \sum_{k=0}^{m-1} M \tilde{f}_{m-1},
\end{aligned} \tag{2.50}$$

$$\mathcal{R}_{\tilde{g},m}(\xi) = \tilde{g}''_{m-1} \frac{1}{\text{Re}} (1+r^*)^{2\varsigma} - 2 \sum_{k=0}^{m-1} \tilde{f}_{m-1-k} \tilde{g}'_k - \sum_{k=0}^{m-1} \tilde{h}_{m-1-k} \tilde{g}'_k - \sum_{k=0}^{m-1} \tilde{f}_{m-1-k} \tilde{g}'_k \varsigma (\xi + \alpha) \epsilon^* - M \tilde{g}_{m-1}, \tag{2.51}$$

$$\begin{aligned}
\mathcal{R}_{\tilde{\theta},m}(\xi) &= \frac{1}{\text{Pr}} (1+R) \frac{1}{\text{Re}} (1+r^*)^{2\varsigma} \tilde{\theta}''_{m-1} - \sum_{k=0}^{m-1} \tilde{f}_{m-1} \tilde{\theta}'_{m-1} \varsigma (\xi + \alpha) \epsilon^* - \sum_{k=0}^{m-1} \tilde{h}_{m-1} \tilde{\theta}'_{m-1} \\
&\quad + \frac{1}{\text{Re}} (1+r^*)^{2\varsigma} \left(Nb \sum_{k=0}^{m-1} \tilde{\theta}'_{m-1} \tilde{\phi}'_{m-1} + Nt \sum_{k=0}^{m-1} \tilde{\theta}'_{m-1} \tilde{\theta}'_{m-1} \right),
\end{aligned} \tag{2.52}$$

$$\mathcal{R}_{\tilde{\phi},m}(\xi) = \frac{1}{\text{Pr}} \frac{1}{Le} \frac{1}{\text{Re}} (1+r^*)^{2\varsigma} \tilde{\phi}''_{m-1} - \sum_{k=0}^{m-1} \tilde{h}_{m-1} \tilde{\phi}'_{m-1} - \varsigma \eta \epsilon^* \sum_{k=0}^{m-1} \tilde{f}_{m-1} \tilde{\phi}'_{m-1} + \frac{Nt}{Nb} \frac{1}{Le} \frac{1}{\text{Pr}} \frac{1}{\text{Re}} (1+r^*)^{2\varsigma} \tilde{\theta}''_{m-1}, \tag{2.53}$$

$$\begin{aligned}
\mathcal{R}_{\tilde{\chi},m}(\xi) &= \frac{1}{\text{Pr}} \frac{1}{Lb} \tilde{\chi}''_{m-1} - \sum_{k=0}^{m-1} \tilde{h}_{m-1} \tilde{\chi}'_{m-1} - \varsigma \eta \epsilon^* \sum_{k=0}^{m-1} \tilde{f}_{m-1} \tilde{\chi}'_{m-1} \\
&\quad - Pe \frac{1}{\text{Re}} (1+r^*)^{2\varsigma} \left(\sum_{k=0}^{m-1} \tilde{\phi}'_{m-1} \tilde{\chi}'_{m-1} + \sum_{k=0}^{m-1} \tilde{\chi}_{m-1} \tilde{\phi}''_{m-1} \right),
\end{aligned} \tag{2.54}$$

$$\tilde{\chi}_m = \begin{cases} 0, & m \leq 1 \\ 1, & m > 1 \end{cases}. \tag{2.55}$$

The solutions $(\tilde{h}_m(\xi), \tilde{f}_m(\xi), \tilde{g}_m(\xi), \tilde{\theta}_m(\xi), \tilde{\phi}_m(\xi), \tilde{\chi}_m(\xi))$ comprising the special solutions $(\tilde{h}_m^*(\xi), \tilde{f}_m^*(\xi), \tilde{g}_m^*(\xi), \tilde{\theta}_m^*(\xi), \tilde{\phi}_m^*(\xi), \tilde{\chi}_m^*(\xi))$ are

$$\left. \begin{aligned} \tilde{h}_m(\xi) &= \tilde{h}_m^*(\xi) + \bar{B}_1, \\ \tilde{f}_m(\xi) &= \tilde{f}_m^*(\xi) + \bar{B}_2 e^\xi + \bar{B}_3 e^{-\xi}, \\ \tilde{g}_m(\xi) &= \tilde{g}_m^*(\xi) + \bar{B}_4 e^\xi + \bar{B}_5 e^{-\xi}, \\ \tilde{\theta}_m(\xi) &= \tilde{\theta}_m^*(\xi) + \bar{B}_6 e^\xi + \bar{B}_7 e^{-\xi}, \\ \tilde{\phi}_m(\xi) &= \tilde{\phi}_m^*(\xi) + \bar{B}_8 e^\xi + \bar{B}_9 e^{-\xi}, \\ \tilde{\chi}_m(\xi) &= \tilde{\chi}_m^*(\xi) + \bar{B}_{10} e^\xi + \bar{B}_{11} e^{-\xi}, \end{aligned} \right\} \quad (2.56)$$

where value of constants \bar{B}_i ($i = 1 - 11$) by using boundary conditions are

$$\begin{aligned} \bar{B}_3 &= -\tilde{f}_m^*(0), \quad \bar{B}_5 = -\tilde{g}_m^*(0), \quad \bar{B}_7 = -\tilde{\theta}_m^*(0), \quad \bar{B}_9 = -\tilde{\phi}_m^*(\xi), \quad \bar{B}_{11} = -\tilde{\chi}_m^*(\xi), \\ \bar{B}_1 &= \bar{B}_2 = \bar{B}_4 = \bar{B}_6 = \bar{B}_8 = \bar{B}_{10} = 0. \end{aligned} \quad (2.57)$$

2.3 Convergence analysis

The series solutions convergence is accelerated by $\tilde{h}_h, \tilde{h}_f, \tilde{h}_g, \tilde{h}_\theta, \tilde{h}_\phi$ and \tilde{h}_χ . For appropriate ranges of these variables the \tilde{h} -curves are drawn at 13th order of approximations. It is apparent from Figs. (2.2-2.4) that suitable ranges of parameters are $-1.2 \leq \tilde{h}_h \leq -0.3$, $-1.2 \leq \tilde{h}_f \leq -0.2$, $-1 \leq \tilde{h}_g \leq -0.5$, $-1.2 \leq \tilde{h}_\theta \leq -0.9$, $-1.1 \leq \tilde{h}_\phi \leq -0.4$ and $-1 \leq \tilde{h}_\chi \leq -0.5$. Table 1 is constructed to analyze the convergent series solutions. It is seen that 21st order of approximation is enough for convergent homotopy solutions. Table 2 gives averaged squared residual errors by optimal values of $\tilde{h}_h, \tilde{h}_f, \tilde{h}_g, \tilde{h}_\theta, \tilde{h}_\phi$ and \tilde{h}_χ . Table 3 is constructed for validation of our problem by giving comparison to numerical limiting solution by Xun et al. [21].

To obtain the values of $\tilde{h}_h, \tilde{h}_f, \tilde{h}_g, \tilde{h}_\theta, \tilde{h}_\phi$ and \tilde{h}_χ , we have utilized concept of minimization proposed by Liao [39] by characterizing the average squared residual errors.

$$\epsilon_m^{\tilde{h}} = \frac{1}{k^\circ + 1} \sum_{j=0}^{k^\circ} \left[\mathcal{N}_{\tilde{h}} \left(\sum_{i=0}^m \tilde{h}(\xi), \sum_{i=0}^m \tilde{f}(\xi) \right)_{\xi=j\delta\xi} \right]^2, \quad (2.58)$$

$$\varepsilon_m^{\tilde{f}} = \frac{1}{k^\circ + 1} \sum_{j=0}^{k^\circ} \left[\mathcal{N}_{\tilde{f}} \left(\sum_{i=0}^m \tilde{f}(\xi), \sum_{i=0}^m \tilde{h}(\xi), \sum_{i=0}^m \tilde{g}(\xi) \right)_{\xi=j\delta\xi} \right]^2, \quad (2.59)$$

$$\varepsilon_m^{\tilde{g}} = \frac{1}{k^\circ + 1} \sum_{j=0}^{k^\circ} \left[\mathcal{N}_{\tilde{g}} \left(\sum_{i=0}^m \tilde{g}(\xi), \sum_{i=0}^m \tilde{h}(\xi), \sum_{i=0}^m \tilde{f}(\xi) \right)_{\xi=j\delta\xi} \right]^2, \quad (2.60)$$

$$\varepsilon_m^{\tilde{\theta}} = \frac{1}{k^\circ + 1} \sum_{j=0}^{k^\circ} \left[\mathcal{N}_{\tilde{\theta}} \left(\sum_{i=0}^m \tilde{\theta}(\xi), \sum_{i=0}^m \tilde{h}(\xi), \sum_{i=0}^m \tilde{f}(\xi), \sum_{i=0}^m \tilde{\phi}(\xi) \right)_{\xi=j\delta\xi} \right]^2, \quad (2.61)$$

$$\varepsilon_m^{\tilde{\phi}} = \frac{1}{k^\circ + 1} \sum_{j=0}^{k^\circ} \left[\mathcal{N}_{\tilde{\phi}} \left(\sum_{i=0}^m \tilde{\phi}(\xi), \sum_{i=0}^m \tilde{h}(\xi), \sum_{i=0}^m \tilde{f}(\xi), \sum_{i=0}^m \tilde{\theta}(\xi) \right)_{\xi=j\delta\xi} \right]^2, \quad (2.62)$$

$$\varepsilon_m^{\tilde{\chi}} = \frac{1}{k^\circ + 1} \sum_{j=0}^{k^\circ} \left[\mathcal{N}_{\tilde{\chi}} \left(\sum_{i=0}^m \tilde{\chi}(\xi), \sum_{i=0}^m \tilde{h}(\xi), \sum_{i=0}^m \tilde{f}(\xi), \sum_{i=0}^m \tilde{\phi}(\xi) \right)_{\xi=j\delta\xi} \right]^2, \quad (2.63)$$

Following Liao [31]

$$\varepsilon_m^t = \varepsilon_m^{\tilde{h}} + \varepsilon_m^{\tilde{f}} + \varepsilon_m^{\tilde{g}} + \varepsilon_m^{\tilde{\theta}} + \varepsilon_m^{\tilde{\phi}} + \varepsilon_m^{\tilde{\chi}}, \quad (2.64)$$

where the total squared residual error is denoted by ε_m^t , $\delta\xi = 0.5$ and $k^\circ = 20$. Total average squared residual error is minimized by using MATHEMATICA BVPb2.0. At 2^{nd} order of approximations, the values of convergence control parameter are $h_{\tilde{h}} = -0.525242$, $h_{\tilde{f}} = -0.438242$, $h_{\tilde{g}} = -0.528742$, $h_{\tilde{\theta}} = -1.18546$, $h_{\tilde{\phi}} = -0.52956$ and $h_{\tilde{\chi}} = -0.54956$ and $\varepsilon_m^t = 0.5 \times 10^{-3}$. Table 2.1 is arranged for the individual average squared residual error at

$m = 2$. Here we noticed that the ε_m^t for higher order approximations is decreased.

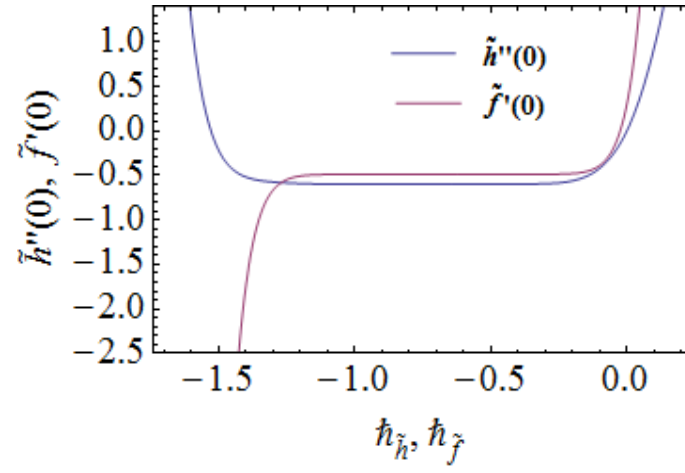


Fig. 2.2: \hbar -curve for $\tilde{h}''(0)$ and $\tilde{f}'(0)$.

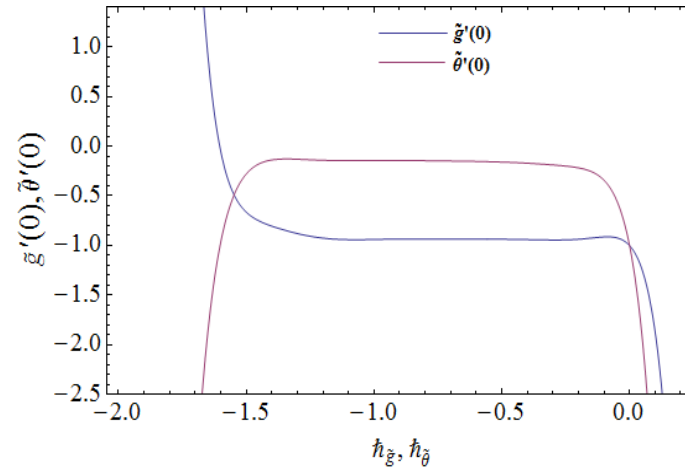


Fig. 2.3: \hbar -curve for $\tilde{g}'(0)$ and $\tilde{\theta}'(0)$.

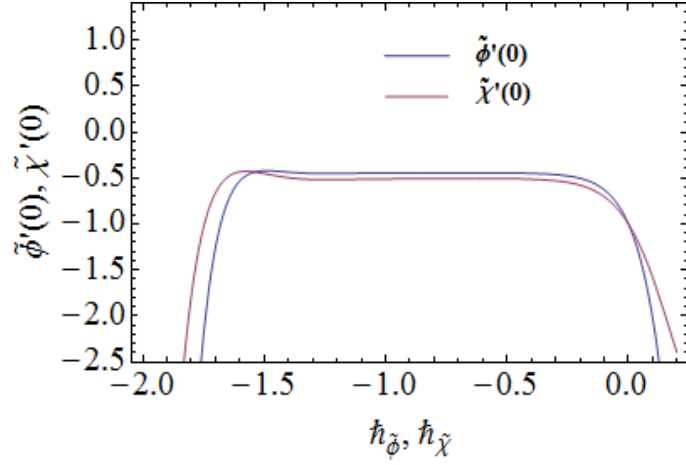


Fig. 2.4: h -curve for $\tilde{\phi}'(0)$ and $\tilde{\chi}'(0)$.

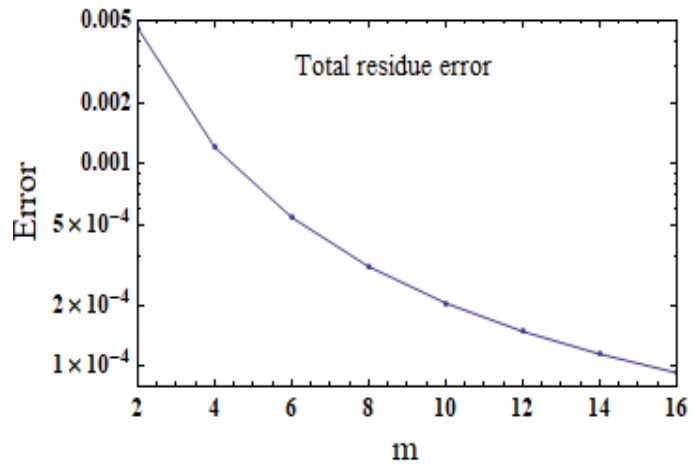


Fig. 2.5: Total residue error.

Table 2.1: Convergence table for solutions when $\zeta = 1$, $\epsilon^* = 0.3$, $\alpha = 1.2$, $\text{Re} = 1$, $r^* = 0.2$, $M = 0.7$, $A_1 = 0.3$, $\text{Pr} = 1.9$, $R = 0.1$, $Le = 1$, $Nb = 1$, $Nt = 0.1$, $Le = 1$, $Pe = 0.1$, $Lb = 0.7$.

Order of approximations	$-\tilde{h}''(0)$	$-\tilde{f}'(0)$	$-\tilde{g}'(0)$	$-\tilde{\theta}'(0)$	$-\tilde{\phi}'(0)$	$-\tilde{\chi}'(0)$
1	0.3444	0.5151	0.8488	0.3064	0.6760	0.7718
10	0.5964	0.4868	0.9367	0.1559	0.4429	0.5049
16	0.5965	0.4868	0.9352	0.1461	0.4448	0.5093
18	0.5966	0.4868	0.9353	0.1453	0.4451	0.5103
21	0.5966	0.4868	0.9353	0.1446	0.4455	0.5101
22	0.5966	0.4868	0.9353	0.1445	0.4456	0.5101
24	0.5966	0.4868	0.9353	0.1445	0.4456	0.5101
30	0.5966	0.4868	0.9353	0.1445	0.4456	0.5101
40	0.5966	0.4868	0.9353	0.1445	0.4456	0.5101
50	0.5966	0.4868	0.9353	0.1445	0.4456	0.5101

Table 2.2: Individual averaged squared residual errors.

m	$\varepsilon_m^{\tilde{h}}$	$\varepsilon_m^{\tilde{f}}$	$\varepsilon_m^{\tilde{g}}$	$\varepsilon_m^{\tilde{\theta}}$	$\varepsilon_m^{\tilde{\phi}}$	$\varepsilon_m^{\tilde{\chi}}$
2	0.000045231	0.000070508	0.00548584	0.00365332	0.00091408	0.00254444
4	0.000012545	0.0000120884	0.00078887	0.000819915	0.000366413	0.00065585
8	3.25888×10^{-7}	8.87321×10^{-7}	4.25545×10^{-5}	0.000127616	0.000181346	5.35894×10^{-6}
10	1.23585×10^{-7}	3.49176×10^{-7}	2.02545×10^{-5}	0.0000622279	0.000142131	2.25655×10^{-6}
16	2.23584×10^{-9}	8.34518×10^{-8}	2.34554×10^{-7}	0.0000110888	0.0000817474	1.25644×10^{-6}

Table 2.3: Validation of results with Ref. [12] when $\varsigma = 0$, $Pr = Re = 1$, $M = R = A_1 = Nb = Nt = 0$.

Articles	$-\tilde{\theta}'(0)$	$\tilde{f}'(0)$	$-\tilde{g}'(0)$
Present	0.3959	0.5109	0.61598
Xun et al. [12]	0.396271	0.510231	0.615921

2.4 Discussion

For clear understanding of the nanofluid flow with involvement of microorganisms we examine the physics of the problem by analyzing the behavior of flow parameters for the velocity, temperature, concentration of nanoparticles, motile density, surface drag force and heat transfer

rate by fixing $\varsigma = 1$, $\epsilon^* = 0.3$, $\alpha = 1.2$, $\text{Re} = 1$, $r^* = 0.2$, $M = 0.7$, $A_1 = 0.3$, $\text{Pr} = 1.9$, $R = 0.1$, $Le = 1$, $Nb = 1$, $Nt = 0.1$, $Le = 1$, $Pe = 0.1$, $Lb = 0.7$, $\tilde{h}_{\tilde{h}} = \tilde{h}_{\tilde{f}} = \tilde{h}_{\tilde{g}} = \tilde{h}_{\tilde{\theta}} = \tilde{h}_{\tilde{\phi}} = \tilde{h}_{\tilde{\chi}} = -0.7$ (See Figs. (2.5-2.30) and Tables 2.4 and 2.5).

2.4.1 Axial, radial and tangential velocity components

Figs. (2.6 – 2.8) show impact of magnetic parameter M on axial, radial and tangential velocity distributions. It is noticed that axial $\tilde{h}(\xi)$, radial $\tilde{f}(\xi)$ and tangential velocity $\tilde{g}(\xi)$ profiles decline for increasing M . For rising magnetic parameter the Lorentz force enhances and consequently the resistance between particles occur. Examination of axial $\tilde{h}(\xi)$, radial $\tilde{f}(\xi)$ and tangential $\tilde{g}(\xi)$ velocity distributions for elevating values of stretching parameter A_1 is shown in Figs. (2.9 – 2.11). With increase in A_1 the stretching rate enhances so velocity in axial and radial direction increases while tangential velocity is decreasing function of A_1 . Impact of disk thickness power law index ς on velocities ($\tilde{h}(\xi)$, $\tilde{f}(\xi)$ and $\tilde{g}(\xi)$) is shown in Figs. (2.12 – 2.14). Here magnitude of $\tilde{h}(\xi)$, $\tilde{f}(\xi)$ and $\tilde{g}(\xi)$ decay for higher ς .

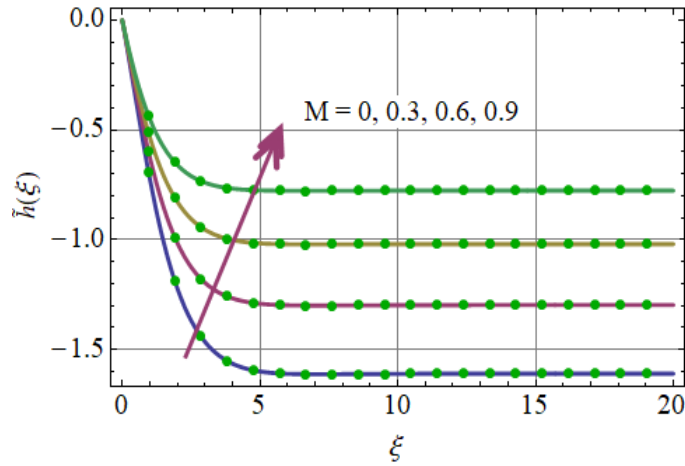


Fig. 2.6: Axial velocity $\tilde{h}(\xi)$ via M .

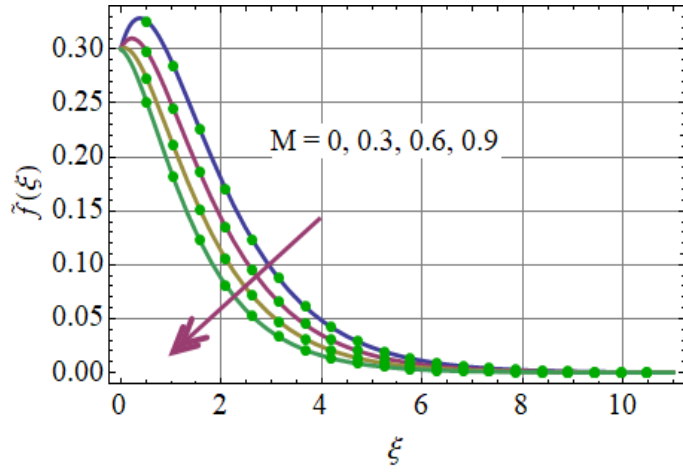


Fig. 2.7: Radial velocity $\tilde{f}(\xi)$ via M .

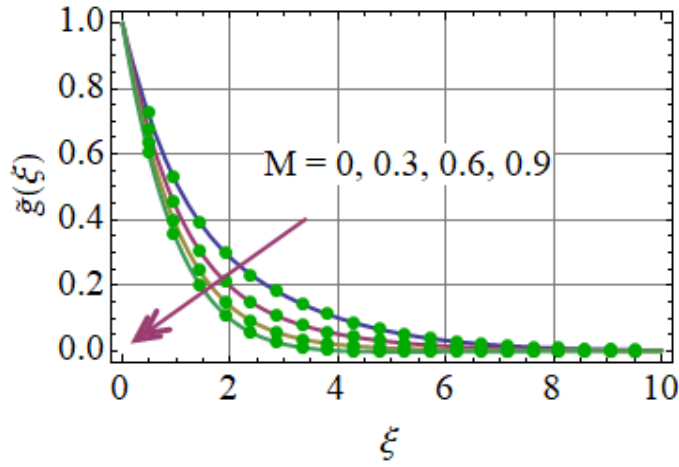


Fig. 2.8: Tangential velocity $\tilde{g}(\xi)$ via M .

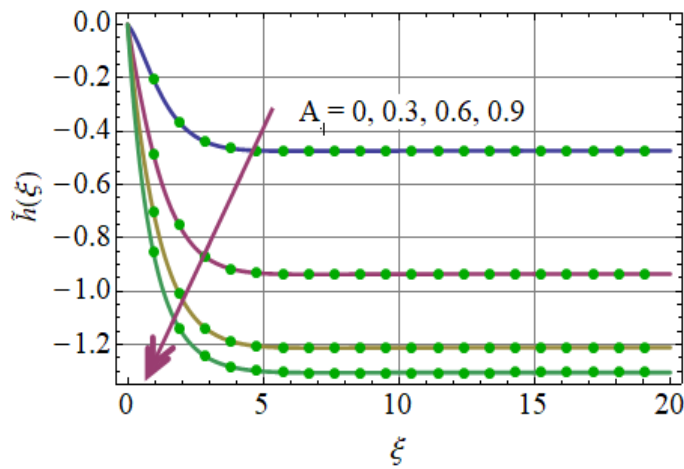


Fig. 2.9: Axial velocity $\tilde{h}(\xi)$ via A_1 .

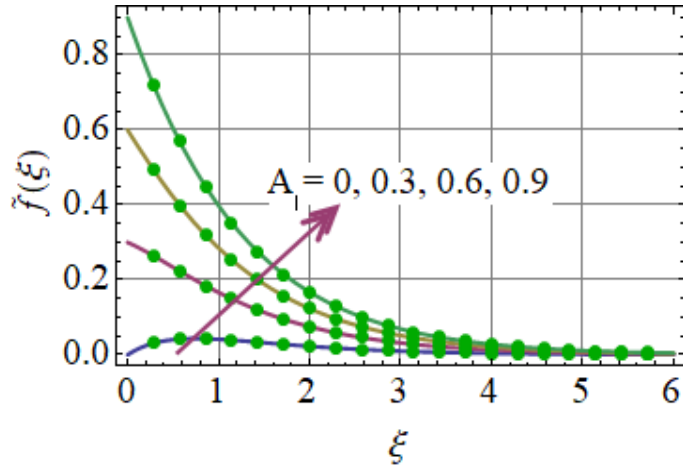


Fig. 2.10: Radial velocity $\tilde{f}(\xi)$ via A_1 .

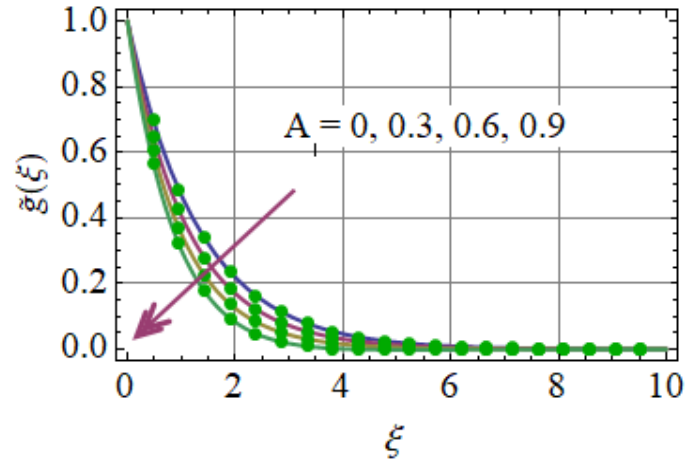


Fig. 2.11: Tangential velocity $\tilde{g}(\xi)$ via A_1 .

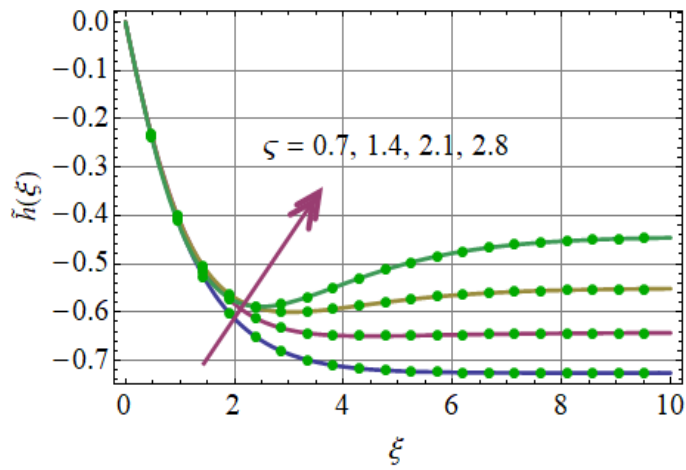


Fig. 2.12: Axial velocity $\tilde{h}(\xi)$ via ζ .

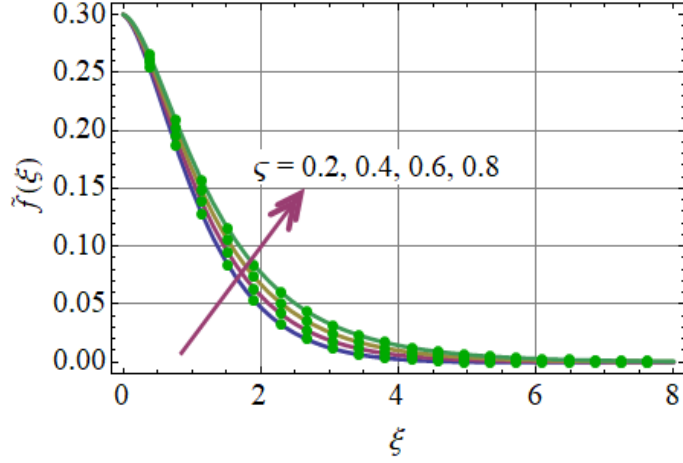


Fig. 2.13: Radial velocity $\tilde{f}(\xi)$ via ζ .

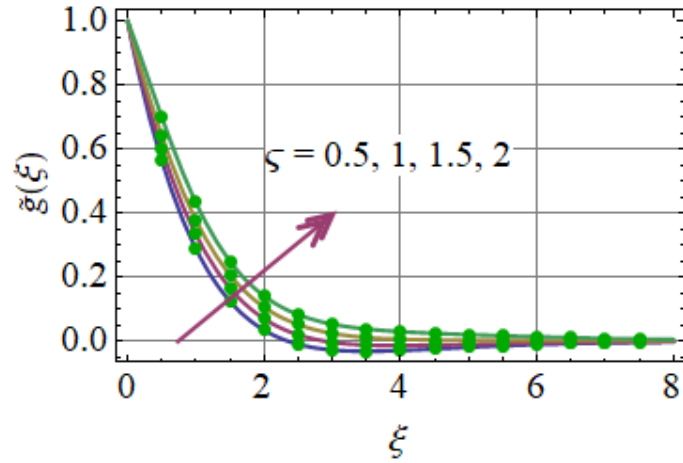


Fig. 2.14: Tangential velocity $\tilde{g}(\xi)$ via ζ .

2.4.2 Temperature

Figs. (2.15 – 2.18) have been displayed to show impacts of involved variables on temperature distribution $\tilde{\theta}(\xi)$. Fig. 2.15 is portrayed for prediction of Nb on temperature. Here temperature and layer thickness are enhanced for higher Nb . It is due to more random motion of particles. Influence of Nt on thermal field is presented in Fig. 2.16. Clearly, temperature of liquid increases when Nt is enhanced. In fact an increment of Nt induces the enhancement of thermophoresis force which will in general move nanoparticles from hot to the cold side and thusly temperature of liquid upgrades. For larger Prandtl number Pr the temperature decays (see Fig. 2.17). For higher Pr the thermal conductivity of fluid reduces so temperature decays. For increasing values

of R temperature of fluid enhances because radiation is ratio of enthalpy to kinetic energy (See Fig. 2.18).

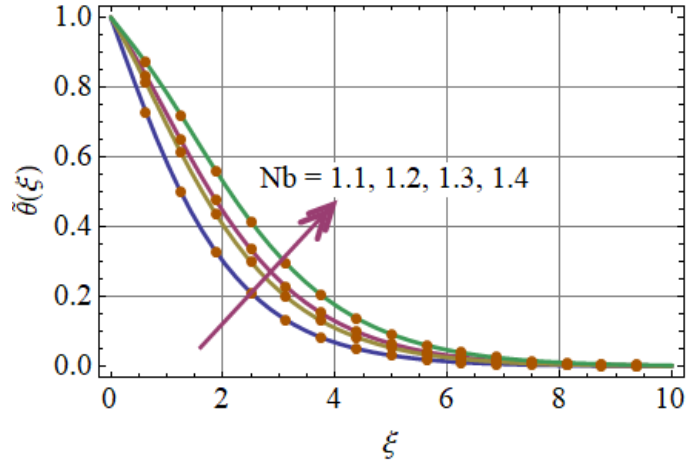


Fig. 2.15: Temperature $\tilde{\theta}(\xi)$ via Nb .

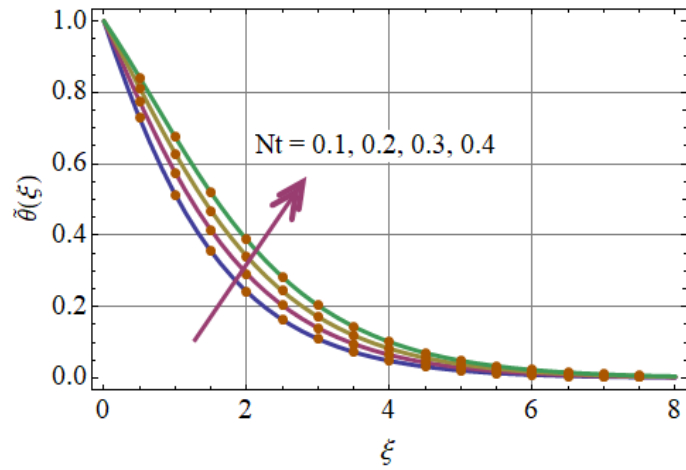


Fig. 2.16: Temperature $\tilde{\theta}(\xi)$ via Nt .

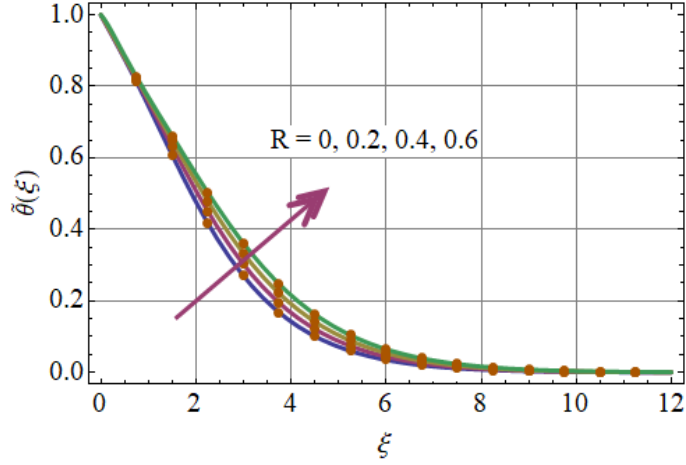


Fig. 2.17: Temperature $\tilde{\theta}(\xi)$ via R .

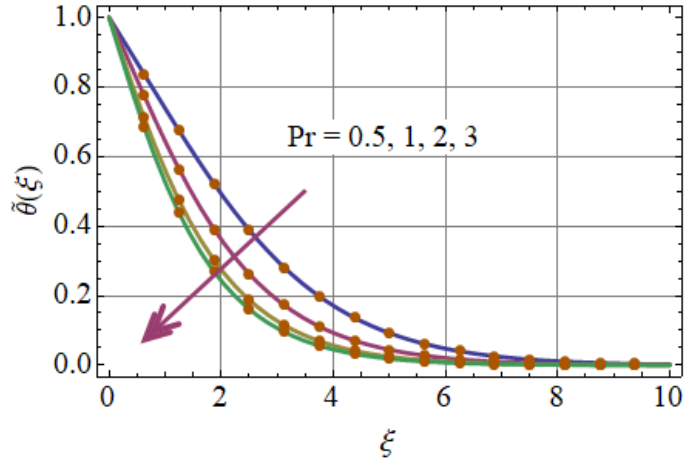


Fig. 2.18: Temperature $\tilde{\theta}(\xi)$ via Pr .

2.4.3 Concentration

Effect of involved parameters of concentration profile $\tilde{\phi}(\xi)$ is seen in Figs. (2.19–2.22). Behavior of Lewis number Le is shown in Fig. 2.19. Concentration enhances for larger Le . Enhancement of Le is proportional to weaker mass diffusivity and thin concentration layer thickness. Impact of Nb and Nt on concentration field is portrayed in Figs. 2.20 and 2.21. For larger Nb the nanoparticles concentration decreases whereas reverse is found via larger Nt . In fact for larger

Pr the concentration decays (See Fig. 2.22).

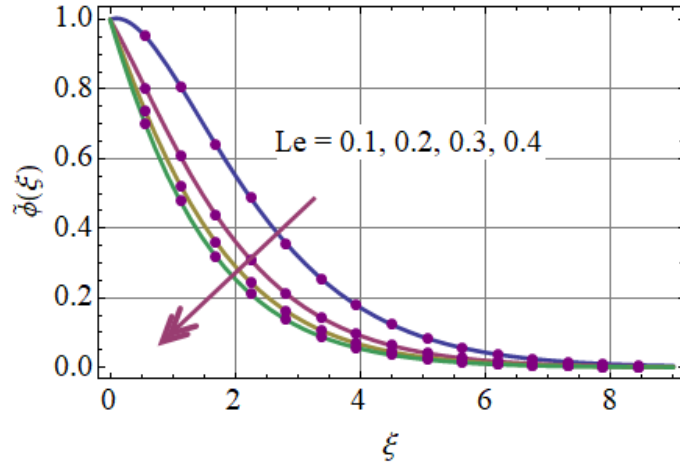


Fig. 2.19: Concentration $\tilde{\phi}(\xi)$ via Le .

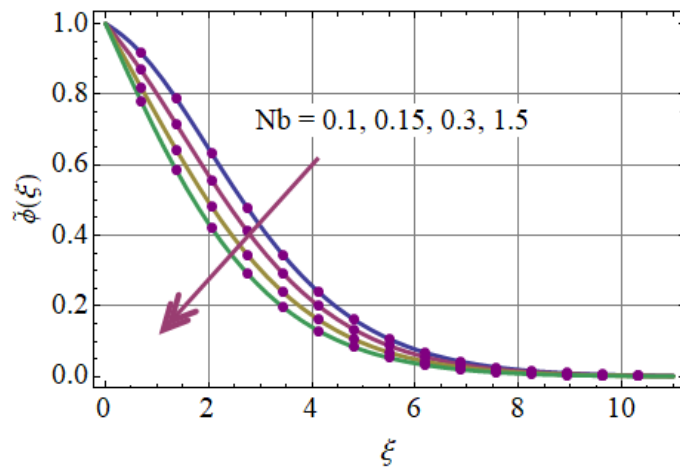


Fig. 2.20: Concentration $\tilde{\phi}(\xi)$ via Nb .

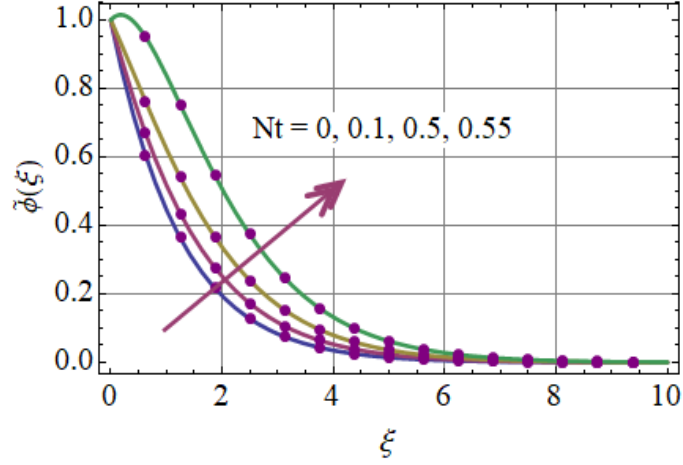


Fig. 2.21: Concentration $\tilde{\phi}(\xi)$ via Nt .

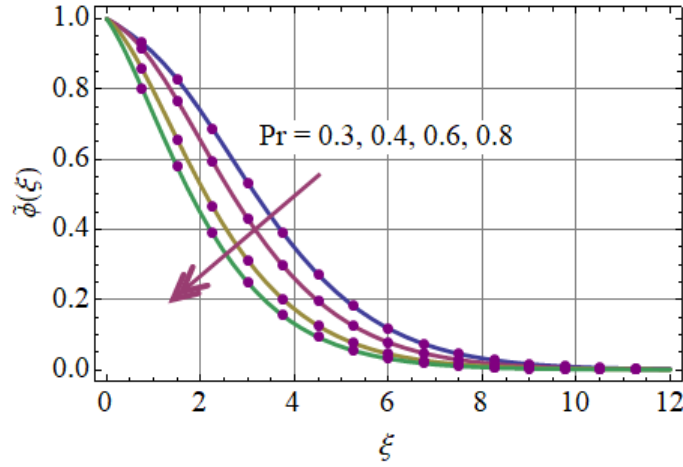


Fig. 2.22: Concentration $\tilde{\phi}(\xi)$ via Pr .

2.4.4 Density

Figs. (2.23-2.27) predict impact of pertinent variables on density $\tilde{\chi}(\xi)$. Figs. 2.23 and 2.24 plot the influence of bioconvection Peclet number Pe and bioconvection Lewis number Lb on density $\tilde{\chi}(\xi)$. Both parameters show decreasing impact on density $\tilde{\chi}(\xi)$. Due to decrease in diffusivity of microorganisms for higher Pe the motile density of fluid decays. Similarly diffusivity of microorganisms decays for larger Lb which is responsible for decay in $\tilde{\chi}(\xi)$. Impacts of Lewis number Le and Prandtl number Pr on $\tilde{\chi}(\xi)$ are shown in Figs. 2.25 and 2.26. For larger Le the density $\tilde{\chi}(\xi)$ enhances whereas reverse is noticed via Pr . Fig. 2.27 plots impact of thermophoresis parameter Nt on motile density $\tilde{\chi}(\xi)$. It is seen that motile density enhances

for larger Nt .

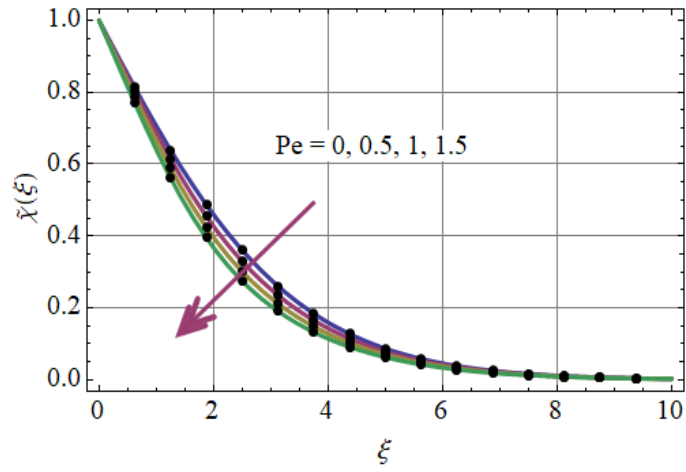


Fig. 2.23: Motile density via Pe .

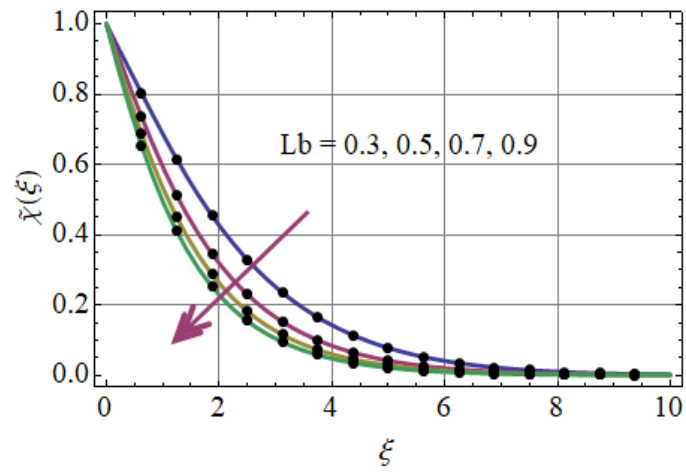


Fig. 2.24: Motile density via Lb .

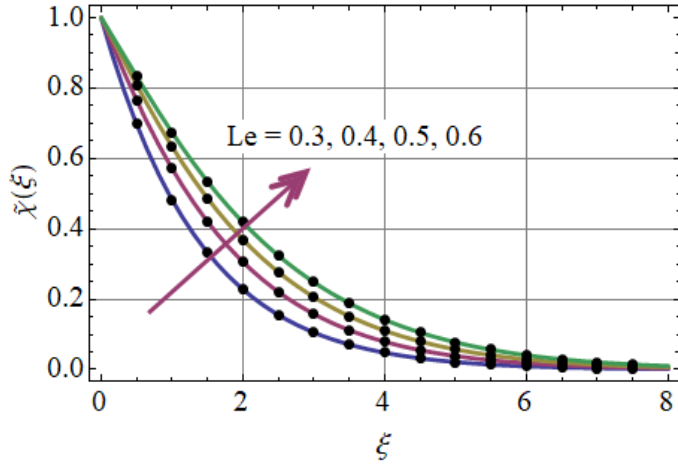


Fig. 2.25: Motile density via Pe .

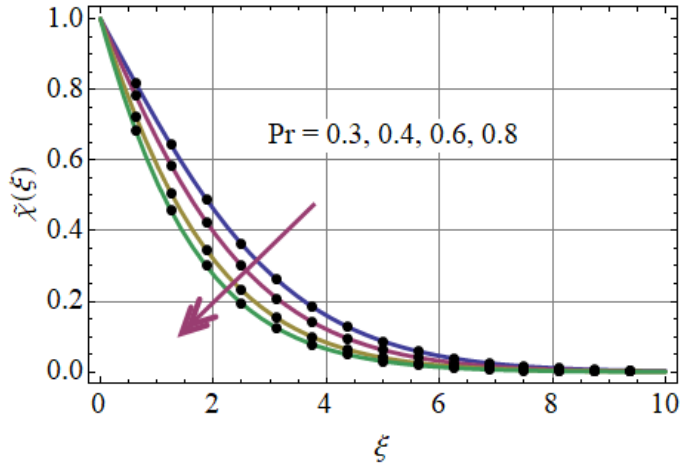


Fig. 2.26: Motile density via Pe .

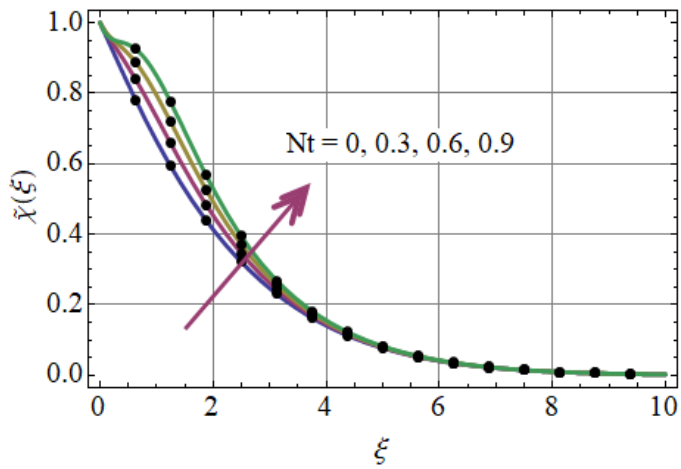


Fig. 2.27: Motile density via Pe .

2.4.5 Surface drag force

Table 2.4 displays the numerical declaration for skin friction coefficient. It is clear that for higher disk thickness coefficient α the drag force at surface reduces while opposite effect is observed for larger stretching parameter A_1 and magnetic parameter M .

Table 2.4: Numerical analysis of skin friction versus α , M and A_1 .

α	M	A_1	$C_{fx} Re$
1.2	0.7	0.3	0.2245
1.3			0.2237
1.4			0.2229
1.2	0.8		0.2316
	0.9		0.2393
	0.7	0.4	0.2384
		0.5	0.2549

2.4.6 Nusselt number

Impacts of R , Nt and Nb on $(Nu_x Re^{\frac{-1}{n+1}})$ is displayed in Table 2.5. Magnitude of $(Nu_x Re^{\frac{-1}{n+1}})$ is more for higher R while it decays via larger Nb and Nt .

Table 2.5: Computational analysis of $(Nu_x Re^{\frac{-1}{n+1}})$.

R	Nb	Nt	$Nu_x Re^{\frac{-1}{n+1}}$
0.1	1	0.1	-0.2235
0.2			-0.2490
0.3			-0.2707
0.1	1.1		-0.1961
	1.2		-0.1735
	1	0.2	-0.2097
		0.3	-0.1992

2.5 Conclusions

Here suspension of nanoparticles and gyrotactic microorganism in radiative flow by variable thicked rotating disk is analyzed. Major results are summarized as follows:

- Magnetic parameter M has opposite impact on velocities (radial, axial and tangential).
- Temperature distribution is enhanced for Nb , Nt and R .
- Larger Le , Nb and Pr give rise to decay in the concentration.
- Impacts of Pe , Lb and Pr on motile density are decreasing.
- Behavior of skin friction for larger M is increasing.
- Nb and Nt decrease the heat transfer rate.

Chapter 3

Rotating disk flow of nanomaterial with mixed convection and entropy generation

Abstract: This chapter addresses mixed convective rotating flow of viscous fluid. Thermal radiation, Joule heating, variable thickness and viscous dissipation have been accounted. Flow under consideration is because of nonlinear stretching of disk. Water is used as base fluid while nanoparticles comprise silver and copper. Fluid is electrically conducting subject to applied magnetic field with constant strength. Heat generation and absorption are neglected. Entropy generation is utilized through second law of thermodynamics. The effects of silver and copper nanoparticles on the thermal conductivity of continuous phase fluid and entropy generation have been also examined. Total entropy generation rate is scrutinized for different involved variables. Nonlinear formulation based upon conservation laws is made. Attention is particularly given to the convergence in the computational process. Velocity and thermal gradients at the surface of disk are obtained in tabular forms. Main conclusions have been indicated.

Keywords: Entropy generation; Bejan number; Rotating disk; Copper and silver nanoparticles; Joule heating; Viscous dissipation; Thermal radiation.

3.1 Problem formulation

Here steady, incompressible viscous liquid flow of silver and copper nanomaterial is addressed by a rotating variable thicked surface of disk. A constant magnetic field is applied normal to the flow. Induced magnetic field is ignored. Thermal radiation and Joule heating are also considered in present flow configuration with additional effects of viscous dissipation. Disk is located at $z = a^* \left(\frac{r}{R_0} + 1 \right)^{-\varsigma}$ with stretching rate a_1 (in r -direction) and angular velocity Ω_1 . The components of flow velocity $(\hat{u}, \hat{v}, \hat{w})$ are in the directions of increasing (r, ϑ, z) respectively. Temperature at surface of disk is denoted by \hat{T}_w while ambient temperature being \hat{T}_∞ . The schematic diagram and coordinate system are depicted in Fig. 3.1.

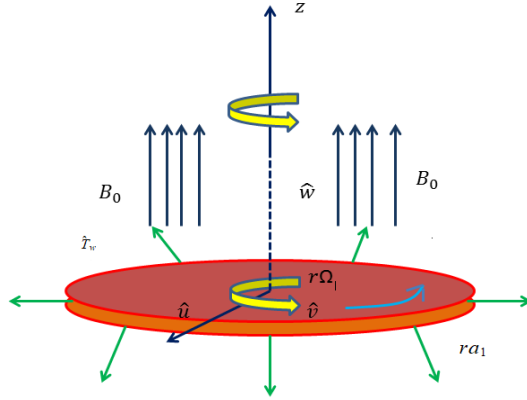


Fig. 3.1: Problem geometry.

The governing equations are

$$\frac{\partial \hat{u}}{\partial r} + \frac{\partial \hat{w}}{\partial z} + \frac{\hat{u}}{r} = 0, \quad (3.1)$$

$$\hat{u} \frac{\partial \hat{u}}{\partial r} - \frac{\hat{v}^2}{r} + \hat{w} \frac{\partial \hat{u}}{\partial z} = \nu_{nf} \frac{\partial^2 \hat{u}}{\partial z^2} - \frac{\sigma_{nf}}{\rho_{nf}} B_0^2 \hat{u} + g \frac{(\beta \rho)_{nf}}{\rho_{nf}} (\hat{T} - \hat{T}_\infty), \quad (3.2)$$

$$\hat{u} \frac{\partial \hat{v}}{\partial r} + \frac{\hat{u} \hat{v}}{r} + \hat{w} \frac{\partial \hat{v}}{\partial z} = \nu_{nf} \frac{\partial^2 \hat{v}}{\partial z^2} - \frac{\sigma_{nf}}{\rho_{nf}} B_0^2 \hat{v}, \quad (3.3)$$

$$(\rho c_p)_{nf} \left(\hat{u} \frac{\partial \hat{T}}{\partial r} + \hat{w} \frac{\partial \hat{T}}{\partial z} \right) = \left(k_{nf} + \frac{16\sigma^* \hat{T}_\infty^3}{3k^*} \right) \frac{\partial^2 \hat{T}}{\partial z^2} + \frac{\sigma_{nf}}{(\rho c_p)_{nf}} B_0^2 (\hat{u}^2 + \hat{v}^2) + \frac{\mu_{nf}}{(\rho c_p)_{nf}} \left[\left(\frac{\partial \hat{u}}{\partial z} \right)^2 + \left(\frac{\partial \hat{v}}{\partial z} \right)^2 \right], \quad (3.4)$$

with conditions

$$\left. \begin{aligned} \hat{u} = ra_1, \hat{v} = r\Omega_1, \hat{w} = 0, \hat{T} = \hat{T}_w \text{ at } z = a^* \left(\frac{r}{R_0} + 1 \right)^{-\varsigma}, \\ \hat{u} = 0, \hat{v} = 0, \hat{T} = \hat{T}_\infty \text{ at } z \rightarrow \infty, \end{aligned} \right\} \quad (3.5)$$

in which $\hat{T}, \sigma^*, a^*, k^*, \eta, \mu_{nf}, (\beta\rho)_{nf}, \rho_{nf}, k_{nf}, \nu_{nf}, \sigma_{nf}$ and $(\rho c_p)_{nf}$ denote the temperature, Stefan-Boltzman constant, small parameter regarding surface, mean absorption coefficient, scaled boundary layer coordinate, effective dynamic viscosity, volumetric thermal expansion coefficient, density, thermal conductivity, kinematic viscosity, electrical conductivity and heat capacitance.

These quantities are defined as [26]:

$$\left. \begin{aligned} \mu_{nf} = \frac{\mu_f}{(1-\phi)^{2.5}}, (\rho\beta)_{nf} = (\rho\beta)_f(1-\phi) + (\rho\beta)_s\phi, \frac{k_{nf}}{k_f} = \frac{k_s+2k_f-2\phi(k_f-k_s)}{k_s+2k_f+2\phi(k_f-k_s)}, \\ \nu_{nf} = \frac{\mu_{nf}}{\rho_{nf}}, \rho_{nf} = \rho_f(1-\phi) + \rho_s\phi, \frac{\sigma_{nf}}{\sigma_f} = 1 + \frac{3\left(\frac{\sigma_s}{\sigma_f}-1\right)\phi}{\left(\frac{\sigma_s}{\sigma_f}+2\right)-\left(\frac{\sigma_s}{\sigma_f}-1\right)\phi}, \\ (\rho c_p)_{nf} = (\rho c_p)_f(1-\phi) + (\rho c_p)_s\phi, \end{aligned} \right\} \quad (3.6)$$

in which subscripts nf, ϕ, s and f stand for nanofluid, nanoparticle volume fraction, nano-solid particles and base liquid.

We consider

$$\left. \begin{aligned} \hat{u} = r^* R_0 \Omega_1 \tilde{F}(\eta), \hat{v} = r^* R_0 \Omega_1 \tilde{G}(\eta), \hat{w} = R_0 \Omega_1 (1+r^*)^{-\varsigma} \left(\frac{\Omega_1 R_0^2 \rho_f}{\mu_f} \right)^{\frac{-1}{n+1}} \tilde{H}(\eta), \\ \tilde{\vartheta} = \frac{\hat{T}-\hat{T}_\infty}{\hat{T}_w-\hat{T}_\infty}, \eta = \frac{z}{R_0} (1+r^*)^\varsigma \left(\frac{\Omega_1 R_0^2 \rho_f}{\mu_f} \right)^{\frac{1}{n+1}}, \end{aligned} \right\} \quad (3.7)$$

where $\varsigma, R_0, n, r^*, \tilde{F}, \tilde{G}, \tilde{H}$, denote disk thickness coefficient, feature radius, power law index, dimensionless radius and self-similar radial, tangential and axial velocities respectively.

Using these transformations the Eqs. (3.1 – 3.5) become

$$2\tilde{F} + \tilde{H}' + \eta\epsilon^*\varsigma\tilde{F}' = 0, \quad (3.8)$$

$$\left. \begin{aligned} \tilde{F}''(\text{Re})^{\frac{1-n}{1+n}} (1+r^*)^{2\varsigma} \frac{1}{(1-\phi)^{5/2}} \left(\frac{1}{1-\phi+\frac{\rho_s}{\rho_f}\phi} \right) - \tilde{F}^2 + \tilde{G}^2 - \tilde{H}\tilde{F}' - \tilde{F}\tilde{F}'\varsigma\eta\epsilon^* \\ - \left(\frac{M}{1-\phi+\frac{\rho_s}{\rho_f}\phi} \right) \frac{\sigma_{nf}}{\sigma_f} \tilde{F} + \lambda \left(\frac{1-\phi+\frac{(\beta\rho)_s}{(\beta\rho)_f}\phi}{1-\phi+\frac{\rho_s}{\rho_f}\phi} \right) \tilde{\vartheta} = 0, \end{aligned} \right\} \quad (3.9)$$

$$\tilde{G}''(\text{Re})^{\frac{1-n}{1+n}}(1+r^*)^{2\varsigma} \frac{1}{(1-\phi)^{5/2}} \left(\frac{1}{1-\phi + \frac{\rho_s}{\rho_f} \phi} \right) - 2\tilde{F}\tilde{G} - \left(\frac{M}{1-\phi + \frac{\rho_s}{\rho_f} \phi} \right) \frac{\sigma_{nf}}{\sigma_f} \tilde{G} - \tilde{H}\tilde{G}' - \tilde{F}\tilde{G}'\varsigma\eta\epsilon^* = 0, \quad (3.10)$$

$$\left. \begin{aligned} & \frac{1}{\text{Pr}} \left(\frac{k_{nf}}{k_f} + R \right) (\text{Re})^{\frac{1-n}{1+n}} (1+r^*)^{2\varsigma} \left(\frac{1}{1-\phi + \frac{(\rho_{cp})_s}{(\rho_{cp})_f} \phi} \right) \tilde{\vartheta}'' - \tilde{F}\tilde{\vartheta}'\varsigma\eta\epsilon^* - \tilde{H}\tilde{\vartheta}' \\ & + MEC \frac{\sigma_{nf}}{\sigma_f} \left(\frac{1}{1-\phi + \frac{(\rho_{cp})_s}{(\rho_{cp})_f} \phi} \right) (\tilde{F}^2 + \tilde{G}^2) + Ec(\text{Re})^{\frac{1-n}{1+n}} (1+r^*)^\varsigma \frac{1}{(1-\phi)^{5/2}} \left(\frac{1}{1-\phi + \frac{(\rho_{cp})_s}{(\rho_{cp})_f} \phi} \right) (\tilde{F}'^2 + \tilde{G}'^2) = 0, \end{aligned} \right\} \quad (3.11)$$

$$\left. \begin{aligned} & \tilde{H}(\alpha) = 0, \quad \tilde{F}(\alpha) = A_1, \quad \tilde{G}(\alpha) = 1, \quad \tilde{\vartheta}(\alpha) = 1, \\ & \tilde{F}(\infty) = 0, \quad \tilde{G}(\infty) = 0, \quad \tilde{\vartheta}(\infty) = 0. \end{aligned} \right\} \quad (3.12)$$

Considering

$$\left. \begin{aligned} & \tilde{H}(\eta) = \tilde{h}(\eta - \alpha) = \tilde{h}(\xi), \\ & \tilde{F}(\eta) = \tilde{f}(\eta - \alpha) = \tilde{f}(\xi), \\ & \tilde{G}(\eta) = \tilde{g}(\eta - \alpha) = \tilde{g}(\xi), \\ & \tilde{\vartheta}(\eta) = \tilde{\theta}(\eta - \alpha) = \tilde{\theta}(\xi), \end{aligned} \right\} \quad (3.13)$$

we obtain

$$2\tilde{f} + \tilde{h}' + (\xi + \alpha)\epsilon^*\varsigma\tilde{f}' = 0, \quad (3.14)$$

$$\left. \begin{aligned} & \tilde{f}''(\text{Re})^{\frac{1-n}{1+n}}(1+r^*)^{2\varsigma} \frac{1}{(1-\phi)^{5/2}} \left(\frac{1}{1-\phi + \frac{\rho_s}{\rho_f} \phi} \right) - \tilde{f}^2 + \tilde{g}^2 - \tilde{h}\tilde{f}' - \tilde{f}\tilde{f}'\varsigma(\xi + \alpha)\epsilon^* \\ & - \left(\frac{M}{1-\phi + \frac{\rho_s}{\rho_f} \phi} \right) \frac{\sigma_{nf}}{\sigma_f} \tilde{f} + \lambda \left(\frac{1-\phi + \frac{(\beta\rho)_s}{(\beta\rho)_f} \phi}{1-\phi + \frac{\rho_s}{\rho_f} \phi} \right) \tilde{\theta} = 0, \end{aligned} \right\} \quad (3.15)$$

$$\left. \begin{aligned} & \tilde{g}''(\text{Re})^{\frac{1-n}{1+n}}(1+r^*)^{2\varsigma} \frac{1}{(1-\phi)^{5/2}} \left(\frac{1}{1-\phi + \frac{\rho_s}{\rho_f} \phi} \right) - 2\tilde{f}\tilde{g} - \tilde{h}\tilde{g}' - \tilde{f}\tilde{g}'\varsigma(\xi + \alpha)\epsilon^* \\ & - \left(\frac{M}{1-\phi + \frac{\rho_s}{\rho_f} \phi} \right) \frac{\sigma_{nf}}{\sigma_f} \tilde{g} = 0, \end{aligned} \right\} \quad (3.16)$$

$$\left. \begin{aligned} & \frac{1}{\text{Pr}} \left(\frac{k_{nf}}{k_f} + R \right) (\text{Re})^{\frac{1-n}{1+n}} (1+r^*)^{2\varsigma} \left(\frac{1}{1-\phi + \frac{(\rho_{cp})_s}{(\rho_{cp})_f} \phi} \right) \tilde{\theta}'' - \tilde{f}\tilde{\theta}'\varsigma(\xi + \alpha)\epsilon^* - \tilde{h}\tilde{\theta}' \\ & + MEC \frac{\sigma_{nf}}{\sigma_f} \left(\frac{1}{1-\phi + \frac{(\rho_{cp})_s}{(\rho_{cp})_f} \phi} \right) (\tilde{f}^2 + \tilde{g}^2) + Ec(\text{Re})^{\frac{1-n}{1+n}} (1+r^*)^\varsigma \frac{1}{(1-\phi)^{5/2}} \left(\frac{1}{1-\phi + \frac{(\rho_{cp})_s}{(\rho_{cp})_f} \phi} \right) (\tilde{f}'^2 + \tilde{g}'^2) = 0, \end{aligned} \right\} \quad (3.17)$$

$$\left. \begin{aligned} & \tilde{h}(0) = 0, \quad \tilde{f}(0) = A_1, \quad \tilde{f}(\infty) = 0, \quad \tilde{g}(0) = 1, \\ & \tilde{g}(\infty) = 0, \quad \tilde{\theta}(0) = 1, \quad \tilde{\theta}(\infty) = 0, \end{aligned} \right\} \quad (3.18)$$

$$\left. \begin{aligned} \text{Re} &= \frac{\Omega_1 R_0^2}{\nu_f}, \quad M = \frac{\sigma_f B_0^2}{\rho_f \Omega_1}, \quad \text{Pr} = \frac{(\rho c_p)_f \nu_f}{k_f}, \quad R = \frac{16\sigma^* \hat{T}_\infty^3}{3k^* k_f}, \quad A_1 = \frac{a_1}{\Omega_1}, \\ Ec &= \frac{r^2 \Omega_1^2}{c_p (\hat{T}_w - \hat{T}_\infty)}, \quad \lambda = \frac{g \beta_f (\hat{T}_w - \hat{T}_\infty)}{r \Omega_1^2}, \quad \alpha = \frac{a^*}{R_0} \left(\frac{\Omega_1 R_0^2 \rho_f}{\mu_f} \right)^{\frac{-1}{n+1}}, \\ \epsilon^* &= \frac{r^*}{R_0 + r^*}, \end{aligned} \right\} \quad (3.19)$$

in which Re denotes Reynold number, M magnetic interaction parameter, Ec the Eckert number, A_1 the ratio of stretching rate to angular velocity, λ the mixed convection parameter, Pr the Prandtl number, α disk thickness coefficient, R the radiation parameter and ϵ^* the dimensionless constant.

3.2 Quantities of engineers interest

3.2.1 Surface drag force

Drag force is defined as

$$C_f = \frac{\sqrt{\tau_{zr}^2 + \tau_{z\theta}^2}}{\rho_f (\Omega_1 r)^2}, \quad (3.20)$$

where τ_{zr} and $\tau_{z\theta}$ is defined as

$$\tau_{zr} = \mu_{nf} \left. \frac{\partial \hat{u}}{\partial z} \right|_{z=0} = \frac{\mu_f r^* \Omega_1 R_0 (1 + r^*)^\varsigma \left(\frac{\Omega R_0^2 \rho_f}{\mu_f} \right)^{\frac{1}{n+1}} \tilde{f}'(0)}{(1 - \phi)^{5/2} R_0}, \quad (3.21)$$

$$\tau_{z\theta} = \mu_{nf} \left. \frac{\partial \hat{v}}{\partial z} \right|_{z=0} = \frac{\mu_f r^* \Omega_1 R_0 (1 + r^*)^\varsigma \left(\frac{\Omega R_0^2 \rho_f}{\mu_f} \right)^{\frac{1}{n+1}} \tilde{g}'(0)}{(1 - \phi)^{5/2} R_0}. \quad (3.22)$$

Total shear stress τ_w is defined by

$$\tau_w = \sqrt{\tau_{zr}^2 + \tau_{z\theta}^2}. \quad (3.23)$$

Putting Eqs. (3.21) and (3.22) in Eq. (3.20) one arrives at

$$C_{fx} \text{Re}^{\frac{n-1}{n+1}} = \frac{\tau_w|_{z=0}}{\rho_f (r \Omega_1)^2} = \frac{1}{(1 - \phi)^{5/2}} \frac{1}{r^*} (1 + r^*)^\varsigma [(\tilde{f}'(0))^2 + (\tilde{g}'(0))^2]^{1/2}. \quad (3.24)$$

3.2.2 Heat transfer rate

Mathematical expression of heat transfer rate is

$$Nu_x = \frac{R_0 q_w}{k_f (\hat{T}_w - \hat{T}_\infty)} \Big|_{z=0}, \quad (3.25)$$

where q_w is

$$q_w|_{z=0} = -k_{nf} \frac{\partial \hat{T}}{\partial z} + q_r \Big|_{z=0} = -k_f (\hat{T}_f - \hat{T}_\infty) (1 + r^*)^\varsigma \left(\frac{\Omega R_0^2 \rho}{\mu_f} \right)^{\frac{1}{n+1}} \left(\frac{k_{nf}}{k_f} + R \right) \tilde{\theta}'(0). \quad (3.26)$$

Finally, one has

$$Nu_x Re^{\frac{-1}{n+1}} = -(1 + r^*)^\varsigma \left(\frac{k_{nf}}{k_f} + R \right) \tilde{\theta}'(0). \quad (3.27)$$

3.3 Exploration of entropy generation

Dimensional equation of entropy generation is

$$S_G = \frac{k_f}{\hat{T}_w^2} \left[\frac{k_{nf}}{k_f} \left(\frac{\partial \hat{T}}{\partial z} \right)^2 + \frac{16\sigma^* \hat{T}_\infty^3}{3k^* k_f} \left(\frac{\partial \hat{T}}{\partial z} \right)^2 \right] + \frac{\mu_{nf}}{\hat{T}_w} \Phi + \frac{\sigma_{nf}}{\hat{T}_w} B_0^2 (\hat{u}^2 + \hat{v}^2), \quad (3.28)$$

where

$$\Phi = 2 \left[\left(\frac{\partial \hat{u}}{\partial r} \right)^2 + \left(\frac{\partial \hat{v}}{\partial z} \right)^2 + \frac{1}{r^2} \left(\frac{\partial \hat{v}}{\partial \vartheta} + \hat{u} \right)^2 \right] + \left[\frac{1}{r} \frac{\partial \hat{w}}{\partial \vartheta} + \frac{\partial \hat{v}}{\partial z} \right]^2 \Bigg\}, \quad (3.29)$$

$$+ \left[\frac{\partial \hat{w}}{\partial r} + \frac{\partial \hat{u}}{\partial z} \right]^2 + \left[r \frac{\partial}{\partial r} \left(\frac{\hat{v}}{r} \right) + \frac{1}{r} \frac{\partial \hat{u}}{\partial \vartheta} \right]^2,$$

$$\Phi = 2 \left[\left(\frac{\partial \hat{u}}{\partial r} \right)^2 + \frac{1}{r^2} (\hat{u})^2 + \left(\frac{\partial \hat{w}}{\partial z} \right)^2 \right] + \left[\frac{\partial \hat{v}}{\partial z} \right]^2 \Bigg\}, \quad (3.30)$$

$$+ \left[\frac{\partial \hat{u}}{\partial z} \right]^2 + \left[r \frac{\partial}{\partial r} \left(\frac{\hat{v}}{r} \right) \right]^2$$

Invoking Eq. (3.30) in (3.28), we arrive

$$S_G = \underbrace{\frac{k_f}{\hat{T}_w^2} \left[\frac{k_{nf}}{k_f} \left(\frac{\partial \hat{T}}{\partial z} \right)^2 + \frac{16\sigma^\circ \hat{T}_\infty^3}{3k^\circ k_f} \left(\frac{\partial \hat{T}}{\partial z} \right)^2 \right]}_{\text{Thermal irreversibility}} + \underbrace{\frac{\mu_{nf}}{\hat{T}_w} \left[2 \left(\frac{\partial \hat{u}}{\partial r} \right)^2 + \frac{2}{r^2} (\hat{u})^2 + 2 \left(\frac{\partial \hat{w}}{\partial z} \right)^2 + \left[\frac{\partial \hat{v}}{\partial z} \right]^2 + \left[\frac{\partial \hat{u}}{\partial z} \right]^2 + \left[r \frac{\partial}{\partial r} \left(\frac{\hat{v}}{r} \right) \right]^2 \right]}_{\text{Fluid friction irreversibility}} + \underbrace{\frac{\sigma_{nf}}{\hat{T}_w} B_0^2 (\hat{u}^2 + \hat{v}^2)}_{\text{Joule dissipation irreversibility}} \quad (3.31)$$

Equation (3.31) witnesses the contribution of three main sources for entropy generation i.e., heat transfer with radiation effects, fluid friction irreversibility and Joule dissipation irreversibility. In dimensionless form, the entropy number is

$$N_G = \left(\frac{k_{nf}}{k_f} + R \right) \tilde{\theta}'^2 \alpha_1 (\text{Re})^{\frac{1-n}{1+n}} (1+r^*)^{2\zeta} + \frac{Br}{\text{Re}} \frac{1}{(1-\phi)^{5/2}} \left[\begin{aligned} &2(\xi + \alpha)^2 \epsilon^2 \zeta^2 \tilde{f}'^2 + 4\tilde{f}^2 + 4\tilde{f}\tilde{f}'(\xi + \alpha)\epsilon^* \zeta \\ &+ 2\tilde{h}'^2 + r^{*2} (\text{Re})^{\frac{2}{1+n}} (1+r^*)^{2\zeta} \tilde{g}'^2 + \\ &r^{*2} (\text{Re})^{\frac{2}{1+n}} (1+r^*)^{2\zeta} \tilde{f}'^2 + (\xi + \alpha)^2 (\epsilon^*)^2 \zeta^2 \tilde{g}'^2 \\ &+ M \frac{\sigma_{nf}}{\sigma_f} Br r^{*2} (\tilde{f}^2 + \tilde{g}^2), \end{aligned} \right] \quad (3.32)$$

$$\alpha_1 = \frac{\hat{T}_w - \hat{T}_\infty}{\hat{T}_f} = \frac{\Delta T}{\hat{T}_w}, \quad Br = \frac{\mu_f \Omega_1^2 R_0^2}{k_f \Delta T}, \quad N_G = \frac{\hat{T}_f S_G \nu_f}{k_f \Delta T \Omega_1}. \quad (3.33)$$

Here α_1 denotes the dimensionless temperature difference, Br Brinkman number and N_G entropy generation rate.

Irreversibility subject to heat transfer dominants when $Be \gg 0.5$. On the other side when $Be \ll 0.5$ the viscous effects dominates. For $Be = 0.5$ both effects are equal. The Bejan number is addressed as

$$Be = \frac{\text{Entropy generation due to heat transfer}}{\text{Total entropy generation}}, \quad (3.34)$$

or

$$Be = \frac{\left(\frac{k_{nf}}{k_f} + R\right) \tilde{\theta}'^2 \alpha_1 (\text{Re})^{\frac{1-n}{1+n}} (1+r^*)^{2\varsigma}}{\left(\frac{k_{nf}}{k_f} + R\right) \tilde{\theta}'^2 \alpha_1 (\text{Re})^{\frac{1-n}{1+n}} (1+r^*)^{2\varsigma} + \frac{Br}{\text{Re}} \frac{1}{(1-\phi)^{5/2}} \left[\begin{array}{l} 2(\xi + \alpha)^2 (\epsilon^*)^2 \varsigma^2 \tilde{f}'^2 + 4\tilde{f}^2 + 4\tilde{f}\tilde{f}'(\xi + \alpha)\epsilon^*\varsigma \\ + 2\tilde{h}'^2 + r^{*2}(\text{Re})^{\frac{2}{1+n}} (1+r^*)^{2\varsigma} \tilde{g}'^2 + \\ r^{*2}(\text{Re})^{\frac{2}{1+n}} (1+r^*)^{2\varsigma} \tilde{f}'^2 + (\xi + \alpha)^2 (\epsilon^*)^2 \varsigma^2 \tilde{g}'^2 \\ + MBrr^{*2} \frac{\sigma_{nf}}{\sigma_f} (\tilde{f}^2 + \tilde{g}^2). \end{array} \right]}. \quad (3.35)$$

3.4 Homotopy procedure

We have

$$\left. \begin{array}{l} \tilde{h}_0(\xi) = 0, \\ \tilde{g}_0(\xi) = e^{-\xi}, \\ \tilde{\theta}_0(\xi) = e^{-\xi}, \\ \tilde{f}_0(\xi) = A_1 e^{-\xi}, \end{array} \right\} \quad (3.36)$$

$$\mathcal{L}_{\tilde{h}} = \tilde{h}', \quad \mathcal{L}_{\tilde{f}} = \tilde{f}'' - \tilde{f}, \quad \mathcal{L}_{\tilde{g}} = \tilde{g}'' - \tilde{g}, \quad \mathcal{L}_{\tilde{\theta}} = \tilde{\theta}'' - \tilde{\theta}, \quad (3.37)$$

with properties

$$\left. \begin{array}{l} \mathcal{L}_{\tilde{h}}[\bar{B}_1] = 0, \\ \mathcal{L}_{\tilde{f}}[\bar{B}_2 e^\xi + \bar{B}_3 e^{-\xi}] = 0, \\ \mathcal{L}_{\tilde{g}}[\bar{B}_4 e^\xi + \bar{B}_5 e^{-\xi}] = 0, \\ \mathcal{L}_{\tilde{\theta}}[\bar{B}_6 e^\xi + \bar{B}_7 e^{-\xi}] = 0, \end{array} \right\} \quad (3.38)$$

in which the constants consist of \bar{B}_i ($i = 1 - 7$).

3.5 Convergence analysis

Auxiliary parameters $\tilde{h}_{\tilde{h}}$, $\tilde{h}_{\tilde{f}}$, $\tilde{h}_{\tilde{g}}$ and $\tilde{h}_{\tilde{\theta}}$ provide us opportunity to adjust the convergence of nonlinear problems. Figs. (3.2-3.3) display the \tilde{h} -curves at 12th order of approximation. Permissible estimations of auxiliary variables for $Ag-H_2O$ and $Cu-H_2O$ nanofluids are established in the ranges $-1.5 \leq \tilde{h}_{\tilde{h}} \leq -0.1$, $-1.1 \leq \tilde{h}_{\tilde{f}} \leq -0.4$, $-1.2 \leq \tilde{h}_{\tilde{g}} \leq -0.3$ and $-1.4 \leq \tilde{h}_{\tilde{\theta}} \leq -1$

and $-1.6 \leq \tilde{h}_{\tilde{h}} \leq -0.2$, $-1.1 \leq \tilde{h}_{\tilde{f}} \leq -0.3$, $-1.2 \leq \tilde{h}_{\tilde{g}} \leq -0.3$ and $-1.4 \leq \tilde{h}_{\tilde{\theta}} \leq -1.05$. Table (3.1 – 3.2) demonstrate the convergence of $\tilde{h}'(0)$, $\tilde{f}'(0)$, $\tilde{g}'(0)$ and $\tilde{\theta}'(0)$ for Ag-water nanofluid and Cu-water nanofluids. It is clear from Table 3.1 that $\tilde{h}'(0)$, $\tilde{f}'(0)$, $\tilde{g}'(0)$ and $\tilde{\theta}'(0)$ of Ag-water nanofluid converge at 11th, 15th, 19th and 25th order of approximations respectively and Table 3.2 shows that $\tilde{h}'(0)$, $\tilde{f}'(0)$, $\tilde{g}'(0)$ and $\tilde{\theta}'(0)$ of Cu-water nanofluid converge at 11th, 16th, 20th and 25th order of approximations respectively.

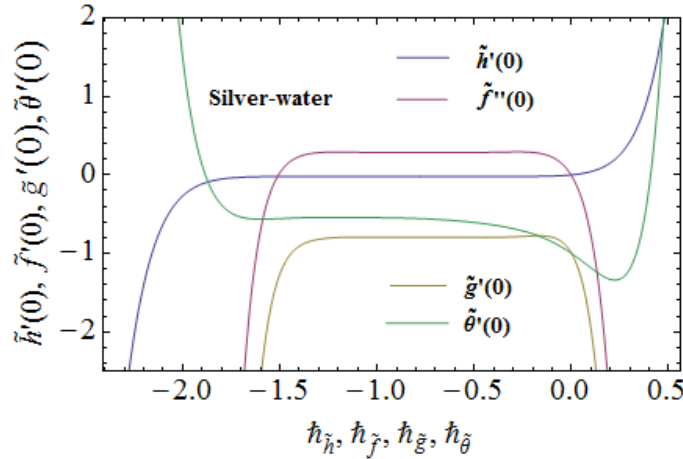


Fig. 3.2. \tilde{h} -graphs for Ag-water

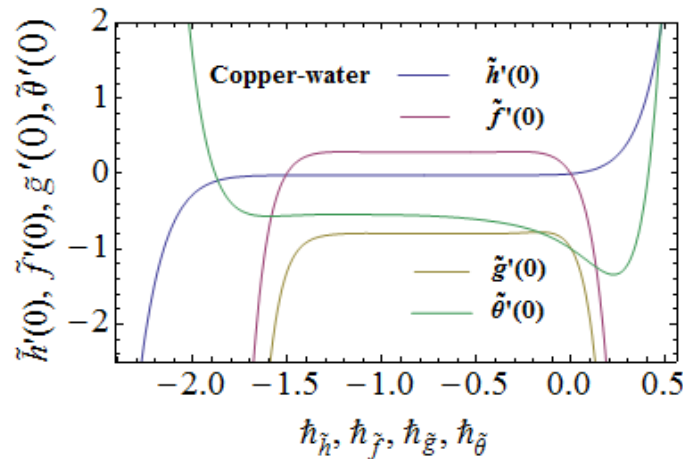


Fig. 3.3. \tilde{h} -graphs for Cu-water

Table 3.1: Various order of approximations for Ag-water nanofluid when $\zeta = 1$, $\epsilon^* = 0.3$, $\text{Pr} = 1.9$, $\alpha = 1.2$, $\text{Re} = 0.9$, $n = 0.5$, $\text{Ec} = 0.5$, $r^* = 0.2$, $M = 0.7$, $A_1 = 0.3$, $R = 0.1$, $\lambda = 0.4$.

Order of approximation	$-\tilde{h}''(0)$	$\tilde{f}'(0)$	$-\tilde{g}'(0)$	$-\tilde{\theta}'(0)$
1	0.009994	0.1610	0.8197	0.8295
11	0.02034	0.2859	0.7965	0.5038
15	0.02034	0.2857	0.7957	0.5233
19	0.02034	0.2857	0.7980	0.5341
25	0.02034	0.2857	0.7980	0.5350
30	0.02034	0.2857	0.7980	0.5350
35	0.02034	0.2857	0.7980	0.5350
40	0.02034	0.2857	0.7980	0.5350
50	0.02034	0.2857	0.7980	0.5350

Table 3.2: Various order of approximations for Cu -water nanofluid when $\zeta = 1$, $\epsilon^* = 0.3$, $Pr = 1.9$, $\alpha = 1.2$, $Re = 0.9$, $n = 0.5$, $Ec = 0.5$, $r^* = 0.2$, $M = 0.7$, $A_1 = 0.3$, $R = 0.1$, $\lambda = 0.4$.

Order of approximation	$-\tilde{h}''(0)$	$\tilde{f}'(0)$	$-\tilde{g}'(0)$	$-\tilde{\theta}'(0)$
1	0.009994	0.1611	0.8197	0.8295
11	0.02034	0.2855	0.7962	0.5037
16	0.02034	0.2854	0.7958	0.5285
20	0.02034	0.2854	0.7970	0.5340
25	0.02034	0.2854	0.7970	0.5330
30	0.02034	0.2854	0.7970	0.5330
35	0.02034	0.2854	0.7970	0.5330
40	0.02034	0.2854	0.7970	0.5330
50	0.02034	0.2854	0.7970	0.5330

3.6 Discussion

This part shows the influences of dimensionless parameters on flow due to rotating disk. Figs. (3.4 – 3.19) are plotted to show the important results of velocity components (axial ($\tilde{h}(\xi)$), radial ($\tilde{f}(\xi)$) and tangential ($\tilde{g}(\xi)$)), temperature $\tilde{\theta}(\xi)$, Nusselt number $(Nu_x Re^{\frac{-1}{n+1}})$ and skin friction $(C_{fx} Re^{\frac{n-1}{n+1}})$ for silver and copper water nanofluids. Figs. (3.4a – 3.4c) display the physical characteristics of Ag -water and Cu -water nanofluids velocities ($\tilde{h}(\xi)$, $\tilde{f}(\xi)$, $\tilde{g}(\xi)$) for

increasing values of magnetic variable M . In fact with increase in M the Lorentz force is more which produces resistance and consequently velocity reduces. Results for both Ag -water and Cu -water nanofluids are qualitatively similar. Influence of power law index n on velocities $(\tilde{h}(\xi), \tilde{f}(\xi), \tilde{g}(\xi))$ of Ag -water and Cu -water nanofluids is shown in Figs. (3.5a – 3.5c). It is evident from plots that motion of fluid particles enhances for larger n . Physically with increase in n the viscosity of fluid reduces and as a result velocity for both nanofluids is enhanced. Figs. (3.6a – 3.6c) elucidate the impact of parameter A_1 on velocities $(\tilde{h}(\xi), \tilde{f}(\xi), \tilde{g}(\xi))$ for Ag -water and Cu -water nanofluids. Here axial $(\tilde{h}(\xi))$ and radial $(\tilde{f}(\xi))$ velocities fields enhance for larger A_1 . It is because of an increase in stretching rate. It is noted that velocity for Ag -water nanofluid is more than Cu -water nanofluids. Impact of mixed convection parameter λ on axial, radial and tangential velocities for Ag -water and Cu -water nanofluids is depicted in Figs. (3.7a – 3.7c). Magnitude of axial and radial velocities enhances for larger λ while opposite impact is noted for tangential velocity. For larger λ thermal buoyancy force increases because λ is ratio of buoyancy to inertial forces. As a result axial and radial velocities grow (see Figs. 3.7a and 3.7b). Results for both nanofluids are qualitatively similar. Velocities $(\tilde{h}(\xi), \tilde{f}(\xi), \tilde{g}(\xi))$ for larger nanoparticle volume fraction ϕ are shown in Figs. (3.8a – 3.8c). Here we noticed that velocity profiles $(\tilde{h}(\xi), \tilde{f}(\xi), \tilde{g}(\xi))$ are increasing functions of ϕ . Velocity for Cu -water nanofluid is more because copper nanoparticles are less dense when compared to silver nanoparticles.

Characteristics of magnetic parameter on temperature is sketched in Fig. 3.9. Temperature increases for higher M . Because of higher in Lorentz force more resistance is offered to the nanoparticles motion. Hence more heat produces and thus temperature enhances for both nanofluids. Figs. 3.10 and 3.11 disclose the effects of mixed convection parameter λ and nanoparticle volume fraction ϕ on temperature of Ag -water and Cu -water nanofluids. Both parameters have direct relation with temperature field. In both cases temperature is slightly more for Ag -water nanofluid because of its higher thermal conductivity. Fig. 3.12 displayed temperature $\tilde{\theta}(\xi)$ for larger Eckert number Ec . A rise in temperature curves with higher Ec is observed. Due to inside friction of molecules the mechanical energy converted to thermal energy is responsible for temperature enhancement. Behavior of temperature for larger radiation R is shown in Fig. 3.13. Mean absorption coefficient decays for larger of R and temperature difference occurs due to diffusion flux which consequently enhances $\tilde{\theta}(\xi)$. Results for both nanofluids

are quite similar in this case.

Figs. (3.14 – 3.16) are portrayed to show the impacts of M , ϕ and λ on skin friction coefficient for Ag –water and Cu –water. As expected the surface drag force enhances for larger M , ϕ and λ . Results are more obvious in case of Ag –water nanofluid for all parameters when compared with Cu –water nanofluid. Figs. (3.17 – 3.19) display the behavior of Eckert number, magnetic parameter and nanoparticle volume fraction on Nusselt number. Heat transfer rate becomes less with Ec and M . Magnitude of Nusselt number is more for Cu –water nanofluid (see Figs. 3.17 and 3.18). For higher ϕ the magnitude of Nusselt number enhances (see Fig. 3.19). Here results of Ag –water nanofluid dominant over Cu –water nanofluid.

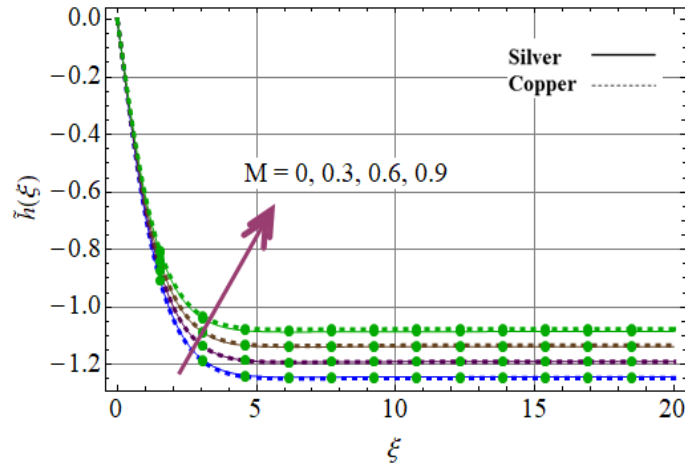


Fig. 3.4a: Axial velocity $\tilde{h}(\xi)$ via M .

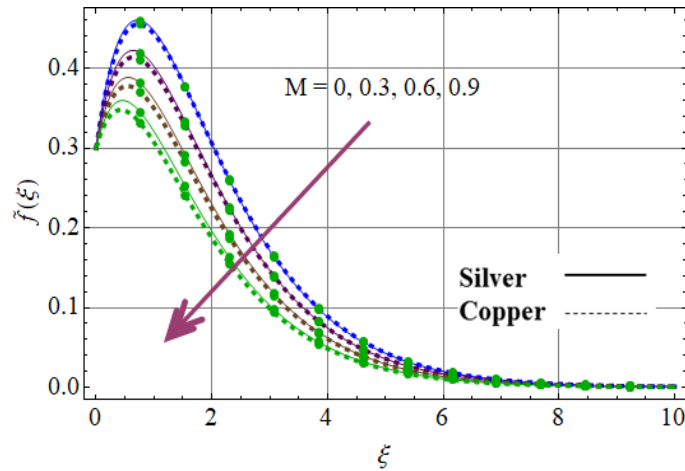


Fig. 3.4b: Radial velocity $\tilde{f}(\xi)$ via M .

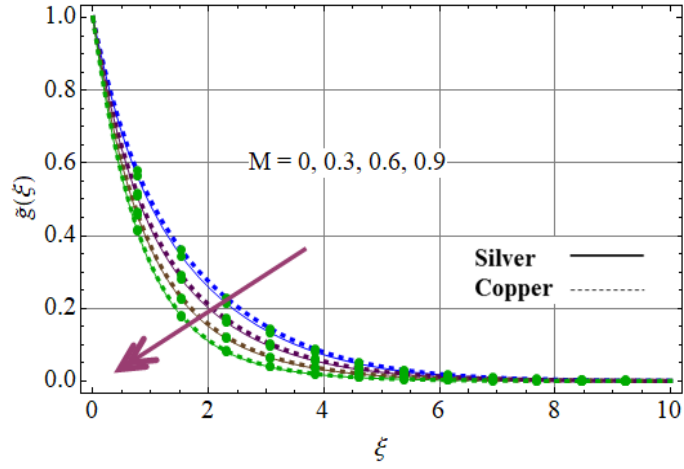


Fig. 3.4c: Tangential velocity $\tilde{g}(\xi)$ via M

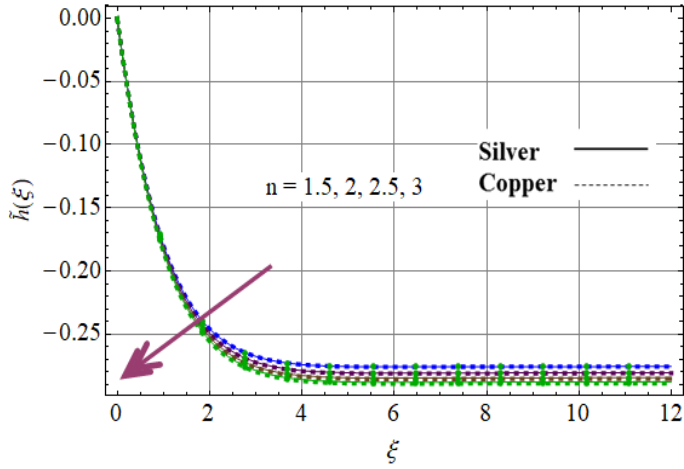


Fig. 3.5a: Axial velocity $\tilde{h}(\xi)$ via n

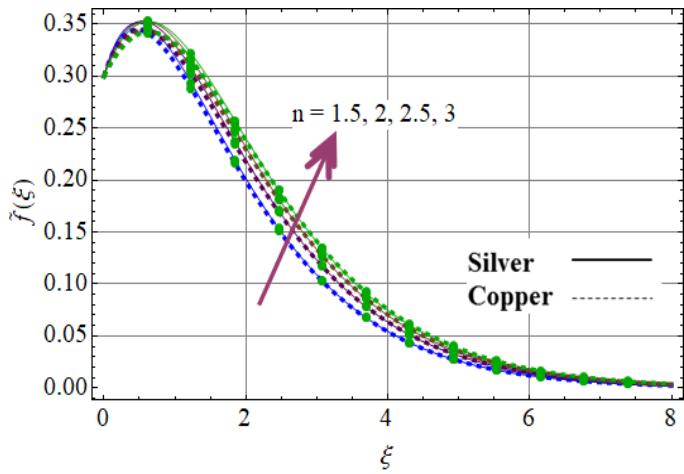


Fig. 3.5b: Radial velocity $\tilde{f}(\xi)$ via n .

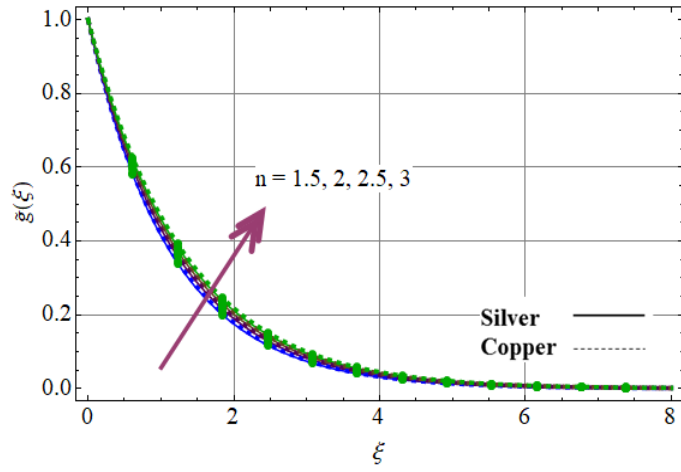


Fig. 3.5c: Tangential velocity $\tilde{g}(\xi)$ via n .

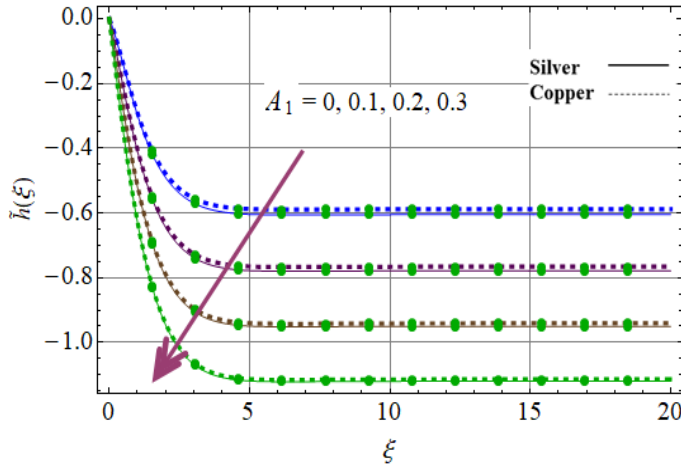


Fig. 3.6a: Axial velocity $\tilde{h}(\xi)$ via A_1

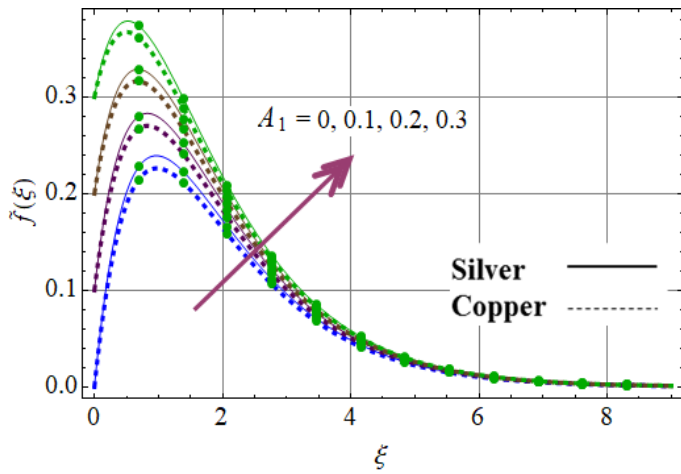


Fig. 3.6b: Radial velocity $\tilde{f}(\xi)$ via A_1 .

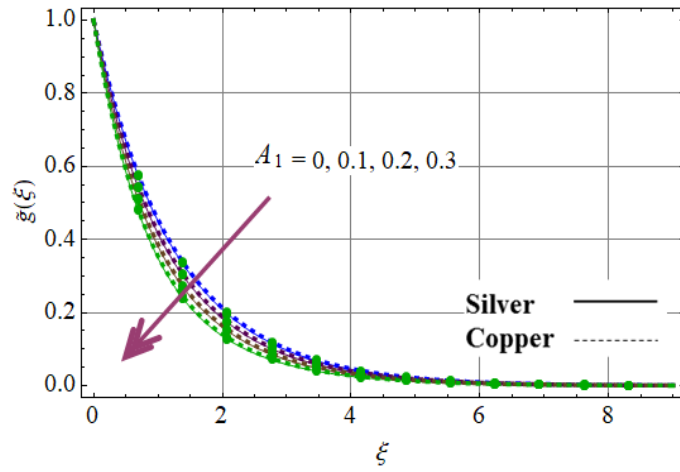


Fig. 3.6c: Tangential velocity $\tilde{g}(\xi)$ via A_1 .

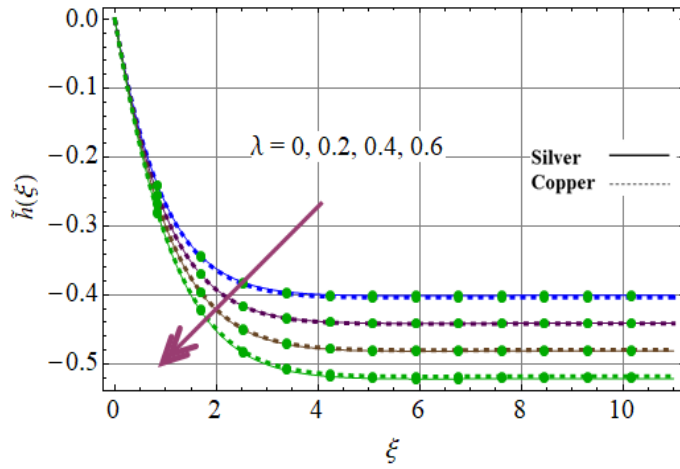


Fig. 3.7a: Axial velocity $\tilde{h}(\xi)$ via λ

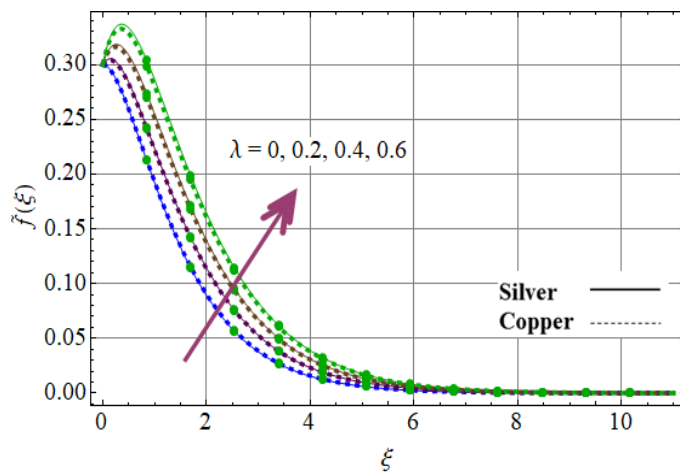


Fig. 3.7b: Radial velocity $\tilde{f}(\xi)$ via λ .

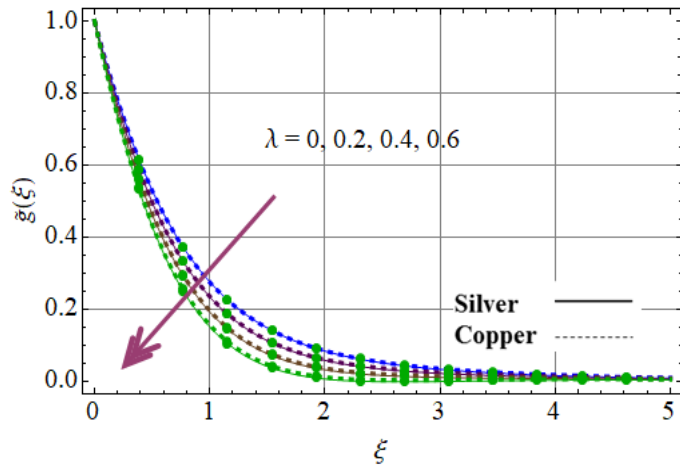


Fig. 3.7c: Tangential velocity $\tilde{g}(\xi)$ via λ .

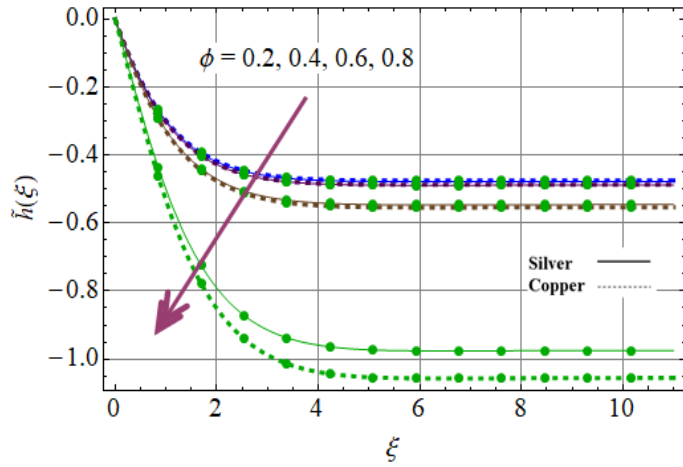


Fig. 3.8a: Axial velocity $\tilde{h}(\xi)$ via ϕ .

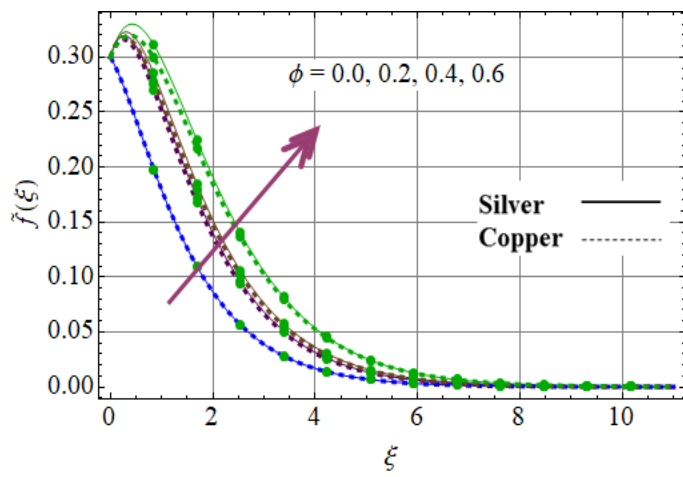


Fig. 3.8b: Radial velocity $\tilde{f}(\xi)$ via ϕ .

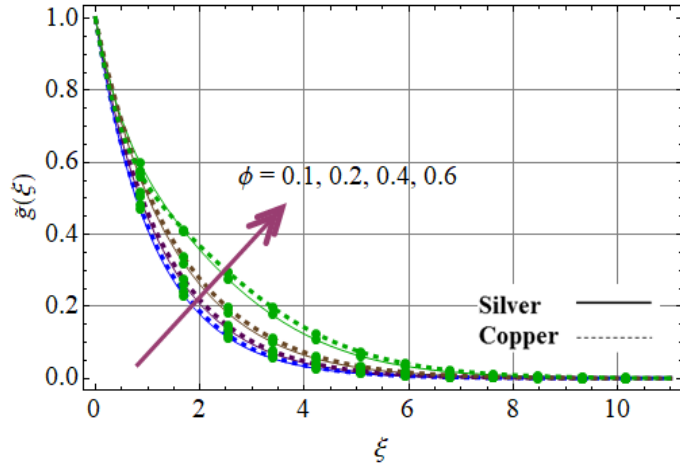


Fig. 3.8c: Tangential velocity $\tilde{g}(\xi)$ via ϕ .

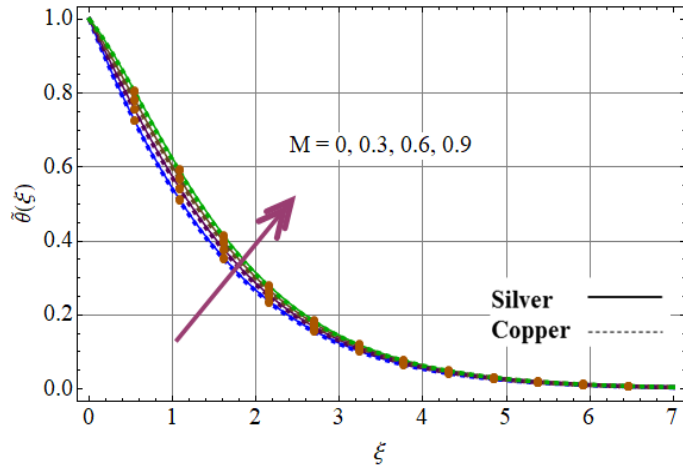


Fig. 3.9: Temperature $\tilde{\theta}(\xi)$ via M .

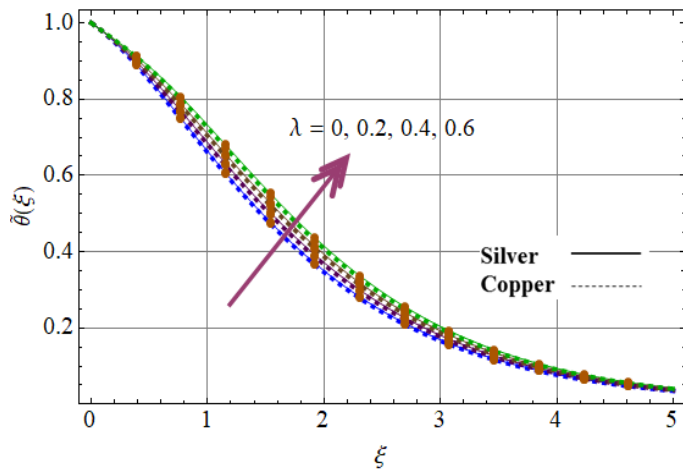


Fig. 3.10: Temperature $\tilde{\theta}(\xi)$ via λ .

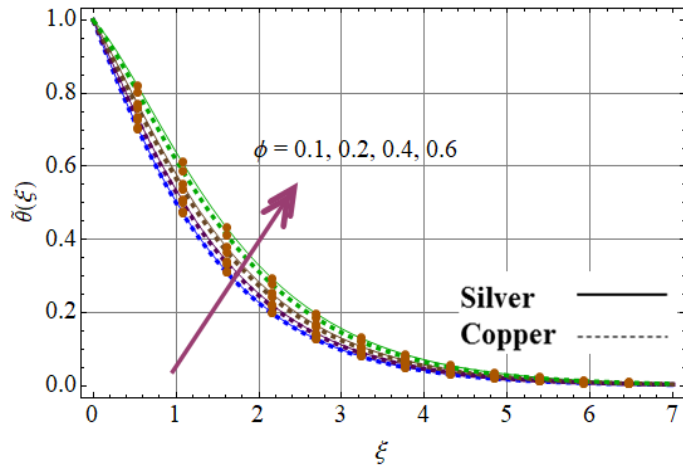


Fig. 3.11: Temperature $\tilde{\theta}(\xi)$ via ϕ .

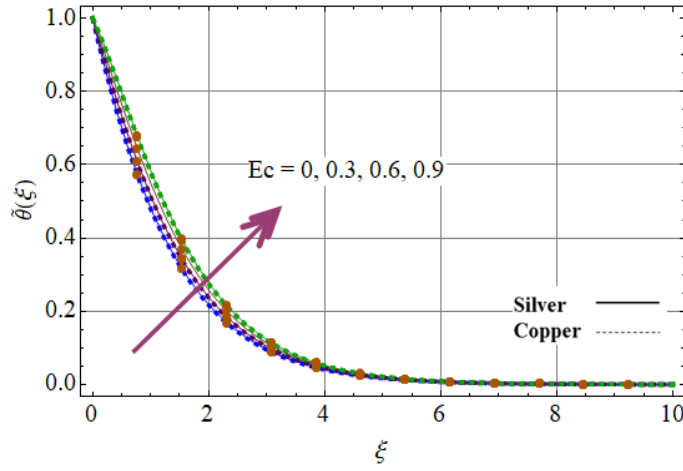


Fig. 3.12: Temperature $\tilde{\theta}(\xi)$ via Ec .

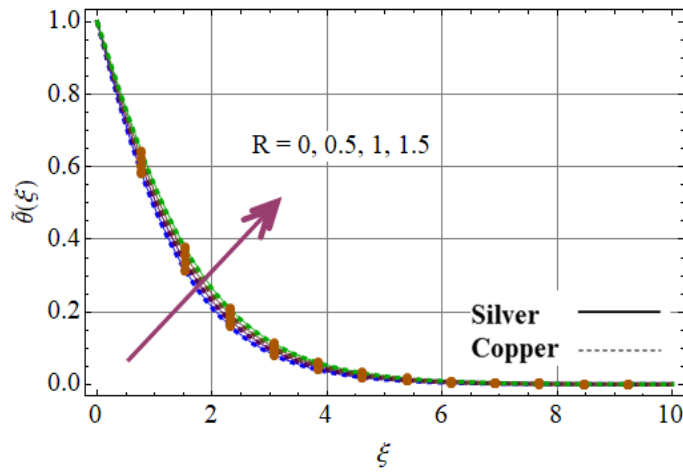


Fig. 3.13: Temperature $\tilde{\theta}(\xi)$ via R .

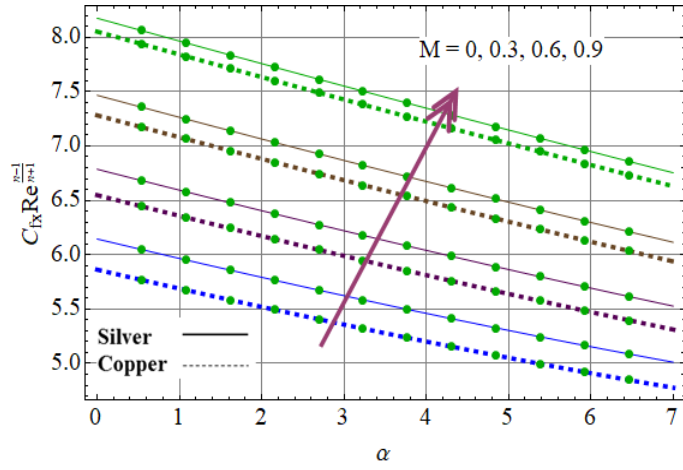


Fig. 3.14: Skin friction via M .

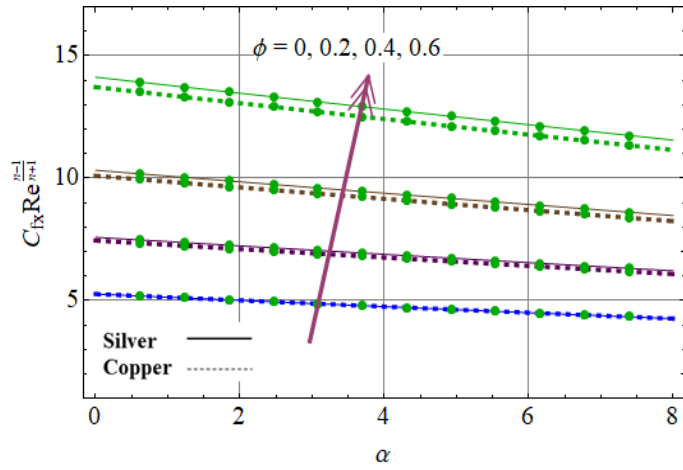


Fig. 3.15: Skin friction via ϕ .

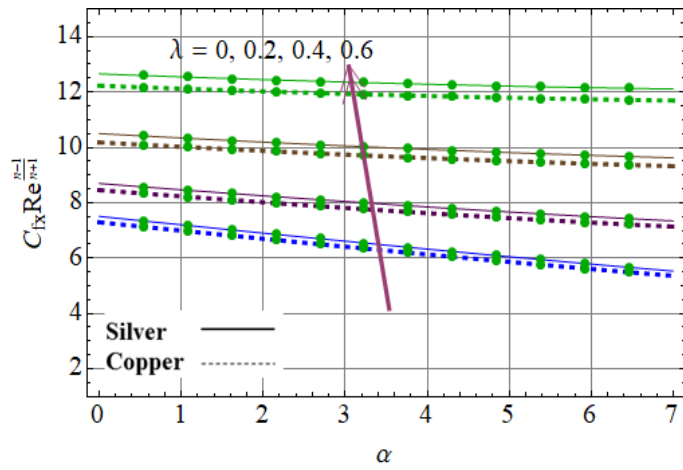


Fig. 3.16: Skin friction via λ .

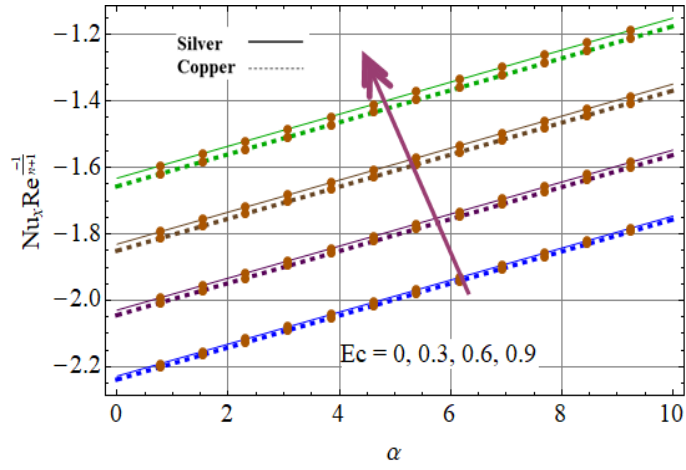


Fig. 3.17: Nusselt number via Ec .

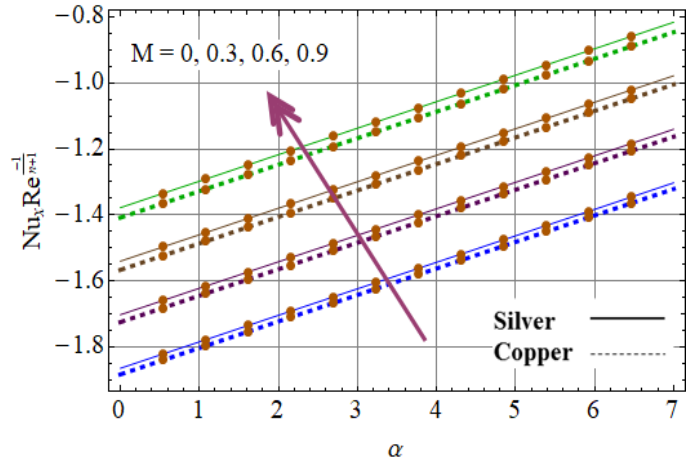


Fig. 3.18: Nusselt number via M .

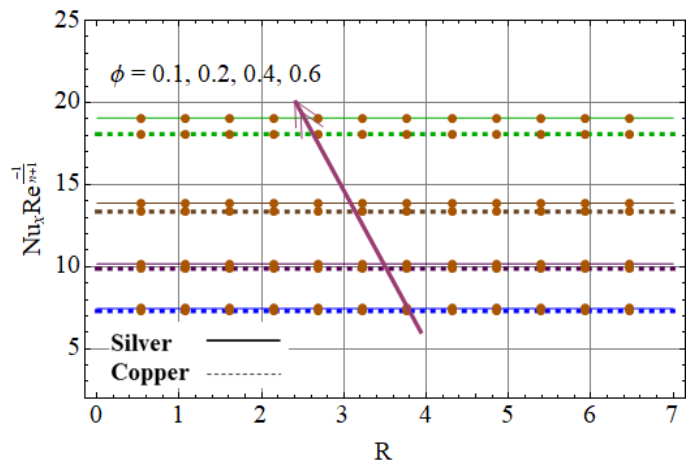


Fig. 3.19: Nusselt number via ϕ .

3.7 Entropy analysis

Behaviors of dimensionless temperature difference parameter, radiation parameter, Brinkman number, nanoparticle volume fraction and Reynolds number on local entropy generation and Bejan number are examined in Figs. (3.20 – 3.29).

Local entropy generation and Bejan number for larger temperature difference parameter α_1 are graphically presented in Figs. 3.20 and 3.21. Here entropy generation rate and Bejan number are increasing functions of α_1 . It is seen that $N_G(\xi)$ approaches to zero far from the boundary. For larger α_1 the heat transfer effects are more prominent than fluid friction and magnetic field effects. That is why Be enhances. Bejan number is more for Ag –water when compared with Cu –water nanofluid. It is because of its higher heat conductive ability. Figs. 3.22 and 3.23 displayed impact of radiation R on $N_G(\xi)$ and Be for silver and copper water nanofluids. Here both entropy and Bejan numbers are increased versus R . It is due to rise in internal energy of system. It is also observed that Be is more for silver water nanofluid. Figs. 3.24 and 3.25 show $N_G(\xi)$ and Be for both $Ag - H_2O$ and $Cu - H_2O$ nanomaterials for higher Br . Physically, Brinkman number governs the releasing of heat through viscous heating in to heat transport by conduction process. Entropy generation is directly affected by Brinkman number closed to the disk surface. Heat transport through conduction process is always higher than the heat released by viscous phenomenon closed to the disk surface. More heat is produced inside the layers of liquids particles and consequently entropy of the system upsures. Fig. 3.25 highlights that Be declines for larger Br . Effect of Cu nanoparticles here is less than Ag nanoparticles. Figs. 3.26 and 3.27 depict the influence of ϕ on $N_G(\xi)$ and Be . Rate of entropy generation enhances for larger ϕ while opposite behavior is noticed for Bejan number for both nanofluids. It means that as values of ϕ increase then the heat transfer dominant over fluid friction and magnetic effects. Figs. 3.28 and 3.29 are sketched to show the important effect of Re on $N_G(\xi)$ and Be . We noticed that rate of entropy generation decays for larger Re while on contrary Bejan number has higher values via increasing Re . Physically for larger Re the flow fluctuation in the fluid

enhances so heat transfer increases and thus more entropy generation for both nanofluids.

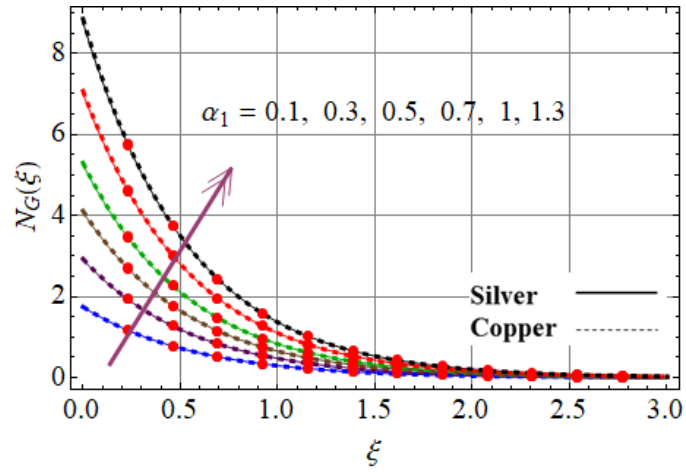


Fig. 3.20: Entropy generation N_G via α_1 .

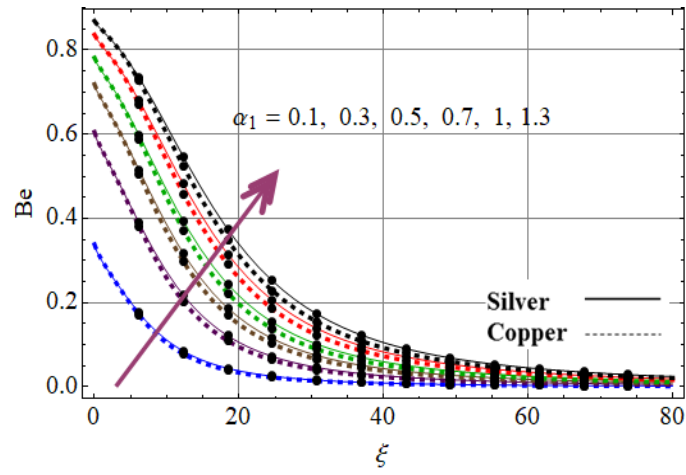


Fig. 3.21: Bejan number Be via α_1 .

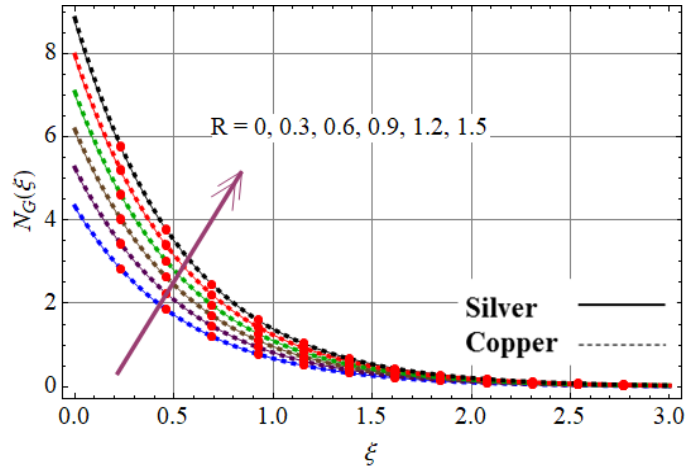


Fig. 3.22: Impact of R on N_G .

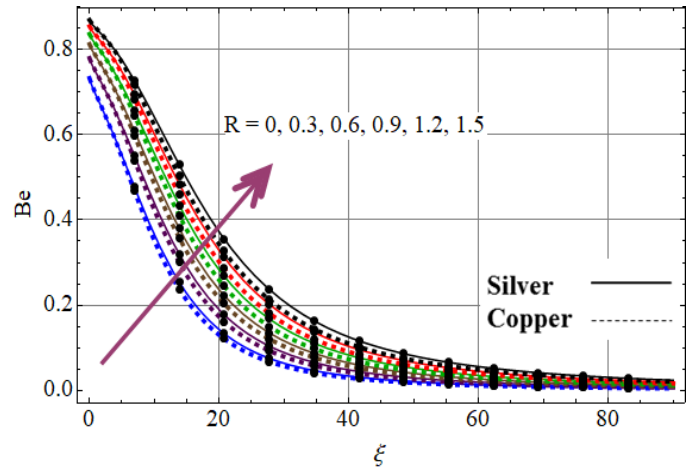


Fig. 3.23: Impact of R on Be .

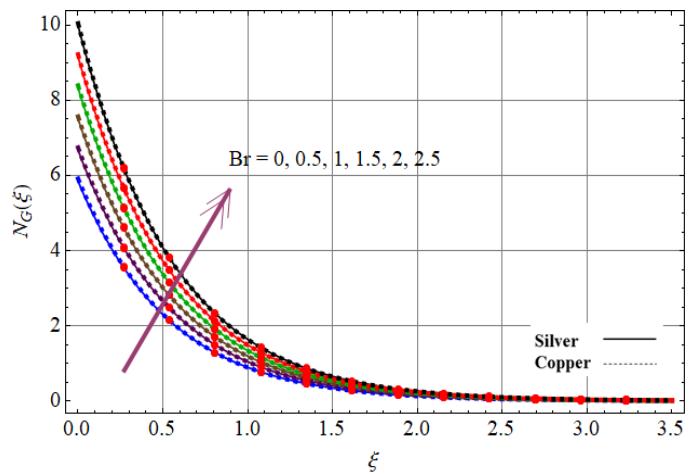


Fig. 3.24: Br impact on N_G .

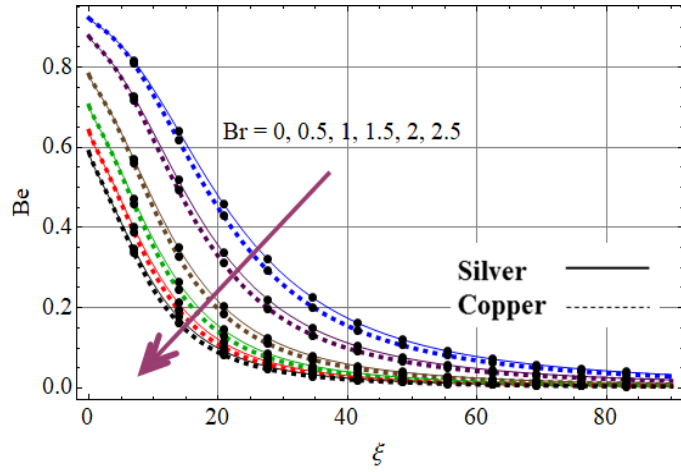


Fig. 3.25: Br impact on Be .

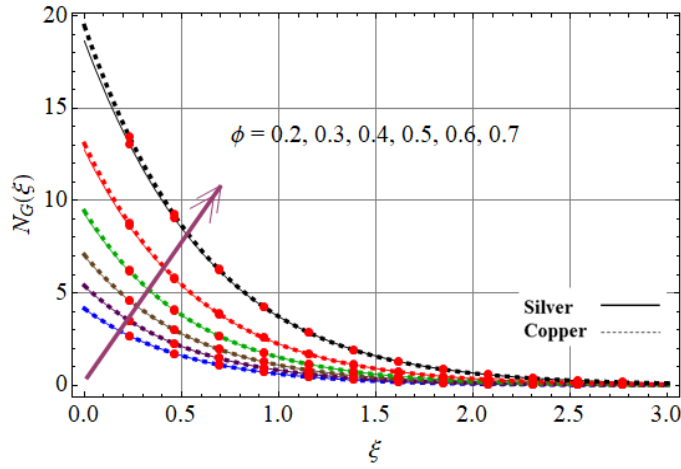


Fig. 3.26: ϕ impact on N_G .

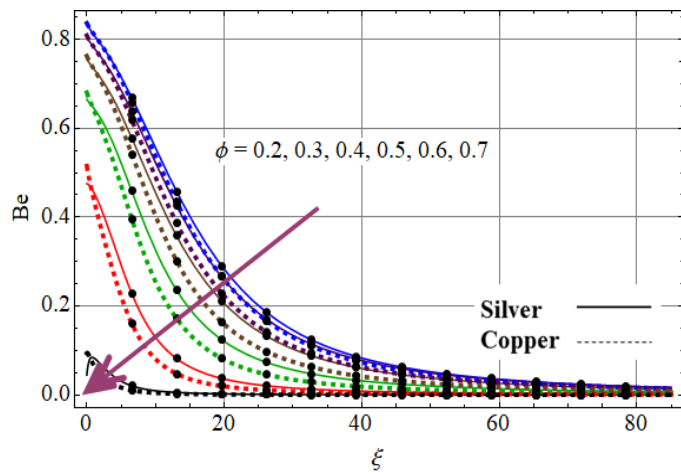


Fig. 3.27: ϕ impact on Be .

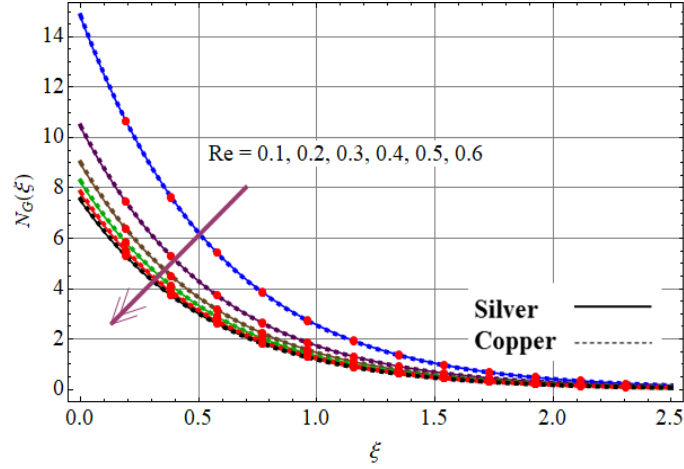


Fig. 3.28: Re impact on N_G .

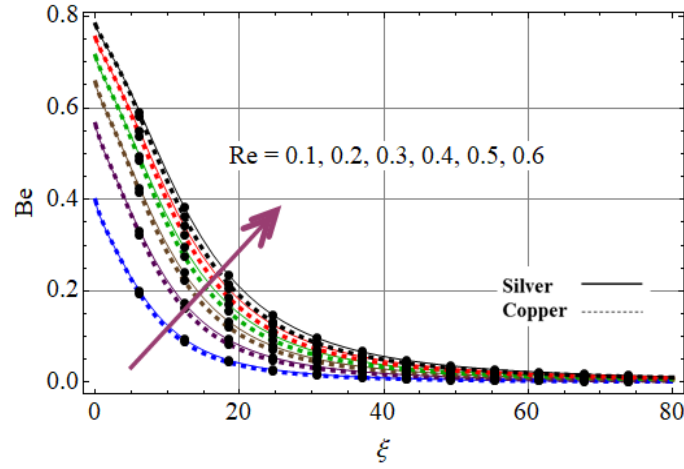


Fig. 3.29: Re impact on Be .

3.8 Conclusions

Mixed convective radiative flow subject to Joule heating and dissipation is discussed. Main findings are as follows:

- Axial $\tilde{h}(\xi)$, radial $\tilde{f}(\xi)$ and tangential $\tilde{g}(\xi)$ velocities increase for larger power law index of fluid and nanoparticle volume fraction.
- Temperature $\tilde{\theta}(\xi)$ enhances for larger R , Ec and λ in both Ag and Cu water nanofluids.
- Surface drag force increases for higher M and ϕ .
- Magnitude of temperature gradient $Nu_x Re^{\frac{-1}{n+1}}$ decays when Ec and M are enhanced.

- Re impact on entropy generation rate N_G is opposite when compared with R , Br and ϕ .
- Effect of Br on Bejan number is reverse when compared with ϕ and Re .
- Bejan number is more for Ag -water nanofluid when compared with Cu -water nanofluid.

Chapter 4

Slip and Joule heating effects in rotating disk flow with nanoparticles

Abstract: This chapter addresses the viscous fluid flow subject to five different types of nanoparticles i.e., Silver, Copper, Copper oxide, Aluminum oxide and Titanium oxide. The flow is discussed by a variable thicked surface of disk with Joule heating. The nonlinear PDE's are converted to ordinary ones through Von-Karman variables and then tackled for series solutions development via homotopy method. Salient characteristics of appropriate flow paraemters are discussed graphically on the velocity components, temperature, skin friction, and Nusselt number. It is witnessed that the velocity components (i.e., axial, radial and tangential) decline via higher slip parameters. Also the axial velocity decreases versus nanoparticle volume fraction. It is clearly remarked that the behavior of nanomaterials is more than base liquid on the velocity components. Thermal field is increased subject to higher values of Eckert number. Temperature in case of Silver-water nanomaterial is more than the other nanomaterials due to its larger thermal conductivity. Skin friction diminishes versus slip variables.

4.1 Modeling

We analyze the incompressible water based nanofluids flow by a rotating disk with angular velocity Ω_1 and stretching rate a_1 . Nanoliquids are suspension of nanomaterials i.e., Copper, Silver, Copper oxide, titanium oxide and aluminium with water as continuous phase liquid. The disk of variable thickness is considered at $z = a^* \left(\frac{r}{R_0} + 1 \right)^{-\zeta}$. The energy equation is modeled

subject to Joule heating. Slip flow is considered. We consider cylindrical coordinates (r, ϑ, z) (see physical model in Fig. 4.1). Under the assumptions $\frac{\partial \hat{p}}{\partial r} = \frac{\partial \hat{p}}{\partial z} = 0$, $O(\hat{u}) = O(\hat{v}) = O(r) = O(1)$ and $O(\hat{w}) = O(z) = O(\delta)$ the equations for flow and heat transfer are as follows [10, 27]:

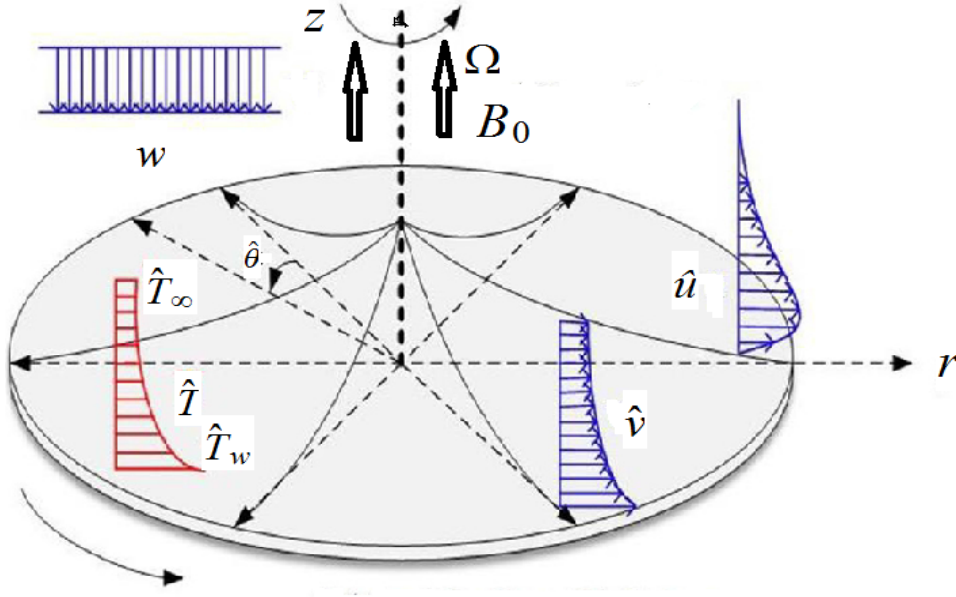


Fig. 4.1: Schematic diagram of problem

$$\frac{\partial \hat{u}}{\partial r} + \frac{\hat{u}}{r} + \frac{\partial \hat{w}}{\partial z} = 0, \quad (4.1)$$

$$\hat{u} \frac{\partial \hat{u}}{\partial r} + \hat{w} \frac{\partial \hat{u}}{\partial z} - \frac{\hat{v}^2}{r} = \nu_{nf} \frac{\partial^2 \hat{u}}{\partial z^2} - \frac{\sigma_{nf}}{\rho_{nf}} B_0^2 \hat{u}, \quad (4.2)$$

$$\hat{u} \frac{\partial \hat{v}}{\partial r} + \hat{w} \frac{\partial \hat{v}}{\partial z} + \frac{\hat{u}\hat{v}}{r} = \nu_{nf} \frac{\partial^2 \hat{v}}{\partial z^2} - \frac{\sigma_{nf}}{\rho_{nf}} B_0^2 \hat{v}, \quad (4.3)$$

$$(\rho c_p)_{nf} \left(\hat{u} \frac{\partial \hat{T}}{\partial r} + \hat{w} \frac{\partial \hat{T}}{\partial z} \right) = k_{nf} \frac{\partial^2 \hat{T}}{\partial z^2} + \sigma_{nf} B_0^2 (\hat{u}^2 + \hat{v}^2), \quad (4.4)$$

with boundary conditions

$$\begin{aligned} \hat{u} &= r a_1 + \lambda_1 \frac{\partial \hat{u}}{\partial z}, \quad \hat{v} = r \Omega_1 + \lambda_2 \frac{\partial \hat{v}}{\partial z}, \quad \hat{w} = 0, \quad \hat{T} = \hat{T}_w \text{ at } z = a^* \left(\frac{r}{R_0} + 1 \right)^{-\zeta}, \\ \hat{u} &= 0, \quad \hat{v} = 0, \quad \hat{w} = 0, \quad \hat{T} = \hat{T}_\infty \text{ when } z \rightarrow \infty, \end{aligned} \quad (4.5)$$

where a^* being thickness coefficient of disk is very small, R_0 the feature radius, ς the disk thickness index, a the stretching rate and λ_1 and λ_2 the velocity slip coefficients, effective nanofluid dynamic viscosity μ_{nf} , heat capacitance $(\rho c_p)_{nf}$, thermal conductivity k_{nf} , density ρ_{nf} and electrical conductivity σ_{nf} are addressed as

$$\mu_{nf} = \frac{\mu_f}{(1 - \phi)^{2.5}}, \quad (4.6)$$

$$\rho_{nf} = \rho_f(1 - \phi) + \rho_s\phi, \quad (4.7)$$

$$(\rho c_p)_{nf} = (\rho c_p)_f(1 - \phi) + (\rho c_p)_s\phi, \quad (4.8)$$

$$\frac{k_{nf}}{k_f} = \frac{k_s + 2k_f - 2\phi(k_f - k_s)}{k_s + 2k_f + 2\phi(k_f - k_s)}, \quad (4.9)$$

$$\frac{\sigma_{nf}}{\sigma_f} = 1 + \frac{3 \left(\frac{\sigma_s}{\sigma_f} - 1 \right) \phi}{\left(\frac{\sigma_s}{\sigma_f} + 2 \right) - \left(\frac{\sigma_s}{\sigma_f} - 1 \right) \phi}. \quad (4.10)$$

Von Karman transformations are

$$\begin{aligned} \hat{u} &= r^* R_0 \Omega_1 \tilde{F}(\eta), \quad \hat{v} = r^* R_0 \Omega_1 \tilde{G}(\eta), \quad \hat{w} = R_0 \Omega_1 (1 + r^*)^{-\varsigma} \left(\frac{\Omega_1 R_0^2 \rho_f}{\mu_f} \right)^{\frac{-1}{n+1}} \tilde{H}(\eta) \\ \tilde{\vartheta} &= \frac{\hat{T} - \hat{T}_\infty}{\hat{T}_w - \hat{T}_\infty}, \quad \eta = \frac{z}{R_0} (1 + r^*)^\varsigma \left(\frac{\Omega_1 R_0^2 \rho_f}{\mu_f} \right)^{\frac{1}{n+1}}. \end{aligned} \quad (4.11)$$

Incompressibility condition is trivially satisfied and Eqs. (4.2 – 4.5) are transformed as

$$2\tilde{F} + \tilde{H}' + \eta \epsilon^* \varsigma \tilde{F}' = 0, \quad (4.12)$$

$$\begin{aligned} &\frac{1}{(1 - \phi)^{2.5} \left(1 - \phi + \frac{\rho_s}{\rho_f} \phi \right)} \tilde{F}'' (\text{Re})^{\frac{1-n}{1+n}} (1 + r^*)^{2\varsigma} - \tilde{F}^2 + \tilde{G}^2 - \tilde{H} \tilde{F}' - \tilde{F} \tilde{F}' \varsigma \eta \epsilon^* \\ &- \frac{M}{(1 - \phi)^{2.5} \left(1 - \phi + \frac{\rho_s}{\rho_f} \phi \right)} \frac{\sigma_{nf}}{\sigma_f} \tilde{F} = 0, \end{aligned} \quad (4.13)$$

$$\begin{aligned} & \frac{1}{(1-\phi)^{2.5}(1-\phi+\frac{\rho_s}{\rho_f}\phi)} \tilde{G}''' (\text{Re})^{\frac{1-n}{1+n}} (1+r^*)^{2\varsigma} - 2\tilde{F}\tilde{G} - \tilde{H}\tilde{G}' - \tilde{F}\tilde{G}'\varsigma\eta\epsilon^* \\ & - \frac{M}{(1-\phi)^{2.5}(1-\phi+\frac{\rho_s}{\rho_f}\phi)} \frac{\sigma_{nf}}{\sigma_f} \tilde{G} = 0, \end{aligned} \quad (4.14)$$

$$\begin{aligned} & \frac{1}{\text{Pr}} \frac{k_{nf}}{k_f} \frac{1}{1-\phi+\frac{(\rho c_p)_s}{(\rho c_p)_f}\phi} (\text{Re})^{\frac{1-n}{1+n}} (1+r^*)^{2\varsigma} \tilde{\vartheta}'' - \tilde{F}\tilde{\vartheta}'\varsigma\eta\epsilon^* - \tilde{H}\tilde{\vartheta}' + \\ & \frac{\sigma_{nf}}{\sigma_f} \frac{MEc}{1-\phi+\frac{(\rho c_p)_s}{(\rho c_p)_f}\phi} (\tilde{F}^2 + \tilde{G}^2) = 0, \end{aligned} \quad (4.15)$$

with boundary conditions

$$\begin{aligned} \tilde{H}(\alpha) &= 0, \quad \tilde{F}(\alpha) = A_1 + \gamma_1(1+r^*)^\varsigma \tilde{F}'(\alpha), \\ \tilde{F}(\infty) &= 0, \quad \tilde{G}(\alpha) = 1 + \gamma_2(1+r^*)^\varsigma \tilde{G}'(\alpha), \\ \tilde{G}(\infty) &= 0, \quad \tilde{\vartheta}(\alpha) = 1, \quad \tilde{\vartheta}(\infty) = 0. \end{aligned} \quad (4.16)$$

Here

$$\begin{aligned} \epsilon^* &= \frac{r^*}{R_0 + r^*}, \quad \alpha = \frac{a^*}{R_0} \left(\frac{\Omega_1 R_0^2 \rho_f}{\mu_f} \right)^{\frac{-1}{n+1}}, \quad \text{Re} = \frac{\Omega_1 R_0^2}{\nu_f}, \quad \text{Pr} = \frac{(\rho c_p)_f \nu_f}{k_f}, \quad A_1 = \frac{a_1}{\Omega_1}, \\ \gamma_1 &= \frac{\lambda_1}{R_0} \left(\frac{\Omega_1 R_0^2 \rho_f}{\mu_f} \right)^{\frac{1}{n+1}}, \quad \gamma_2 = \frac{\lambda_2}{R_0} \left(\frac{\Omega_1 R_0^2 \rho_f}{\mu_f} \right)^{\frac{1}{n+1}}, \quad M = \frac{\sigma_f B_0^2}{\rho_f \Omega_1}, \quad Ec = \frac{\Omega_1^2 r^2}{(\hat{T}_w - \hat{T}_\infty) c_p} \end{aligned} \quad (4.17)$$

where ϵ^* indicates dimensionless constant, Pr Prandtl number, r^* dimensionless radius, α coefficient of disk thickness, A_1 scaled stretching parameter, Re Reynolds number, γ_1 and γ_2 slip parameters, M magnetic parameter and Ec Eckert number.

Considering

$$\begin{aligned} \tilde{H} &= \tilde{h}(\eta - \alpha) = \tilde{h}(\xi), \quad \tilde{F} = \tilde{f}(\eta - \alpha) = \tilde{f}(\xi), \\ \tilde{G} &= \tilde{g}(\eta - \alpha) = \tilde{g}(\xi), \quad \tilde{\vartheta} = \tilde{\theta}(\eta - \alpha) = \tilde{\theta}(\xi). \end{aligned} \quad (4.18)$$

Eqs. (4.12 – 4.16) are reduced to

$$2\tilde{f} + \tilde{h}' + (\xi + \alpha)\epsilon^* \zeta \tilde{f}' = 0, \quad (4.19)$$

$$\frac{1}{(1-\phi)^{2.5}(1-\phi + \frac{\rho_s}{\rho_f}\phi)} \tilde{f}'' (\text{Re})^{\frac{1-n}{1+n}} (1+r^*)^{2\zeta} - \tilde{f}^2 + \tilde{g}^2 - \tilde{h}\tilde{f}' - \tilde{f}\tilde{f}' \zeta (\xi + \alpha)\epsilon^* - \frac{M}{(1-\phi + \frac{\rho_s}{\rho_f}\phi)} \frac{\sigma_{nf}}{\sigma_f} \tilde{f} = 0, \quad (4.20)$$

$$\frac{1}{(1-\phi)^{2.5}(1-\phi + \frac{\rho_s}{\rho_f}\phi)} \tilde{g}'' (\text{Re})^{\frac{1-n}{1+n}} (1+r^*)^{2\zeta} - 2\tilde{f}\tilde{g} - \tilde{h}\tilde{g}' - \tilde{f}\tilde{g}' \zeta (\xi + \alpha)\epsilon^* - \frac{M}{(1-\phi + \frac{\rho_s}{\rho_f}\phi)} \frac{\sigma_{nf}}{\sigma_f} \tilde{g} = 0, \quad (4.21)$$

$$\frac{1}{\text{Pr}} \frac{k_{nf}}{k_f} \frac{1}{1-\phi + \frac{(\rho c_p)_s}{(\rho c_p)_f} \phi} (\text{Re})^{\frac{1-n}{1+n}} (1+r^*)^{2\zeta} \tilde{\theta}'' - \tilde{f}\tilde{\theta}' \zeta (\xi + \alpha)\epsilon^* - \tilde{h}\tilde{\theta}' + \frac{\sigma_{nf}}{\sigma_f} \frac{MEc}{1-\phi + \frac{(\rho c_p)_s}{(\rho c_p)_f} \phi} (\tilde{f}^2 + \tilde{g}^2) = 0, \quad (4.22)$$

$$\begin{aligned} \tilde{h}(0) &= 0, \quad \tilde{f}(0) = A_1 + \gamma_1 \tilde{f}'(0), \quad \tilde{f}(\infty) = 0, \quad \tilde{g}(0) = 1 + \gamma_2 \tilde{g}'(0), \\ \tilde{g}(\infty) &= 0, \quad \tilde{\theta}(0) = 1, \quad \tilde{\theta}(\infty) = 0. \end{aligned} \quad (4.23)$$

In above expression prime depicts derivative with respect of ξ and \tilde{h} , \tilde{f} , \tilde{g} and $\tilde{\theta}$ the axial, radial, tangential velocities and temperature respectively.

At lower disk the shear stress in radial and tangential directions are τ_{zr} and $\tau_{z\theta}$

$$\begin{aligned} \tau_{zr} &= \mu_f \left. \frac{\partial \hat{u}}{\partial z} \right|_{z=0} = \frac{\mu_f r^* \Omega_1 R_0 (1+r^*)^\zeta \left(\frac{\Omega R_0^2 \rho_f}{\mu_f} \right)^{\frac{1}{n+1}} \tilde{f}'(0)}{R_0}, \\ \tau_{z\theta} &= \mu_f \left. \frac{\partial \hat{v}}{\partial z} \right|_{z=0} = \frac{\mu_f r^* \Omega_1 R_0 (1+r^*)^\zeta \left(\frac{\Omega R_0^2 \rho_f}{\mu_f} \right)^{\frac{1}{n+1}} \tilde{g}'(0)}{R_0}. \end{aligned} \quad (4.24)$$

Total shear stress τ_w is defined by

$$\tau_w = \sqrt{\tau_{zr}^2 + \tau_{z\theta}^2}. \quad (4.25)$$

Skin friction coefficients C_{fx} is

$$C_{fx} \text{Re}^{\frac{n-1}{n+1}} = \frac{\tau_w|_{z=0}}{\rho_f (r\Omega)^2} = \frac{1}{r^*} (1+r^*)^\zeta [(\tilde{f}'(0))^2 + (\tilde{g}'(0))^2]^{1/2}. \quad (4.26)$$

Nusselt number is defined as

$$Nu_x = \frac{R_0 q_w}{k_f(\hat{T}_w - \hat{T}_\infty)} \Big|_{z=0}. \quad (4.27)$$

The wall heat flux q_w satisfies

$$q_w|_{z=0} = -k_f \frac{\partial \hat{T}}{\partial z} \Big|_{z=0} = -k_f(\hat{T}_w - \hat{T}_\infty)(1+r^*)^\varsigma \left(\frac{\Omega R_0^2 \rho_f}{\mu_f} \right)^{\frac{1}{n+1}} \tilde{\theta}'(0), \quad (4.28)$$

and so

$$Nu_x \text{Re}^{\frac{-1}{n+1}} = -(1+r^*)^\varsigma \tilde{\theta}'(0). \quad (4.29)$$

4.2 Solutions expressions

Expressions of initial approximations and operators satisfy

$$\tilde{h}_0(\xi) = 0, \quad (4.30)$$

$$\tilde{f}_0(\xi) = \frac{A_1}{1 + \gamma_1(1+r^*)^\varsigma} \exp(-\xi), \quad (4.31)$$

$$\tilde{g}_0(\xi) = \frac{1}{1 + \gamma_2(1+r^*)^\varsigma} \exp(-\xi), \quad (4.32)$$

$$\tilde{\theta}_0(\xi) = \exp(-\xi), \quad (4.33)$$

$$\mathcal{L}_{\tilde{h}} = \tilde{h}', \quad \mathcal{L}_{\tilde{f}} = \tilde{f}'' - \tilde{f}, \quad \mathcal{L}_{\tilde{g}} = \tilde{g}'' - \tilde{g}, \quad \mathcal{L}_{\tilde{\theta}} = \tilde{\theta}'' - \tilde{\theta}, \quad (4.34)$$

with

$$\left. \begin{aligned} \mathcal{L}_{\tilde{h}}[c_1] &= 0, \\ \mathcal{L}_{\tilde{f}}[c_2 e^\xi + c_3 e^{-\xi}] &= 0, \\ \mathcal{L}_{\tilde{g}}[c_4 e^\xi + c_5 e^{-\xi}] &= 0, \\ \mathcal{L}_{\tilde{\theta}}[c_6 e^\xi + c_7 e^{-\xi}] &= 0, \end{aligned} \right\} \quad (4.35)$$

4.3 Convergence analysis

HAM has great benefit of adjusting the convergence region for nonlinear system of equations by using appropriate $\tilde{h}_{\tilde{h}}$, $\tilde{h}_{\tilde{f}}$, $\tilde{h}_{\tilde{g}}$ and $\tilde{h}_{\tilde{\theta}}$. Curves are drawn at 14th order of iteration. Admissible

ranges for all nanofluids are shown in Table 4.1. Solutions converge in the whole region of ξ ($0 \leq \xi \leq 1$) when $\tilde{h}_{\tilde{h}} = \tilde{h}_{\tilde{f}} = \tilde{h}_{\tilde{g}} = -0.7$ and $\tilde{h}_{\tilde{\theta}} = -1.2$. Tables (4.2 – 4.6) show the convergence of nanofluids for $\tilde{h}''(0)$, $\tilde{f}'(0)$, $\tilde{g}'(0)$ and $\tilde{\theta}'(0)$. Table 4.7 shows some physical properties of nanofluids.

Table 4.1: Ranges of \tilde{h} -curves for five nanofluids.

Nanofluids	$\tilde{h}_{\tilde{h}}$	$\tilde{h}_{\tilde{f}}$	$\tilde{h}_{\tilde{g}}$	$\tilde{h}_{\tilde{\theta}}$
<i>Ag</i> -water	-1.4 to -0.3	-1.3 to -0.4	-1.5 to -0.1	-1.6 to -1.1
<i>Cu</i> -water	-1.5 to -0.3	-1.3 to -0.2	-1.4 to -0.2	-1.55 to -1
<i>CuO</i> -water	-1.4 to -0.3	-1.4 to -0.3	-1.55 to -0.3	-1.4 to -1.1
<i>Al₂O₃</i> -water	-1.4 to -0.3	-1.3 to -0.2	-1.4 to -0.2	-1.4 to -1.05
<i>TiO₂</i> -water	-1.4 to -0.3	-1.2 to -0.5	-1.4 to -0.2	-1.4 to -1.1

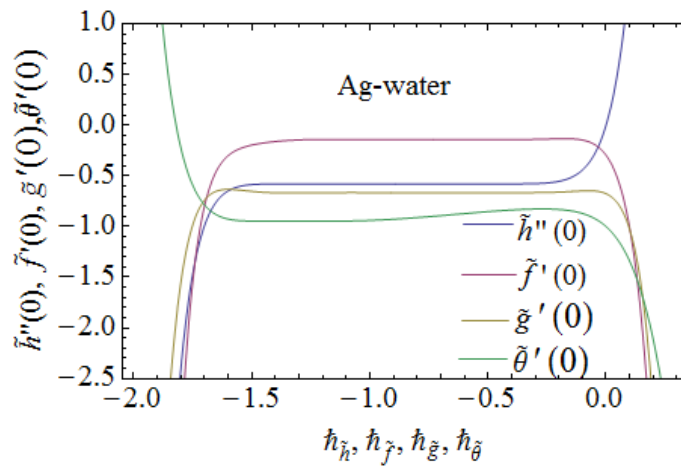


Fig. 4.2: \tilde{h} -curves for $\tilde{h}''(0)$, $\tilde{f}'(0)$, $\tilde{g}'(0)$ and $\tilde{\theta}'(0)$.

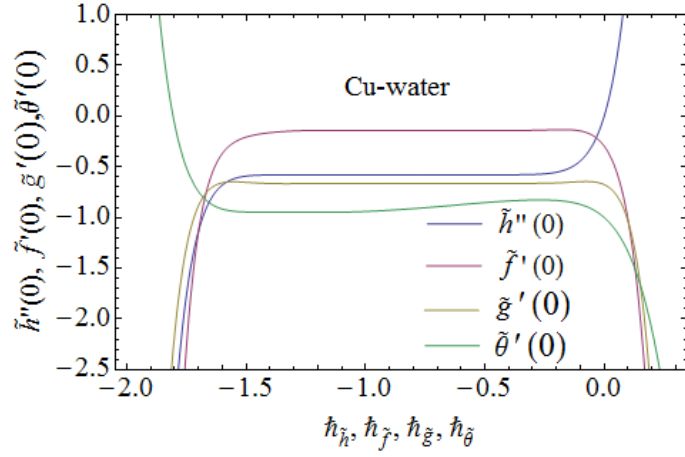


Fig. 4.3: \tilde{h} -curves for $\tilde{h}''(0)$, $\tilde{f}'(0)$, $\tilde{g}'(0)$ and $\tilde{\theta}'(0)$.

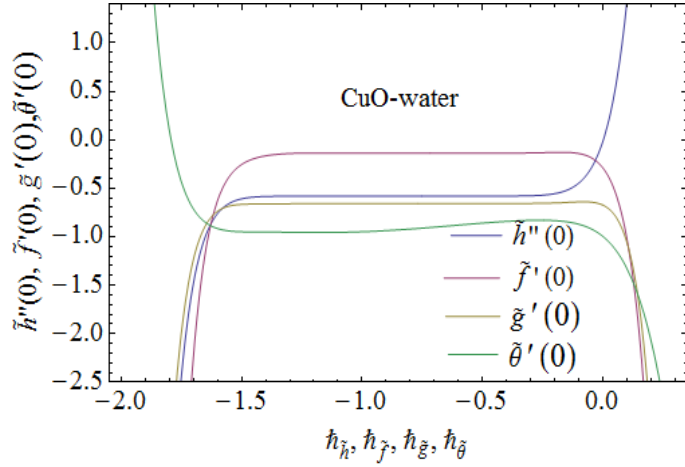


Fig. 4.4: \tilde{h} -curves for $\tilde{h}''(0)$, $\tilde{f}'(0)$, $\tilde{g}'(0)$ and $\tilde{\theta}'(0)$.

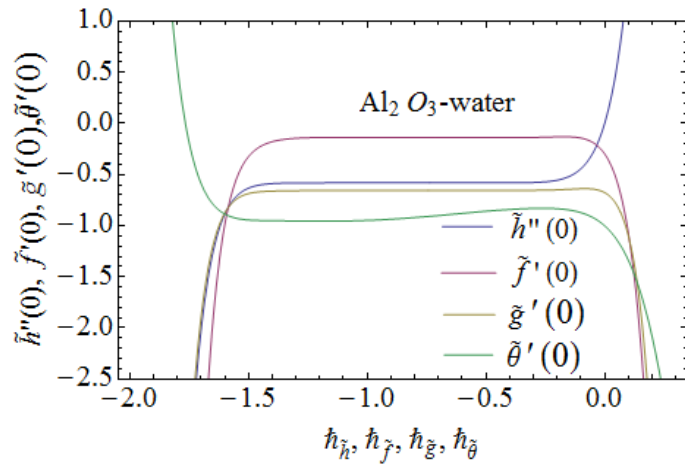


Fig. 4.5: \tilde{h} -curves for $\tilde{h}''(0)$, $\tilde{f}'(0)$, $\tilde{g}'(0)$ and $\tilde{\theta}'(0)$.

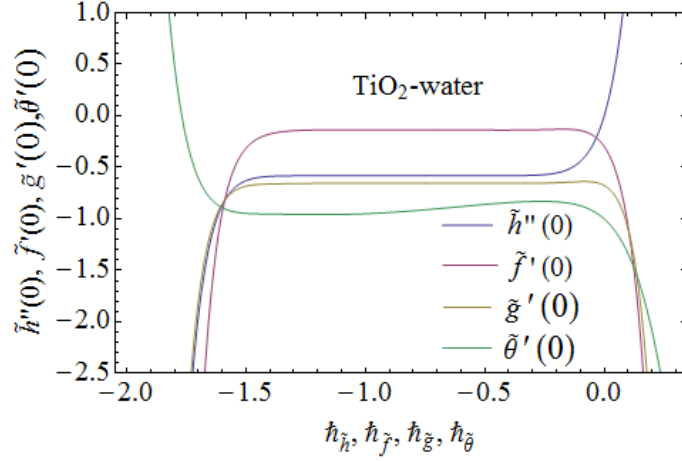


Fig. 4.6: \tilde{h} -curves for $\tilde{h}''(0)$, $\tilde{f}'(0)$, $\tilde{g}'(0)$ and $\tilde{\theta}'(0)$.

Table 4.2: Series solutions convergence for Ag -water nanofluid.

Order of approximations (Ag)	$\tilde{h}''(0)$	$\tilde{f}'(0)$	$\tilde{g}'(0)$	$\tilde{\theta}'(0)$
1	-0.3901	-0.1376	-0.6238	-0.8219
5	-0.5795	-0.1353	-0.6676	-0.7710
10	-0.5795	-0.1418	-0.6656	-0.9006
11	-0.5796	-0.1418	-0.6656	-0.9232
16	-0.5796	-0.1418	-0.6656	-0.9702
25	-0.5796	-0.1418	-0.6656	-0.9702
35	-0.5796	-0.1418	-0.6656	-0.9702

Table 4.3: Series solutions convergence for Cu -water nanofluid.

Order of approximations (Cu)	$\tilde{h}''(0)$	$-\tilde{f}'(0)$	$-\tilde{g}'(0)$	$-\tilde{\theta}'(0)$
1	-0.3901	-0.1366	-0.6222	-0.8223
5	-0.5794	-0.1423	-0.6659	-0.7718
10	-0.5795	-0.1421	-0.6639	-0.9017
11	-0.5795	-0.1422	-0.6640	-0.9245
15	-0.5795	-0.1422	-0.6640	-0.9717
25	-0.5795	-0.1422	-0.6640	-0.9717
35	-0.5795	-0.1422	-0.6640	-0.9717

Table 4.4: Convergence iterations for CuO –water nanofluid.

Iterations	$\tilde{h}''(0)$	$-\tilde{f}'(0)$	$-\tilde{g}'(0)$	$-\tilde{\theta}'(0)$
1	-0.3901	-0.1317	-0.6146	-0.8230
5	-0.5802	-0.1372	-0.6584	-0.7751
11	-0.5802	-0.1371	-0.6565	-0.9325
15	-0.5802	-0.1372	-0.6565	-0.9801
20	-0.5802	-0.1372	-0.6565	-0.9747
30	-0.5802	-0.1372	-0.6565	-0.9747
35	-0.5802	-0.1372	-0.6565	-0.9747

Table 4.5: Convergence of series solutions for Al_2O_3 –water nanofluid.

Order of approximations (Al_2O_3)	$\tilde{h}''(0)$	$-\tilde{f}'(0)$	$-\tilde{g}'(0)$	$-\tilde{\theta}'(0)$
1	-0.3901	-0.1300	-0.6119	-0.8230
7	-0.5800	-0.1389	-0.6539	-0.8264
11	-0.5800	-0.1377	-0.6539	-0.9324
13	-0.5800	-0.1378	-0.6539	-0.9663
17	-0.5800	-0.1378	-0.6539	-0.9746
25	-0.5800	-0.1378	-0.6539	-0.9746
35	-0.5800	-0.1378	-0.6539	-0.9746

Table 4.6: Series solutions convergence for TiO_2 –water nanofluid.

Order of approximations (TiO_2)	$\tilde{h}''(0)$	$-\tilde{f}'(0)$	$-\tilde{g}'(0)$	$-\tilde{\theta}'(0)$
1	-0.3901	-0.1302	-0.6122	-0.8235
10	-0.5802	-0.1375	-0.6541	-0.9106
11	-0.5802	-0.1376	-0.6542	-0.9341
12	-0.5802	-0.1377	-0.6542	-0.9535
17	-0.5802	-0.1377	-0.6542	-0.9766
25	-0.5802	-0.1377	-0.6542	-0.9766
35	-0.5802	-0.1377	-0.6542	-0.9766

Table 4.7: Thermophysical properties of nanoparticles.

	$k(W/mk)$	$\rho(kg/m^3)$	$\sigma(Um)^{-1}$	$c_p(J/kgk)$	$\beta \times 10^{-6}(1/k)$
Silver (<i>Ag</i>)	429	10490	6.30×10^7	235	18.9
Copper (<i>Cu</i>)	401	8933	5.96×10^7	385	16.7
Copper oxide (<i>CuO</i>)	76.1	6320	2.7×10^{-8}	531.8	18.0
Aluminium oxide (<i>Al₂O₃</i>)	40	3970	1×10^{-10}	765	8.5
Titanium oxide (<i>TiO₂</i>)	8.9538	4250	1×10^{-12}	686.2	9.0
Water (<i>H₂O</i>)	0.613	997.1	0.05	4179	210

4.4 Discussion

This section elucidates the influences of flow field, temperature, Nusselt number and skin friction coefficient versus different flow parameters.

4.4.1 Axial, radial and tangential velocity components

Figs. (4.7 – 4.27) show the outcome of axial, radial and tangential velocities via involved parameters for *Ag*-water, *Cu*-water, *CuO*-water, *Al₂O₃*-water and *TiO₂*-water nanofluids. Impact of disk thickness power law index ς for velocity components (axial, radial and tangential) is presented in Figs. (4.7 – 4.9). It is clear from the Figs. that magnitude of axial velocity reduces for larger ς while radial and tangential velocities increase. Effects of *CuO*, *Al₂O₃* and *TiO₂* water nanofluids dominant over *Ag* and *Cu* water nanofluids. It is due to the fact because *Ag* and *Cu* nanoparticles are more dense than rest of the nanoparticles. Behavior of constant number ϵ^* for all velocities components is shown in Figs. (4.10 – 4.12). For larger ϵ^* the axial, radial and tangential velocities enhance. In fact with an increase in ϵ^* the radius R_0 decreases so less particles are in contact with the surface and consequently less resistance leads to increase in velocity. Also *Ag* and *Cu* water nanofluids have less velocity when compared with other nanofluids. Figs. (4.13 – 4.15) are organized to see the outcomes of $\tilde{h}(\xi)$, $\tilde{f}(\xi)$ and $\tilde{g}(\xi)$ for increasing values of stretching parameter A_1 . It is worth mentioning that velocities in radial and axial directions are increasing while there is decrease in tangential velocity component. When we increase the value of A_1 the stretching rate at disk is increasing so axial and radial velocity

enhance while decrease in tangential velocity is observed for reduction in Ω_1 . We noticed from Fig. 4.15 that tangential velocity is less for Ag and Cu water nanofluid than CuO , Al_2O_3 and TiO_2 water nanofluids (due to their higher densities). Fig. 4.16 shows that larger disk thickness coefficient α lead to decrease in axial velocity component. Magnitude of axial velocity increases for larger nanoparticles volume fraction ϕ (see Fig. 4.17). Impact of velocity slip parameter γ_1 for $\tilde{h}(\xi)$ and $\tilde{f}(\xi)$ is displayed in Figs. 4.18 and 4.19. Here magnitude of velocity decays with an increase in γ_1 . In fact when slip velocity enhances then there is less transport of momentum in radial direction. In these Figs. the results overlap for all nanofluids. Radial and tangential velocities are reduced for larger γ_2 (see Figs. 4.20 and 4.21). Behavior of magnetic parameter M against $\tilde{f}(\xi)$ and $\tilde{g}(\xi)$ is mentioned in Figs. 4.22 and 4.23. Both velocities reduce because M is associated with resistive force known as Lorentz force. Power law index n affecting within boundary layer of five nanofluids for $\tilde{f}(\xi)$ and $\tilde{g}(\xi)$ is illustrated in Figs. 4.24 and 4.25. For higher n both velocities enhance. In fact the power of radius R_0 decays and thus velocity enhances. Effect of Reynolds number Re on radial and tangential velocities is depicted in Figs. 4.26 and 4.27. These velocities increase for larger Re . For higher Re the viscosity decays so less resistance is offered to fluid particles and so velocity enhances.

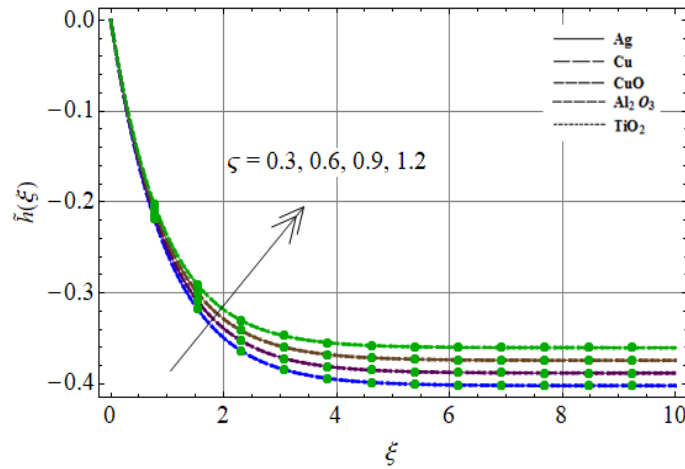


Fig. 4.7: $\tilde{h}(\xi)$ versus ς .

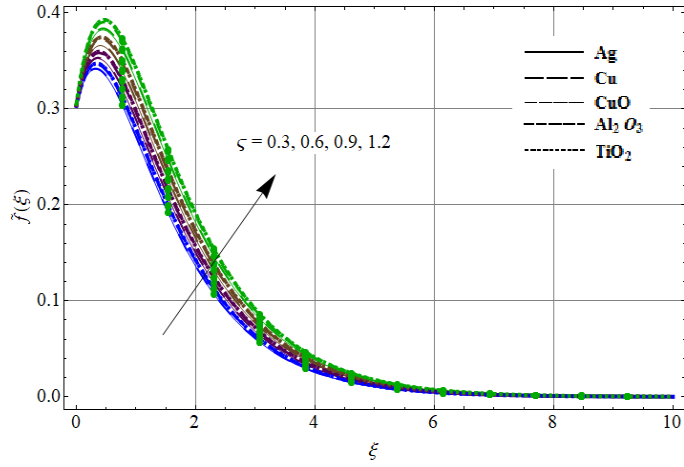


Fig. 4.8: $\tilde{f}(\xi)$ versus ζ .

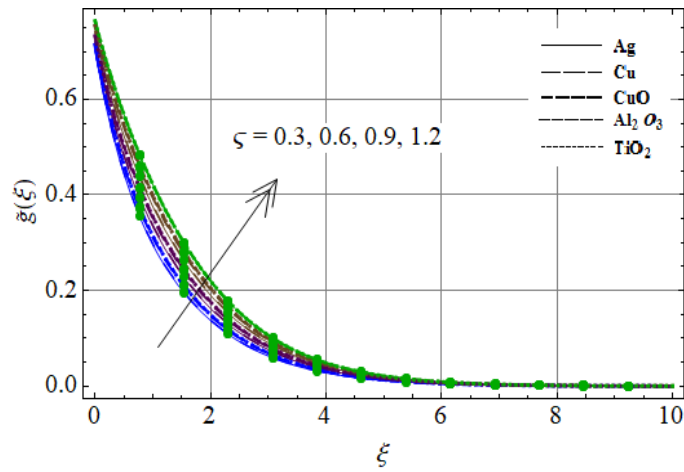


Fig. 4.9: $\tilde{g}(\xi)$ versus ζ .

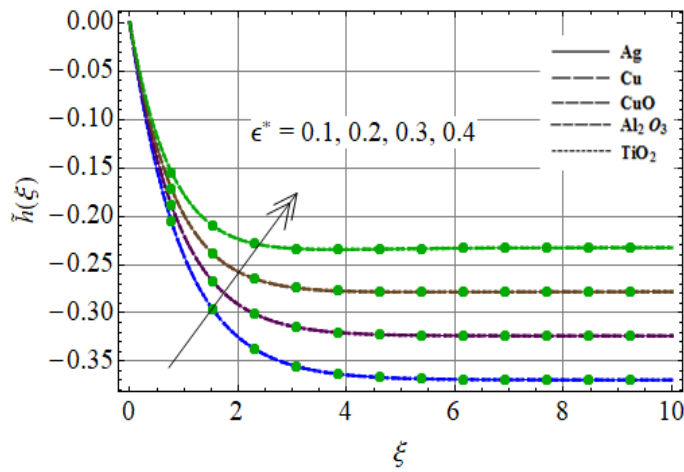


Fig. 4.10: $\tilde{h}(\xi)$ versus ϵ^* .

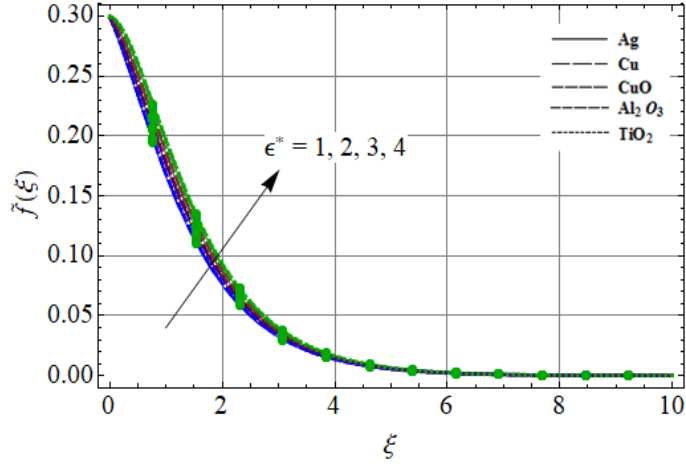


Fig. 4.11: $\tilde{f}(\xi)$ versus ϵ^* .

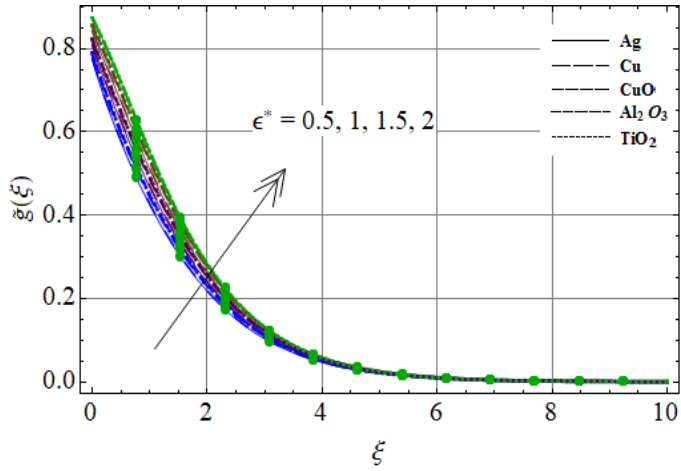


Fig. 4.12: $\tilde{g}(\xi)$ versus ϵ^* .

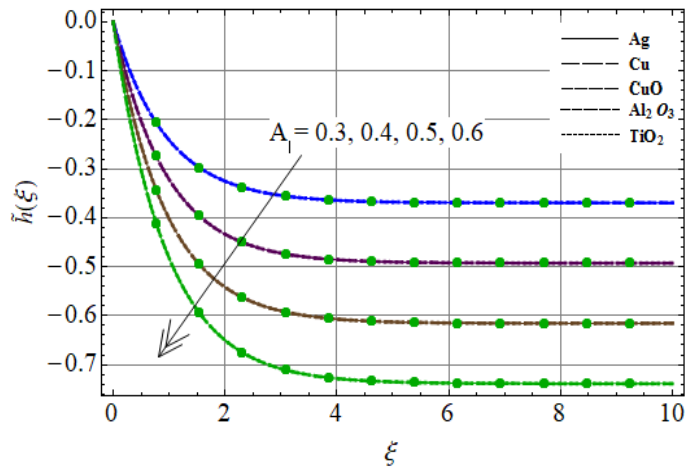


Fig. 4.13: $\tilde{h}(\xi)$ versus A_1 .

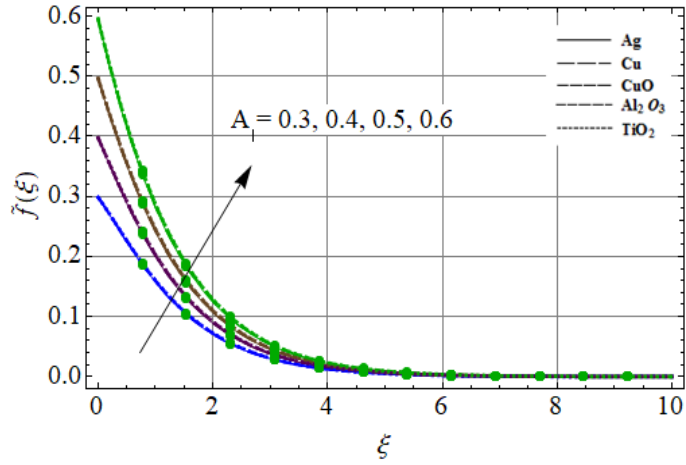


Fig. 4.14: $\tilde{f}(\xi)$ versus A_1 .

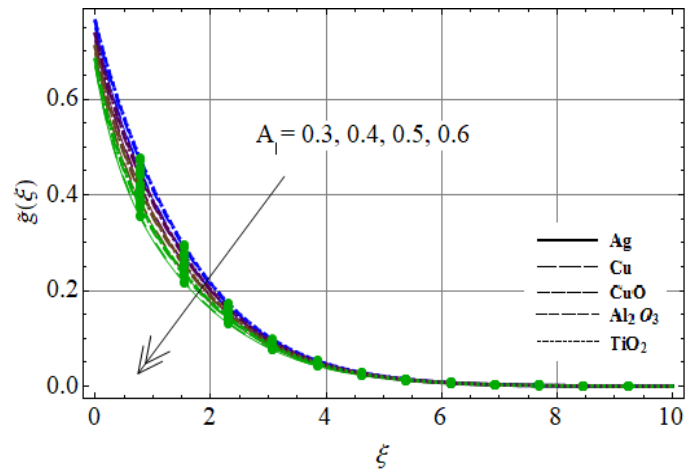


Fig. 4.15: $\tilde{g}(\xi)$ versus A_1 .

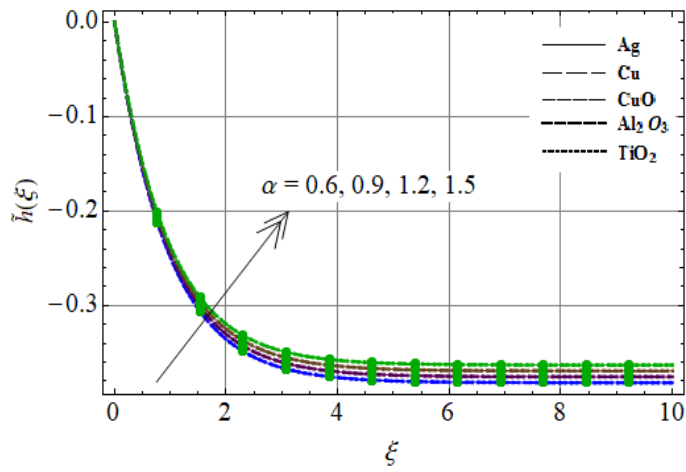


Fig. 4.16: $\tilde{h}(\xi)$ versus α .

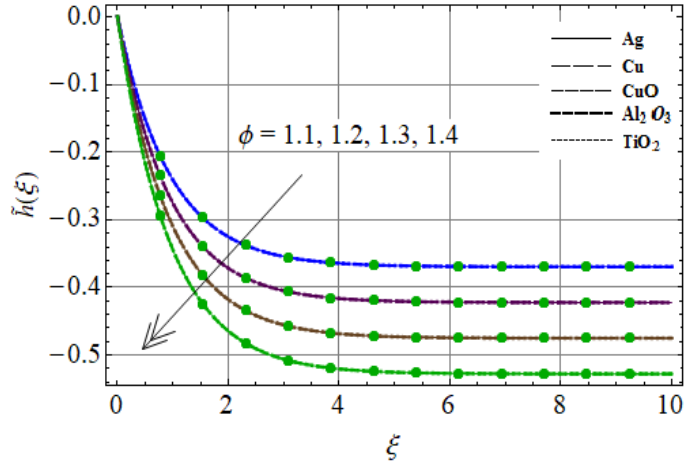


Fig. 4.17: $\tilde{h}(\xi)$ versus ϕ .

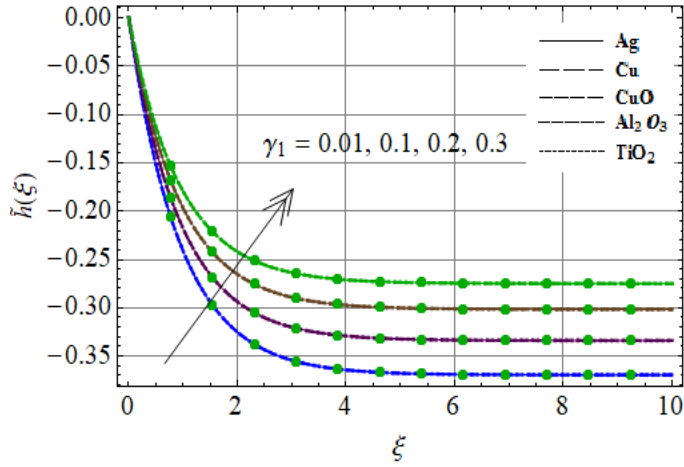


Fig. 4.18: $\tilde{h}(\xi)$ versus γ_1 .

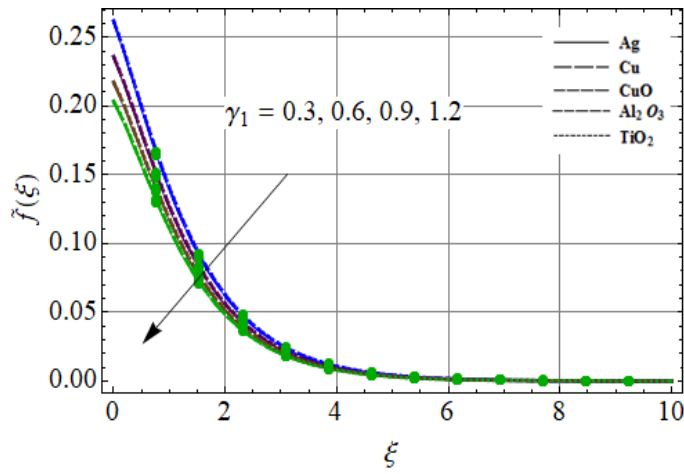


Fig. 4.19: $\tilde{f}(\xi)$ versus γ_1 .

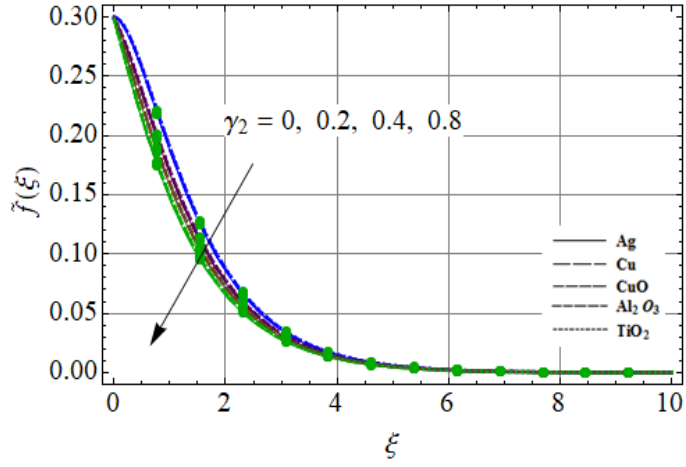


Fig. 4.20: $\tilde{f}(\xi)$ versus γ_2 .

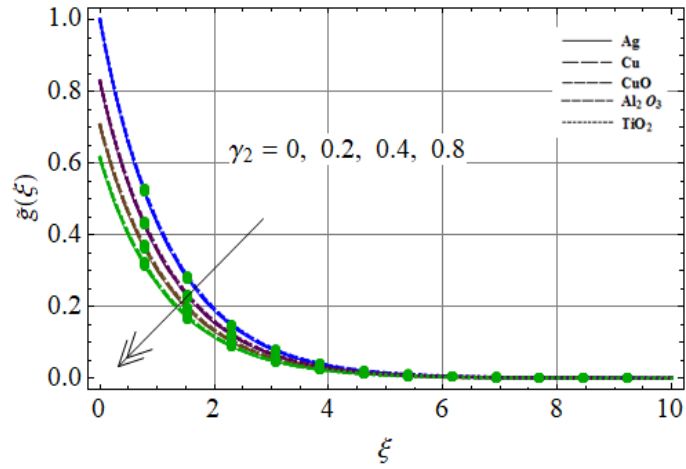


Fig. 4.21: $\tilde{g}(\xi)$ versus γ_2 .

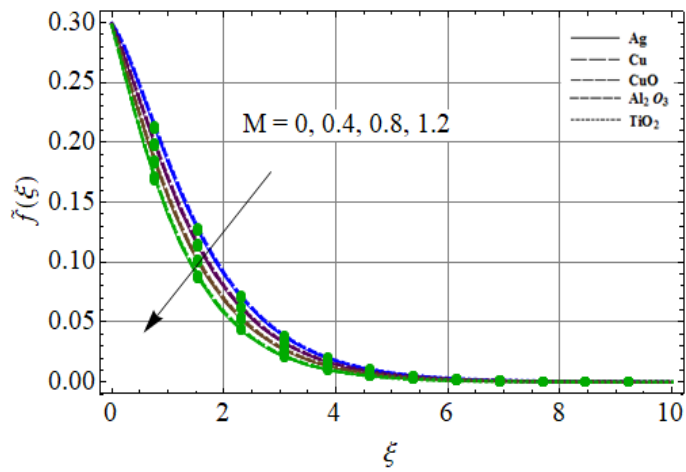


Fig. 4.22: $\tilde{f}(\xi)$ versus M .

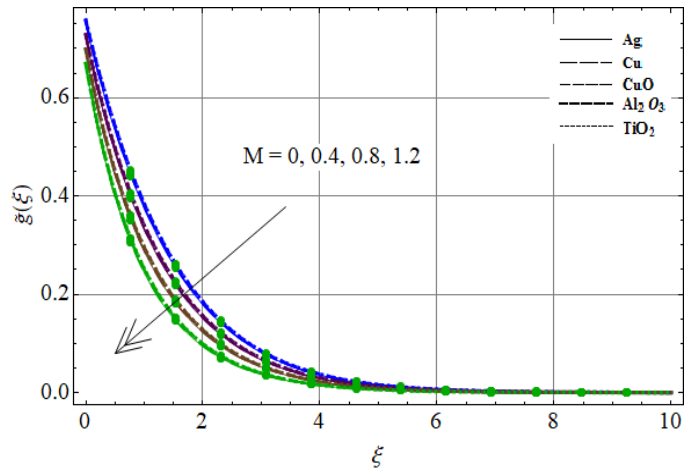


Fig. 4.23: $\tilde{g}(\xi)$ versus M .

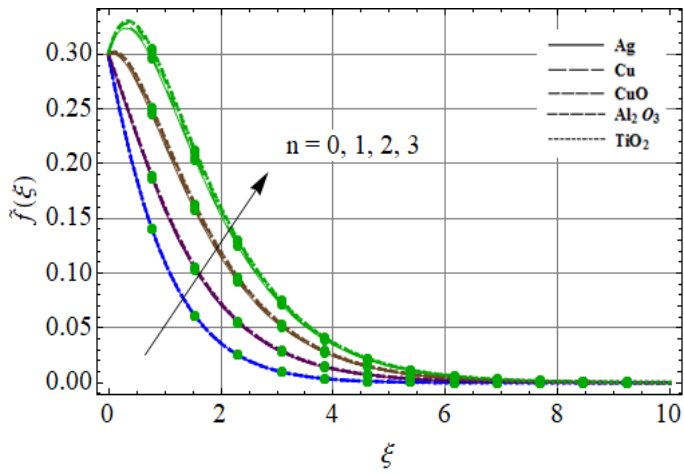


Fig. 4.24: $\tilde{f}(\xi)$ versus n .

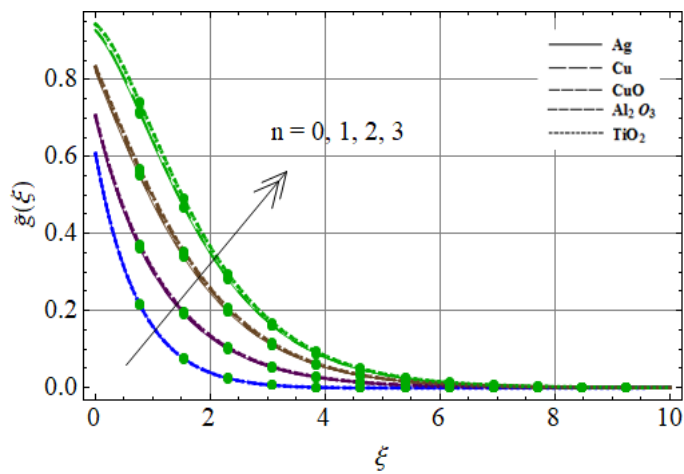


Fig. 4.25: $\tilde{g}(\xi)$ versus n .

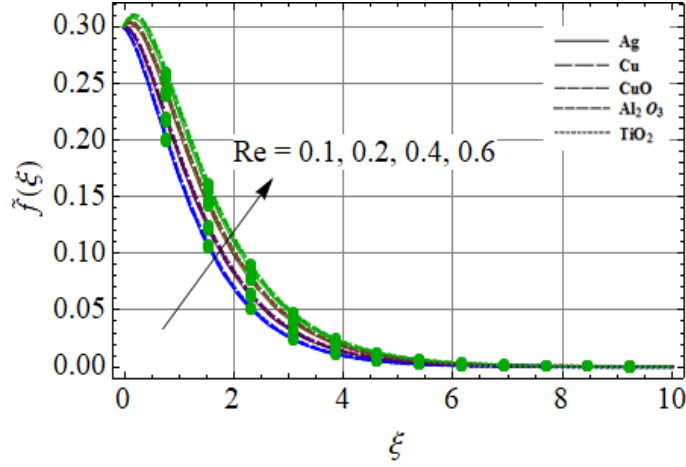


Fig. 4.26: $\tilde{f}(\xi)$ versus Re .

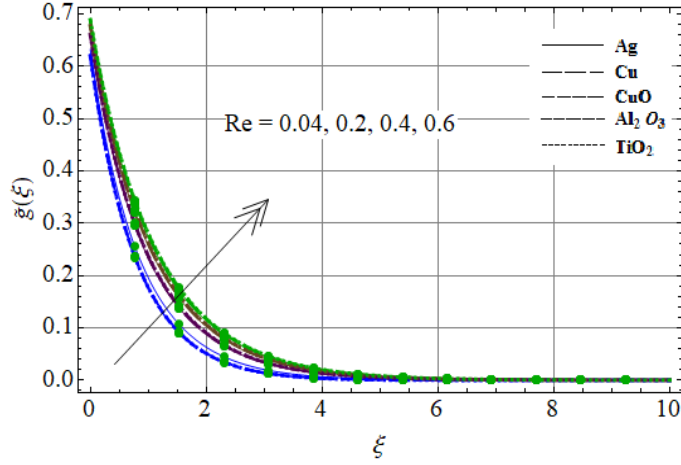


Fig. 4.27: $\tilde{g}(\xi)$ versus Re .

4.4.2 Temperature

Figs. (4.28 – 4.33) portray the effect of involved parameter on temperature for *Ag*-water, *Cu*-water, *CuO*-water, *Al₂O₃*-water and *TiO₂*-water nanofluids. Graph of temperature $\tilde{\theta}(\xi)$ against constant number ϵ^* is shown in Fig. 4.28. Temperature rises for larger ϵ^* . Behavior of $\tilde{\theta}(\xi)$ for increasing Re is analyzed in Fig. 4.29. Direct relation is observed between Re and $\tilde{\theta}(\xi)$. Results overlap for all nanofluids. Fig. 4.30 assures the enhancement in temperature with increase in n for *Ag*-water, *Cu*-water, *CuO*-water, *Al₂O₃*-water and *TiO₂*-water nanofluids. Fig. 4.31 shows that with rise in nanoparticle volume fraction $\tilde{\phi}$ the temperature enhances. Larger values of $\tilde{\phi}$ correspond to larger thermal conductivity and thermal layer thickness. As a result

the temperature increases. Effects of *Ag*–water nanofluid dominant over *Cu*–water, *CuO*–water, *Al₂O₃*–water and *TiO₂*–water nanofluids. It is because of its higher thermal conductivity. Impact of Hartmann number *M* is predicted in Fig. 4.32. Here temperature has direct relation with *M*. Magnetic field depend upon Lorentz force which yield resistance to the nanomaterials motion. Thus more heat is produced. It consequently boosts the thermal field and layer thickness. Outcome of *Ec* against thermal field is shown in Fig. 4.33. We noticed that $\tilde{\theta}(\xi)$ enhances for larger *Ec*. Effects of nanofluids on temperature dominant with respect to their higher thermal conductivity. Hence silver water nanofluid dominants because *Ag* nanoparticles have highest thermal conductivity than *Cu*, *CuO*, *Al₂O₃* and *TiO₂* nanoparticles.

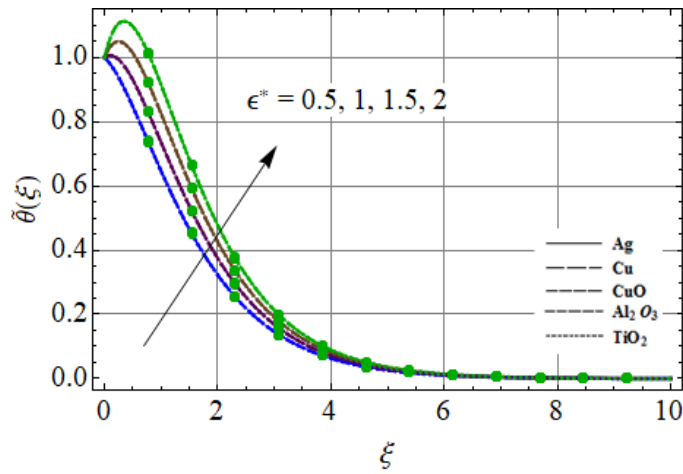


Fig. 4.28: Outcome of ϵ^* on $\tilde{\theta}(\xi)$.

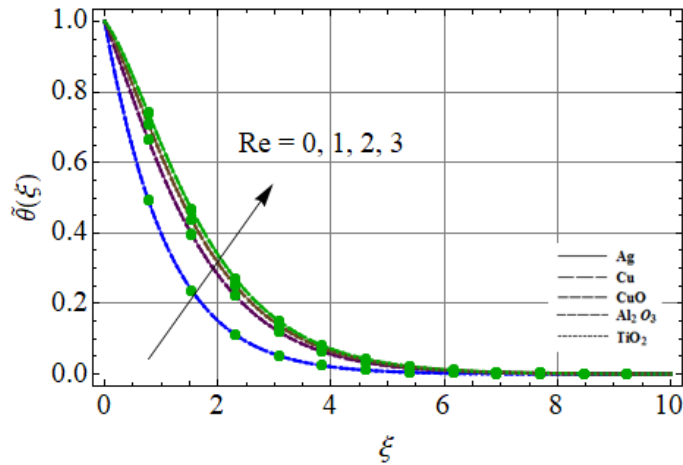


Fig. 4.29: Outcome of *Re* on $\tilde{\theta}(\xi)$.

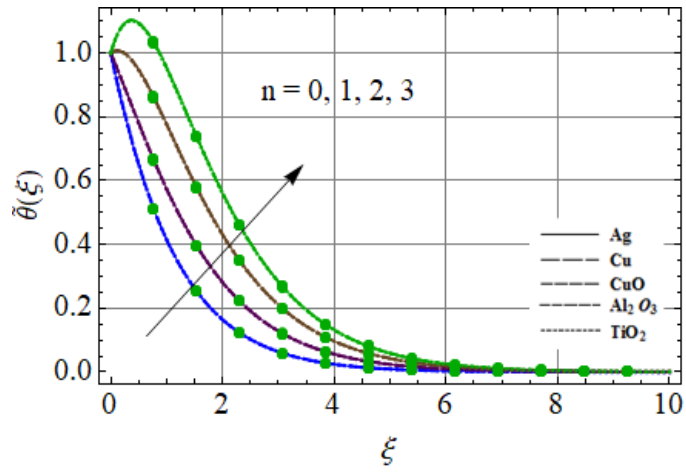


Fig. 4.30: Outcome of n on $\tilde{\theta}(\xi)$.

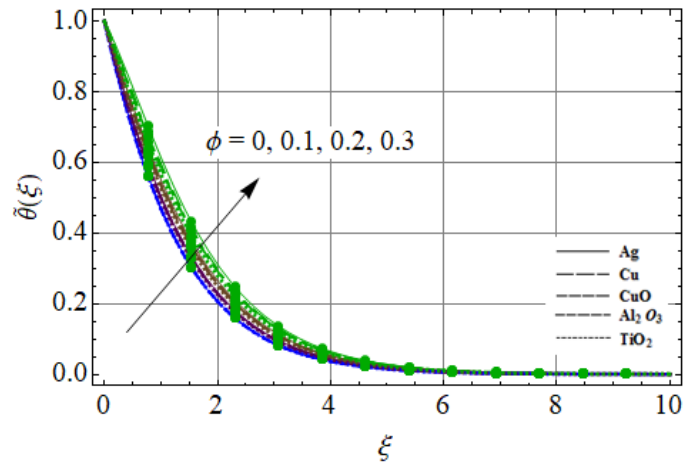


Fig. 4.31: Outcome of ϕ on $\tilde{\theta}(\xi)$.

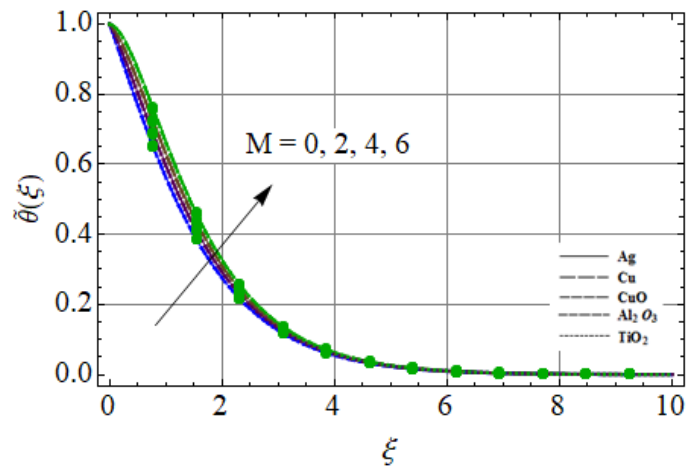


Fig. 4.32: Outcome of M on $\tilde{\theta}(\xi)$.

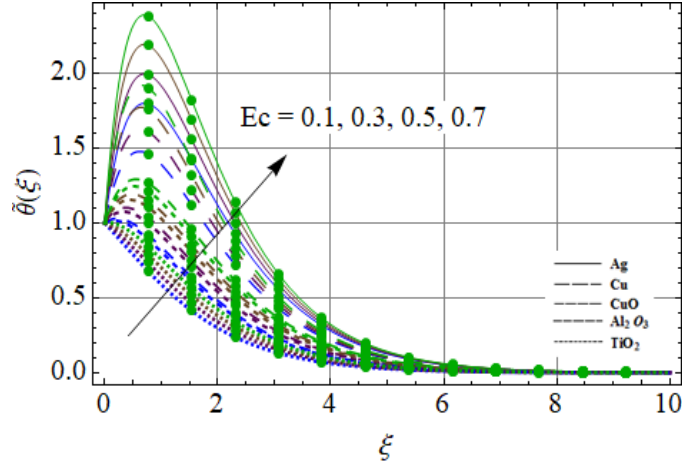


Fig. 4.33: Outcome of Ec on $\tilde{\theta}(\xi)$.

4.4.3 Surface drag force

Figs. (4.34–4.36) display the impact of slip parameters γ_1 and γ_2 , stretching parameter A_1 and disk thickness index ς on skin friction coefficient for Ag -water, Cu -water, CuO -water, Al_2O_3 -water and TiO_2 -water nanofluids. It is noted that surface drag force reduces for rising γ_1 and γ_2 while opposite trend is witnessed for A_1 and ς . Moreover skin friction decreases by enhancing the density of nanoparticles. That is why dominance of nanofluids depends upon the densities of respective nanoparticles.

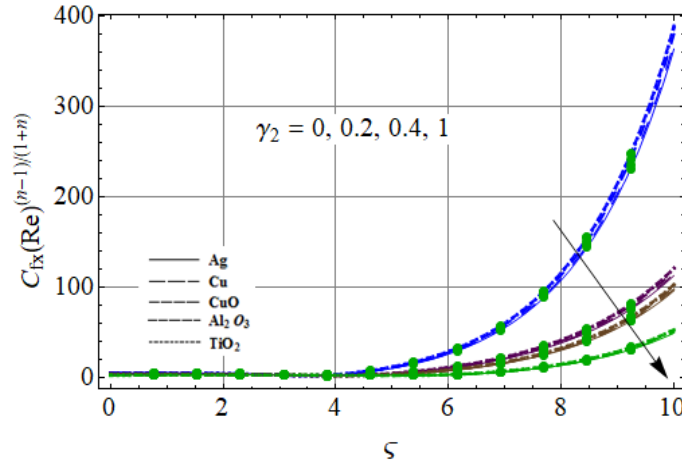


Fig. 4.34: Behavior of γ_2 against $C_{fx}(\text{Re})^{(n-1)/(n+1)}$.

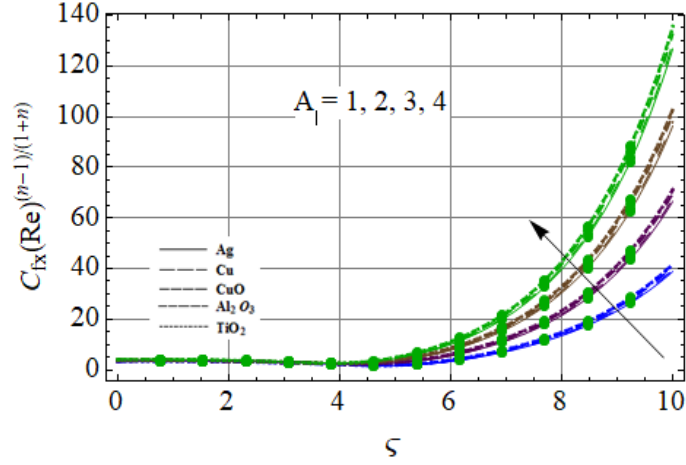


Fig. 4.35: Behavior of A_1 against $C_{fx}(\text{Re})^{(n-1)/(n+1)}$.

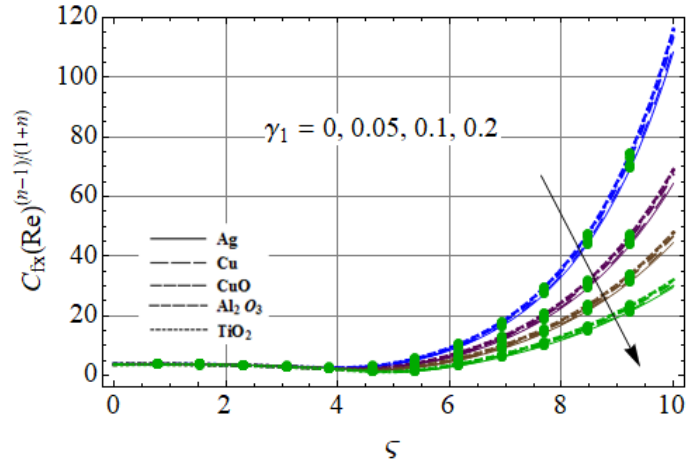


Fig. 4.36: Behavior of γ_1 against $C_{fx}(\text{Re})^{(n-1)/(n+1)}$.

4.4.4 Nusselt number

Impact of disk thickness coefficient α , stretching parameter A_1 , Eckert number Ec and disk thickness index ζ on Nusselt number is analyzed in Figs. (4.37 – 4.39). It is remarked that heat

transfer rate upsurges for larger α , A_1 and Ec for all nanofluids.

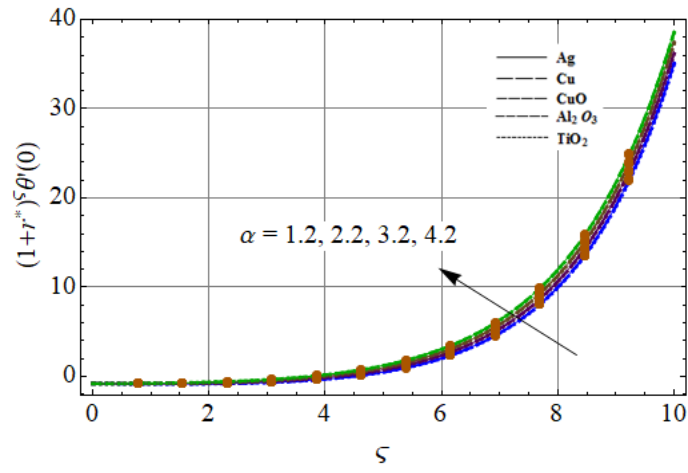


Fig. 4.37: Behavior of α against $(1+r^*)^\zeta \tilde{\theta}'(0)$.

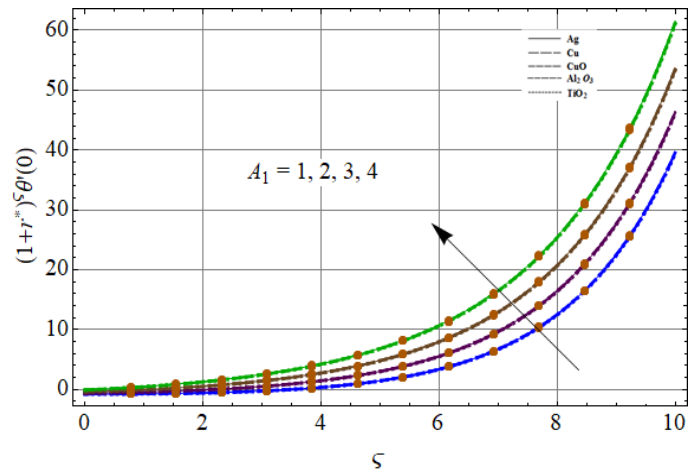


Fig. 4.38: Behavior of A_1 against $(1+r^*)^\zeta \tilde{\theta}'(0)$.

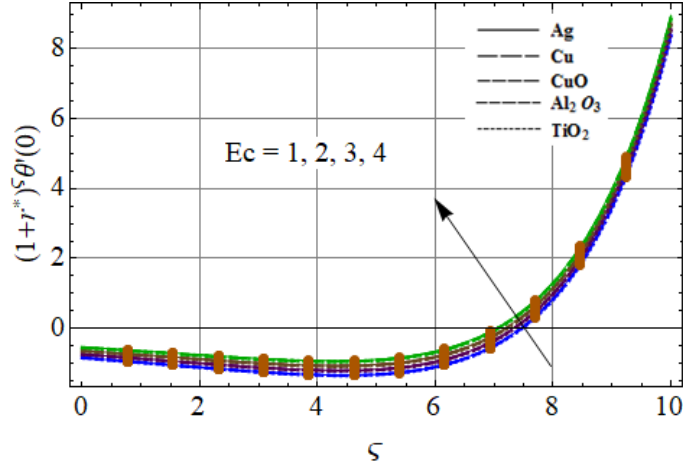


Fig. 4.39: Behavior of Ec against $(1+r^*)^{\zeta}\tilde{\theta}'(0)$.

4.5 Conclusions

Here we studied partial slip and Joule heating in flow of nanomaterials. Main points are as follows:

- For larger stretching parameter A_1 the velocities in axial radial and tangential direction are enhanced.
- Axial velocity reduces for higher nanoparticle volume fraction ϕ .
- With rise in slip parameters γ_1 and γ_2 the velocities in axial, radial and tangential directions are reduced.
- Velocity for TiO_2 -water nanofluid is highest.
- For larger Ec the temperature of fluid increases and impact of Ag -water nanofluid dominant over all.
- Reduction in surface drag force is noticed for larger γ_2 and γ_1 .
- Rate of heat transfer rises for increasing A_1 .

Chapter 5

Flow of magnetite- Fe_3O_4 nanoparticles in presence of partial slip conditions

Abstract: This chapter addresses the flow of magnetic nanofluid (ferrofluid) between two rotating stretchable disks with different rotating and stretching velocities. Water based fluid comprising magnetite- Fe_3O_4 nanoparticles is addressed. Velocity slip and temperature jump at solid-fluid interface are also taken into account. Appropriate transformations reduce the nonlinear PDE's system to ordinary ones. Homotopy solutions are established. Velocity, temperature, Nusselt number and skin friction coefficient are analyzed. It is interesting to note that tangential velocity of fluid decreases for higher velocity slip variable. Fluid temperature also reduces for increasing value of thermal slip parameter. Nusselt number and skin friction at lower disk are enhanced for higher magnetic field strength.

5.1 Problem formulation

Consider an axisymmetric flow of incompressible ferrofluid bounded by two continuously stretching coaxial disks. Magnetite- Fe_3O_4 nanoparticles in water are known as ferrofluid. It is assumed that the lower disk is located at $z = 0$ while the upper disk is at a constant distance h apart. Both disks are rotating in axial direction with angular frequencies Ω_1 and Ω_2 . Further both

disks stretch in radial direction with a_1 and a_2 (see Fig. 5.1).

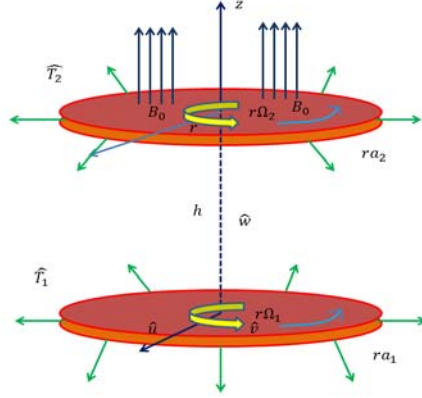


Fig. 5.1: Physical model.

Electrically conducting fluid is taken. Slip conditions for velocity and temperature are imposed.

The flow expressions are stated as

$$\frac{\partial \hat{u}}{\partial r} + \frac{\hat{u}}{r} + \frac{\partial w}{\partial z} = 0, \quad (5.1)$$

$$\hat{u} \frac{\partial \hat{u}}{\partial r} + \hat{w} \frac{\partial \hat{u}}{\partial z} - \frac{\hat{v}^2}{r} = -\frac{1}{\rho_{nf}} \frac{\partial \hat{p}}{\partial r} + \nu_{nf} \left(\frac{\partial^2 \hat{u}}{\partial r^2} + \frac{1}{r} \frac{\partial \hat{u}}{\partial r} + \frac{\partial^2 \hat{u}}{\partial z^2} - \frac{\hat{u}}{r^2} \right) - \frac{\sigma_{nf}}{\rho_{nf}} B_0^2 \hat{u}, \quad (5.2)$$

$$\hat{u} \frac{\partial \hat{v}}{\partial r} + \hat{w} \frac{\partial \hat{v}}{\partial z} + \frac{\hat{u} \hat{v}}{r} = \nu_{nf} \left(\frac{\partial^2 \hat{v}}{\partial r^2} + \frac{1}{r} \frac{\partial \hat{v}}{\partial r} + \frac{\partial^2 \hat{v}}{\partial z^2} - \frac{\hat{v}}{r^2} \right) - \frac{\sigma_{nf}}{\rho_{nf}} B_0^2 \hat{v}, \quad (5.3)$$

$$\hat{w} \frac{\partial \hat{w}}{\partial r} + \hat{u} \frac{\partial \hat{w}}{\partial z} = -\frac{1}{\rho_{nf}} \frac{\partial \hat{p}}{\partial z} + \nu_{nf} \left(\frac{\partial^2 \hat{w}}{\partial r^2} + \frac{1}{r} \frac{\partial \hat{w}}{\partial r} + \frac{\partial^2 \hat{w}}{\partial z^2} \right), \quad (5.4)$$

$$(\rho c_p)_{nf} \left(\hat{u} \frac{\partial \hat{T}}{\partial r} + \hat{w} \frac{\partial \hat{T}}{\partial z} \right) = k_{nf} \left(\frac{1}{r} \frac{\partial \hat{T}}{\partial r} + \frac{\partial^2 \hat{T}}{\partial r^2} + \frac{\partial^2 \hat{T}}{\partial z^2} \right), \quad (5.5)$$

$$\begin{aligned} \hat{u} &= ra_1 + \lambda_1 \frac{\partial \hat{u}}{\partial z}, \quad \hat{v} = r\Omega_1 + \lambda_2 \frac{\partial \hat{v}}{\partial z}, \quad \hat{w} = 0, \quad \hat{T} = \hat{T}_1 + \lambda_3 \frac{\partial \hat{T}}{\partial z} \quad \text{at } z = 0, \\ \hat{u} &= ra_2 - \lambda_1 \frac{\partial \hat{u}}{\partial z}, \quad \hat{v} = r\Omega_2 - \lambda_2 \frac{\partial \hat{v}}{\partial z}, \quad \hat{w} = 0, \quad \hat{T} = \hat{T}_2 - \lambda_3 \frac{\partial \hat{T}}{\partial z} \quad \text{at } z = h, \end{aligned} \quad (5.6)$$

The effective nanofluid dynamic viscosity μ_{nf} , density ρ_{nf} , heat capacitance $(\rho c_p)_{nf}$, thermal conductivity k_{nf} and electrical conductivity σ_{nf} are

$$\mu_{nf} = \frac{\mu_f}{(1 - \phi)^{2.5}}, \quad (5.7)$$

$$\rho_{nf} = \rho_f(1 - \phi) + \rho_s\phi, \quad (5.8)$$

$$(\rho c_p)_{nf} = (\rho c_p)_f(1 - \phi) + (\rho c_p)_s\phi, \quad (5.9)$$

$$\frac{k_{nf}}{k_f} = \frac{k_s + 2k_f - 2\phi(k_f - k_s)}{k_s + 2k_f + 2\phi(k_f - k_s)}, \quad (5.10)$$

$$\frac{\sigma_{nf}}{\sigma_f} = 1 + \frac{3 \left(\frac{\sigma_s}{\sigma_f} - 1 \right) \phi}{\left(\frac{\sigma_s}{\sigma_f} + 2 \right) - \left(\frac{\sigma_s}{\sigma_f} - 1 \right) \phi}, \quad (5.11)$$

where ϕ denotes the solid volume fraction of nanoparticles.

Using Von-Karman transformations [7]

$$\hat{u} = r\Omega_1 \tilde{f}'(\xi), \quad \hat{v} = r\Omega_1 \tilde{g}(\xi), \quad \hat{w} = -2h\Omega_1 \tilde{f}(\xi), \quad \tilde{\theta} = \frac{\hat{T} - \hat{T}_2}{\hat{T}_1 - \hat{T}_2}, \quad \hat{p} = \rho_f \Omega_1 \nu_f \left(P(\xi) + \frac{1}{2} \frac{r^2}{h^2} \epsilon \right), \quad \xi = \frac{z}{h}, \quad (5.12)$$

the continuity equation is satisfied and Eqs. (5.2 – 5.6) become

$$\frac{1}{(1 - \phi)^{2.5} \left(1 - \phi + \frac{\rho_s}{\rho_f} \phi \right)} \tilde{f}'''' + \text{Re} \left(2\tilde{f}\tilde{f}'' - \tilde{f}'^2 + \tilde{g}^2 - \frac{M}{1 - \phi + \frac{\rho_s}{\rho_f} \phi} \frac{\sigma_{nf}}{\sigma_f} \tilde{f}' \right) - \frac{\epsilon}{1 - \phi + \frac{\rho_s}{\rho_f} \phi} = 0, \quad (5.13)$$

$$\frac{1}{(1 - \phi)^{2.5} \left(1 - \phi + \frac{\rho_s}{\rho_f} \phi \right)} \tilde{g}'' + \text{Re} \left(2\tilde{f}\tilde{g}' - 2\tilde{f}'\tilde{g} - \frac{M}{1 - \phi + \frac{\rho_s}{\rho_f} \phi} \frac{\sigma_{nf}}{\sigma_f} \tilde{g} \right) = 0, \quad (5.14)$$

$$\frac{1}{1 - \phi + \frac{\rho_s}{\rho_f} \phi} P' = -4 \text{Re} \tilde{f}\tilde{f}' - \frac{2}{(1 - \phi)^{2.5} \left(1 - \phi + \frac{\rho_s}{\rho_f} \phi \right)} \tilde{f}'' , \quad (5.15)$$

$$\frac{1}{\text{Pr}} \frac{k_{nf}}{k_f} \tilde{\theta}'' + 2 \text{Re} \left(1 - \phi + \frac{(\rho c_p)_s}{(\rho c_p)_f} \phi \right) \tilde{f}\tilde{\theta}' = 0, \quad (5.16)$$

$$\begin{aligned} \tilde{f}(0) &= 0, \quad \tilde{f}(1) = 0, \quad \tilde{f}'(0) = A_1 + \gamma_1 \tilde{f}''(0), \quad \tilde{f}'(1) = A_2 - \gamma_1 \tilde{f}''(1), \quad \tilde{g}(0) = 1 + \gamma_2 \tilde{g}'(0), \\ \tilde{g}(1) &= \Omega - \gamma_2 \tilde{g}'(1), \quad \tilde{\theta}(0) = 1 + \gamma_3 \tilde{\theta}'(0), \quad \tilde{\theta}(1) = -\gamma_3 \tilde{\theta}'(1), \quad P(0) = 0, \end{aligned} \quad (5.17)$$

$$\begin{aligned}
\text{Re} &= \frac{\Omega_1 h^2}{\nu_f}, \quad \text{Pr} = \frac{(\rho c_p)_f \nu_f}{k_f}, \quad M = \frac{B_0^2 \sigma_f}{\rho_f \Omega_1}, \quad A_1 = \frac{a_1}{\Omega_1}, \\
A_2 &= \frac{a_2}{\Omega_1}, \quad \Omega = \frac{\Omega_2}{\Omega_1}, \quad \gamma_1 = \frac{\lambda_1}{d}, \quad \gamma_2 = \frac{\lambda_2}{d}, \quad \gamma_3 = \frac{\lambda_3}{d}.
\end{aligned} \tag{5.18}$$

Here Re depicts the Reynolds number, M the Hartmann number, Pr the Prandtl number, A_1 and A_2 the scaled stretching variables, γ_1, γ_2 the velocity slip parameters, Ω the rotation number and γ_3 the thermal slip parameter.

To acquire a more simplified form and to remove ϵ , Eq. (5.13) is differentiated with respect to ξ as follows:

$$\frac{1}{(1-\phi)^{2.5}(1-\phi+\frac{\rho_s}{\rho_f}\phi)} \tilde{f}^{iv} + \text{Re} \left(2\tilde{f}\tilde{f}''' + 2\tilde{g}\tilde{g}' - \frac{M}{1-\phi+\frac{\rho_s}{\rho_f}\phi} \frac{\sigma_{nf}}{\sigma_f} \tilde{f}'' \right) = 0, \tag{5.19}$$

and the pressure parameter ϵ can be determined by using Eqs. (5.13) and (5.17)

$$\epsilon = \frac{1}{(1-\phi)^{2.5}} \tilde{f}'''(0) - \text{Re} \left(1 - \phi + \frac{\rho_s}{\rho_f} \phi \right) \left[(\tilde{f}'(0))^2 - (\tilde{g}(0))^2 + \frac{M}{1-\phi+\frac{\rho_s}{\rho_f}\phi} \frac{\sigma_{nf}}{\sigma_f} \tilde{f}'(0) \right]. \tag{5.20}$$

Also pressure term can be computed by integrating Eq. (5.15) w.r.t ξ and taking limit from 0 to ξ . It is

$$\frac{1}{1-\phi+\frac{\rho_s}{\rho_f}\phi} P = -2 \left[\text{Re} \tilde{f}^2 + \frac{1}{(1-\phi)^{2.5}(1-\phi+\frac{\rho_s}{\rho_f}\phi)} (\tilde{f}' - \tilde{f}'(0)) \right]. \tag{5.21}$$

Shear stresses at lower rotating disk in radial and tangential directions are τ_{zr} and $\tau_{z\theta}$

$$\tau_{zr} = \mu_{nf} \left. \frac{\partial \hat{u}}{\partial z} \right|_{z=0} = \frac{\mu_f r \Omega_1'' \tilde{f}(0)}{(1-\phi)^{2.5} h}, \quad \tau_{z\theta} = \mu \left. \frac{\partial \hat{v}}{\partial z} \right|_{z=0} = \frac{\mu_f r \Omega_1' \tilde{g}(0)}{(1-\phi)^{2.5} h}. \tag{5.22}$$

Total shear stress is defined in the form

$$\tau_w = \sqrt{\tau_{zr}^2 + \tau_{z\theta}^2}. \tag{5.23}$$

At lower and upper disks, the C_{f1} and C_{f2} are expressed as

$$C_{f1} = \frac{\tau_w|_{z=0}}{\rho_f(r\Omega_1)^2} = \frac{1}{\text{Re}_r(1-\phi)^{2.5}} [(\tilde{f}''(0))^2 + (\tilde{g}'(0))^2]^{1/2}, \quad (5.24)$$

$$C_{f2} = \frac{\tau_w|_{z=h}}{\rho_f(r\Omega_1)^2} = \frac{1}{\text{Re}_r(1-\phi)^{2.5}} [(\tilde{f}''(1))^2 + (\tilde{g}'(1))^2]^{1/2}, \quad (5.25)$$

where $\text{Re}_r = r\Omega_1 h/\nu_f$ is the local Reynolds number. Rates of heat transfer for lower and upper disks are

$$Nu_{x1} = \left. \frac{hq_w}{k_f(\hat{T}_1 - \hat{T}_2)} \right|_{z=0}, \quad Nu_{x2} = \left. \frac{hq_w}{k_f(\hat{T}_1 - \hat{T}_2)} \right|_{z=h}, \quad (5.26)$$

where wall heat flux q_w is given by

$$q_w|_{z=0} = -k_{nf} \left. \frac{\partial \hat{T}}{\partial z} \right|_{z=0} = -\frac{k_{nf}(\hat{T}_1 - \hat{T}_2)\tilde{\theta}'(0)}{h}, \quad (5.27)$$

$$q_w|_{z=h} = -k_{nf} \left. \frac{\partial \hat{T}}{\partial z} \right|_{z=h} = -\frac{k_{nf}(\hat{T}_1 - \hat{T}_2)\tilde{\theta}'(1)}{h}. \quad (5.28)$$

Nusselt numbers are as follows:

$$Nu_{x1} = -\frac{k_{nf}}{k_f}\tilde{\theta}'(0), \quad Nu_{x2} = -\frac{k_{nf}}{k_f}\tilde{\theta}'(1). \quad (5.29)$$

5.2 Solutions

We have

$$\tilde{f}_0(\xi) = \frac{A_1\xi + 4\gamma_1 A_1\xi - 2\gamma_1 A_2\xi - 2A_1\xi^2 - A_2\xi^2 - 6\gamma_1 A_1\xi^2 + A_1\xi^3 + A_2\xi^3 + 2A_2\gamma_1\xi^3 + 2\gamma_3 A_1\xi^3}{(1+2\gamma_1)(1+6\gamma_1)}, \quad (5.30)$$

$$\tilde{g}_0(\xi) = \frac{1 + \gamma_2 + \gamma_2\Omega + (\Omega - 1)\xi}{1 + 2\gamma_2}, \quad (5.31)$$

$$\tilde{\theta}_0(\xi) = \frac{1 + \gamma_3 - \xi}{1 + 2\gamma_3}, \quad (5.32)$$

$$\mathcal{L}_{\tilde{f}} = \tilde{f}''''', \quad \mathcal{L}_{\tilde{g}} = \tilde{g}''', \quad \mathcal{L}_{\tilde{\theta}} = \tilde{\theta}''', \quad (5.33)$$

with

$$\mathcal{L}_{\tilde{f}} [c_1 + c_2\xi + c_3\xi^2 + c_4\xi^3] = 0, \quad (5.34)$$

$$\mathcal{L}_{\tilde{g}} [c_5 + c_6\xi] = 0, \quad (5.35)$$

$$\mathcal{L}_{\tilde{\theta}} [c_7 + c_8\xi] = 0, \quad (5.36)$$

where c_i ($i = 1 - 8$) are the constants.

5.3 Convergence analysis

The HAM is very powerful technique to construct the series solutions of highly nonlinear differential system. In this technique, auxiliary variables $\tilde{h}_{\tilde{f}}$, $\tilde{h}_{\tilde{g}}$ and $\tilde{h}_{\tilde{\theta}}$ have important role for adjusting the convergence of series solutions. The \tilde{h} -curves are displayed in order to obtain meaning values ensuring the convergence (see Figs. (5.2 – 5.4)). Admissible values of the auxiliary parameters are $-1 \leq \tilde{h}_{\tilde{f}} \leq -0.4$, $0.2 \leq \tilde{h}_{\tilde{g}} \leq 0.7$ and $-1.1 \leq \tilde{h}_{\tilde{\theta}} \leq -0.05$. Further the series solutions converge in the whole region of ξ ($0 \leq \xi \leq \infty$) when $\tilde{h}_{\tilde{f}} = -1$, $\tilde{h}_{\tilde{g}} = 0.5$ and $\tilde{h}_{\tilde{\theta}} = -0.5$.

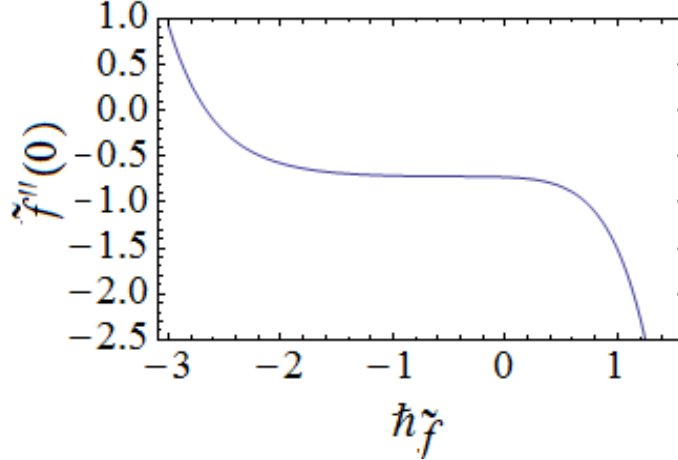


Fig. 5.2: $\tilde{h}_{\tilde{f}}$ -curve for $\tilde{f}''(0)$.

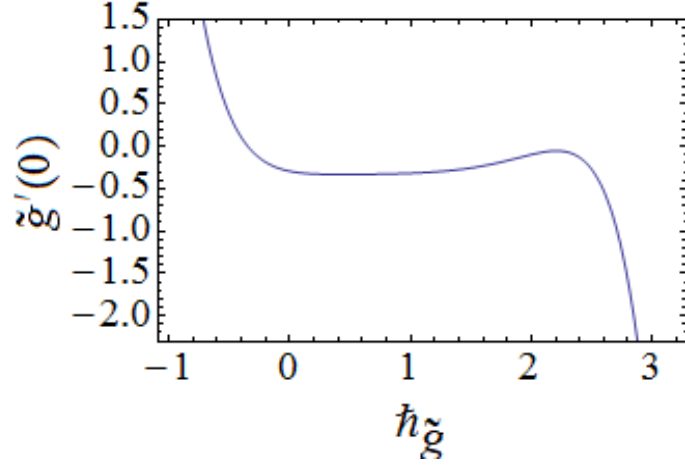


Fig. 5.3: \tilde{h}_g -curve for $\tilde{g}'(0)$.

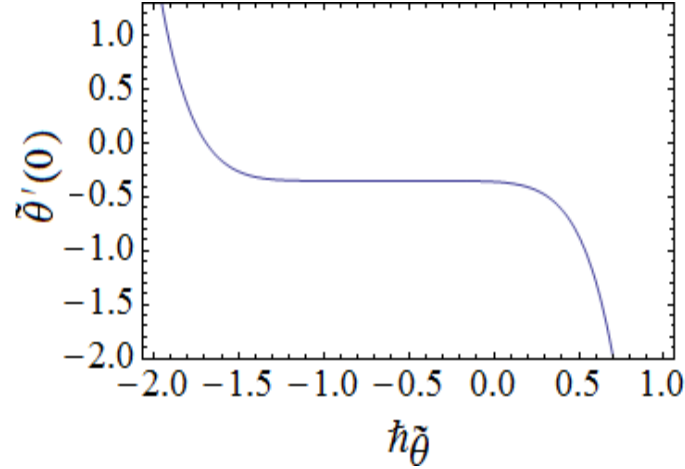


Fig. 5.4: \tilde{h}_θ -curve for $\tilde{\theta}'(0)$.

Table 5.1: Thermophysical properties of magnetite- Fe_3O_4 and water.

	$k(W/mk)$	$\rho(kg/m^3)$	$\sigma(Um)^{-1}$	$\rho c_p(j/m^3k)$
Ferrofluid (Fe_3O_4)	9.7	5180	25000	3470600
Water (H_2O)	0.613	997.1	0.05	4166880.9

Table 5.2: HAM solutions convergence when $\text{Re} = \gamma_1 = \Omega = 0.3$, $M = A_2 = 0.5$, $\gamma_2 = 0.7$, $\gamma_3 = 0.1$, $A_1 = 0.4$, $\text{Pr} = 6.2$ and $\phi = 0.2$.

Order of approximation	$-\tilde{f}''(0)$	$-\tilde{g}'(0)$	$-\tilde{\theta}'(0)$
1	0.718142	0.312365	0.350649
5	0.718050	0.331853	0.349395
10	0.718062	0.333083	0.349391
14	0.718063	0.333120	0.349391
16	0.718063	0.333122	0.349391
20	0.718063	0.333122	0.349391
25	0.718063	0.333122	0.349391
30	0.718063	0.333122	0.349391
35	0.718063	0.333122	0.349391
40	0.718063	0.333122	0.349391
45	0.718063	0.333122	0.349391

Table 5.1 is plotted for the thermophysical characteristics of magnetite-Fe₃O₄ and water. Table. 5.2 ensures that the series solutions of functions $\tilde{f}''(0)$, $\tilde{g}'(0)$ and $\tilde{\theta}'(0)$ are convergent at six decimal places. It is also witnessed that the 14th, 16th and 10th iterations are sufficient for the convergence solutions respectively for $\tilde{f}''(0)$, $\tilde{g}'(0)$ and $\tilde{\theta}'(0)$.

5.4 Discussion

Here impact of significant variables are discussed on the flow field, skin friction, temperature and Nusselt number.

5.4.1 Radial and axial velocities

Characteristics of Re on radial and axial velocities are portrayed in Figs. 5.5 and 5.6 respectively. These Figs. show that by increasing Re there is a decrease in magnitude of radial and axial velocities of fluid near the lower disk. It is in view of the fact that when Re increases then inertial effects due to the rotation of lower plate increases which causes the flow slow. Negative values of axial velocity near the lower disk demonstrates that upper disk is moving faster than the lower disk. Influence of stretching parameter A_2 on radial and axial velocities is presented in Figs. 5.7 and 5.8. By increasing stretching parameter of upper disk A_2 the radial velocity reduces at

lower disk and it enhances near upper disk while axial velocity $\tilde{f}(\xi)$ decreases. Radial velocity has negative value near the lower disk. It is because of high stretching and rotation at upper disk. Likewise axial velocity also have negative value at lower disk (because of low stretching at the surface of lower disk). Figs. 5.9 and 5.10 depict impact of velocity slip parameter γ_1 on radial and axial components. Near the surface of lower and upper disks, the radial velocity of fluid decreases as γ_1 is enhanced. There are two point of variation i.e. $\xi = 0.2$ and $\xi = 0.75$. Fig. 5.10 shows that $\tilde{f}(\xi)$ is decreased versus γ_1 . This type of velocity shows that as fluid become more rarefied velocity at both disks decreases because when slip velocity enhances then there is less transport of momentum in radial direction.

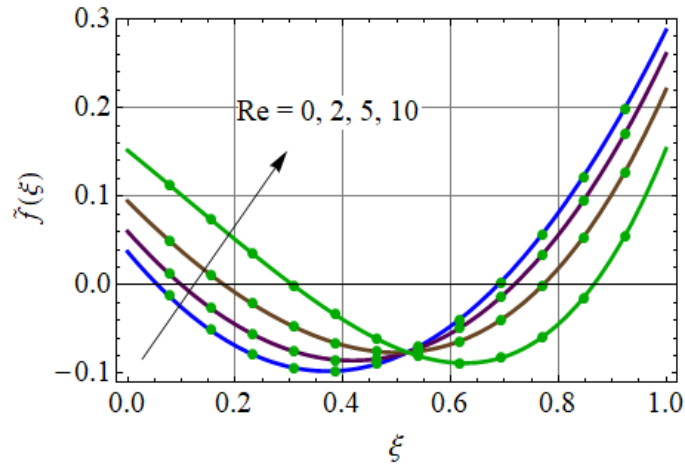


Fig. 5.5: Impact of Re on $f'(\xi)$.

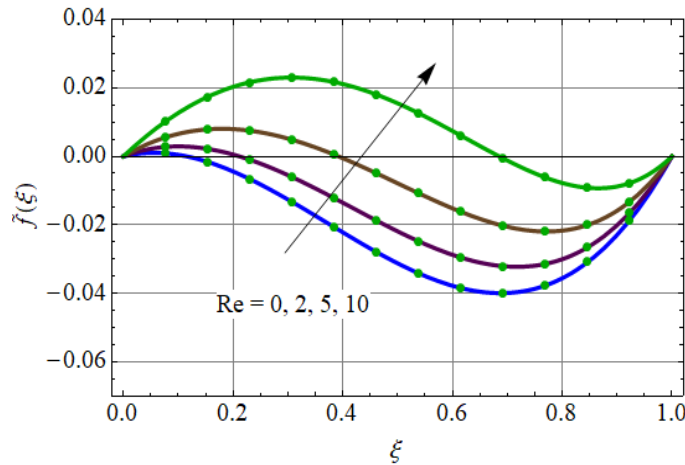


Fig. 5.6: $f(\xi)$ against Re.

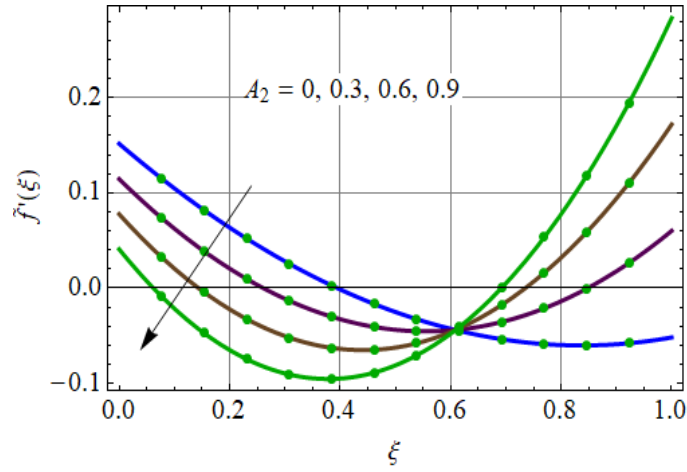


Fig. 5.7: $\tilde{f}'(\xi)$ against A_2 .

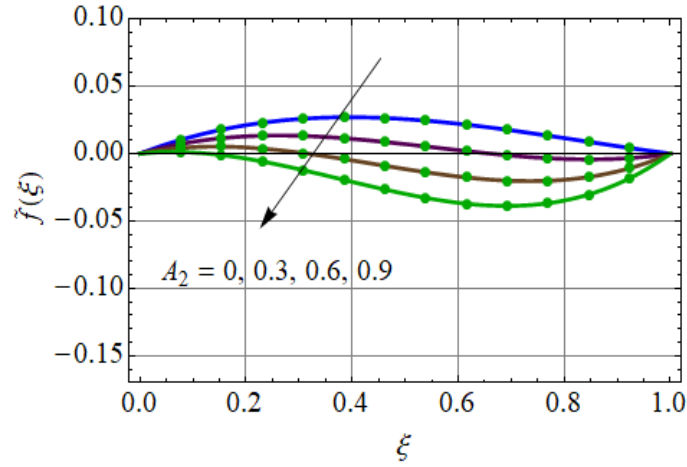


Fig. 5.8: $\tilde{f}(\xi)$ against A_2 .

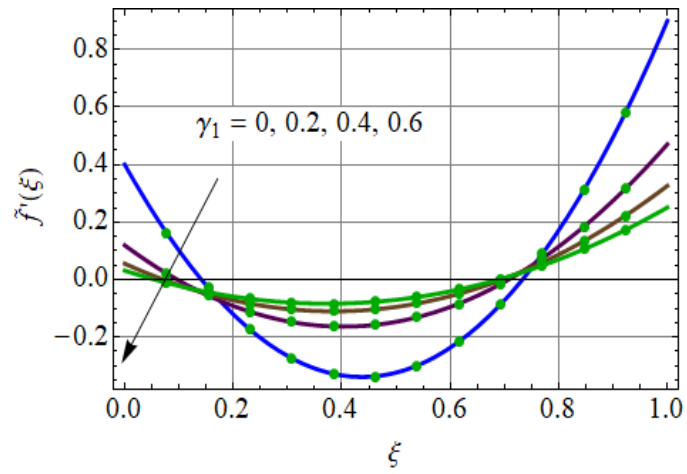


Fig. 5.9: $\tilde{f}'(\xi)$ against γ_1 .

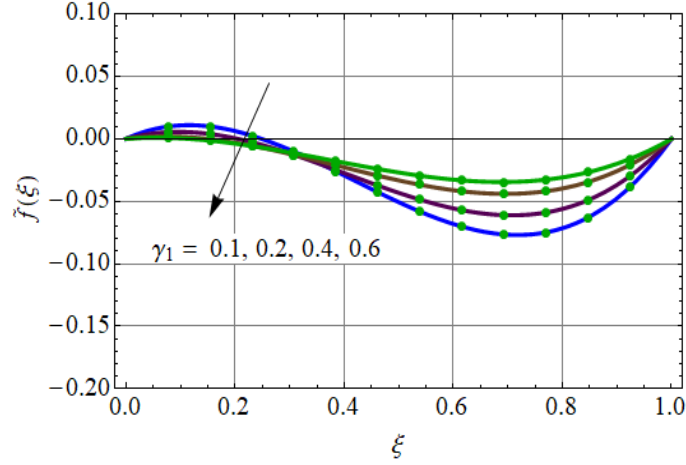


Fig. 5.10: Impact of γ_1 on $\tilde{f}(\xi)$.

5.4.2 Tangential velocity

Impact of Reynolds number Re , Hartmann number M , velocity slip parameter γ_2 , rotational parameter Ω and nanoparticles volume fraction ϕ is shown in the Figs. (5.11 – 5.15). Fig. 5.11 indicates behavior of Re on tangential velocity $\tilde{g}(\xi)$. Here the tangential velocity of fluid decreases when Re is enhanced. Fig. 5.12 shows outcome of Hartmann number on $\tilde{g}(\xi)$. Higher M lead to reduction in the tangential velocity. As magnetic field yields retarding force. It decelerates the motion of liquid particles. Effect of velocity slip parameter γ_2 is portrayed in Fig. 5.13. Tangential velocity of fluid decreases near the lower disk but it has increasing behavior towards the upper disk for larger values of γ_2 . Due to slip the fluid velocity near the disk is not equal to the stretching velocity of disk and under the effect of slip the pulling of stretching disk is transmitted partially to fluid. Fig. 5.14 presents the impact of Ω on tangential velocity. Here tangential velocity is diminished for both disks for larger Ω . Fig. 5.15 highlights

the salient aspects of ϕ on $\tilde{g}(\xi)$. Liquid velocity decreases when ϕ enhances.

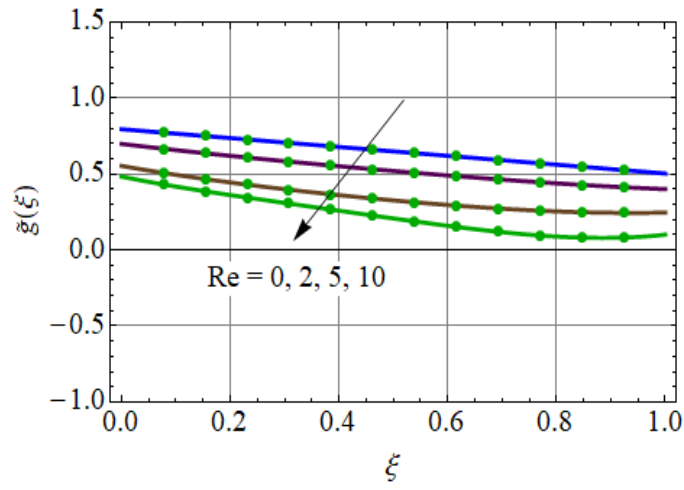


Fig. 5.11: Impact of Re on $\tilde{g}(\xi)$.

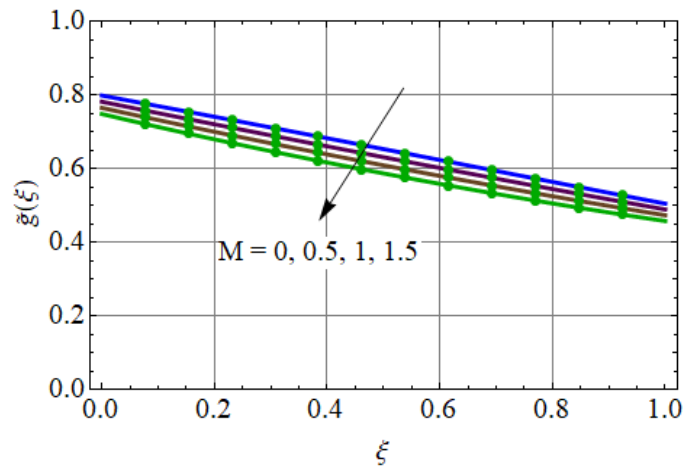


Fig. 5.12: $\tilde{g}(\xi)$ against M .

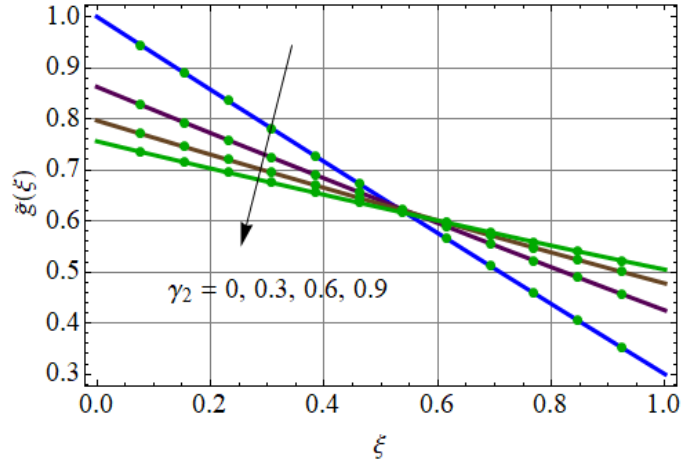


Fig. 5.13: $\tilde{g}(\xi)$ against γ_2 .

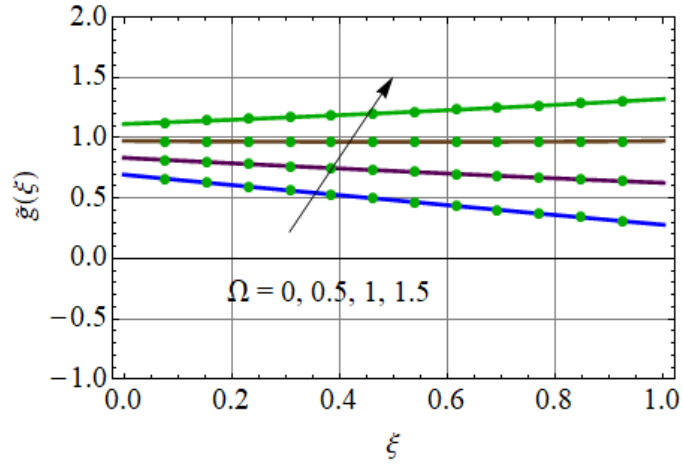


Fig. 5.14: $\tilde{g}(\xi)$ against Ω .

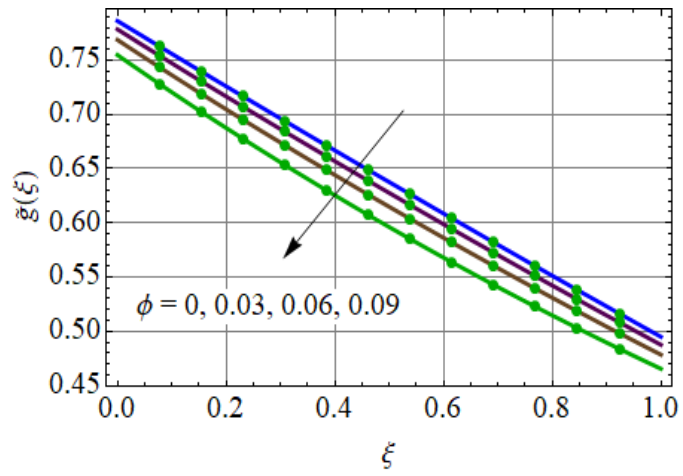


Fig. 5.15: $\tilde{g}(\xi)$ against ϕ .

5.4.3 Dimensionless temperature

In Figs. (5.16 – 5.18) the impact of Re , ϕ and γ_3 on thermal field is demonstrated. Fig. 5.16 witnesses impact of Re on temperature $\tilde{\theta}(\xi)$. It shows that by increasing Re the temperature enhances. Fig. 5.17 shows outcome of ϕ on temperature. Fluid temperature increases when ϕ is enhanced. Physically, for higher ϕ , the thermal conductivity and thermal layer are increased. Importance of thermal slip γ_3 on $\tilde{\theta}$ is portrayed in Fig. 5.18. Near the lower disk the fluid temperature decreases while at upper disk the temperature is increased for increasing γ_5 . In fact when we increase thermal slip, resistance to transfer heat to the fluid particles enhances and consequently the temperature decreases.

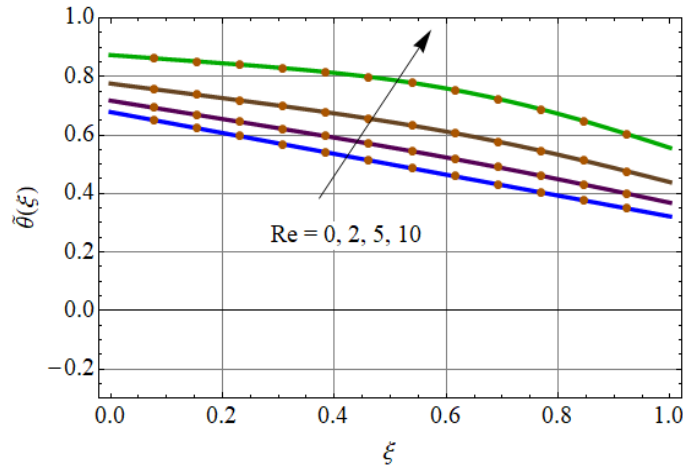


Fig. 5.16: $\tilde{\theta}(\xi)$ against Re .

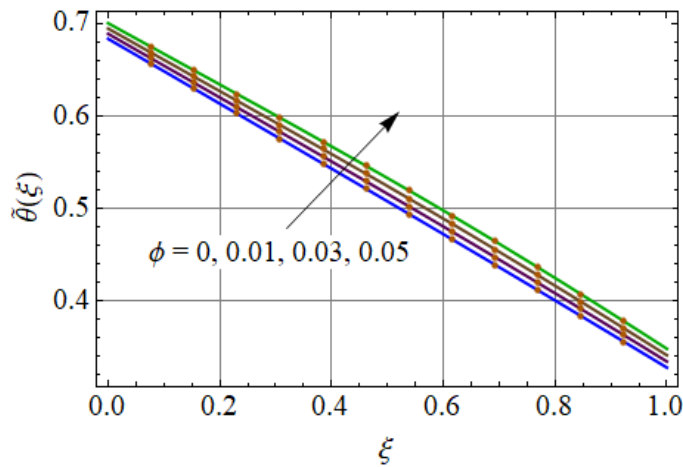


Fig. 5.17: $\tilde{\theta}(\xi)$ against ϕ .

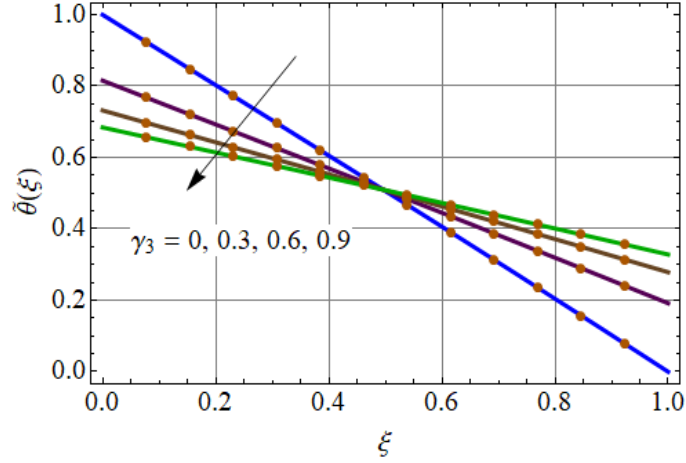


Fig. 5.18: $\tilde{\theta}(\xi)$ against γ_3 .

5.4.4 Skin friction coefficient

Table 5.3 depicts the impact of stretching variables, scaled stretching parameters, Reynolds number Re and Hartmann number M on skin friction at both disks. It is found that at lower disk the $Re_r C_{f1}$ reduces for higher velocity slip variables γ_1, γ_2 while it increases for the scaled stretching parameters A_1, A_2, Re and M . It also shows that skin friction coefficient at upper disk reduces for increasing value of γ_1, γ_2 and M and it increases for higher A_1, A_2 and Re .

Table 5.3: Numerical investigation for $(Re_r C_{f1}, Re_r C_{f2})$ versus various parameters.

γ_1	γ_2	A_1	A_2	Re	M	$Re_r C_{f1}$	$Re_r C_{f2}$
0.5	0.7	0.4	0.9	0.3	0.5	1.3828	2.1972
0.6						1.2215	1.9391
0.7						1.1038	1.7393
0.5	0.8					1.3673	2.1892
	0.9					1.3549	2.1829
	0.7	0.5				1.5853	2.2393
		0.6				1.7921	2.2813
		0.4	1.0			1.4206	2.4130
			1.1			1.4585	2.6296
			0.9	0.4		1.3890	2.1970
				0.5		1.3952	2.1972
				0.3	0.6	1.3892	2.1950
					0.7	1.3957	2.1930

5.4.5 Nusselt number

Table 5.4 witnesses outcome of thermal slip parameter γ_3 , velocity slip parameter γ_1 , solid volume fraction ϕ , Reynolds number Re and Hartmann number M on Nusselt number at lower and upper disks. Clearly the Nusselt number at lower disk is increased when γ_1 , ϕ and M are enhanced and it decays for larger values of γ_3 and Re . Moreover Nusselt number at upper disk is decreasing function of γ_3 , γ_1 and M and increasing function of ϕ and Re .

Table 5.4: Numerical investigation for $(\tilde{\theta}'(0), \tilde{\theta}'(1))$ versus different parameters.

γ_3	γ_1	ϕ	Re	M	$-\frac{k_{nf}}{k_f}\tilde{\theta}'(0)$	$-\frac{k_{nf}}{k_f}\tilde{\theta}'(1)$
0.9	0.5	0.2	0.3	0.5	0.55853	0.58602
1.0					0.52121	0.54686
1.1					0.48857	0.51261
0.9	0.6				0.55966	0.58453
	0.7				0.56062	0.58330
	0.5	0.3			0.70067	0.72876
		0.4			0.87827	0.90705
		0.2	0.4		0.55465	0.59082
			0.5		0.55089	0.59551
			0.3	0.6	0.55855	0.58600
				0.7	0.55857	0.58598

5.5 Conclusions

Here flow and heat transport of ferrofluid induced by two stretched rotating disks with velocity and thermal slips are explored. Key points are as follows:

- For increasing value of Re the magnitude of radial velocity of fluid decreases near the surfaces of the disks.
- Outcomes of γ_2 and Ω on tangential velocity are different.
- Fluid temperature increases for larger solid volume fraction of nanofluid ϕ .
- Skin friction coefficient reduces for increasing velocity slip parameters.
- Heat transfer rate decreases by increasing thermal slip parameter.

Chapter 6

Computations of probable error and statistical declaration for radiated reactive flow

Abstract: This chapter focuses upon computations of statistical declaration and probable error for radiative flow between two stretchable rotating disks. Thermal radiation and Joule heating are present. Homogenous and heterogeneous reactions are also implemented. The thermophysical characteristics of nanofluids are scrutinized using silver and copper nanoparticles. Statistical declaration and probable error for coefficient of skin friction and heat transfer rate are calculated. Convergent solutions of the involved problems are obtained and discussed. Coefficient of skin friction and Nusselt number are calculated and discussed. Radial and axial velocities have opposite impacts for stretching parameters of lower and upper disks. Concentration decays for both Schmidt number and homogeneous reaction variable. Coefficient of skin friction is less for larger rotational parameter at both disks. Opposite behavior of heat transfer rate is observed at lower and upper disks for increasing Eckert number. For limiting cases comparisons with previously available results [23, 52, 53] in the literature are made and an excellent agreement is noticed.

6.1 Physical model and mathematical formulation

Consider nanofluid flow between two continuously stretching rotating disks. Skin friction and heat transfer rate are discussed and calculated via statistical declaration and probable error. We have considered $Ag - H_2O$ and $Cu - H_2O$ as nanoparticles. Lower disk is stretched and rotating rate with a_1 and Ω_1 at $z = 0$. Both disks are at a distance h (see Fig. 6.1).

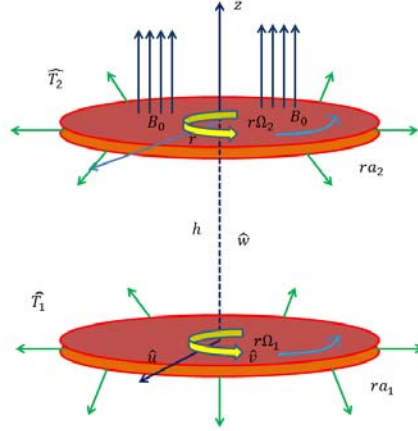
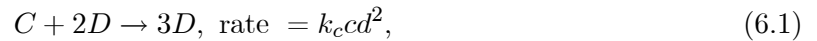


Fig. 6.1: Flow geometry.

Liquid is conducting electrically with magnetic field of strength B_0 . Flow under consideration is in presence of Joule heating and radiation. Homogeneous-heterogeneous reactions are considered. The cubic autocatalytic homogeneous reaction is



at the stretched surface the first order isothermal reaction satisfies



Here k_c and k_s are the rate constants and C and D are chemical species with concentrations c and d . We adopted cylindrical coordinates (r, ϑ, z) with velocity $(\hat{u}, \hat{v}, \hat{w})$. The resulting

problems satisfies the following expressions

$$\frac{\partial \hat{u}}{\partial r} + \frac{\hat{u}}{r} + \frac{\partial \hat{w}}{\partial z} = 0, \quad (6.3)$$

$$\hat{u} \frac{\partial \hat{u}}{\partial r} + \hat{w} \frac{\partial \hat{u}}{\partial z} - \frac{\hat{v}^2}{r} = -\frac{1}{\rho_{nf}} \frac{\partial \hat{p}}{\partial r} + \nu_{nf} \left(\frac{\partial^2 \hat{u}}{\partial r^2} + \frac{1}{r} \frac{\partial \hat{u}}{\partial r} + \frac{\partial^2 \hat{u}}{\partial z^2} - \frac{\hat{u}}{r^2} \right) - \frac{\sigma_{nf}}{\rho_{nf}} B_0^2 \hat{u}, \quad (6.4)$$

$$\hat{u} \frac{\partial \hat{v}}{\partial r} + \hat{w} \frac{\partial \hat{v}}{\partial z} + \frac{\hat{u} \hat{v}}{r} = \nu_{nf} \left(\frac{\partial^2 \hat{v}}{\partial r^2} + \frac{1}{r} \frac{\partial \hat{v}}{\partial r} + \frac{\partial^2 \hat{v}}{\partial z^2} - \frac{\hat{v}}{r^2} \right) - \frac{\sigma_{nf}}{\rho_{nf}} B_0^2 \hat{v}, \quad (6.5)$$

$$\hat{w} \frac{\partial \hat{w}}{\partial r} + \hat{u} \frac{\partial \hat{w}}{\partial z} = -\frac{1}{\rho_{nf}} \frac{\partial \hat{p}}{\partial z} + \nu_{nf} \left(\frac{\partial^2 \hat{w}}{\partial r^2} + \frac{1}{r} \frac{\partial \hat{w}}{\partial r} + \frac{\partial^2 \hat{w}}{\partial z^2} \right), \quad (6.6)$$

$$(\rho c_p)_{nf} \left(\hat{u} \frac{\partial \hat{T}}{\partial r} + \hat{w} \frac{\partial \hat{T}}{\partial z} \right) = \left(k_{nf} + \frac{16\sigma^* \hat{T}_2^3}{3k^*} \right) \left(\frac{1}{r} \frac{\partial \hat{T}}{\partial r} + \frac{\partial^2 \hat{T}}{\partial r^2} + \frac{\partial^2 \hat{T}}{\partial z^2} \right) + \sigma_{nf} B_0^2 (\hat{u}^2 + \hat{v}^2), \quad (6.7)$$

$$\hat{u} \frac{\partial c}{\partial r} + \hat{w} \frac{\partial c}{\partial z} = D_C \left(\frac{\partial^2 c}{\partial r^2} + \frac{1}{r} \frac{\partial c}{\partial r} + \frac{\partial^2 c}{\partial z^2} \right) - k_c c d^2, \quad (6.8)$$

$$\hat{u} \frac{\partial d}{\partial r} + \hat{w} \frac{\partial d}{\partial z} = D_D \left(\frac{\partial^2 d}{\partial r^2} + \frac{1}{r} \frac{\partial d}{\partial r} + \frac{\partial^2 d}{\partial z^2} \right) + k_c c d^2, \quad (6.9)$$

$$\begin{aligned} \hat{u} &= r a_1, \quad \hat{v} = r \Omega_1, \quad \hat{w} = 0, \quad \hat{T} = \hat{T}_1, \quad D_C \frac{\partial c}{\partial z} = k_s c, \quad D_D \frac{\partial d}{\partial z} = -k_s c \quad \text{at } z = 0, \\ \hat{u} &= r a_2, \quad \hat{v} = r \Omega_2, \quad \hat{T} = \hat{T}_2, \quad c \rightarrow c_0, \quad d \rightarrow 0 \quad \text{at } z = h, \end{aligned} \quad (6.10)$$

in which \hat{p} indicates pressure, \hat{T}, \hat{T}_1 and \hat{T}_2 the temperature of fluid, lower disk and upper disk, σ^* Stefan Boltzmann constant, ρ_{nf} the density, k^* the mean absorption coefficient, k_{nf} the thermal conductivity, σ_{nf} the electrical conductivity, $(\rho c_p)_{nf}$ the heat capacitance and μ_{nf} dynamic viscosity. These definitions satisfy

$$\rho_{nf} = \rho_f (1 - \phi) + \rho_s \phi, \quad (6.11)$$

$$\frac{k_{nf}}{k_f} = \frac{k_s + 2k_f - 2\phi(k_f - k_s)}{k_s + 2k_f + 2\phi(k_f - k_s)}, \quad (6.12)$$

$$(\rho c_p)_{nf} = (\rho c_p)_f (1 - \phi) + (\rho c_p)_s \phi, \quad (6.13)$$

$$\mu_{nf} = \frac{\mu_f}{(1 - \phi)^{2.5}}, \quad (6.14)$$

$$\frac{\sigma_{nf}}{\sigma_f} = 1 + \frac{3 \left(\frac{\sigma_s}{\sigma_f} - 1 \right) \phi}{\left(\frac{\sigma_s}{\sigma_f} + 2 \right) - \left(\frac{\sigma_s}{\sigma_f} - 1 \right) \phi}, \quad (6.15)$$

where subscript nf represents thermophysical properties of nanofluid, s for nano-solid particles, f explains base fluid and ϕ denotes the solid volume fraction of nanoparticles.

We consider Von-Karman transformations

$$\begin{aligned} \hat{u} &= r\Omega_1 \tilde{f}'(\xi), \quad \hat{v} = r\Omega_1 \tilde{g}(\xi), \quad \hat{w} = -2h\Omega_1 \tilde{f}(\xi), \quad \tilde{\theta} = \frac{\hat{T} - \hat{T}_2}{\hat{T}_1 - \hat{T}_2}, \\ \hat{p} &= \rho_f \Omega_1 \nu_f \left(P(\xi) + \frac{1}{2} \frac{r^2}{h^2} \epsilon \right), \quad c = c_0 \tilde{\phi}, \quad d = c_0 \tilde{l}, \quad \xi = \frac{z}{h}. \end{aligned} \quad (6.16)$$

We arrive

$$\frac{1}{(1-\phi)^{2.5} \left(1 - \phi + \frac{\rho_s}{\rho_f} \phi \right)} \tilde{f}''' + \text{Re} \left(2\tilde{f}\tilde{f}'' - \tilde{f}'^2 + \tilde{g}^2 - \frac{M}{1-\phi + \frac{\rho_s}{\rho_f} \phi} \frac{\sigma_{nf}}{\sigma_f} \tilde{f}' \right) - \frac{\epsilon}{1-\phi + \frac{\rho_s}{\rho_f} \phi} = 0, \quad (6.17)$$

$$\frac{1}{(1-\phi)^{2.5} \left(1 - \phi + \frac{\rho_s}{\rho_f} \phi \right)} \tilde{g}'' + \text{Re} \left(2\tilde{f}\tilde{g}' - 2\tilde{f}'\tilde{g} - \frac{M}{1-\phi + \frac{\rho_s}{\rho_f} \phi} \frac{\sigma_{nf}}{\sigma_f} \tilde{g} \right) = 0, \quad (6.18)$$

$$\frac{1}{1-\phi + \frac{\rho_s}{\rho_f} \phi} P' = -4 \text{Re} \tilde{f}\tilde{f}' - \frac{2}{(1-\phi)^{2.5} \left(1 - \phi + \frac{\rho_s}{\rho_f} \phi \right)} \tilde{f}'', \quad (6.19)$$

$$\frac{1}{\text{Pr}} \left(\frac{k_{nf}}{k_f} + R \right) \tilde{\theta}'' + 2 \text{Re} \left(1 - \phi + \frac{(\rho c_p)_s}{(\rho c_p)_f} \phi \right) \tilde{f}\tilde{\theta}' + \text{Re} M \frac{\sigma_{nf}}{\sigma_f} Ec (\tilde{f}'^2 + \tilde{g}^2) = 0, \quad (6.20)$$

$$\frac{1}{\text{Re}} \frac{1}{Sc} \tilde{\phi}'' + 2\tilde{f}\tilde{\phi}' - k_1 \tilde{\phi} \tilde{l}^2 = 0, \quad (6.21)$$

$$\frac{\delta}{Sc} \frac{1}{\text{Re}} \tilde{l}'' + 2\tilde{f}\tilde{l}' + k_1 \tilde{\phi} \tilde{l}^2 = 0, \quad (6.22)$$

$$\begin{aligned} \tilde{f}(0) &= 0, \quad \tilde{f}(1) = 0, \quad \tilde{f}'(0) = A_1, \quad \tilde{f}'(1) = A_2, \quad \tilde{g}(0) = 1, \\ \tilde{g}(1) &= \Omega, \quad \tilde{\theta}(0) = 1, \quad \tilde{\theta}(1) = 0, \quad \tilde{\phi}'(0) = k_2 \tilde{\phi}(0), \quad \tilde{\phi}(1) = 1, \\ \delta \tilde{l}'(0) &= -k_2 \tilde{\phi}(0), \quad \tilde{l}(1) = 0, \quad P(0) = 0, \end{aligned} \quad (6.23)$$

with

$$\begin{aligned}
\text{Re} &= \frac{\Omega_1 h^2}{\nu_f}, \quad \text{Pr} = \frac{(\rho c_p)_f \nu_f}{k_f}, \quad M = \frac{B_0^2 \sigma_f}{\rho_f \Omega_1}, \quad Ec = \frac{r^2 \Omega_1^2}{c_p (\hat{T}_1 - \hat{T}_2)} \\
Sc &= \frac{\nu_f}{D_B}, \quad \delta = \frac{D_C}{D_B}, \quad A_1 = \frac{a_1}{\Omega_1}, \quad A_2 = \frac{a_2}{\Omega_1}, \quad \Omega = \frac{\Omega_2}{\Omega_1}, \\
k_1 &= \frac{k_c b_0^2}{\Omega_1}, \quad k_2 = \frac{k_s h}{D_B}.
\end{aligned} \tag{6.24}$$

where $\text{Re}, \text{Pr}, Ec, M, \delta, Sc, \Omega, A_1, A_2, k_1$ and k_2 and D denote the Reynolds number, Prandtl number, Eckert number, Hartmann number, ratio of diffusion coefficients, Schmidt number, rotation number, scaled stretching parameters, homogeneous reaction variable, and heterogeneous reaction variable. For comparable size $D_C = D_D = 1$ i.e., $\delta = 1$, one has

$$\tilde{\phi}(\xi) + \tilde{l}(\xi) = 1. \tag{6.25}$$

From expressions (6.21) and (6.22) one obtains

$$\frac{1}{\text{Re}} \frac{1}{Sc} \tilde{\phi}'' + 2\tilde{f}\tilde{\phi}' - k_1 \tilde{\phi}(1 - \tilde{\phi})^2 = 0, \tag{6.26}$$

subject to

$$\tilde{\phi}'(0) = k_2 \tilde{\phi}(0), \quad \tilde{\phi}(1) = 1. \tag{6.27}$$

Considering Eq. (6.17) and removing ϵ we differentiate it with respect to ξ and obtain

$$\frac{1}{(1 - \phi)^{2.5} (1 - \phi + \frac{\rho_s}{\rho_f} \phi)} \tilde{f}^{iv} + \text{Re} \left(2\tilde{f}\tilde{f}''' + 2\tilde{g}\tilde{g}' - \frac{M}{1 - \phi + \frac{\rho_s}{\rho_f} \phi} \frac{\sigma_{nf}}{\sigma_f} \tilde{f}'' \right) = 0. \tag{6.28}$$

Also the pressure parameter ϵ can be obtained by using Eq. (6.17) and Eq. (6.24) as

$$\epsilon = \frac{1}{(1 - \phi)^{2.5}} \tilde{f}'''(0) - \text{Re} \left(1 - \phi + \frac{\rho_s}{\rho_f} \phi \right) \left[(\tilde{f}'(0))^2 - (\tilde{g}(0))^2 + \frac{M}{1 - \phi + \frac{\rho_s}{\rho_f} \phi} \frac{\sigma_{nf}}{\sigma_f} \tilde{f}'(0) \right]. \tag{6.29}$$

Integrating Eq. (6.19) with respect to ξ to get pressure term and taking limit from 0 to ξ we

have

$$\frac{1}{1 - \phi + \frac{\rho_s}{\rho_f}\phi} P = -2 \left[\text{Re } \tilde{f}^2 + \frac{1}{(1 - \phi)^{2.5} (1 - \phi + \frac{\rho_s}{\rho_f}\phi)} (\tilde{f}' - \tilde{f}'(0)) \right]. \quad (6.30)$$

At lower disk the shear stress in radial and tangential directions are τ_{zr} and $\tau_{z\theta}$

$$\tau_{zr} = \mu_{nf} \left. \frac{\partial \hat{u}}{\partial z} \right|_{z=0} = \frac{\mu_f r \Omega_1 \tilde{f}''(0)}{(1 - \phi)^{2.5} h}, \quad \tau_{z\theta} = \mu_{nf} \left. \frac{\partial \hat{v}}{\partial z} \right|_{z=0} = \frac{\mu_f r \Omega_1 \tilde{g}'(0)}{(1 - \phi)^{2.5} h}. \quad (6.31)$$

Total shear stress τ_w is

$$\tau_w = \sqrt{\tau_{zr}^2 + \tau_{z\theta}^2}. \quad (6.32)$$

Mathematically C_{f1} and C_{f2} is defined as

$$C_{f1} = \frac{\tau_w|_{z=0}}{\rho_f (r \Omega_1)^2} = \frac{1}{\text{Re}_r (1 - \phi)^{2.5}} [(\tilde{f}''(0))^2 + (\tilde{g}'(0))^2]^{1/2}, \quad (6.33)$$

$$C_{f2} = \frac{\tau_w|_{z=h}}{\rho_f (r \Omega_1)^2} = \frac{1}{\text{Re}_r (1 - \phi)^{2.5}} [(\tilde{f}''(1))^2 + (\tilde{g}'(1))^2]^{1/2}, \quad (6.34)$$

in which local Reynolds number is $\text{Re}_r = \frac{r \Omega_1 h}{\nu_f}$. Nusselt numbers are

$$Nu_{x1} = \left. \frac{hq_w}{k_f (\hat{T}_1 - \hat{T}_2)} \right|_{z=0}, \quad Nu_{x2} = \left. \frac{hq_w}{k_f (\hat{T}_1 - \hat{T}_2)} \right|_{z=h}. \quad (6.35)$$

Wall heat flux q_w satisfies

$$q_w|_{z=0} = -k_{nf} \left. \frac{\partial \hat{T}}{\partial z} \right|_{z=0} + q_r \Big|_{z=0} = -\frac{(\hat{T}_1 - \hat{T}_2)}{h} \left(k_{nf} + \frac{16\sigma^* \hat{T}_2^3}{3k^*} \right) \tilde{\theta}'(0), \quad (6.36)$$

$$q_w|_{z=h} = -k_{nf} \left. \frac{\partial \hat{T}}{\partial z} \right|_{z=h} + q_r \Big|_{z=h} = -\frac{(\hat{T}_1 - \hat{T}_2)}{h} \left(k_{nf} + \frac{16\sigma^* \hat{T}_2^3}{3k^*} \right) \tilde{\theta}'(1). \quad (6.37)$$

Nusselt numbers can be written as follows:

$$Nu_{x1} = -\left(\frac{k_{nf}}{k_f} + R \right) \tilde{\theta}'(0), \quad Nu_{x2} = -\left(\frac{k_{nf}}{k_f} + R \right) \tilde{\theta}'(1). \quad (6.38)$$

6.2 Solution technique

We have

$$\tilde{f}_0(\xi) = A_1\xi - 2A_1\xi^2 - A_2\xi^2 + A_1\xi^3 + A_2\xi^3, \quad (6.39)$$

$$\tilde{g}_0(\xi) = 1 + (\Omega - 1)\xi, \quad (6.40)$$

$$\tilde{\theta}_0(\xi) = 1 - \xi, \quad (6.41)$$

$$\tilde{\phi}_0(\xi) = \frac{1 + k_2\xi}{1 + k_2}, \quad (6.42)$$

$$\mathcal{L}_{\tilde{f}} = \tilde{f}'''' , \quad \mathcal{L}_{\tilde{g}} = \tilde{g}'' , \quad \mathcal{L}_{\tilde{\theta}} = \tilde{\theta}'' , \quad \mathcal{L}_{\tilde{\phi}} = \tilde{\phi}'' , \quad (6.43)$$

with

$$\mathcal{L}_{\tilde{f}} [c_1 + c_2\xi + c_3\xi^2 + c_4\xi^3] = 0, \quad (6.44)$$

$$\mathcal{L}_{\tilde{g}} [c_5 + c_6\xi] = 0, \quad (6.45)$$

$$\mathcal{L}_{\tilde{\theta}} [c_7 + c_8\xi] = 0, \quad (6.46)$$

$$\mathcal{L}_{\tilde{\phi}} [c_9 + c_{10}\xi] = 0, \quad (6.47)$$

6.3 Convergence region

Figs. 6.2 and 6.3 are sketched for the graphical representation of convergence series solution with the help of auxiliary variables $\tilde{h}_{\tilde{f}}$, $\tilde{h}_{\tilde{g}}$, $\tilde{h}_{\tilde{\theta}}$ and $\tilde{h}_{\tilde{\phi}}$. These variable show significant role in series solutions. The suitable ranges for both $Ag - H_2O$ and $Cu - H_2O$ are $-2.2 \leq \tilde{h}_{\tilde{f}} \leq -0.4$, $-2.4 \leq \tilde{h}_{\tilde{g}} \leq -0.1$, $-0.9 \leq \tilde{h}_{\tilde{\theta}} \leq -0.1$, $-1.2 \leq \tilde{h}_{\tilde{\phi}} \leq -0.1$ and $-2.2 \leq \tilde{h}_{\tilde{f}} \leq -0.4$, $-2.4 \leq \tilde{h}_{\tilde{g}} \leq$

$$-0.1, -0.8 \leq \hbar_{\tilde{\phi}} \leq -0.2, -1 \leq \hbar_{\tilde{\phi}'} \leq -0.1.$$

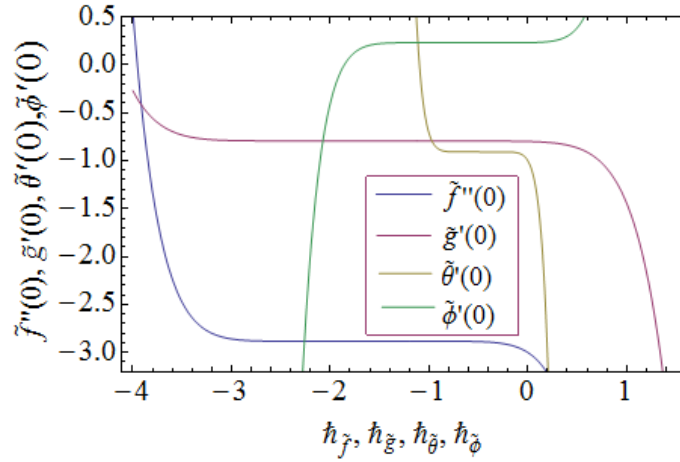


Fig. 6.2: \hbar -curve for Ag -water.

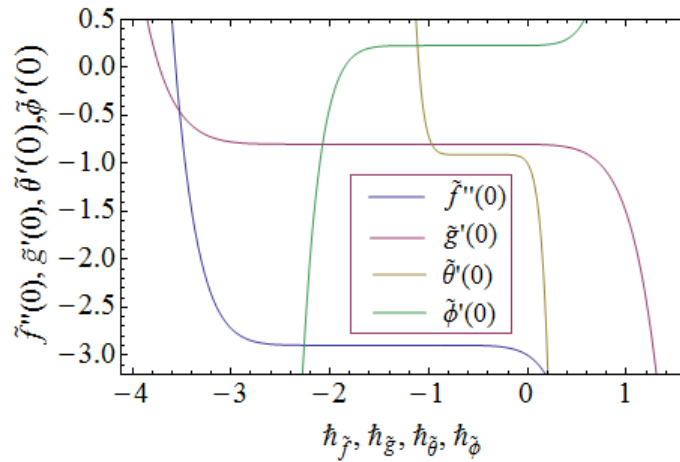


Fig. 6.3: \hbar -curve for Cu -water.

Table 6.1 includes thermophysical properties of nanofluids (Ag, Cu, H_2O). Also the convergence of series solutions for both $Ag - H_2O$ and $Cu - H_2O$ is displayed in Tables (6.2, 6.3). For silver water nanofluid the 7th order of approximation is appropriate for convergence of velocity in x -direction $\tilde{f}''(0)$ and temperature $\tilde{\theta}'(0)$ and 8th and 11th order of approximations are sufficient for convergence of velocity in y -direction $\tilde{g}''(0)$ and concentration $\tilde{\phi}'(0)$ (see Table 6.2). Now for copper water nanofluid 11th iteration is sufficient for the convergence of velocity in both directions and temperature and concentration converge upto 10th and 15th order of approximations respectively (see Table 6.3). Table 6.4 shows the comparison of present flow

with previous literature and we found in an excellent agreement.

Table 6.1: Thermophysical properties of silver, copper and water.

	$k(W/mk)$	$\rho(kg/m^3)$	$\sigma(Um)^{-1}$	$c_p(J/kgk)$	$\rho c_p(j/m^3k)$	$\beta \times 10^{-5}(1/k)$
Silver (<i>Ag</i>)	429	10490	6.30×10^7	235	2465150	1.89
Copper (<i>Cu</i>)	401	8933	5.96×10^7	385	3439205	1.67
Water (<i>H₂O</i>)	0.613	997.1	0.05	4179	4166880.9	21

Table 6.2: Convergence series solutions for *Ag* – *H₂O* nanoliquid when $\phi = 0.2$, $Re = 0.7$, $M = 0.1$, $A_1 = 0.4$, $A_2 = 0.7$, $\Omega = 0.2$, $R = 0.4$, $Ec = 0.7$, $Sc = 0.9$, $k_1 = 0.4$ and $k_2 = 0.3$.

Order of approximations	<i>Ag</i> –water			
	$-\tilde{f}''(0)$	$-\tilde{g}''(0)$	$-\tilde{\theta}'(0)$	$\tilde{\phi}'(0)$
1	2.85359	0.794533	0.923518	0.229412
7	2.88268	0.798022	0.910076	0.229946
8	2.88268	0.798023	0.910076	0.229967
10	2.88268	0.798023	0.910076	0.229962
11	2.88268	0.798023	0.910076	0.229959
13	2.88268	0.798023	0.910076	0.229959
14	2.88268	0.798023	0.910076	0.229960
15	2.88268	0.798023	0.910076	0.229960
30	2.88268	0.798023	0.910076	0.229960
40	2.88268	0.798023	0.910076	0.229960
45	2.88268	0.798023	0.910076	0.229960

Table 6.3: Convergence of series solution for $Cu-H_2O$ nanoliquid when $\phi = 0.2$, $Re = 0.7$, $M = 0.1$, $A_1 = 0.4$, $A_2 = 0.7$, $\Omega = 0.2$, $R = 0.4$, $Ec = 0.7$, $Sc = 0.9$, $k_1 = 0.4$ and $k_2 = 0.3$.

Order of approximations	$Cu-water$			
	$-\tilde{f}''(0)$	$-\tilde{g}''(0)$	$-\tilde{\theta}'(0)$	$\tilde{\phi}'(0)$
1	2.85390	0.798260	0.922977	0.229412
7	2.89500	0.800865	0.909389	0.229936
8	2.89513	0.800914	0.909393	0.229960
10	2.89510	0.800902	0.909392	0.229954
11	2.89509	0.800900	0.909392	0.229950
13	2.89509	0.800900	0.909392	0.229951
14	2.89509	0.800900	0.909392	0.229952
15	2.89509	0.800900	0.909392	0.229951
30	2.89509	0.800900	0.909392	0.229951
40	2.89509	0.800900	0.909392	0.229951
45	2.89509	0.800900	0.909392	0.229951

Table 6.4: Comparison of $\tilde{f}''(0)$ and $\tilde{g}'(0)$ with [3], [9] and [11] when $\phi = A_1 = A_2 = M = 0$ and $Re = 1$.

Ω	-1	-0.8	-0.3	0.0	0.5
$\tilde{f}''(0)[3]$	0.066666	0.08394	0.10395	0.09997	0.06663
$-\tilde{g}'(0)[3]$	2.00095	1.80259	1.30442	1.00428	0.50261
$\tilde{f}''(0)[9]$	0.066666	0.08394	0.10395	0.09997	0.06663
$-\tilde{g}'(0)[9]$	2.00095	1.80259	1.30442	1.00428	0.50261
$\tilde{f}''(0)[11]$	0.066666	0.08399	0.10395	0.09997	0.06667
$-\tilde{g}'(0)[11]$	2.00095	1.80259	1.30443	1.00428	0.50261
Present result for $\tilde{f}''(0)$	0.06666314	0.08394207	0.1039509	0.09997221	0.06663419
Present result for $-\tilde{g}'(0)$	2.000952	1.802588	1.304424	1.004278	0.5026135

6.3.1 Surface drag force

Here surface drag force at lower and upper disks for $M = 0.1$ and $M = 0.7$ is examined in Table 6.5 and 6.6. It is noted that for silver and copper water nanofluids the skin friction is an increasing behavior of Hartmann number, stretching parameter, nanoparticle volume fraction while it depicts declining behavior for Reynolds number and rotation variable at lower disk. At upper disk the surface drag force enhances versus M , A_2 , Re , ϕ and it decreases for Ω . It is noted that $Ag - H_2O$ and $Cu - H_2O$ nanofluids have same results qualitatively.

Table 6.5: Analysis of (C_{f0}, C_{f1}) for both $Ag - H_2O$ and $Cu - H_2O$ nanofluid at $M = 0.1$ when $Pr = 6.2$, $A_1 = 0.4$ and $\Omega = 0.2$.

				$M = 0.1$			
A_2	Re	ϕ	Ω	$C_{f0}(Ag)$	$C_{f1}(Ag)$	$C_{f0}(Cu)$	$C_{f1}(Cu)$
0.7	0.7	0.2	0.2	5.225243	6.714171	5.2474	6.6843
0.8				5.530797	7.440644	5.5563	7.4062
0.9				5.835775	8.174176	5.8647	8.1346
0.7	0.8			5.198350	6.754186	5.2234	6.7198
	0.9			5.171846	6.794497	5.1997	6.7554
	0.7	0.3		7.308686	9.355921	7.3421	9.3113
		0.4		10.80334	13.67265	10.849	13.613
		0.2	0.3	5.193760	6.669382	5.2147	6.6404
			0.4	5.170936	6.626625	5.19020	6.5989

Table 6.6: Analysis of (C_{f0}, C_{f1}) for both $Ag - H_2O$ and $Cu - H_2O$ nanofluid at $M = 0.7$ when $Pr = 6.2$, $A_1 = 0.4$ and $\Omega = 0.2$.

				$M = 0.7$			
A_2	Re	ϕ	Ω	$C_{f0}(Ag)$	$C_{f1}(Ag)$	$C_{f0}(Cu)$	$C_{f1}(Cu)$
0.7	0.7	0.2	0.2	5.327599	6.722489	5.349147	6.694619
0.8				5.625798	7.460950	5.650759	7.428612
0.9				5.923961	8.205939	5.952477	8.168640
0.7	0.8			5.317195	6.761664	5.341417	6.729878
	0.9			5.307636	6.800607	5.334426	6.764926
	0.7	0.3		7.441537	9.367453	7.474079	9.325591
		0.4		10.97524	13.69127	11.02121	13.63493
		0.2	0.3	5.289705	6.678586	5.310216	6.651652
			0.4	5.259247	6.638323	5.278385	6.612600

6.3.2 Nusselt number

Behaviors of embedded parameters on Nusselt number at both disks for $M = 0.1$ and $M = 0.7$ are examined in Tables 6.7 and 6.8. It is noted that for both $Ag-H_2O$ and $Cu-H_2O$ nanofluids the Nusselt number enhances for larger nanoparticle volume fraction ϕ , stretching parameter A_1 , radiation parameter R while it displays decreasing impact for Reynolds number Re and Eckert number Ec at lower disk. At upper disk the Nusselt number is enhanced versus Ec , R , Re , ϕ and it decreased only for A_1 . It is noted that both $Ag-H_2O$ and $Cu-H_2O$ nanofluids have similar results qualitatively.

Table 6.7: Analysis of (Nu_{x0}, Nu_{x1}) for both $Ag-H_2O$ and $Cu-H_2O$ at $M = 0.1$ when $Pr = 6.2$, $A_1 = 0.4$, $A_2 = 0.7$, $R = 0.4$, $Sc = 0.9$ and $\Omega = 0.2$.

				$M = 0.1$			
R	Ec	Re	A_1	$Nu_{x0}(Ag)$	$Nu_{x1}(Ag)$	$Nu_{x0}(Cu)$	$Nu_{x1}(Cu)$
0.4	0.7	0.7	0.4	1.9530	2.4153	1.9513	2.4246
0.5				2.0532	2.5148	2.0515	2.5241
0.6				2.1535	2.6144	2.1518	2.6236
0.4	0.8			1.9282	2.4297	1.9266	2.4390
	0.9			1.9034	2.4441	1.9018	2.4533
	0.7	0.8		1.9251	2.4547	1.9232	2.4654
		0.9		1.8971	2.4942	1.8949	2.5066
		0.7	0.5	1.9888	2.3883	1.9891	2.3961
			0.6	2.0237	2.3619	2.0261	2.3681

Table 6.8: Analysis of (Nu_{x0}, Nu_{x1}) for both $Ag - H_2O$ and $Cu - H_2O$ at $M = 0.7$ when $Pr = 6.2$, $A_1 = 0.4$, $A_2 = 0.7$, $R = 0.4$, $Sc = 0.9$ and $\Omega = 0.2$.

				$M = 0.7$			
R	Ec	Re	A_1	$Nu_{x0}(Ag)$	$Nu_{x1}(Ag)$	$Nu_{x0}(Cu)$	$Nu_{x1}(Cu)$
0.4	0.7	0.7	0.4	0.97233	2.9740	1.9513	2.4246
0.5				1.0735	3.0721	2.0516	2.5241
0.6				1.1745	3.1705	2.1518	2.6236
0.4	0.8			0.80738	3.0683	1.9266	2.4390
	0.9			0.64243	3.1626	1.9018	2.4533
	0.7	0.8		0.80587	3.0946	1.9232	2.4654
		0.9		0.63979	3.2157	1.8949	2.5066
		0.7	0.5	0.98604	2.9483	1.9891	2.3960
			0.6	0.99264	2.9253	2.0262	2.3681

6.3.3 Statistical approach

Now we discuss outcome of important variables on flow and temperature. First we calculate the surface drag force and Nusselt number of $Ag-$ and $Cu-$ water nanofluids for M . In Tables 6.9 and 6.10 we construct the values of correlation coefficient r^0 . Values of r^0 always range

from -1 to 1. Interdependence of parameters on skin friction and Nusselt number for $Ag - H_2O$ and $Cu - H_2O$ nanofluids is shown in these tables. Direction and magnitude of correlation is found by coefficient of correlation (r^0).

Table 6.9: Esimations of r^0 for (C_{f0}, C_{f1}) .

r^0	$C_{f0}(Ag)$		$C_{f1}(Ag)$	
	$M = 0.1$	$M = 0.7$	$M = 0.1$	$M = 0.7$
A_2	0.9999999	0.9999999	0.99999610	0.99999677
Re	-0.9999911	-0.99970151	0.99999773	0.99999853
ϕ	0.98950025	0.98963065	0.99048074	0.99046514
Ω	-0.9957896	-0.99803328	-0.99991022	-0.9996884
r^0	$C_{f0}(Cu)$		$C_{f1}(Cu)$	
	$M = 0.1$	$M = 0.7$	$M = 0.1$	$M = 0.7$
A_2	0.99999989	0.9999999	0.9999966	0.9999972
Re	-0.9999934	-0.9995802	0.9999996	0.9999984
ϕ	0.9895724	0.98968364	0.9904030	0.9903933
Ω	-0.9965923	-0.9983263	-0.9998683	-0.9996204

Table 6.10: Values of r^0 for Nusselt number.

r^0	$Nu_{x0}(Ag)$		$Nu_{x1}(Ag)$	
	$M = 0.1$	$M = 0.7$	$M = 0.1$	$M = 0.7$
R	0.9999999	0.9999999	0.9999999	0.88087129
Ec	-0.9999999	-0.9999999	0.9999999	0.8801457
Re	-0.9999994	-0.999999	0.9999997	0.88377981
A_1	0.9999729	0.9801799	-0.9999789	0.8622275
r^0	$Nu_{x0}(Cu)$		$Nu_{x1}(Cu)$	
	$M = 0.1$	$M = 0.7$	$M = 0.1$	$M = 0.7$
R	0.9999999	0.9999999	0.9999999	0.9999999
Ec	-0.999999	-0.999999	0.9999979	0.9999979
Re	-0.9999979	-0.9999979	0.9999960	0.9999960
A_1	0.9999809	0.9999854	-0.9999869	-0.9999744

6.3.4 Probable error (P.E)

Probable error of skin friction (drag force) and Nusselt number (heat transfer rate) for both disks is shown in Tables 6.11 and 6.12 respectively. Probable error is dependent on the value of r^0 . We calculate $P.E$ to check how much authentic and accurate is value of r^0 . Fisher [51] gave the idea of probable error. Mathematically

$$P.E(r^0) = \frac{1 - r^{02}}{\sqrt{n}} \times 0.6745$$

where n highlights the number of observations and value 0.6745 is utilized because in expression $\hat{\mu} \pm 0.6745\hat{\sigma}$ 50% of total area is covered in a normal distribution. Here $\hat{\mu}$ and $\hat{\sigma}$ denote the mean and standard deviation.

Table 6.11: Estimations of $P.E(r^0)$ for (C_{f0}, C_{f1}) for $Ag - H_2O$.

$P.E(r^0)$	$C_{f0}(Ag)$		$C_{f1}(Ag)$	
	$M = 0.1$	$M = 0.7$	$M = 0.1$	$M = 0.7$
A_2	0.000000778	0.0000000778	0.000003037	0.000002515
Re	0.000007009	0.0002324429	0.000001767	0.000001144
ϕ	0.008134751	0.0080342496	0.007378744	0.007390779
Ω	0.003272347	0.0015302647	0.000069921	0.000242650
$P.E(r^0)$	$C_{f0}(Cu)$		$C_{f1}(Cu)$	
	$M = 0.1$	$M = 0.7$	$M = 0.1$	$M = 0.7$
A_2	0.0000000155	0.000000778	0.0000026480	0.0000021807
Re	0.00000511403	0.000326890	0.0000031153	0.0000012461
ϕ	0.00807914565	0.007993405	0.0074387136	0.0074461958
τ	0.0026495497	0.001302462	0.0001025671	0.0002955936

Table 6.12: Values of $P.E(r)$ for Nusselt number.

$P.E(r)$	$Nu_{x0}(Ag)$		$Nu_{x1}(Ag)$	
	$M = 0.1$	$M = 0.7$	$M = 0.1$	$M = 0.7$
R	0.0000000778	0.0000000778	0.0000000778	0.08725630
Ec	0.0000000778	0.0000000778	0.0000000778	0.08775390
Re	0.0000004673	0.0000000778	0.0000002336	0.085257588
A_1	0.0000211064	0.0152838165	0.0000164334	0.099911758
$P.E(r^0)$	$Nu_{x0}(Cu)$		$Nu_{x1}(Cu)$	
	$M = 0.1$	$M = 0.7$	$M = 0.1$	$M = 0.7$
R	0.0000000778	0.0000000778	0.0000000778	0.0000000778
Ec	0.0000000778	0.0000000778	0.000001635	0.000001635
Re	0.000001635	0.000001635	0.000003115	0.0000031153
A_1	0.000014875	0.000011371	0.000010202	0.0000199381

We conclude our final result as

$$r^0 < P.E(r^0) \text{ for in significant correlation}$$

$$r^0 > 6P.E(r^0) \text{ for significant correlation}$$

6.3.5 Statistical declaration about parameters

Values of $\frac{r^0}{P.E(r^0)}$ for (C_{f0}, C_{f1}) and (Nu_{x0}, Nu_{x1}) are shown in Tables 6.13 and 6.14. We conclude our result by checking the all values of $\frac{r^0}{P.E(r^0)}$ in tables that they are satisfying the relation $\frac{r^0}{P.E(r^0)} > 6$. Hence we concluded that parameters are strongly related to the physical characteristics and correlation is noteworthy.

Table 6.13: Values of $\frac{r^0}{P.E(r^0)}$ for (C_{f0}, C_{f1}) .

$\frac{r^0}{P.E(r^0)}$	$C_{f0}(Ag)$		$C_{f1}(Ag)$	
	$M = 0.1$	$M = 0.7$	$M = 0.1$	$M = 0.7$
A_2	128534.69	128534.69	329271.02	397613.02
Re	142672.43	4300.8643	565929.67	135.3035
ϕ	121.63866	123.17663	134.23432	134.01379
Ω	304.305053	652.1964991	14300.570	4119.8780
$\frac{r^0}{P.E(r^0)}$	$C_{f0}(Cu)$		$C_{f1}(Cu)$	
	$M = 0.1$	$M = 0.7$	$M = 0.1$	$M = 0.7$
A_2	645161219.4	128534.69	377642.2205	458567.0656
Re	195539.2127	125.050613	321027.1589	802502.5279
ϕ	122.484868	123.812522	133.1417034	133.0066153
τ	376.1364809	766.491690	9748.431027	3382.810152

Table 6.14: Values of $\frac{r^0}{P.E(r^0)}$ for (Nu_{x0}, Nu_{x1}) .

$\frac{r^0}{P.E(r^0)}$	$Nu_{x0}(Ag)$		$Nu_{x1}(Ag)$	
	$M = 0.1$	$M = 0.7$	$M = 0.1$	$M = 0.7$
R	128534.69	128534.69	128534.69	10.095217
Ec	128534.69	128534.69	128534.69	10.0297046
Re	2139952.79	128534.69	4280820.6	10.3659959
A_1	47377.7100	64.1318809	60862.988	8.629890
$\frac{r^0}{P.E(r^0)}$	$Nu_{x0}(Cu)$		$Nu_{x1}(Cu)$	
	$M = 0.1$	$M = 0.7$	$M = 0.1$	$M = 0.7$
R	128534.69	128534.69	128534.69	128534.69
Ec	128534.69	128534.69	611619.5107	611619.5107
Re	611619.5107	611619.5107	321026.0032	321026.0032
A_1	67225.60672	87949.4635	98018.7120	50154.19801

6.4 Graphical illustration

This section is arranged for the physical interpretation of flow variables on the flow field, skin friction, temperature and Nusselt number in the presence of both $Ag - H_2O$ and $Cu - H_2O$

nanoliquids.

6.4.1 Radial and axial velocity components

Impact of Reynolds number Re for velocity components (radial, axial) is described in Figs. 6.4 and 6.5. For an increase in Re the magnitude of velocity decreases for lower disk because inertial forces have direct relation with Reynolds number. Here clearly remarked that velocity for upper disk is more than lower one. Impact of A_1 velocity components (radial, axial) is shown in Figs. 6.6 and 6.7. Velocities in radial and axial directions enhance closed to the lower disk for larger A_1 and magnitude of these velocities decays near the upper disk. Negative values of axial velocity near the upper disk indicate that velocity of lower disk is more than upper disk. Figs. 6.8 and 6.9 indicate A_2 effect on $\tilde{f}'(\xi)$ and $\tilde{f}(\xi)$. Clearly these velocities at lower disk decay for A_2 while magnitude increases near upper disk. Physically, the stretching rate of upper is more. Behavior of rotational parameter Ω is examined in Figs. 6.10 and 6.11. We noted that $\tilde{f}'(\xi)$ and $\tilde{f}(\xi)$ decay near the lower disk and magnitude of these velocities increases at upper disk. It is due to the fact that for larger Ω the rotation at upper disk enhances so velocity is more at upper disk. Impact of Hartmann number for axial velocity is plotted in Fig. 6.12. Hartmann number is associated with the Lorentz force (which is resistive force) and as a result the velocity decays. Graphs overlap for silver and copper water nanofluids.

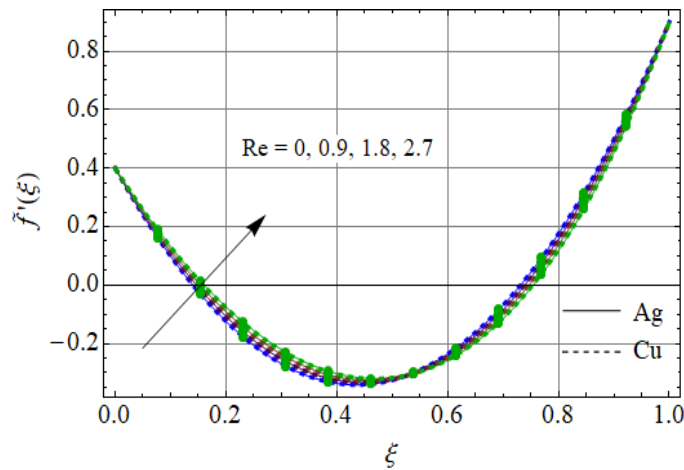


Fig. 6.4: $\tilde{f}'(\xi)$ via Re .

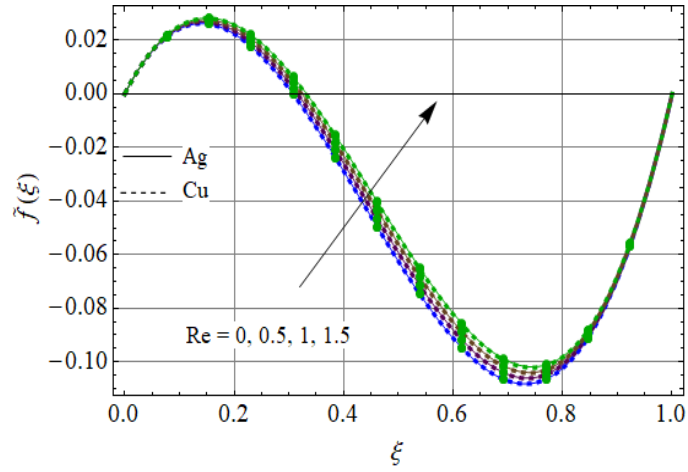


Fig. 6.4: $\tilde{f}(\xi)$ via Re .

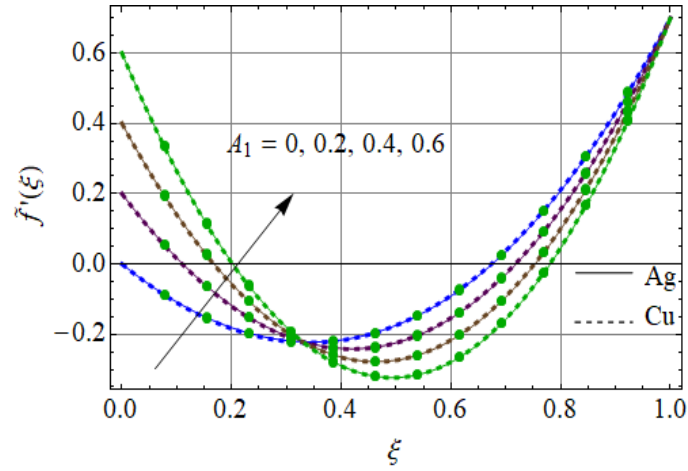


Fig. 6.6: $\tilde{f}'(\xi)$ via A_1 .

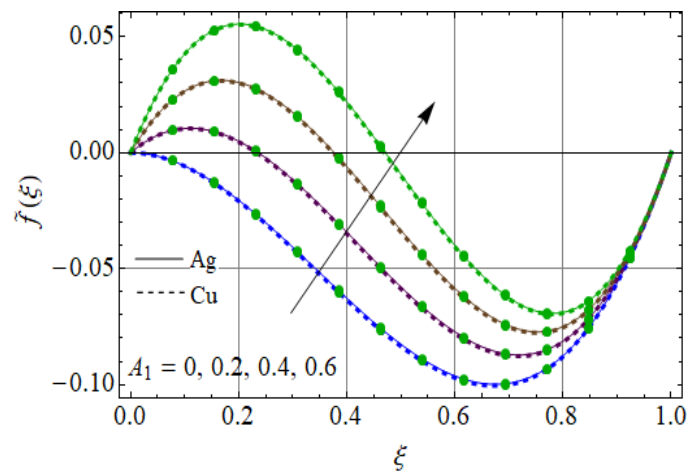


Fig. 6.7: $\tilde{f}(\xi)$ against A_1 .

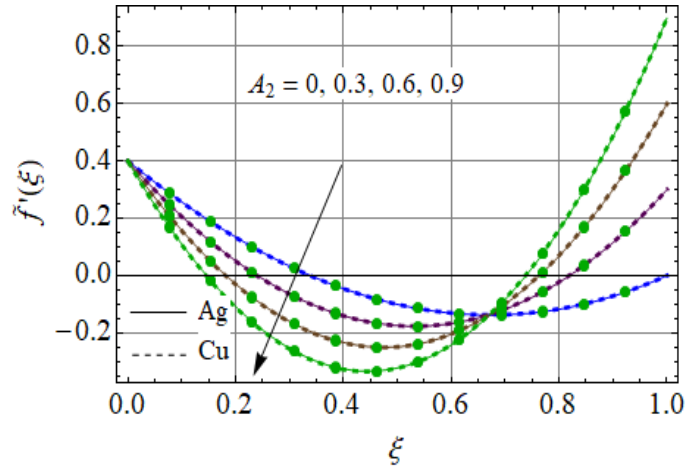


Fig. 6.8: $\tilde{f}'(\xi)$ against A_2 .

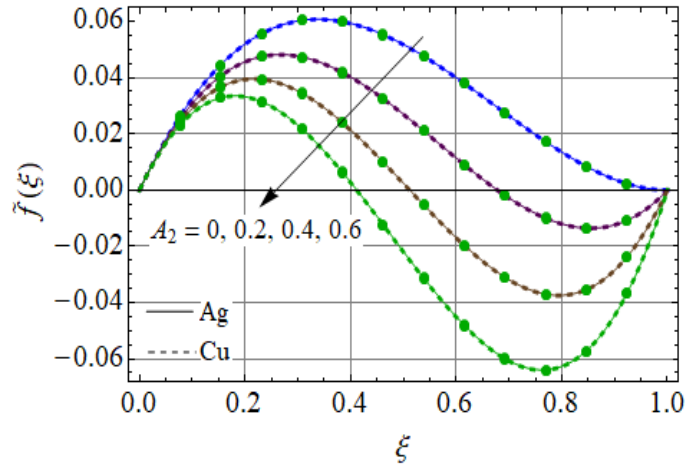


Fig. 6.9: $\tilde{f}(\xi)$ against A_2 .

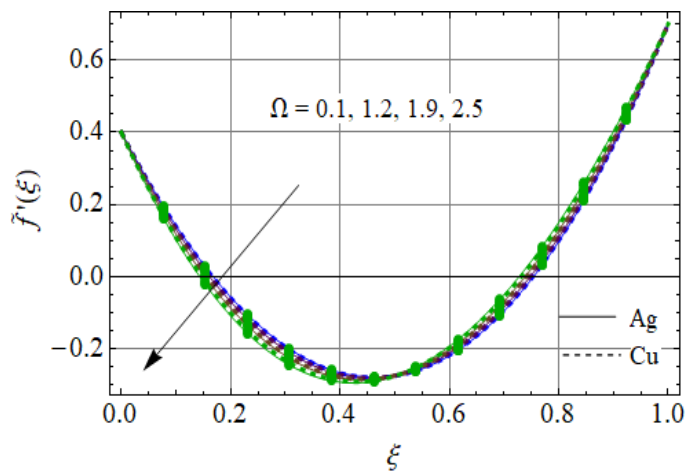


Fig. 6.10: $\tilde{f}'(\xi)$ against Ω .

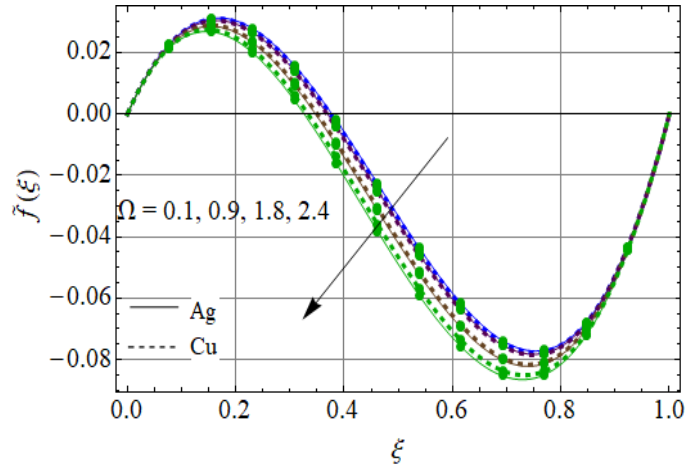


Fig. 6.11: $\tilde{f}(\xi)$ against Ω .

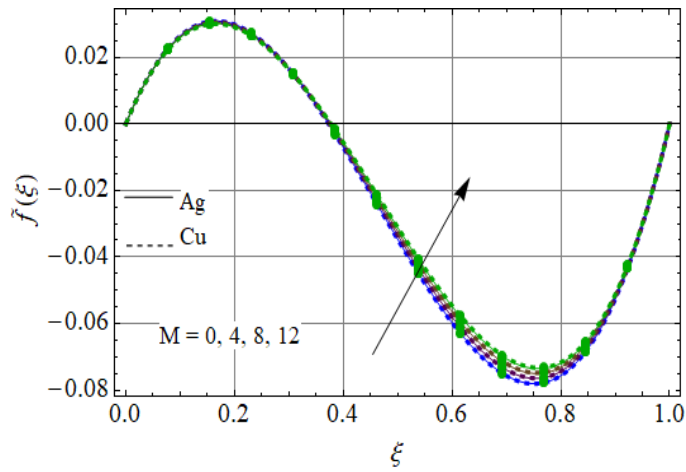


Fig. 6.12: $\tilde{f}(\xi)$ against M .

6.4.2 Tangential velocity

Impact of M on $\tilde{g}(\xi)$ is displayed in Fig. 6.13. It is worth mentioning that $\tilde{g}(\xi)$ decreases when M is increased. Impact of A_2 on $\tilde{g}(\xi)$ is shown in Fig. 6.14. Here tangential velocity is more for higher A_2 . Fig. 6.15 is displayed for Ω on $\tilde{g}(\xi)$. Tangential velocity is increased for larger

Ω . Outcomes of Re on $\tilde{g}(\xi)$ is examined in Fig. 6.16. Here $\tilde{g}(\xi)$ for Re is enhanced.

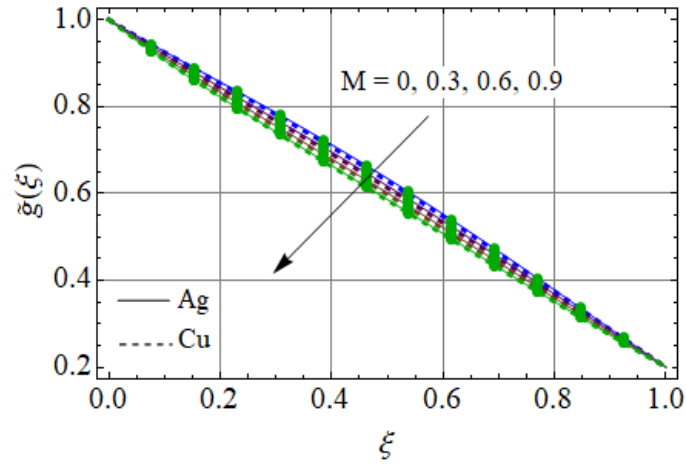


Fig. 6.13: $\tilde{g}(\xi)$ against M .

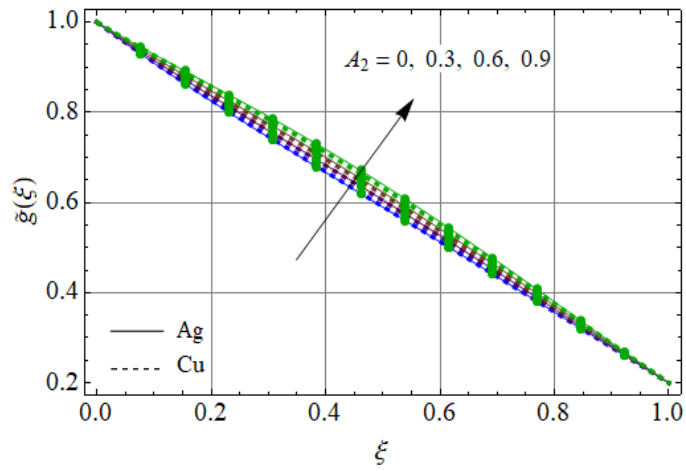


Fig. 6.14: $\tilde{g}(\xi)$ against A_2 .

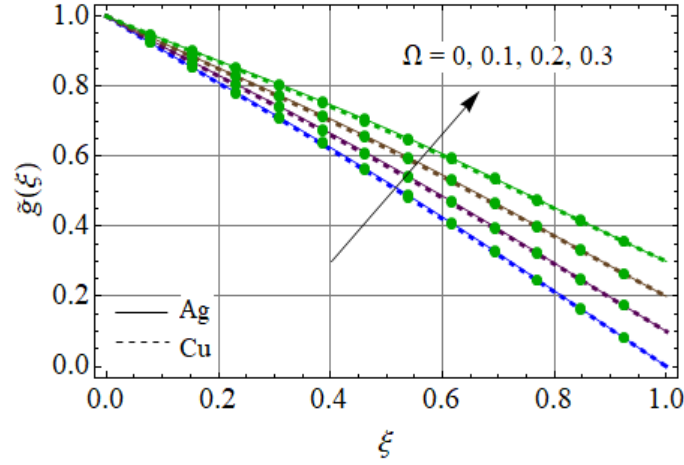


Fig. 6.15: $\tilde{g}(\xi)$ against Ω .

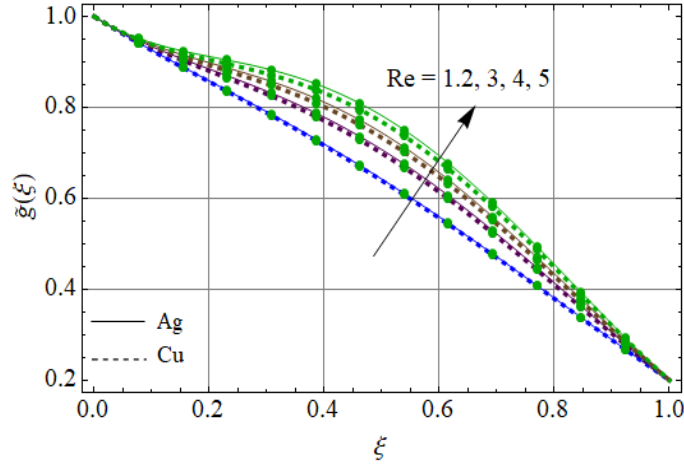


Fig. 6.16: $\tilde{g}(\xi)$ against Re .

6.4.3 Temperature

Fig. 6.17 is displayed to predict impact of Hartmann number M on $\theta(\xi)$. Temperature enhances for higher M . Resistive force in view of M increases. As a result temperature enhances. Figs. 6.18 and 6.19 show that temperature has opposite behavior for larger A_1 and A_2 . Influence of Re on temperature is described in Fig. 6.20. Here $\tilde{\theta}(\xi)$ is increased for Re . Figs. 6.21 and 6.22 portrayed outcome of radiation parameter R and Eckert number Ec on $\tilde{\theta}(\xi)$. Radiative heat transfer rate enhances for higher R because for larger R the coefficient of mean absorption decreases and thus fluid temperature increases (see Fig. 6.21). With an increase in values of the Ec resistance between the particles enhances and heat produces. This leads to an increase

in temperature (see Fig. 6.22).

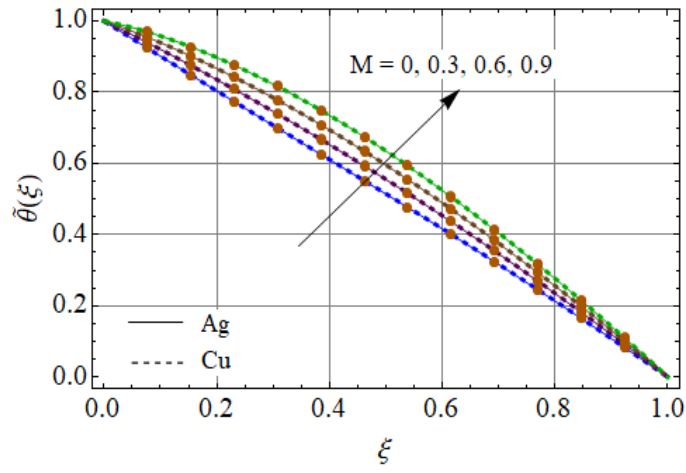


Fig. 6.17: $\tilde{\theta}(\xi)$ against M .

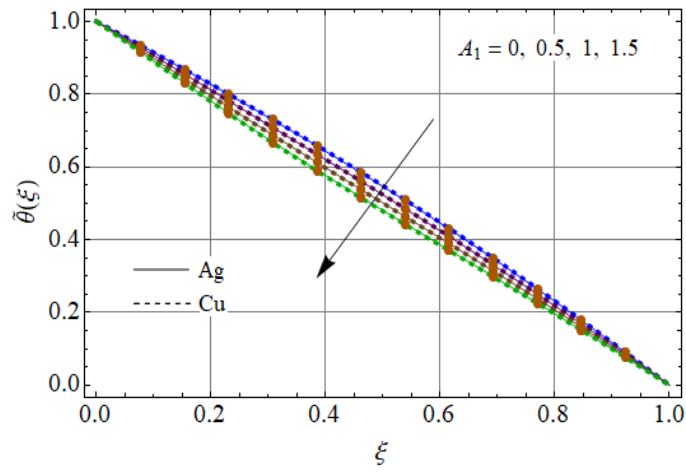


Fig. 6.18: $\tilde{\theta}(\xi)$ against A_1 .

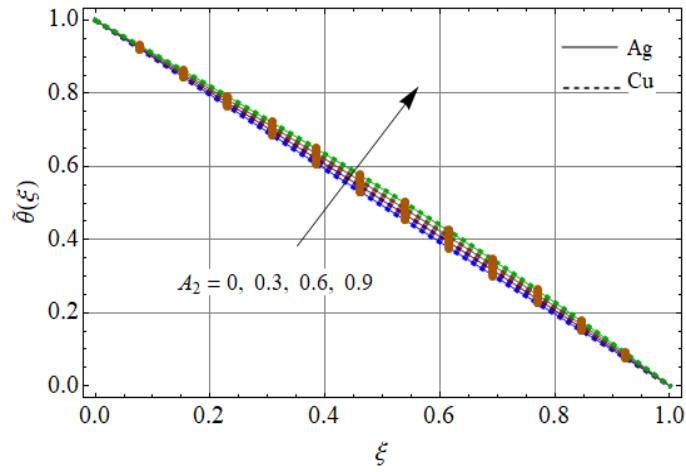


Fig. 6.19: $\tilde{\theta}(\xi)$ against A_2 .

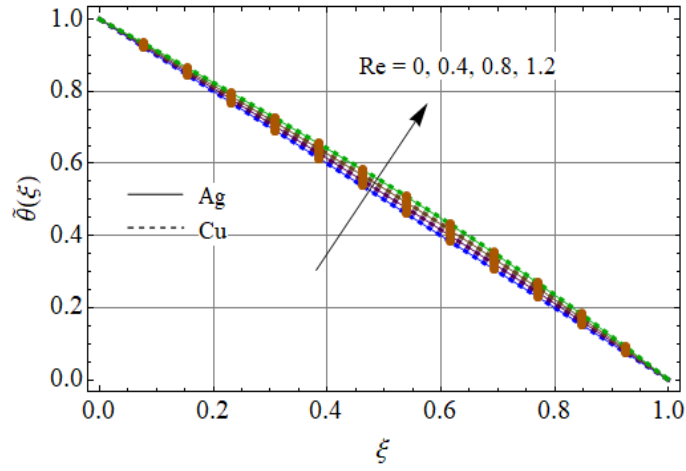


Fig. 6.20: $\tilde{\theta}(\xi)$ against Re .

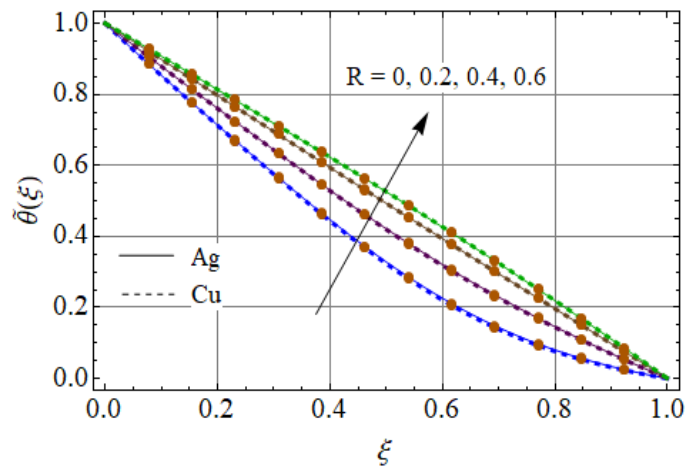


Fig. 6.21: $\tilde{\theta}(\xi)$ against R .

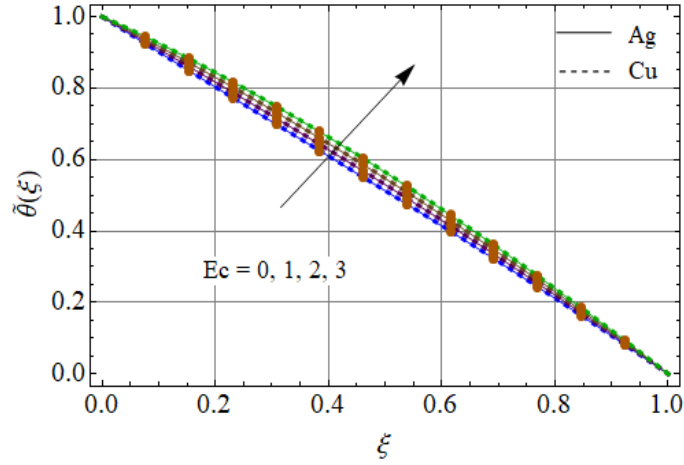


Fig. 6.22: $\tilde{\theta}(\xi)$ against Ec .

6.4.4 Concentration

Figs. 6.23 and 6.24 are depicted to display the characteristics of A_1 and A_2 on concentration field $\tilde{\phi}(\xi)$. For larger A_1 the fluid concentration enhances while concentration reduces for larger A_2 . Fig. 6.25 displays the impact of Re on fluid concentration $\tilde{\phi}(\xi)$. Fluid concentration declines versus rising Re . Schmidt number Sc impact on $\tilde{\phi}(\xi)$ is portrayed in Fig. 6.26. For higher Sc there is reduction in mass diffusivity because Sc is the ratio of viscosity to mass diffusivity so there is reduction in the fluid concentration. Fig. 6.27 shows that concentration of fluid decays by increasing k_1 because reactants are consumed during the homogeneous reactions. Same results are observed for Ag and Cu nanoparticles.

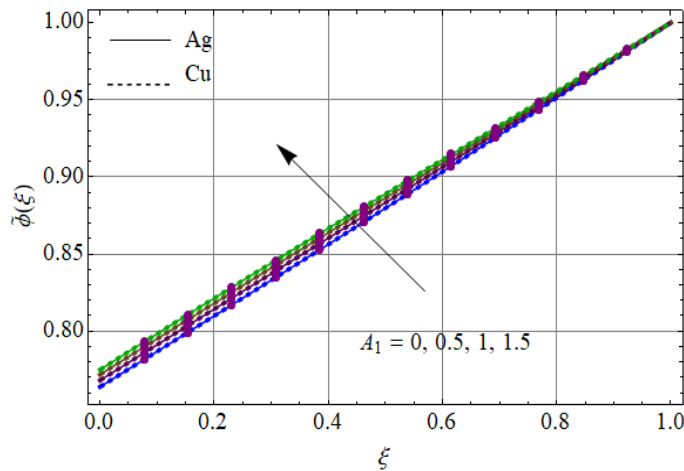


Fig. 6.23: $\tilde{\phi}(\xi)$ against A_1 .

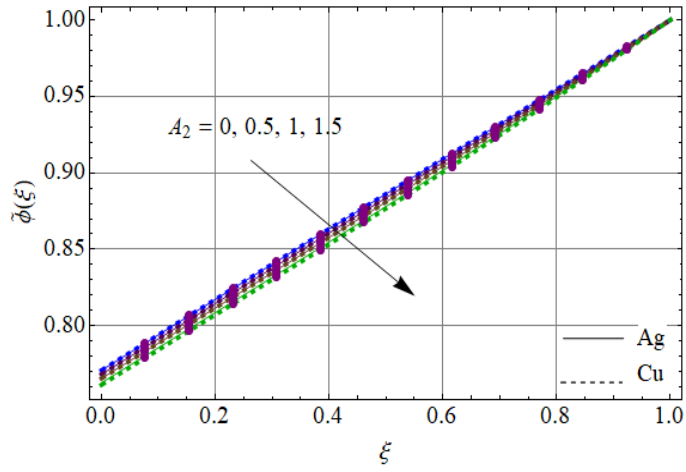


Fig. 6.24: $\tilde{\phi}(\xi)$ against A_2 .

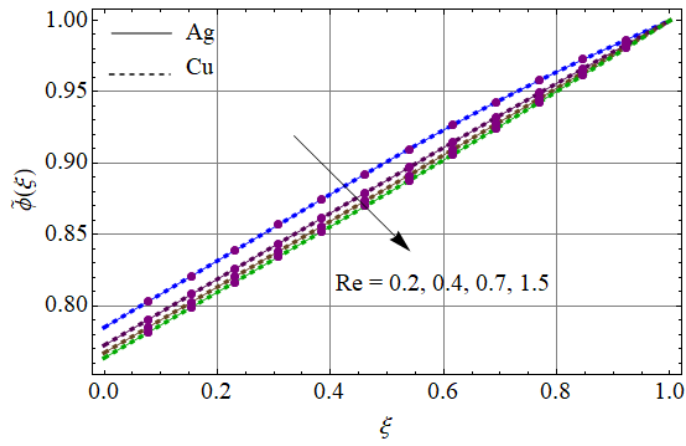


Fig. 6.25: $\tilde{\phi}(\xi)$ against Re .

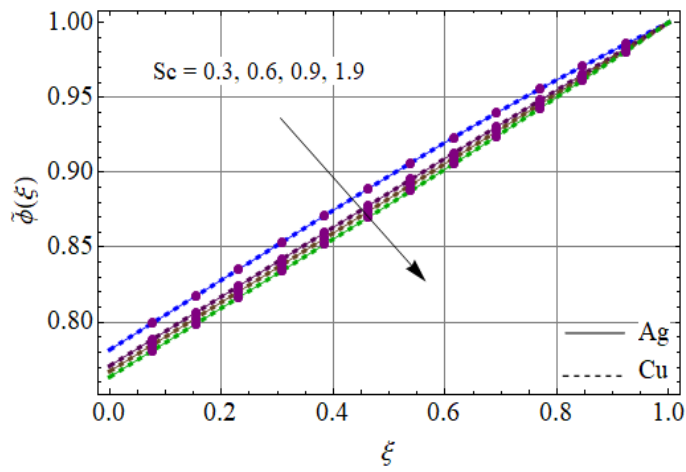


Fig. 6.26: $\tilde{\phi}(\xi)$ against Sc .

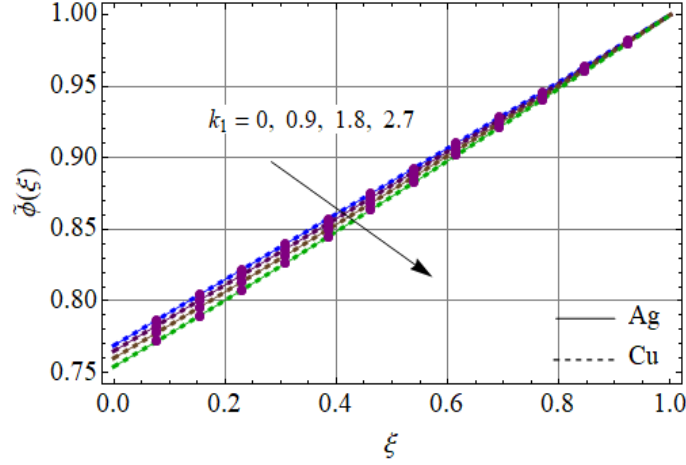


Fig. 6.27: $\tilde{\phi}(\xi)$ against k_1 .

6.5 Final remarks

Here MHD radiated reactive flow between two rotating disks is considered subject to Joule heating. The key points are

- Radial and axial components are increased at lower disk for A_1 while for A_2 these components are increased at upper disk.
- Tangential velocity for higher stretching and rotational parameters is enhanced.
- R and Ec on temperature have similar effect.
- Stretching parameters A_1 and A_2 have opposite impact for concentration profile $\phi(\xi)$.
- Concentration of fluid reduces for larger Sc and k_1 .
- Surface drag force is less for larger Ω at both disks.
- Influences of A_1 on heat transfer rate for upper and lower disks are opposite.
- All results are quantitatively similar for silver and copper water nanofluids.

Chapter 7

Entropy optimized unsteady reactive flow between two rotating disks with thermo-diffusion effects

Abstract: This chapter communicates the salient aspects of thermo-diffusions in unsteady reactive flow with entropy generation. The flow is discussed between two disks. Joule heating and heat generation/absorption contribution is incorporated in the thermal equation. Thermo-diffusion effect is also considered. MHD fluid is considered. Velocity and thermal slip conditions at both disks are implemented. Flow problem is modeled by using Navier-Stokes equations. Homotopy method for convergent series solutions by resulting problems is implemented. The nonlinear expressions for total entropy generation rate is obtained. The flow parameters are graphically discussed.

7.1 Modeling

Here we consider the MHD nanofluid flow between two rotating disks with chemical reaction. Lower disk is located at $z = 0$ and upper disk at distance h apart. Both disks are stretched with different rates i.e., a_1 and a_2 . The corresponding angular velocities on lower and upper disks are taken Ω_1 and Ω_2 . Effects of velocity and thermal slips with Joule heating are accounted. \hat{T}_1 , $\hat{\psi}_1$ and \hat{C}_1 represent the temperature, solutal and nanofluid concentrations of lower disk while temperature, solutal and nanofluid concentration of upper disk are denoted by \hat{T}_2 , $\hat{\psi}_2$ and \hat{C}_2 .

Magnetic field effects are taken through $B^2(t) = \frac{B_0^2}{1-c^*t}$ (see Fig. 7.1).

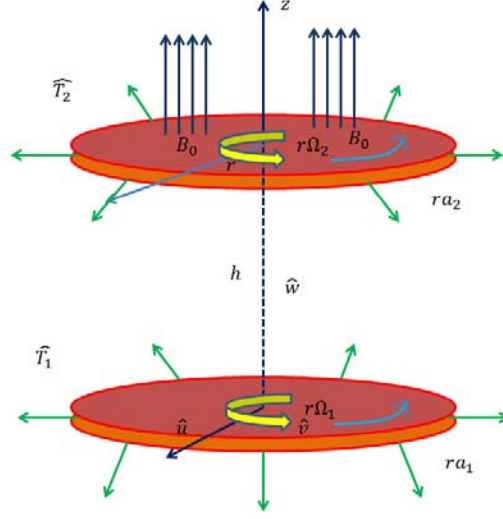


Fig. 7.1: Flow geometry.

The expressions which can govern the present problem are

$$\frac{\partial \hat{u}}{\partial r} + \frac{\partial \hat{w}}{\partial z} + \frac{\hat{u}}{r} = 0, \quad (7.1)$$

$$\frac{\partial \hat{u}}{\partial t} + \hat{u} \frac{\partial \hat{u}}{\partial r} + \hat{w} \frac{\partial \hat{u}}{\partial z} - \frac{\hat{v}^2}{r} = -\frac{1}{\rho} \frac{\partial \hat{p}}{\partial r} + \nu \left(\frac{\partial^2 \hat{u}}{\partial r^2} + \frac{1}{r} \frac{\partial \hat{u}}{\partial r} + \frac{\partial^2 \hat{u}}{\partial z^2} - \frac{\hat{u}}{r^2} \right) - \frac{\sigma}{\rho} B^2(t) \hat{u}, \quad (7.2)$$

$$\frac{\partial \hat{v}}{\partial t} + \hat{u} \frac{\partial \hat{v}}{\partial r} + \hat{w} \frac{\partial \hat{v}}{\partial z} + \frac{\hat{u} \hat{v}}{r} = \nu \left(\frac{\partial^2 \hat{v}}{\partial r^2} + \frac{1}{r} \frac{\partial \hat{v}}{\partial r} + \frac{\partial^2 \hat{v}}{\partial z^2} - \frac{\hat{v}}{r^2} \right) - \frac{\sigma}{\rho} B^2(t) \hat{v}, \quad (7.3)$$

$$\frac{\partial \hat{w}}{\partial t} + \hat{u} \frac{\partial \hat{w}}{\partial r} + \hat{w} \frac{\partial \hat{w}}{\partial z} = -\frac{1}{\rho} \frac{\partial \hat{p}}{\partial z} + \nu \left(\frac{\partial^2 \hat{w}}{\partial r^2} + \frac{1}{r} \frac{\partial \hat{w}}{\partial r} + \frac{\partial^2 \hat{w}}{\partial z^2} \right), \quad (7.4)$$

$$\begin{aligned}
(\rho c_p)_f \left(\frac{\partial \hat{T}}{\partial t} + \hat{u} \frac{\partial \hat{T}}{\partial r} + \hat{w} \frac{\partial \hat{T}}{\partial z} \right) &= k \left(\frac{1}{r} \frac{\partial \hat{T}}{\partial r} + \frac{\partial^2 \hat{T}}{\partial r^2} + \frac{\partial^2 \hat{T}}{\partial z^2} \right) \\
&+ (\rho c_p)_p \left[\begin{aligned} &D_B \left\{ \frac{\partial \hat{C}}{\partial z} \frac{\partial \hat{T}}{\partial z} + \frac{\partial \hat{C}}{\partial r} \frac{\partial \hat{T}}{\partial r} \right\} \\ &+ \frac{D_T}{T_2} \left\{ \left(\frac{\partial \hat{T}}{\partial r} \right)^2 + \left(\frac{\partial \hat{T}}{\partial z} \right)^2 \right\} \right] \\
&+ D_{TC} \left(\frac{1}{r} \frac{\partial \hat{\psi}}{\partial r} + \frac{\partial^2 \hat{\psi}}{\partial r^2} + \frac{\partial^2 \hat{\psi}}{\partial z^2} \right) + Q_0 (\hat{T} - \hat{T}_2), \quad (7.5)
\end{aligned}
\end{aligned}$$

$$\frac{\partial \hat{\psi}}{\partial t} + \hat{u} \frac{\partial \hat{\psi}}{\partial r} + \hat{w} \frac{\partial \hat{\psi}}{\partial z} = D_S \left(\frac{1}{r} \frac{\partial \hat{\psi}}{\partial r} + \frac{\partial^2 \hat{\psi}}{\partial r^2} + \frac{\partial^2 \hat{\psi}}{\partial z^2} \right) + D_{CT} \left(\frac{1}{r} \frac{\partial \hat{T}}{\partial r} + \frac{\partial^2 \hat{T}}{\partial r^2} + \frac{\partial^2 \hat{T}}{\partial z^2} \right) - K (\hat{\psi} - \hat{\psi}_2), \quad (7.6)$$

$$\frac{\partial \hat{C}}{\partial t} + \hat{u} \frac{\partial \hat{C}}{\partial r} + \hat{w} \frac{\partial \hat{C}}{\partial z} = D_B \left(\frac{1}{r} \frac{\partial \hat{C}}{\partial r} + \frac{\partial^2 \hat{C}}{\partial r^2} + \frac{\partial^2 \hat{C}}{\partial z^2} \right) + \frac{D_T}{T_2} \left(\frac{1}{r} \frac{\partial \hat{T}}{\partial r} + \frac{\partial^2 \hat{T}}{\partial r^2} + \frac{\partial^2 \hat{T}}{\partial z^2} \right), \quad (7.7)$$

$$\begin{aligned}
\hat{u} &= \frac{ra_1}{1-c^*t} + \lambda_1 \frac{\partial \hat{u}}{\partial z}, \quad \hat{v} = \frac{r\Omega_1}{1-c^*t} + \lambda_2 \frac{\partial \hat{v}}{\partial z}, \quad \hat{w} = 0, \quad \hat{T} = \frac{\hat{T}_1}{1-c^*t} + \lambda_3 \frac{\partial \hat{T}}{\partial z}, \quad \hat{\psi} = \hat{\psi}_1, \quad \hat{C} = \hat{C}_1 \quad \text{at } z = 0, \\
\hat{u} &= \frac{ra_2}{1-c^*t} - \lambda_1 \frac{\partial \hat{u}}{\partial z}, \quad \hat{v} = \frac{r\Omega_2}{1-c^*t} - \lambda_2 \frac{\partial \hat{v}}{\partial z}, \quad \hat{T} = \frac{\hat{T}_2}{1-c^*t} - \lambda_3 \frac{\partial \hat{T}}{\partial z}, \quad \hat{\psi} = \hat{\psi}_2, \quad \hat{C} = \hat{C}_2 \quad \text{at } z = h, \quad (7.8)
\end{aligned}$$

where we denote fluid temperature (\hat{T}), nanoparticles concentration (\hat{C}), solutal concentration ($\hat{\psi}$), electrical conductivity (σ), fluid pressure (\hat{p}), dynamic viscosity (μ), thermal conductivity (k), density (ρ), kinematic viscosity (ν), thermophoretic diffusion coefficient (D_T), (D_{CT}) and (D_{TC}) the Soret and Dufour diffusivities, unsteadiness parameter (c^*), Brownian diffusion coefficient (D_B), solutal diffusivity (D_S), chemical reaction coefficient (K), (λ_1) and (λ_2) the velocity slip coefficients, thermal slip coefficient (λ_3) and heat capacitance of fluid and nanofluid $(\rho c_p)_f$ and $(\rho c_p)_p$ respectively.

Considering

$$\begin{aligned}
\hat{u} &= \frac{r\Omega_1}{1-c^*t} \tilde{f}'(\xi), \quad \hat{v} = \frac{r\Omega_1}{1-c^*t} \tilde{g}(\xi), \quad \hat{w} = \frac{-2h\Omega_1}{\sqrt{1-c^*t}} \tilde{f}(\xi), \quad \tilde{\theta} = \frac{\hat{T} - \hat{T}_2}{\hat{T}_1 - \hat{T}_2}, \\
\tilde{\chi} &= \frac{\hat{\psi} - \hat{\psi}_2}{\hat{\psi}_1 - \hat{\psi}_2}, \quad \tilde{\phi} = \frac{\hat{C} - \hat{C}_2}{\hat{C}_1 - \hat{C}_2}, \quad \hat{p} = \frac{\rho\Omega_1\nu}{(1-c^*t)^2} \left(P(\xi) + \frac{1}{2} \frac{r^2}{h^2} \epsilon \right), \quad \xi = \frac{z}{h\sqrt{1-c^*t}}. \quad (7.9)
\end{aligned}$$

equation (1) is satisfied identically and Eqs. (7.2 – 7.8) become

$$\tilde{f}''' + \text{Re} \left(2\tilde{f}\tilde{f}'' - \tilde{f}'^2 + \tilde{g}^2 - A^0\tilde{f}' - \frac{A^0}{2}\xi\tilde{f}'' - M\tilde{f}' \right) - \epsilon = 0, \quad (7.10)$$

$$\tilde{g}'' + \text{Re} \left(2\tilde{f}\tilde{g}' - 2\tilde{f}'\tilde{g} - A^0\tilde{g} - \frac{A^0}{2}\xi\tilde{g}' - M\tilde{g} \right) = 0, \quad (7.11)$$

$$P' = \text{Re}(A^0\tilde{f} + A^0\xi\tilde{f}' - 4\tilde{f}\tilde{f}') - 2\tilde{f}'', \quad (7.12)$$

$$\frac{1}{\text{Pr}}\tilde{\theta}'' + Nt\tilde{\theta}'^2 + Nb\tilde{\theta}'\tilde{\chi}' + Nd\tilde{\phi}'' + 2\text{Re}\tilde{f}\tilde{\theta}' - \text{Re}\tilde{\theta}'\xi\frac{A^0}{2} + \text{Re}MEc(\tilde{f}'^2 + \tilde{g}^2) + Q^*\tilde{\theta} = 0, \quad (7.13)$$

$$\frac{1}{Sc}\tilde{\chi}'' + Ld\tilde{\theta}'' - R^*\tilde{\chi}\text{Re} + 2\text{Re}\tilde{f}\tilde{\chi}' - \text{Re}\xi\frac{A^0}{2}\tilde{\chi}' = 0, \quad (7.14)$$

$$\frac{1}{Sc}\tilde{\phi}'' + \frac{1}{Sc}\frac{Nt}{Nb}\tilde{\theta}'' + 2\text{Re}\tilde{f}\tilde{\phi}' - \text{Re}\xi\frac{A^0}{2}\tilde{\phi}' = 0, \quad (7.15)$$

$$\begin{aligned} \tilde{f}(0) &= 0, \tilde{f}(1) = 0, \tilde{f}'(0) = A_1 + \gamma_1\tilde{f}''(0), \tilde{f}'(1) = A_2 - \gamma_1\tilde{f}''(1), \tilde{g}(0) = 1 + \gamma_2\tilde{g}'(0), \\ \tilde{g}(1) &= \Omega - \gamma_2\tilde{g}'(1), \tilde{\theta}(0) = 1 + \gamma_3\tilde{\theta}'(0), \tilde{\theta}(1) = -\gamma_3\tilde{\theta}'(1), \tilde{\chi}(0) = 1, \tilde{\chi}(1) = 0, \\ \tilde{\phi}(0) &= 1, \tilde{\phi}(1) = 0, P(0) = 0, \end{aligned} \quad (7.16)$$

with

$$\begin{aligned} \text{Re} &= \frac{\Omega_1 h^2}{\nu}, \text{Pr} = \frac{(\rho c_p)\nu}{k}, M = \frac{B_0^2 \sigma}{\rho \Omega_1}, A_1 = \frac{a_1}{\Omega_1}, \\ A_2 &= \frac{a_2}{\Omega_1}, \Omega = \frac{\Omega_2}{\Omega_1}, Ec = \frac{\Omega_1^2 r^2}{(\hat{T}_1 - \hat{T}_2)c_p}, Nt = \frac{(\rho c_p)_p D_T (\hat{T}_1 - \hat{T}_2)}{(\rho c_p)_f \nu T_2}, \\ Nb &= \frac{(\rho c_p)_p D_B (\hat{\psi}_1 - \hat{\psi}_2)}{(\rho c_p)_f \nu}, Nd = \frac{D_{TC}(\hat{C}_1 - \hat{C}_2)}{(\hat{T}_1 - \hat{T}_2)\nu}, A^0 = \frac{c^*}{\Omega_1}, \\ Q^* &= \frac{Q_0}{(\rho c_p)_f \Omega_1}, Ld = \frac{D_{CT}(\hat{T}_1 - \hat{T}_2)}{\nu(\hat{C}_1 - \hat{C}_2)}, R^* = \frac{K}{\Omega_1}, Sc = \frac{\nu}{D_B}, \gamma_1 = \frac{\lambda_1}{h\sqrt{1-ct}}, \\ \gamma_2 &= \frac{\lambda_2}{h\sqrt{1-ct}}, \gamma_3 = \frac{\lambda_3}{h\sqrt{1-ct}}. \end{aligned} \quad (7.17)$$

Note that Re denote Reynolds number, M the magnetic parameter, Pr the Prandtl number, A_1 and A_2 the stretching variables, Ec the Eckert number, Ω the rotational parameter, Nt the thermophoresis variable, Nd the modified Dufour parameter, Nb Brownian motion variable,

Q the heat generation/absorption variable, Ld the modified Soret variable, k the chemical reaction variable, γ_1, γ_2 the velocity slip variables, Sc the Schmidt number, A^0 the unsteadiness parameter, ϵ the dimensionless pressure constant and γ_3 the thermal slip parameter.

To omit ϵ , Eq. (7.12) is differentiated with respect to ξ and get

$$\tilde{f}^{iv} + \text{Re} \left(2\tilde{f}\tilde{f}''' + 2\tilde{g}\tilde{g}' - \frac{3}{2}A^0\tilde{f}'' - \frac{A^0}{2}\xi\tilde{f}''' - M\tilde{f}'' \right) = 0, \quad (7.18)$$

and ϵ can be determined by utilizing Eqs. (7.10) and (7.16) as follows:

$$\epsilon = \tilde{f}'''(0) + \text{Re} \left(-(\tilde{f}'(0))^2 + (\tilde{g}(0))^2 - A^0\tilde{f}'(0) - \frac{A^0}{2}\xi\tilde{f}''(0) - M\tilde{f}'(0) \right) = 0, \quad (7.19)$$

Integrating Eq. (7.12) from 0 to ξ one obtain

$$P = 2 \left[\text{Re} \left(\frac{A^0}{2}\xi\tilde{f} - \tilde{f}^2 \right) - \tilde{f}' + \tilde{f}'(0) \right]. \quad (7.20)$$

Denoting shear stresses τ_{zr} and $\tau_{z\theta}$ at lower disk in radial and tangential directions one have

$$\tau_{zr} = \mu \left. \frac{\partial \hat{u}}{\partial z} \right|_{z=0} = \frac{\mu r \Omega_1 \tilde{f}''(0)}{h\sqrt{1-c^*t}}, \quad \tau_{z\theta} = \mu \left. \frac{\partial \hat{v}}{\partial z} \right|_{z=0} = \frac{\mu r \Omega_1 \tilde{g}'(0)}{h\sqrt{1-c^*t}}. \quad (7.21)$$

Total shear stress is

$$\tau_w = \sqrt{\tau_{zr}^2 + \tau_{z\theta}^2}. \quad (7.22)$$

Skin friction coefficients C_{f0} and C_{f1} at lower and upper disks are

$$C_{f0} = \frac{\tau_w|_{z=0}}{\rho \left(\frac{r\Omega_1}{\sqrt{1-c^*t}} \right)^2} = \frac{1}{\text{Re}_r} [(\tilde{f}''(0))^2 + (\tilde{g}'(0))^2]^{1/2}, \quad (7.23)$$

$$C_{f1} = \frac{\tau_w|_{z=h}}{\rho \left(\frac{r\Omega_1}{\sqrt{1-c^*t}} \right)^2} = \frac{1}{\text{Re}_r} [(\tilde{f}''(1))^2 + (\tilde{g}'(1))^2]^{1/2}, \quad (7.24)$$

where $\text{Re}_r = r\Omega_1 h / \nu \sqrt{1-c^*t}$ is the local Reynolds number.

Heat transfer rates (Nu_{x0}, Nu_{x1}) are defined as

$$Nu_{x0} = \left. \frac{hq_w \sqrt{1-c^*t}}{k(\hat{T}_1 - \hat{T}_2)} \right|_{z=0}, \quad Nu_{x1} = \left. \frac{hq_w \sqrt{1-c^*t}}{k(\hat{T}_1 - \hat{T}_2)} \right|_{z=h}, \quad (7.25)$$

in which wall heat flux q_w is

$$q_w|_{z=0} = -k \frac{\partial \hat{T}}{\partial z} \Big|_{z=0} = -\frac{k(\hat{T}_1 - \hat{T}_2)}{h\sqrt{1-c^*t}} \tilde{\theta}'(0), \quad (7.26)$$

$$q_w|_{z=h} = -k \frac{\partial \hat{T}}{\partial z} \Big|_{z=h} = -\frac{k(\hat{T}_1 - \hat{T}_2)}{h\sqrt{1-c^*t}} \tilde{\theta}'(1). \quad (7.27)$$

Nusselt numbers can be written as follows:

$$Nu_{x0} = -\tilde{\theta}'(0), \quad Nu_{x1} = -\tilde{\theta}'(1). \quad (7.28)$$

Sherwood number is

$$Sh_r = \frac{rh_m}{D_s(C_1 - C_2)}, \quad (7.29)$$

where

$$h_m = -D_s \left(\frac{\partial C}{\partial z} \right) \Big|_{z=0,h}. \quad (7.30)$$

In dimensionless variables one has

$$\begin{aligned} (\text{Re})^{-0.5} Sh_r &= -\tilde{\chi}'(0), \\ (\text{Re})^{-0.5} Sh_r &= -\tilde{\chi}'(1). \end{aligned} \quad (7.31)$$

7.2 Entropy modeling

Volumetric expression for entropy generation is addressed as

$$\begin{aligned} S_G &= \underbrace{\frac{k}{\hat{T}_m^2} \left[\left(\frac{\partial \hat{T}}{\partial r} \right)^2 + \left(\frac{\partial \hat{T}}{\partial z} \right)^2 \right]}_{\text{Thermal irreversibility}} + \underbrace{\frac{\mu}{\hat{T}_m} \Phi}_{\text{Fluid friction irreversibility}} + \underbrace{\frac{\sigma}{\hat{T}_m} B_0^2 (\hat{u}^2 + \hat{v}^2)}_{\text{Joule dissipation irreversibility}} \\ &+ \underbrace{\frac{R_g D}{\hat{\psi}_m} \left[\left(\frac{\partial \hat{\psi}}{\partial r} \right)^2 + \left(\frac{\partial \hat{\psi}}{\partial z} \right)^2 \right]}_{\text{Diffusive irreversibility}} + \frac{R_g D}{\hat{T}_m} \left[\frac{\partial \hat{T}}{\partial r} \frac{\partial \hat{\psi}}{\partial r} + \frac{\partial \hat{T}}{\partial z} \frac{\partial \hat{\psi}}{\partial z} \right], \end{aligned} \quad (7.32)$$

$$\Phi = 2 \left[\left(\frac{\partial \hat{u}}{\partial r} \right)^2 + \frac{1}{r^2} (\hat{u})^2 + \left(\frac{\partial \hat{w}}{\partial z} \right)^2 + \left[\frac{\partial \hat{v}}{\partial z} \right]^2 + \left[\frac{\partial \hat{w}}{\partial r} + \frac{\partial \hat{u}}{\partial z} \right]^2 + \left[r \frac{\partial}{\partial r} \left(\frac{\hat{v}}{r} \right) \right]^2 \right] \quad (7.33)$$

$$S_G = \frac{k}{\hat{T}_m^2} \left[\underbrace{\left(\frac{\partial \hat{T}}{\partial r} \right)^2 + \left(\frac{\partial \hat{T}}{\partial z} \right)^2}_{\text{Thermal irreversibility}} + \frac{\mu}{\hat{T}_m} \underbrace{\left[\frac{2 \left(\frac{\partial \hat{u}}{\partial r} \right)^2 + \frac{2}{r^2} (\hat{u})^2 + 2 \left(\frac{\partial \hat{w}}{\partial z} \right)^2}{+ \left[\frac{\partial \hat{v}}{\partial z} \right]^2 + \left[\frac{\partial \hat{w}}{\partial r} + \frac{\partial \hat{u}}{\partial z} \right]^2 + \left[r \frac{\partial}{\partial r} \left(\frac{\hat{v}}{r} \right) \right]^2} \right]}_{\text{Fluid friction irreversibility}} \right] + \underbrace{\frac{\sigma}{\hat{T}_m} B_0^2 (\hat{u}^2 + \hat{v}^2)}_{\text{Joule dissipation irreversibility}} + \underbrace{\frac{R_g D}{\hat{\psi}_m} \left[\left(\frac{\partial \hat{\psi}}{\partial r} \right)^2 + \left(\frac{\partial \hat{\psi}}{\partial z} \right)^2 \right] + \frac{R_g D}{T_m} \left[\frac{\partial \hat{T}}{\partial r} \frac{\partial \hat{\psi}}{\partial r} + \frac{\partial \hat{T}}{\partial z} \frac{\partial \hat{\psi}}{\partial z} \right]}_{\text{Diffusive irreversibility}} \quad (7.34)$$

Equation (7.34) represents the four factors which effect entropy generation. First, Second, third and fourth term represent the thermal irreversibility, fluid friction irreversibility, Joule heating irreversibility and diffusive irreversibility respectively. After making use of transformations we obtain

$$N_G = \tilde{\theta}'^2 \alpha_1 \frac{1}{\text{Re}} + \frac{Br}{\text{Re}} (12\tilde{f}'^2 + A\tilde{g}'^2 + A\tilde{f}''^2) + MBrA(\tilde{f}'^2 + \tilde{g}'^2) + L\alpha_1\alpha_2 \frac{1}{\text{Re}} \chi'^2 + L \frac{1}{\text{Re}} \theta' \chi' \quad (7.35)$$

$$\hat{T}_m = \frac{\hat{T}_1 - \hat{T}_2}{2}, \quad \hat{\psi}_m = \frac{\hat{\psi}_1 - \hat{\psi}_2}{2}, \quad \alpha_1 = \frac{\hat{T}_1 - \hat{T}_2}{\hat{T}_m} = \frac{\Delta T}{\hat{T}_m}, \quad \alpha_2 = \frac{\hat{\psi}_1 - \hat{\psi}_2}{\hat{\psi}_m} = \frac{\Delta \hat{\psi}}{\hat{\psi}_m},$$

$$Br = \frac{\mu \Omega_1^2 h^2}{k \Delta T}, \quad N_G = \frac{\hat{T}_m S_G \nu}{k \Delta T \Omega_1}, \quad A = \frac{r^2}{h^2}, \quad L = \frac{R_g D (C_w - C_\infty)}{k} \quad (7.36)$$

where \hat{T}_m , $\hat{\psi}_m$, α_1 , α_2 , L , Br and A denote the mean temperature, mean concentration, temperature difference parameter, concentration difference parameter, diffusive parameter, Brinkman number and dimensionless parameter respectively.

Dimensionless form of Bejan number (Be) is

$$Be = \frac{\text{Entropy generation due to heat and mass transfer}}{\text{Total entropy generation}} \quad (7.37)$$

or

$$Be = \frac{\tilde{\theta}'^2 \alpha_1 \frac{1}{\text{Re}} + L\alpha_1\alpha_2 \frac{1}{\text{Re}} \tilde{\phi}'^2 + L \frac{1}{\text{Re}} \tilde{\theta}' \tilde{\phi}'}{\tilde{\theta}'^2 \alpha_1 \frac{1}{\text{Re}} + \frac{Br}{\text{Re}} (12\tilde{f}'^2 + A\tilde{g}'^2 + A\tilde{f}'^2) + MBrA(\tilde{f}'^2 + \tilde{g}'^2) + L\alpha_1\alpha_2 \frac{1}{\text{Re}} \tilde{\chi}'^2 + L \frac{1}{\text{Re}} \tilde{\theta}' \tilde{\chi}'}. \quad (7.38)$$

7.3 Technique Procedure

Initial approximations and linear operators are

$$\tilde{f}_0(\xi) = \frac{A_1\xi + 4A_1\gamma_1\xi - 2A_2\gamma_1\xi - 2A_1\xi^2 - A_2\xi^2 - 6A_1\gamma_1\xi^2 + A_1\xi^3 + A_2\xi^3 + 2A_1\gamma_1\xi^3 + 2A_2\gamma_1\xi^3}{(1 + 2\gamma_1)(1 + 6\gamma_1)}, \quad (7.39)$$

$$\tilde{g}_0(\xi) = \frac{1 + \gamma_2 - \xi + \gamma_2\Omega + \xi\Omega}{1 + 2\gamma_2}, \quad (7.40)$$

$$\tilde{\theta}_0(\xi) = \frac{1 + \gamma_3 - \xi}{1 + 2\gamma_3}, \quad (7.41)$$

$$\tilde{\chi}_0(\xi) = 1 - \xi, \quad (7.42)$$

$$\tilde{\phi}_0(\xi) = 1 - \xi, \quad (7.43)$$

$$\mathcal{L}_{\tilde{f}} = \tilde{f}''''', \quad \mathcal{L}_{\tilde{g}} = \tilde{g}''', \quad \mathcal{L}_{\tilde{\theta}} = \tilde{\theta}''', \quad \mathcal{L}_{\tilde{\chi}} = \tilde{\chi}''', \quad \mathcal{L}_{\tilde{\phi}} = \tilde{\phi}''', \quad (7.44)$$

with

$$\left. \begin{aligned} \mathcal{L}_{\tilde{f}} [c_1 + c_2\xi + c_3\xi^2 + c_4\xi^3] &= 0, \\ \mathcal{L}_{\tilde{g}} [c_5 + c_6\xi] &= 0, \\ \mathcal{L}_{\tilde{\theta}} [c_7 + c_8\xi] &= 0, \\ \mathcal{L}_{\tilde{\chi}} [c_{11} + c_{12}\xi] &= 0, \\ \mathcal{L}_{\tilde{\phi}} [c_9 + c_{10}\xi] &= 0, \end{aligned} \right\} \quad (7.45)$$

where c_i ($i = 1 - 12$) are the constants.

7.4 Convergence analysis

HAM is very useful for solving nonlinear equations. To adjust convergence of nonlinear equations the convergence control variables $\tilde{h}_{\tilde{f}}$, $\tilde{h}_{\tilde{g}}$, $\tilde{h}_{\tilde{\theta}}$, $\tilde{h}_{\tilde{\chi}}$ and $\tilde{h}_{\tilde{\phi}}$ have vital role. The \tilde{h} -curves of $\tilde{f}''(0)$, $\tilde{g}'(0)$, $\tilde{\theta}'(0)$, $\tilde{\chi}'(0)$ and $\tilde{\phi}'(0)$ are displayed in Fig. 7.2. Admissible ranges are $-2.5 \leq$

$\hbar_{\tilde{f}} \leq -0.5$, $-2.8 \leq \hbar_{\tilde{g}} \leq -0.4$, $-2.9 \leq \hbar_{\tilde{\theta}} \leq -0.6$, $-2.9 \leq \hbar_{\tilde{\chi}} \leq -0.6$ and $-2.9 \leq \hbar_{\tilde{\phi}} \leq -0.6$. Table 1 shows the convergence of $\tilde{f}''(0)$, $\tilde{g}'(0)$, $\tilde{\theta}'(0)$, $\tilde{\chi}'(0)$ and $\tilde{\phi}'(0)$ upto 7 decimal places. It illustrates that 11th, 15th, 19th and 25th orders of approximations are sufficient for $\tilde{f}''(0)$, $\tilde{g}'(0)$, $\tilde{\theta}'(0)$, $\tilde{\chi}'(0)$ and $\tilde{\phi}'(0)$.

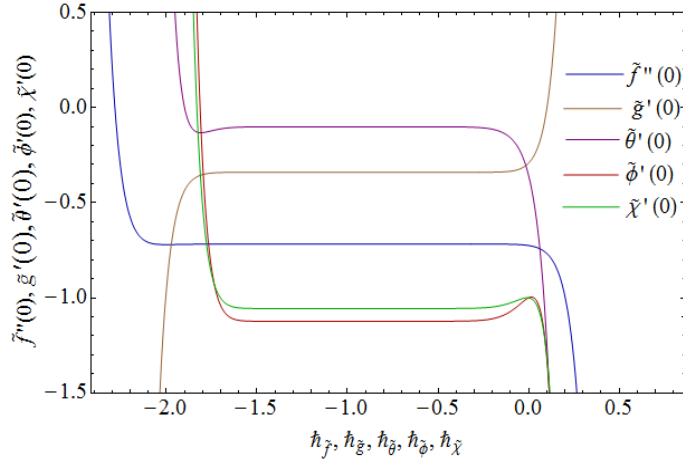


Fig. 7.2: \hbar -curves for $\tilde{f}''(0)$, $\tilde{g}'(0)$, $\tilde{\theta}'(0)$, $\tilde{\chi}'(0)$ and $\tilde{\phi}'(0)$.

Table 7.1: Different iterations when $\text{Re} = 0.3$, $M = 0.5$, $\text{Pr} = 1$, $A_1 = 0.4$, $A_2 = 0.9$, $\Omega = 0.3$, $\gamma_1 = 0.5$, $\gamma_2 = 0.7$, $\gamma_3 = 0.9$, $Ec = 0.7$, $Nt = 0.1$, $Nb = 0.4$, $Sc = 1$, $Nd = 0.2$, $Ld = 0.4$, $A = 0.1$, $Q = 0.4$, $k = 0.3$.

Order of approximation	$-\tilde{f}''(0)$	$-\tilde{g}'(0)$	$-\tilde{\theta}'(0)$	$-\tilde{\chi}'(0)$	$-\tilde{\phi}'(0)$
1	0.71726100	0.34336328	0.15805891	1.0228750	0.99287500
6	0.71760417	0.34018052	0.10126114	1.1231882	1.0562045
13	0.71760417	0.34018052	0.10125987	1.1232292	1.0562331
14	0.71760417	0.34018052	0.10125994	1.1232291	1.0562331
15	0.71760417	0.34018052	0.10125996	1.1232291	1.0562331
20	0.71760417	0.34018052	0.10125996	1.1232291	1.0562331
30	0.71760417	0.34018052	0.10125996	1.1232291	1.0562331
40	0.71760417	0.34018052	0.10125996	1.1232291	1.0562331

7.5 Discussion

7.5.1 Velocity and temperature

Figs. (7.3 – 7.12) show outcomes of magnetic parameter, Reynolds number, slip parameters, stretching parameters, rotational parameter, thermophoresis parameter, Brownian motion parameter, heat source parameter, Eckert number and Prandtl number on velocity components and temperature. Figs. 7.3((a)-(d)) describe the significance of magnetic parameter on axial, radial, tangential velocities and temperature. Magnitude of axial, radial and tangential velocities is less for M (see Figs. 7.3 ((a)-(c))). Since M is related with Lorentz force which acts opposite to liquid motion so velocity reduces. Temperature enhances for larger M (see Fig. 7.3(d)). With increasing M the resistance between fluid enhances and thus more heat produces and temperature grows. Figs. 7.4((a)-(d)) depict results of Reynolds number Re on velocities ($\tilde{f}(\xi)$, $\tilde{f}'(\xi)$ and $\tilde{g}(\xi)$) and temperature $\tilde{\theta}(\xi)$. At lower disk the magnitude of axial and radial velocities enhances. It is because of decrease in viscous effects (see Figs. 7.4((a)-(b))). In Fig. 7.4(c) for larger Re the tangential velocity $\tilde{g}(\xi)$ reduces. Fig. 7.4(d) elucidate outcome of Re on thermal field. It is noticed that thermal field boosts for larger Re . Figs. 7.5((a)-(d)) show the impact of velocity slip γ_1 , γ_2 and thermal slip γ_3 variables on velocity components and temperature. Figs. 7.5((a)-(b)) depict that axial and radial velocities decay for larger γ_1 . Fig. 7.5(c) depicts that tangential velocity is decreasing function of γ_2 . Under slip condition the stretching of disk is partially transmitted to the fluid and this causes the fluid velocity to reduce. Impact of γ_3 on temperature is depicted in Fig. 7.5(d). Here temperature enhances via γ_3 . Figs. 7.6((a)-(c)) show the impact of stretching parameters A_1 and A_2 on axial ($\tilde{f}(\xi)$) and radial ($\tilde{f}'(\xi)$) velocities. Axial velocity increases at lower disk for larger A_1 and magnitude of velocity starts decreasing near the upper disk (see Fig. 7.6(a)). As expected the stretching rate of lower disk (a_1) enhances for larger A_1 . Radial velocity is also increasing for larger A_1 (see Fig. 7.6(b)). Magnitude of axial velocity reduces at lower disk for larger A_2 and it boosts near upper disk (see Fig. 7.6(c)). It is for an increase in stretching rate of upper disk (a_2). For higher Ω the rotational velocity increases for upper disk which is responsible for an increase in tangential velocity $\tilde{g}(\xi)$ (see Fig. 7.7). Fig. 7.8 gives behavior of thermophoresis parameter Nt on temperature $\tilde{\theta}(\xi)$. When Nt enhances then thermophoresis force increases which tends to

move nanoparticles from hot side to cold side and finally it enhances temperature of fluid. Fig. 7.9 depicts influence of Nb on $\tilde{\theta}(\xi)$. Temperature increases in view of more random motion of fluid particles for higher Nb . Impact of Q on temperature is shown in Fig. 7.10. For higher Q the temperature enhances. Impact of Eckert number Ec from 0 to 5 is portrayed in Fig. 7.11. As Ec increases the mechanical energy of fluid is converted to thermal energy due to inside friction of molecules. Hence temperature enhancement is observed. For larger values of Pr the magnitude of temperature diminishes for decrease in liquid thermal diffusivity.

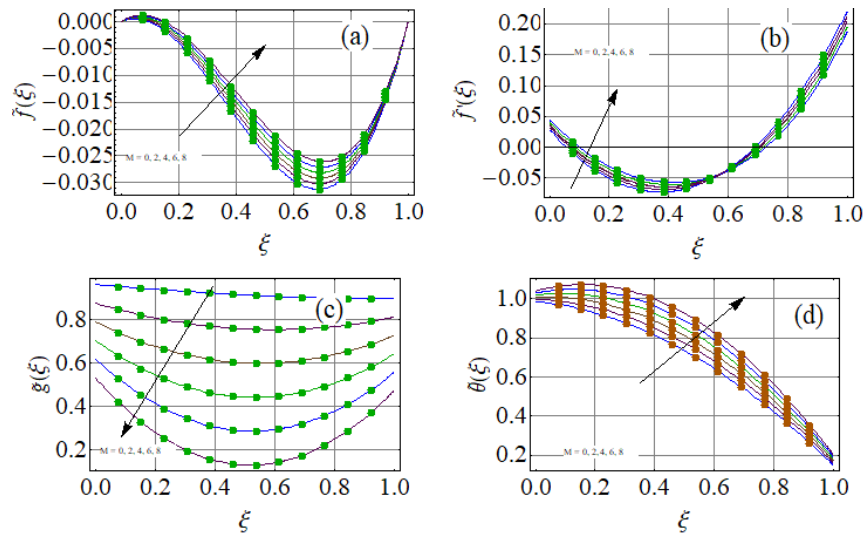


Fig. 7.3: Variation of M on $\tilde{f}(\xi)$, $\tilde{f}'(\xi)$, $\tilde{g}(\xi)$ and $\tilde{\theta}(\xi)$.

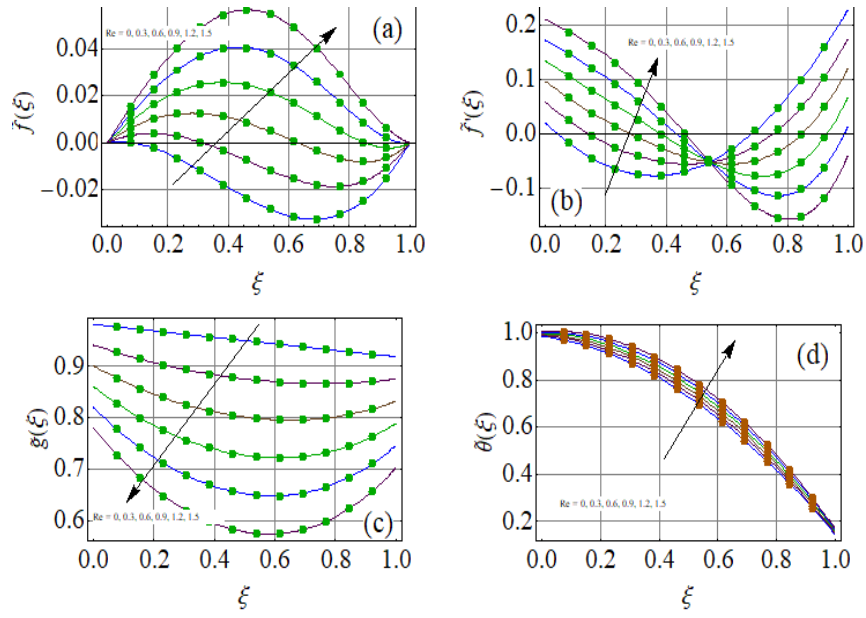


Fig. 7.4: $\tilde{f}(\xi)$, $\tilde{f}'(\xi)$, $\tilde{g}(\xi)$ and $\tilde{\theta}(\xi)$ against Re.

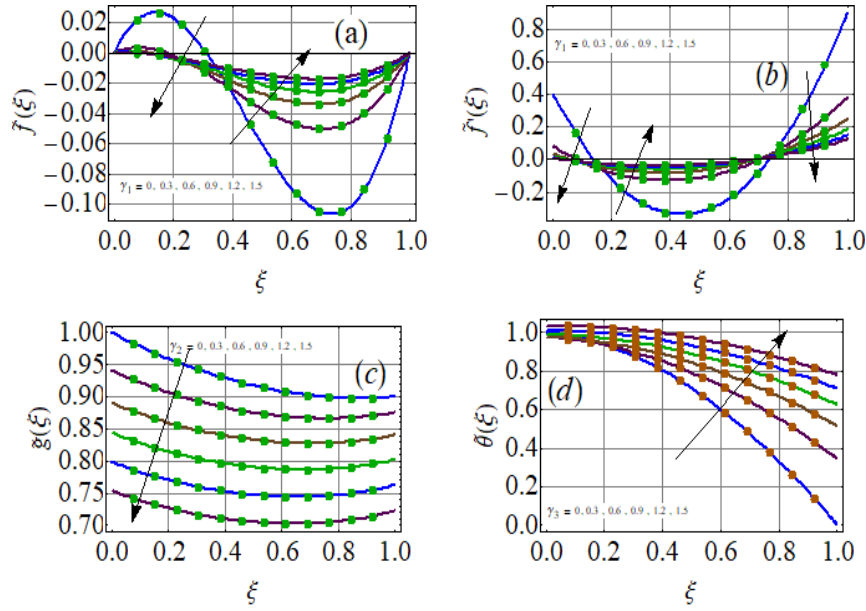


Fig. 7.5: γ_1 , γ_2 and γ_3 variation for $\tilde{f}(\xi)$, $\tilde{f}'(\xi)$, $\tilde{g}(\xi)$ and $\tilde{\theta}(\xi)$.

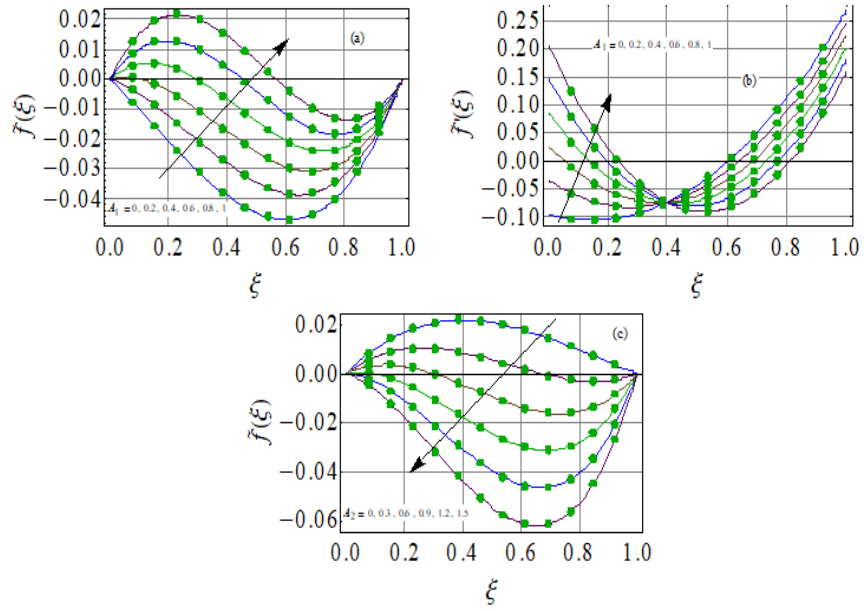


Fig. 7.6: Variations of A_1 and A_2 on $\tilde{f}(\xi)$ and $\tilde{f}'(\xi)$.

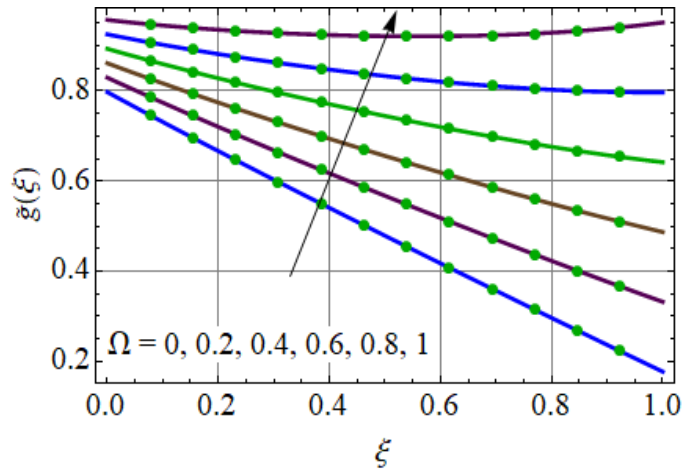


Fig. 7.7: Ω variation for $\tilde{g}(\xi)$.

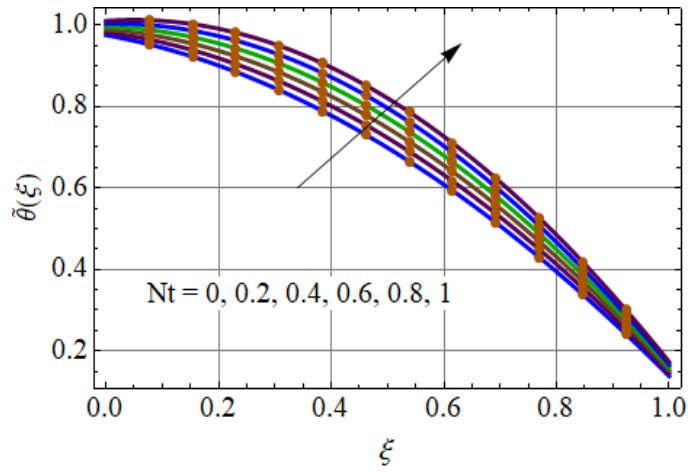


Fig. 7.8: Nt variation for $\tilde{\theta}(\xi)$.

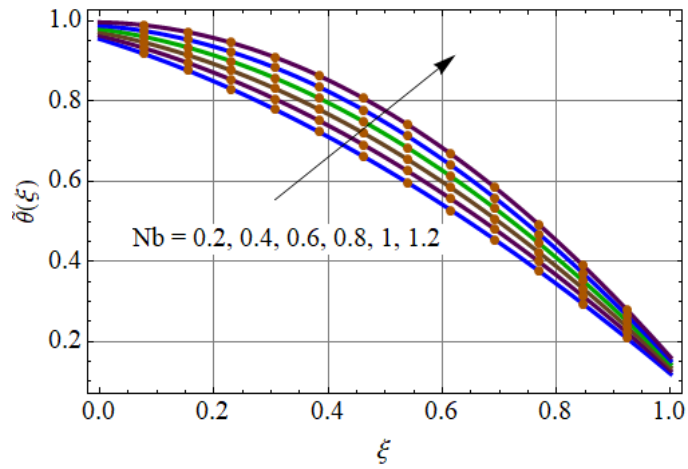


Fig. 7.9: Nb variation for $\tilde{\theta}(\xi)$.

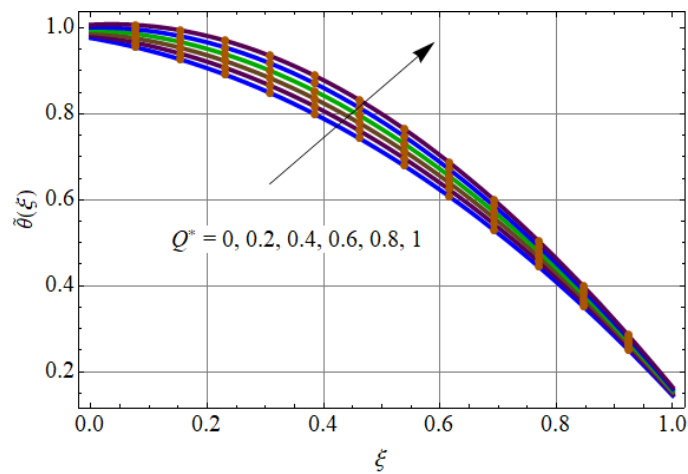


Fig. 7.10: Q^* variation for $\tilde{\theta}(\xi)$.

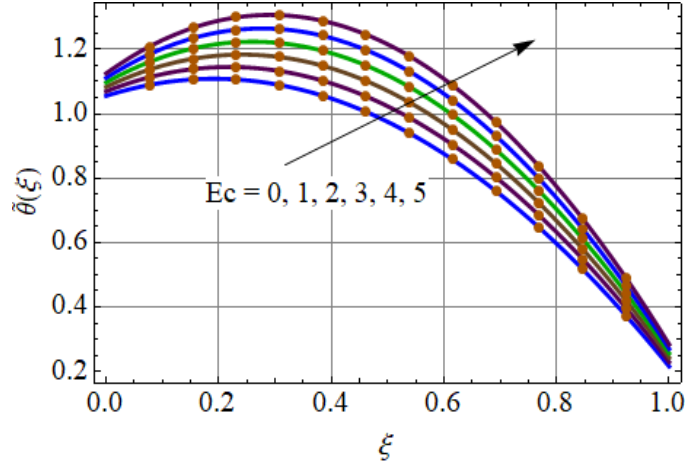


Fig. 7.11: Ec variation for $\tilde{\theta}(\xi)$.

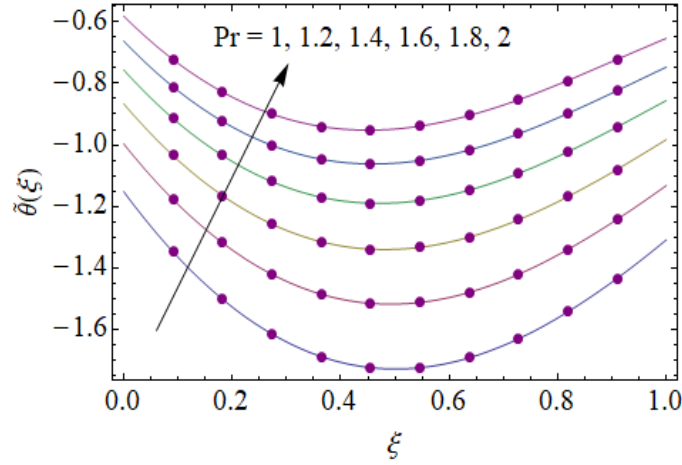


Fig. 7.12: Pr variation for $\tilde{\theta}(\xi)$.

7.5.2 Solutal ($\tilde{\chi}(\xi)$) and nanoparticles ($\tilde{\phi}(\xi)$) concentration profiles

Figs. (7.13 – 7.20) displayed the outcomes of parameters for solutal $\tilde{\chi}(\xi)$ and nanoparticles concentration $\tilde{\phi}(\xi)$. Impact of Sc on $\tilde{\chi}(\xi)$ is examined in Fig. 7.13. Magnitude of $\tilde{\chi}(\xi)$ reduces for larger Sc . Impact of modified Soret parameter Ld is elucidated in Fig. 7.14. Magnitude of $\tilde{\chi}(\xi)$ enhances for larger Ld . Here concentration layer thickness upsures. Outcome of chemical reaction k on $\tilde{\chi}(\xi)$ is analyzed in Fig. 7.15. Here $\tilde{\chi}(\xi)$ is an increasing function of k . Magnitude of $\tilde{\chi}(\xi)$ increases for larger thermophoresis Nt (see Fig. 7.16). Effect of Sc on $\tilde{\phi}(\xi)$ is depicted in Fig. 7.17. Magnitude of $\tilde{\phi}(\xi)$ is decreasing for Sc . Influence of Sc is opposite to the Brownian diffusion coefficient. For smaller D_B the penetration depth of nanoparticle reduces

and penetration depth for larger Sc decays. Moreover an enhancement in Sc leads to decay for both concentration rate and heat transfer rate. Fig. 7.18 is displayed to show impact of Nt on $\tilde{\phi}(\xi)$. Increase in $\tilde{\phi}(\xi)$ is noticed for larger Nt . Temperature gradient enhances via Nt . As we know that concentration field is associated with temperature gradient and temperature is an increasing function of Nt therefore larger Nt increase the concentration and related layer thickness. Behavior of Nb on nanoparticles concentration $\tilde{\phi}(\xi)$ is sketched in Fig. 7.19. With increase in Nb the collision and random motion of nanoparticles of fluid grows which produces more heat and eventually it results decrease in $\tilde{\phi}(\xi)$. Clearly $\tilde{\phi}(\xi)$ reduces against Nb . Influence of A^0 on $\tilde{\phi}(\xi)$ is depicted in Fig. 7.20. For higher A^0 the nanoparticles concentration $\tilde{\phi}(\xi)$ reduces.

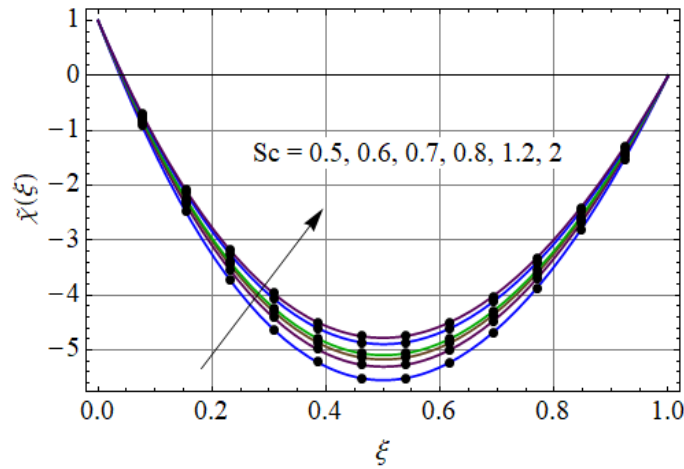


Fig. 7.13: Sc variation for $\tilde{\chi}(\xi)$.

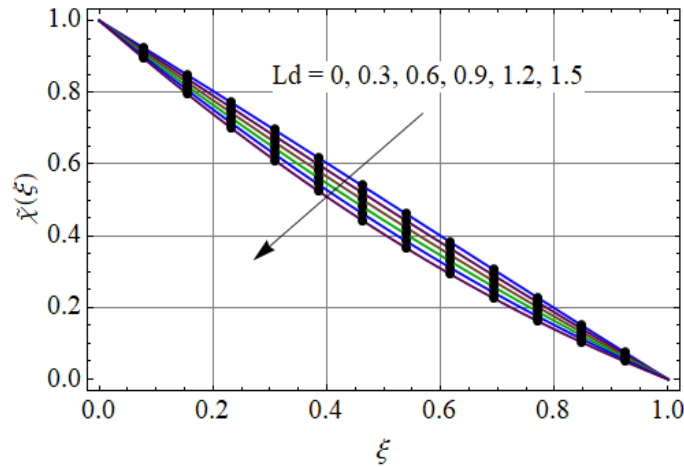


Fig. 7.14: Ld variation for $\tilde{\chi}(\xi)$.

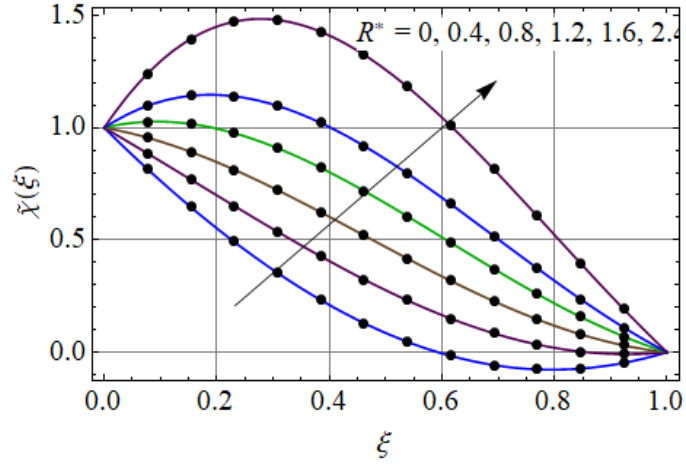


Fig. 7.15: R^* variation for $\tilde{\chi}(\xi)$.

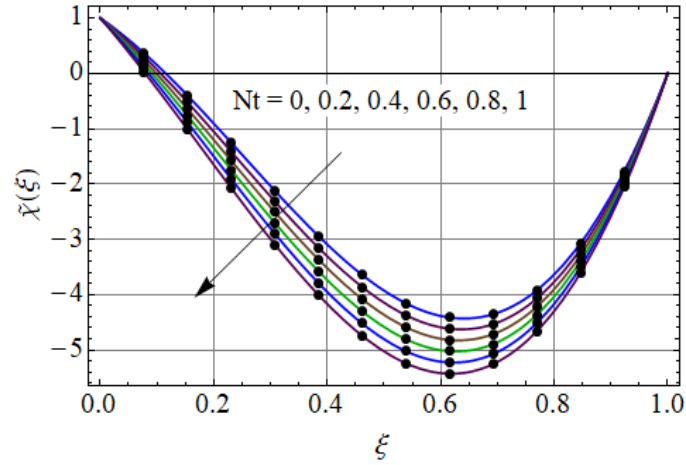


Fig. 7.16: Nt variation for $\tilde{\chi}(\xi)$.

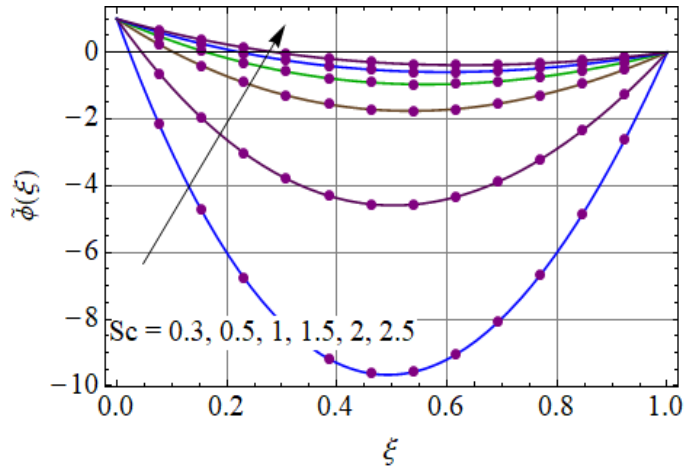


Fig. 7.17: Sc variation for $\tilde{\phi}(\xi)$.

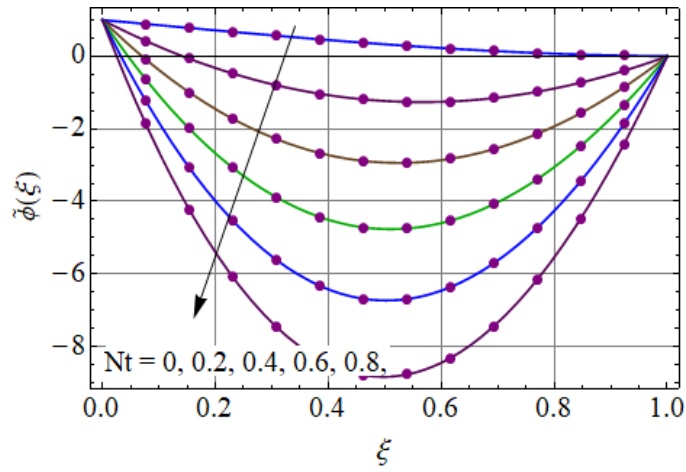


Fig. 7.18: Nt variation for $\tilde{\phi}(\xi)$.

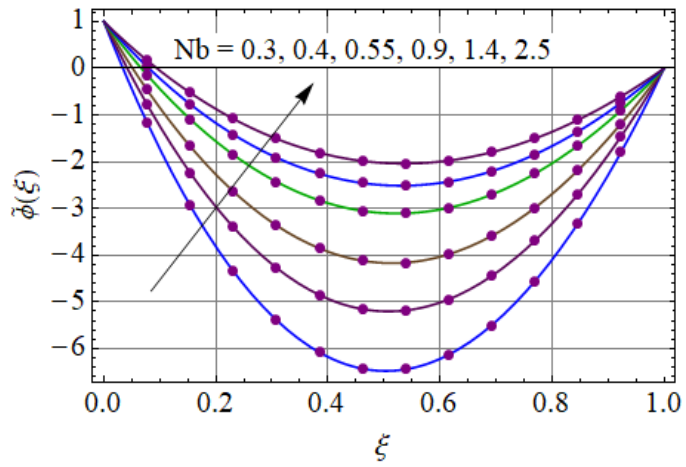


Fig. 7.19: Nb variation for $\tilde{\phi}(\xi)$.

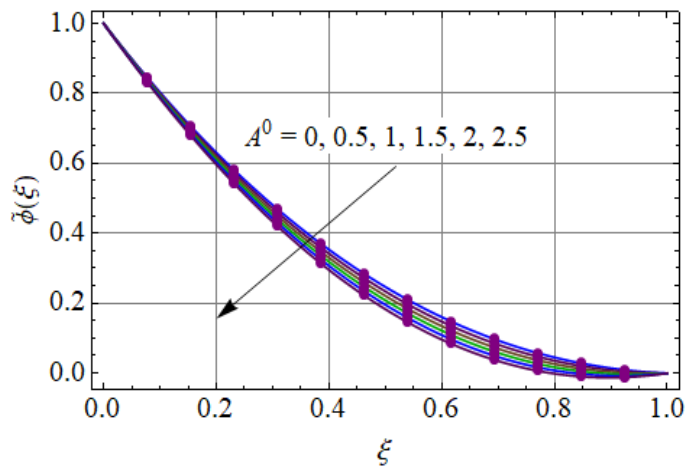


Fig. 7.20: A^0 variation for $\tilde{\phi}(\xi)$.

7.5.3 Entropy generation

Impacts of involved parameters on $(N_G(\xi))$ and (Be) are examined in Figs. (7.21-7.36). Opposite effects of magnetic parameter M are observed for $(N_G(\xi))$ and (Be) in Figs. 7.21 and 7.22. For larger M the entropy generation is sensitive for an enhancement (see Fig. 7.21). Physically for larger (M) the relation between magnetic fields and fluid strengthens dissipative energy to thermal diffusion. Also for larger M the resistance increases which causes more heat transfer rate and as a result $N_G(\xi)$ increases. Behavior of M for Bejan number is highlighted in Fig. 7.22. Here Be is decreased via M . We conclude from it that liquid friction irreversibility dominates over heat and mass transfer irreversibilities. Figs. 7.23 and 7.24 are portrayed to show the influence of Re on $N_G(\xi)$ and Be . Both $(N_G(\xi))$ and (Be) are reduced for higher Re . Retarding force increases for more Re which resists the liquid flow and so entropy generation decreases. Further Bejan number Be also reduces for higher Re (see Fig. 7.24). Friction between fluid is more than heat transfer for larger Re . That is why Be reduces. Figs. 7.25 and 7.26 show that for more temperature difference α_1 the entropy generation and Bejan number are enhanced. For higher α_1 the temperature of fluid enhances which increases the heat transfer rate and consequently $N_G(\xi)$ increases (see Fig. 7.25). Since α_1 is the dimensionless temperature difference parameter which increases the heat transfer contribution so Be increases (see Fig. 7.26). Similar behavior of $N_G(\xi)$ and Be is remarked for larger dimensionless concentration difference parameter α_2 (see Figs. 7.27 and 7.28). Impact of diffusion coefficient parameter L on $N_G(\xi)$ and Be is sketched in Figs. 7.29 and 7.30. For higher L the $N_G(\xi)$ and Be are enhanced. Effect of Brinkman number Br on $N_G(\xi)$ and Be is displayed in Figs. 7.31 and 7.32. For higher Br entropy generation enhances while opposite impact is examined for Be . Brinkman number measures the relative importance of production of heat through transportation of heat production by molecular conduction and viscous dissipation. Meaningful heat generation occurs between the layers of fluid particles which is responsible for an increase in entropy generation $N_G(\xi)$ (see Fig. 7.31). For larger Br the contribution of viscous dissipation and Joule heating is more than heat and mass transfer irreversibilities (see Fig. 7.32). Impact of thermal slip parameter γ_3 on $N_G(\xi)$ and Be is depicted in Figs. 7.33 and 7.34. Both $(N_G(\xi))$ and (Be) against γ_3 are reduced. Figs. 7.35 and 7.36 elucidate the influence of thermophoresis parameter Nt on

$(N_G(\xi))$ and (Be) . Clearly both $(N_G(\xi))$ and (Be) are decreased versus for higher Nt .

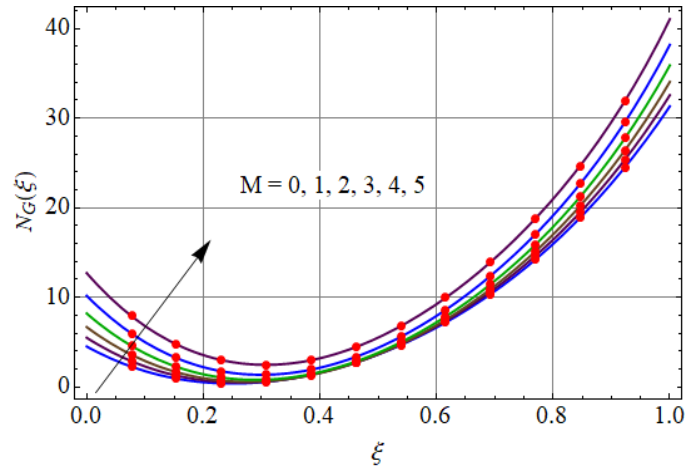


Fig. 7.21: $N_G(\xi)$ against M .

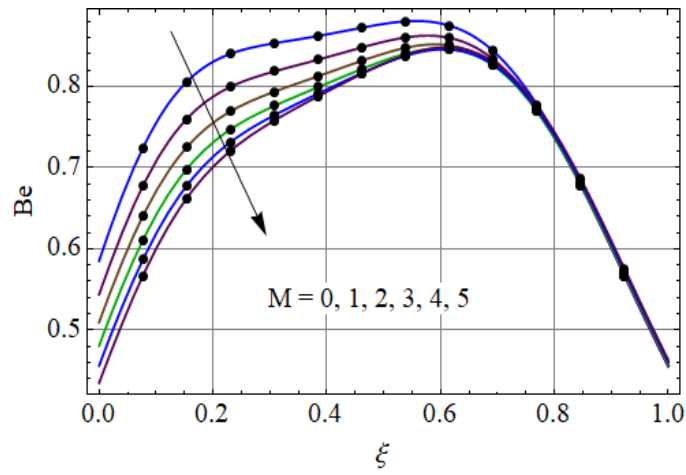


Fig. 7.22: Be against M .

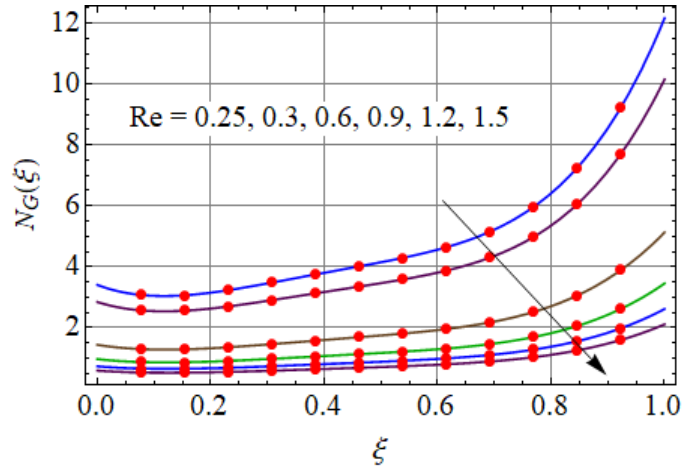


Fig. 7.23: $N_G(\xi)$ against Re.

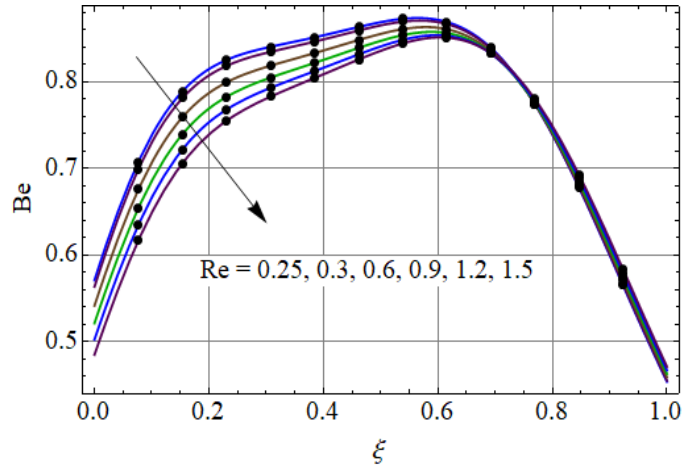


Fig. 7.24: Be against Re.

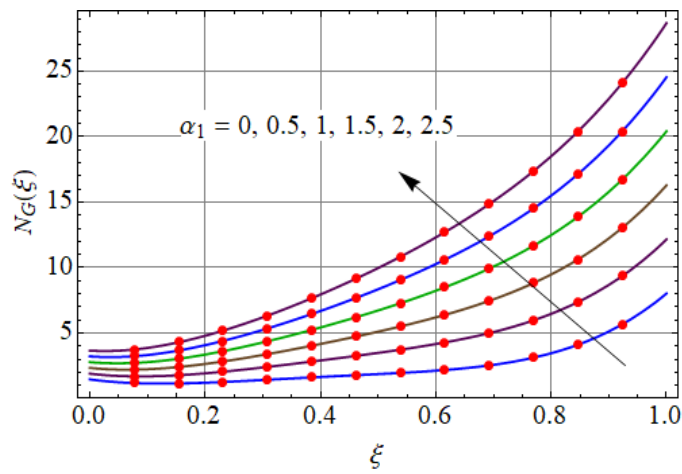


Fig. 7.25: α_1 variation for $N_G(\xi)$.

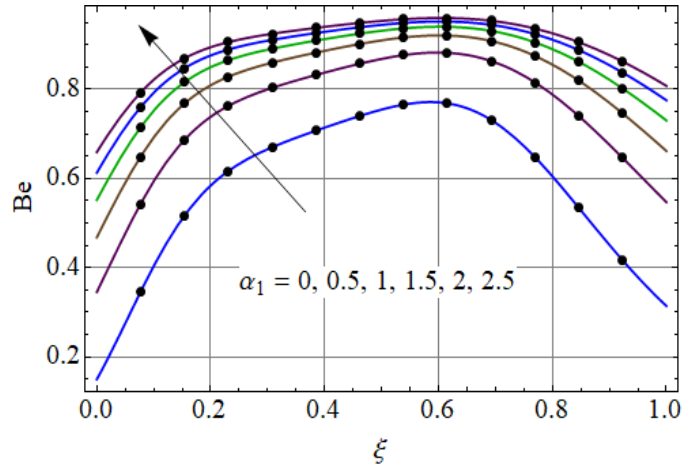


Fig. 7.26: α_1 variation for Be .

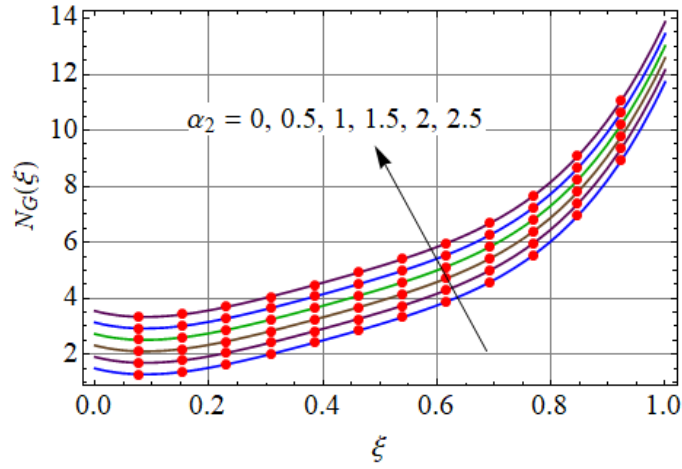


Fig. 7.27: α_2 variation for $N_G(\xi)$.

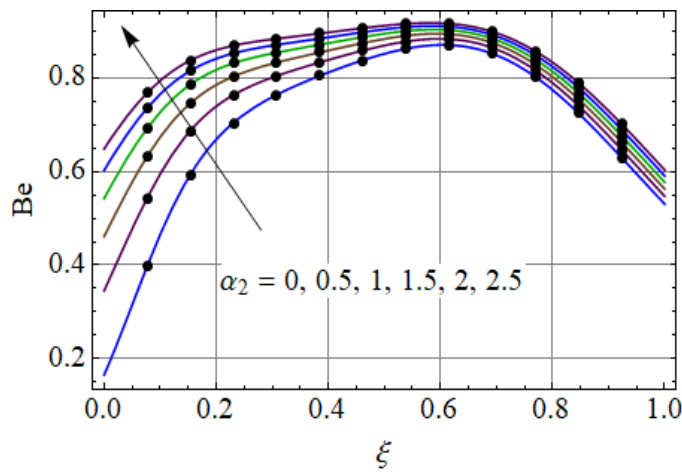


Fig. 7.28: Be against α_2 .

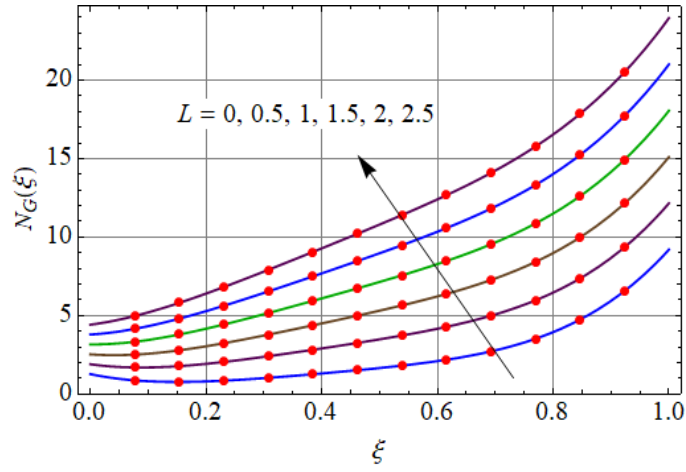


Fig. 7.29: $N_G(\xi)$ against L .

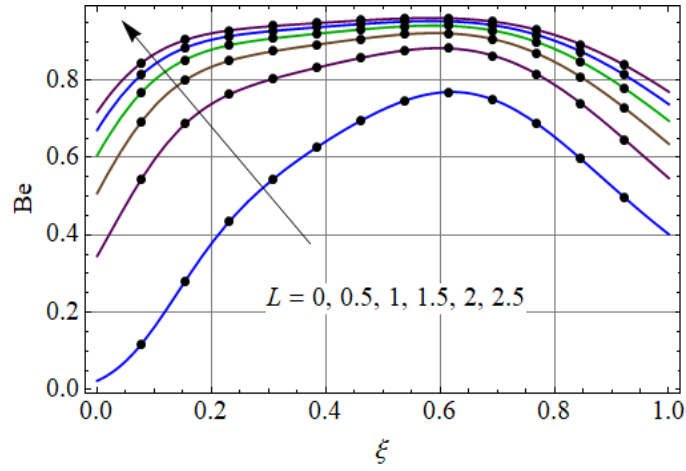


Fig. 7.30: Be against L .

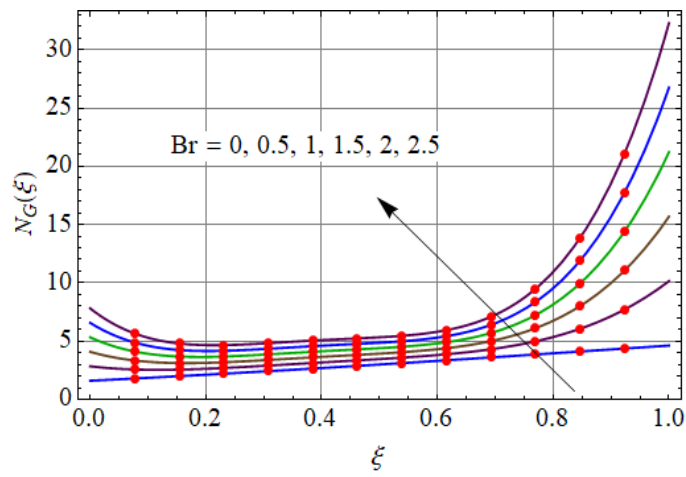


Fig. 7.31: $N_G(\xi)$ against Br .

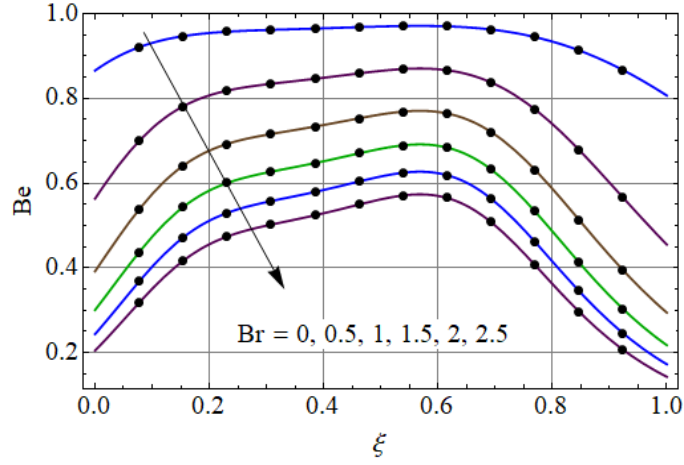


Fig. 7.32: Be against Br .

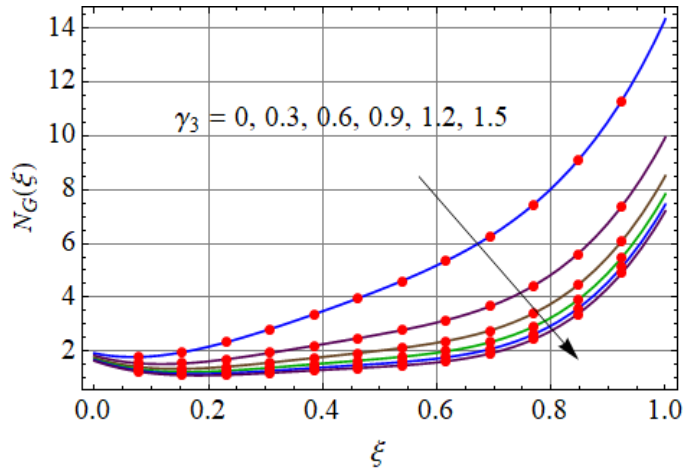


Fig. 7.33: γ_3 variation for $N_G(\xi)$.

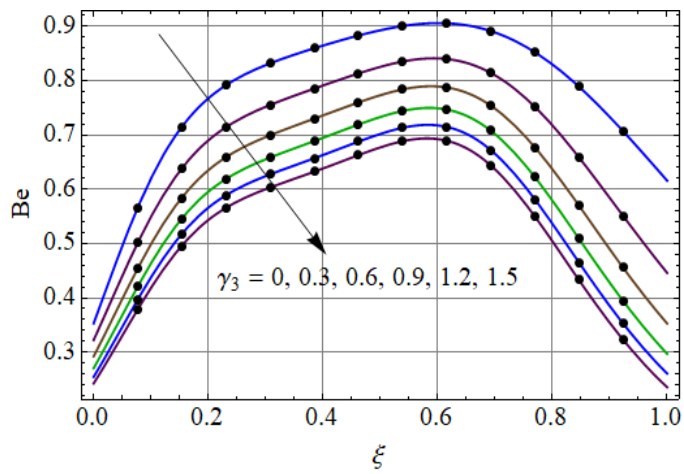


Fig. 7.34: Be against γ_3 .

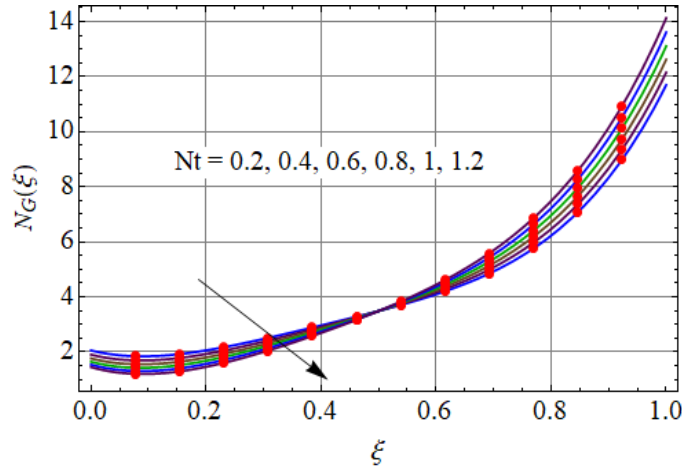


Fig. 7.35: $N_G(\xi)$ against Nt .

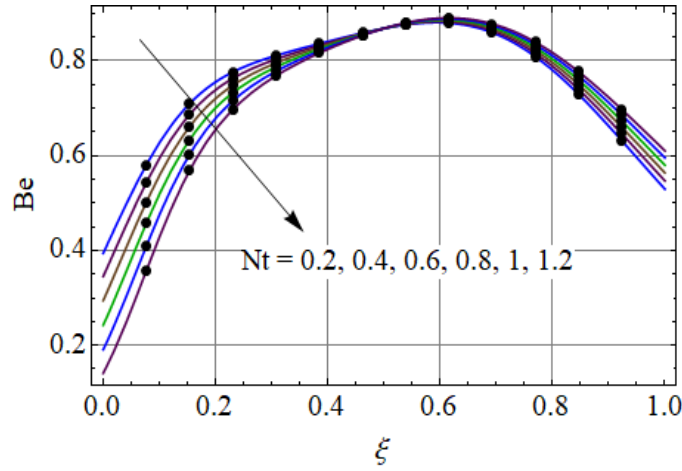


Fig. 7.36: Nt variation for Be .

7.5.4 Skin friction

Behaviors of skin friction coefficient for slip parameter γ_1 , Reynolds number Re and magnetic parameter M are shown in Table 7.2. Results show that surface drag force at lower and upper disks reduces for larger γ_1 . For higher Reynolds number Re the surface drag force increases at lower and upper disks. Opposite behaviors are observed at both lower and upper disks for larger M .

Table 7.2: Analysis of (C_{f0}, C_{f1}) when $Re = 0.3$, $M = 0.5$, $Pr = 1$, $A_1 = 0.4$, $A_2 = 0.9$, $\Omega = 0.3$, $\gamma_1 = 0.5$, $\gamma_2 = 0.7$, $\gamma_3 = 0.9$, $Ec = 0.4$, $Nt = 0.1$, $Nb = 0.4$, $Sc = 1$, $Nd = 0.2$, $Ld = 0.4$, $A = 0.1$, $Q = 0.4$, $k = 0.3$.

γ_1	Re	M	C_{f0}	C_{f1}
0.5	0.3	0.5	0.79415	1.2575
0.6			0.70231	1.1093
0.7			0.63536	0.99463
0.5	0.4		0.79856	1.2574
	0.5		0.80303	1.2576
	0.3	0.6	0.79782	1.2563
		0.7	0.80147	1.2552
		0.8	0.80511	1.2542

7.5.5 Nusselt number

Impacts of Eckert number Ec , heat source Q and thermophoresis Nt on Nusselt numbers of lower and upper disk are displayed in Table 7.3. Magnitude of Nusselt number decreases for Ec , Q and Nt at lower disk. However opposite behaviors are observed for all these parameters at upper disk.

Table 7.3: Analysis of (Nu_{x0}, Nu_{x1}) when $Re = 0.3$, $M = 0.5$, $Pr = 1$, $A_1 = 0.4$, $A_2 = 0.9$, $\Omega = 0.3$, $\gamma_1 = 0.5$, $\gamma_2 = 0.7$, $\gamma_3 = 0.9$, $Ec = 0.7$, $Nt = 0.1$, $Nb = 0.4$, $Sc = 1$, $Nd = 0.2$, $Ld = 0.4$, $A = 0.1$, $Q = 0.4$, $k = 0.3$.

Ec	Q	Nt	Nu_{x0}	Nu_{x1}
0.4	0.4	0.1	0.10126	0.61712
0.5			0.097256	0.62102
0.6			0.093253	0.62493
0.4	0.5		0.045504	0.67379
	0.6		-0.019176	0.73993
	0.4	0.2	0.075502	0.64750
		0.3	0.046172	0.68285

7.5.6 Sherwood number

Table 7.4 displays the physical importance of Sherwood numbers (Sh_{x0}, Sh_{x1}) for higher Schmidt number, thermophoresis, Brownian motion and Reynolds number. For larger values of Sc the

Sherwood number reduces at lower disk while opposite impact is found at upper disk. Rate of mass transfer is more for higher Nt while mass transfer reduces at upper disk. Sherwood number diminishes for larger Nb and Re at lower disk while at upper disk the opposite behavior is found.

Table 7.4: Analysis of (Sh_{x0}, Sh_{x1}) when $M = 0.5$, $Pr = 1$, $A_1 = 0.4$, $A_2 = 0.9$, $\Omega = 0.3$, $\gamma_1 = 0.5$, $\gamma_2 = 0.7$, $\gamma_3 = 0.9$, $Ec = 0.7$, $Nt = 0.1$, $Nb = 0.4$, $Sc = 1$, $Nd = 0.2$, $Ld = 0.4$, $A = 0.1$, $Q = 0.4$, $k = 0.3$.

Sc	Nt	Nb	Re	Sh_{x0}	Sh_{x1}
1	0.1	0.4	0.3	1.0562	0.94638
1.1				1.0555	0.94782
1.2				1.0548	0.94926
1	0.2			1.1301	0.86278
	0.3			1.2165	0.75716
	0.1	0.5		1.0461	0.95492
		0.6		1.0393	0.96053
		0.4	0.4	1.0554	0.94901
			0.5	1.0544	0.95168

7.6 Conclusions

Flow between two rotating disks with slip, chemical reaction and Joule heating is examined. Main findings are as follows:

- For larger values of velocity slip parameter γ_1 , the radial and axial velocities reduce but temperature enhances via γ_3 .
- Temperature is enhanced for Nt , Nb , Q and Ec .
- Solutal and nanoparticle concentration reduce for larger Sc .
- Solutal concentration reduces for larger Sc and Ld .
- Nt and Nb have opposite impacts for concentration.

- $N_G(\xi)$ enhances for larger L , Nt and Br .
- Surface drag force is decreasing function of γ_1 .
- Sherwood number reduces for Nb and Re .

Chapter 8

Nonlinear radiative flow by rotating disks with entropy generation and Soret and Dufour effects

Abstract: A computational study is presented for nonlinear radiative flow between two impermeable stretchable rotating disks. Thermo-diffusion and diffusion-thermo effects are also implemented. Further nonlinear radiative heat flux, chemical reaction, dissipation and heat source/sink are considered. Thermodynamics second law is used for the investigation of entropy generation and Bejan number. Total entropy generation is inspected for various flow variables. Von-Karman transformations are implemented to develop nonlinear ordinary differential systems. Resulting systems are tackled by semi computational/analytical technique namely homotopy analysis technique. Particular consideration is given to the convergence procedure. The impacts of different variables like magnetic interaction, porosity, thermal diffusion, Prandtl number, diffusion thermo, radiation, heat source, Schmidt number and chemical reaction on fluid velocity, concentration, temperature, volumetric entropy generation rate and Bejan number are analyzed. Velocity, temperature and concentration gradients at the disk surface are calculated numerically and discussed through Tables. Velocity reduces for both Hartmann number and porosity. Hartmann number and radiation parameter enhance the entropy generation and Bejan number.

8.1 Formulation

Here we consider the incompressible steady flow of viscous fluid between two stretchable rotating disks. Our target is analyze the entropy generation in the flow with thermo-diffusion and diffusion-thermo effects. Flow is generated due to stretching of two rotating disks. Lower disk with stretching rate a_1 is placed at $z = 0$.and angular velocity Ω_1 while upper disk situated at $z = h$ stretching rate a_2 and rotational velocity Ω_2 . Liquid fills the porous space. Porous medium has permeability K^* . In z -direction the magnetic field is applied with strength B_0 (see Fig. 8.1). Additionally heat transfer analysis is subject to nonlinear radiative flux, heat source/sink and Joule heating. Chemical reaction effect is also taken in consideration. The problem under consideration are

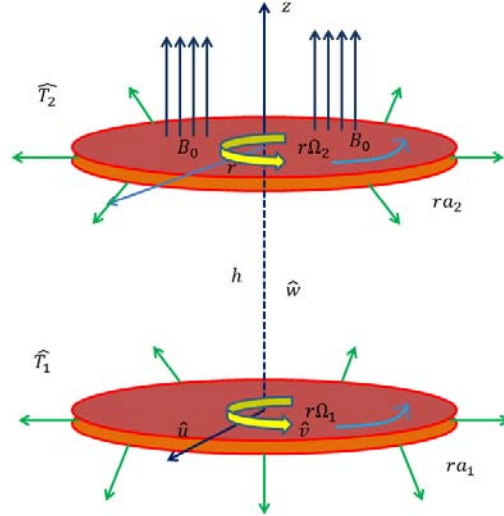


Fig. 8.1: Flow geometry.

$$\frac{\partial \hat{u}}{\partial r} + \frac{\hat{u}}{r} + \frac{\partial \hat{w}}{\partial z} = 0, \quad (8.1)$$

$$\hat{u} \frac{\partial \hat{u}}{\partial r} + \hat{w} \frac{\partial \hat{u}}{\partial z} - \frac{\hat{v}^2}{r} + \frac{1}{\rho} \frac{\partial \hat{p}}{\partial r} = \nu \left(\frac{\partial^2 \hat{u}}{\partial z^2} - \frac{\hat{u}}{r^2} + \frac{\partial^2 \hat{u}}{\partial r^2} + \frac{1}{r} \frac{\partial \hat{u}}{\partial r} \right) - \frac{\sigma}{\rho} B_0^2 \hat{u} - \frac{\nu}{K^*} \hat{u}, \quad (8.2)$$

$$\hat{u} \frac{\partial \hat{v}}{\partial r} + \hat{w} \frac{\partial \hat{v}}{\partial z} + \frac{\hat{v} \hat{u}}{r} = \nu \left(\frac{\partial^2 \hat{v}}{\partial z^2} - \frac{\hat{v}}{r^2} + \frac{\partial^2 \hat{v}}{\partial r^2} + \frac{1}{r} \frac{\partial \hat{v}}{\partial r} \right) - \frac{\sigma}{\rho} B_0^2 \hat{v} - \frac{\nu}{K^*} \hat{v}, \quad (8.3)$$

$$\hat{u} \frac{\partial \hat{w}}{\partial r} + \hat{w} \frac{\partial \hat{w}}{\partial z} + \frac{1}{\rho} \frac{\partial \hat{p}}{\partial z} = \nu \left(\frac{\partial^2 \hat{w}}{\partial z^2} + \frac{\partial^2 \hat{w}}{\partial r^2} + \frac{1}{r} \frac{\partial \hat{w}}{\partial r} \right) - \frac{\nu}{K^*} \hat{w}, \quad (8.4)$$

$$\left. \begin{aligned} \left(\hat{u} \frac{\partial \hat{T}}{\partial r} + \hat{w} \frac{\partial \hat{T}}{\partial z} \right) &= \frac{k}{\rho c_p} \left(\frac{1}{r} \frac{\partial \hat{T}}{\partial r} + \frac{\partial^2 \hat{T}}{\partial r^2} + \frac{\partial^2 \hat{T}}{\partial z^2} \right) + \frac{\sigma}{\rho c_p} B_0^2 (\hat{u}^2 + \hat{v}^2) \\ &+ \frac{DK_T}{C_s c_p} \left(\frac{1}{r} \frac{\partial \hat{C}}{\partial r} + \frac{\partial^2 \hat{C}}{\partial r^2} + \frac{\partial^2 \hat{C}}{\partial z^2} \right) - \frac{1}{\rho c_p} \nabla \cdot q_r + \frac{Q_0}{\rho c_p} (\hat{T} - \hat{T}_2), \end{aligned} \right\} \quad (8.5)$$

$$\left. \begin{aligned} \hat{u} \frac{\partial \hat{C}}{\partial r} + \hat{w} \frac{\partial \hat{C}}{\partial z} &= D \left(\frac{\partial^2 \hat{C}}{\partial z^2} + \frac{\partial^2 \hat{C}}{\partial r^2} + \frac{1}{r} \frac{\partial \hat{C}}{\partial r} \right) \\ &+ \frac{DK_T}{T_m} \left(\frac{1}{r} \frac{\partial \hat{T}}{\partial r} + \frac{\partial^2 \hat{T}}{\partial r^2} + \frac{\partial^2 \hat{T}}{\partial z^2} \right) - K (\hat{C} - \hat{C}_2), \end{aligned} \right\} \quad (8.6)$$

with

$$\left. \begin{aligned} \hat{u} = r a_1, \quad \hat{v} = r \Omega_1, \quad \hat{w} = W_0, \quad \hat{T} = \hat{T}_1, \quad \hat{C} = \hat{C}_1 \quad \text{at } z = 0, \\ \hat{u} = r a_2, \quad \hat{v} = r \Omega_2, \quad \hat{p} = 0, \quad \hat{T} = \hat{T}_2, \quad \hat{C} = \hat{C}_2 \quad \text{at } z = h, \end{aligned} \right\} \quad (8.7)$$

and radiative heat flux q_r is defined as follows:

$$q_r = -\frac{16\sigma^*}{3k^*} \hat{T}^3 \frac{\partial \hat{T}}{\partial z}, \quad (8.8)$$

We consider the transformations [2, 4, 5]:

$$\hat{u} = r \Omega_1 \tilde{f}'(\xi), \quad \hat{v} = r \Omega_1 \tilde{g}(\xi), \quad \hat{w} = -2h \Omega_1 \tilde{f}(\xi), \quad \tilde{\theta} = \frac{\hat{T} - \hat{T}_2}{\hat{T}_1 - \hat{T}_2}, \quad \hat{p} = \rho_f \Omega_1 \nu_f \left(P(\xi) + \frac{1}{2} \frac{r^2}{h^2} \epsilon \right), \quad \xi = \frac{z}{h}, \quad (8.9)$$

After employing transformations to Eqs. (8.2–8.7) the dimensionless forms of equations become

$$\tilde{f}''' + \text{Re} \left(2\tilde{f}\tilde{f}'' - \tilde{f}'^2 + \tilde{g}^2 - M\tilde{f}' - \beta^* \tilde{f}' \right) - \epsilon = 0, \quad (8.10)$$

$$\tilde{g}'' + \text{Re} \left(2\tilde{f}\tilde{g}' - 2\tilde{f}'\tilde{g} - M\tilde{g} - \beta^* \tilde{g} \right) = 0, \quad (8.11)$$

$$P' = -4 \text{Re} \tilde{f}\tilde{f}' - 2\tilde{f}'' + \beta^* \tilde{f}, \quad (8.12)$$

$$\begin{aligned} \frac{1}{\text{Pr}} \frac{1}{\text{Re}} \tilde{\theta}'' + 2\tilde{f}\tilde{\theta}' + \text{MEC}(\tilde{f}'^2 + \tilde{g}^2) + \frac{R}{\text{Pr}} (\tilde{\theta}(\theta_w - 1) + 1)^2 [3(\theta_w - 1)\tilde{\theta}'^2 + (\tilde{\theta}(\theta_w - 1) + 1)\tilde{\theta}''] \\ + \frac{Du}{\text{Re}} \tilde{\phi}'' + Q^* \tilde{\theta} = 0, \end{aligned} \quad (8.13)$$

$$\frac{1}{Sc} \frac{1}{\text{Re}} \tilde{\phi}'' + \frac{Sr}{\text{Re}} \tilde{\theta}'' + 2\tilde{f}\tilde{\phi}' - R^* \tilde{\phi} = 0, \quad (8.14)$$

$$\begin{aligned}
\tilde{f}(0) &= W_s, \tilde{f}(1) = 0, \tilde{f}'(0) = A_1, \tilde{f}'(1) = A_2, \tilde{g}(0) = 1, \\
\tilde{g}(1) &= \Omega, \tilde{\theta}(0) = 1, \tilde{\theta}(1) = 0, \tilde{\phi}(0) = 1, \tilde{\phi}(1) = 0, P(1) = 0,
\end{aligned} \tag{8.15}$$

$$\begin{aligned}
M &= \frac{\sigma B_0^2}{\rho \Omega_1}, \beta = \frac{\nu}{K^* \Omega_1}, \text{Pr} = \frac{\rho c_p \nu}{k}, R = \frac{16 \sigma^* \hat{T}_2^3}{3 k k^*}, \theta_w = \frac{\hat{T}_1}{\hat{T}_2}, Ec = \frac{r^2 \Omega_1^2}{c_p (\hat{T}_1 - \hat{T}_2)}, \\
Du &= \frac{DK_T (\hat{C}_1 - \hat{C}_2)}{C_s c_p (\hat{T}_1 - \hat{T}_2) \nu}, Sr = \frac{D (\hat{T}_1 - \hat{T}_2) K_T}{T_m \nu (\hat{C}_1 - \hat{C}_2)}, Q^* = \frac{Q_0}{\rho c_p \Omega_1}, Sc = \frac{\nu}{D}, R^* = \frac{K}{\Omega_1}, \\
W_s &= \frac{W_0}{\sqrt{\Omega_1 \nu}}, A_1 = \frac{a_1}{\Omega_1}, A_2 = \frac{a_2}{\Omega_1}, \Omega = \frac{\Omega_2}{\Omega_1}.
\end{aligned} \tag{8.16}$$

We remove ϵ from Eq. (8.17) by differentiating it with respect to ξ and obtain

$$\tilde{f}^{iv} + \text{Re} \left(2\tilde{f}\tilde{f}''' + 2\tilde{g}\tilde{g}' - M\tilde{f}'' - \beta^* \tilde{f}'' \right) = 0. \tag{8.17}$$

8.1.1 Physical quantities

Surface drag forces for upper C_{f1} and lower disk C_{f0} in dimensional form are

$$\left. \begin{aligned} C_{f0} &= \frac{\tau_w|_{z=0}}{\rho(r\Omega_1)^2}, \\ C_{f1} &= \frac{\tau_w|_{z=h}}{\rho(r\Omega_1)^2}, \end{aligned} \right\} \tag{8.18}$$

where total shear stress τ_w is

$$\tau_w = \sqrt{\tau_{zr}^2 + \tau_{z\theta}^2}. \tag{8.19}$$

$$\tau_{zr} = \mu \left. \frac{\partial \hat{u}}{\partial z} \right|_{z=0} = \frac{\mu r \Omega_1 \tilde{f}''(0)}{h}, \quad \tau_{z\theta} = \mu \left. \frac{\partial \hat{v}}{\partial z} \right|_{z=h} = \frac{\mu r \Omega_1 \tilde{g}'(0)}{h}. \tag{8.19}$$

Dimensionless forms become

$$\left. \begin{aligned} C_{f0} &= \frac{\tau_w|_{z=0}}{\rho(r\Omega_1)^2} = \frac{1}{\text{Re}_r} [(\tilde{f}''(0))^2 + (\tilde{g}'(0))^2]^{1/2}, \\ C_{f1} &= \frac{\tau_w|_{z=h}}{\rho(r\Omega_1)^2} = \frac{1}{\text{Re}_r} [(\tilde{f}''(1))^2 + (\tilde{g}'(1))^2]^{1/2}, \end{aligned} \right\} \tag{8.20}$$

where $\text{Re}_r = \frac{r\Omega_1 h}{\nu}$ is Reynolds number.

Heat transfer rates are defined by

$$Nu_{x0} = \frac{hq_w}{k(\hat{T}_1 - \hat{T}_2)} \Big|_{z=0}, \quad Nu_{x1} = \frac{hq_w}{k(\hat{T}_1 - \hat{T}_2)} \Big|_{z=h}. \quad (8.21)$$

where wall heat flux q_w is

$$\left. \begin{aligned} q_w|_{z=0} &= -k \frac{\partial \hat{T}}{\partial z} + q_r \Big|_{z=0}, \\ q_w|_{z=h} &= -k \frac{\partial \hat{T}}{\partial z} + q_r \Big|_{z=h}, \end{aligned} \right\} \quad (8.22)$$

Nusselt numbers can be written as follows:

$$Nu_{x0} = - (1 + R\theta_w^3) \tilde{\theta}'(0), \quad Nu_{x1} = - (1 + R\theta_w^3) \tilde{\theta}'(1). \quad (8.23)$$

Sherwood number for lower and upper disks are

$$\left. \begin{aligned} Sh_{r0} &= \frac{hh_m}{D(\hat{C}_1 - \hat{C}_2)} \Big|_{z=0}, \\ Sh_{r1} &= \frac{hh_m}{D(\hat{C}_1 - \hat{C}_2)} \Big|_{z=h}, \end{aligned} \right\} \quad (8.24)$$

with

$$h_m = -D \frac{\partial \hat{C}}{\partial z} \Big|_{z=0}, \quad h_m = -D \frac{\partial \hat{C}}{\partial z} \Big|_{z=h}, \quad (8.25)$$

In dimensionless form the Sherwood numbers become

$$\left. \begin{aligned} (\text{Re})^{-0.5} Sh_{r0} &= -\tilde{\phi}'(0), \\ (\text{Re})^{-0.5} Sh_{r1} &= -\tilde{\phi}'(1). \end{aligned} \right\} \quad (8.26)$$

8.2 Solutions technique

We have

$$\tilde{f}_0(\xi) = W_s + A_1\xi - 2A_1\xi^2 - A_2\xi^2 - 3W_s\xi^2 + A_1\xi^3 + A_2\xi^3 + 2W_s\xi^3, \quad (8.27)$$

$$\tilde{g}_0(\xi) = 1 + (\Omega - 1)\xi, \quad (8.28)$$

$$\tilde{\theta}_0(\xi) = 1 - \xi, \quad (8.29)$$

$$\tilde{\phi}_0(\xi) = 1 - \xi, \quad (8.30)$$

$$\mathcal{L}_{\tilde{f}} = \tilde{f}''''', \quad \mathcal{L}_{\tilde{g}} = \tilde{g}''', \quad \mathcal{L}_{\tilde{\theta}} = \tilde{\theta}''', \quad \mathcal{L}_{\tilde{\phi}} = \tilde{\phi}''', \quad (8.31)$$

with

$$\mathcal{L}_{\tilde{f}} [Z_1 + Z_2\xi + Z_3\xi^2 + Z_4\xi^3] = 0, \quad (8.32)$$

$$\mathcal{L}_{\tilde{g}} [Z_5 + Z_6\xi] = 0, \quad (8.33)$$

$$\mathcal{L}_{\tilde{\theta}} [Z_7 + Z_8\xi] = 0, \quad (8.34)$$

$$\mathcal{L}_{\tilde{\phi}} [Z_9 + Z_{10}\xi] = 0, \quad (8.35)$$

where $Z_i (i = 1 - 9)$ are the constants.

8.3 Entropy generation minimization

In this section mathematical modeling of entropy generation subject to nonlinear thermal radiation, viscous dissipation, Joule heating and thermo-diffusion and diffusion-thermo effects is presented. Dimensional entropy generation subject to magnetic field only

$$S_{gen}''' = \underbrace{\frac{k}{\hat{T}_m^2} \left(1 + \frac{16\sigma^* \hat{T}_2^3}{3kk^*} \right) [\nabla \hat{T}]^2}_{\text{heat transfer irreversibility}} + \underbrace{\frac{\mu}{\hat{T}_m} \Phi}_{\text{viscous dissipation irreversibility}} + \underbrace{\frac{1}{\hat{T}_m} [(J - QV) \cdot (V \times B)]}_{\text{Joule heating irreversibility}} + \underbrace{\frac{R_g D}{\hat{C}_m} [\nabla \hat{C}]^2 + \frac{R_g D}{\hat{T}_m} [\nabla \hat{T} \cdot \nabla \hat{C}]}_{\text{mass transfer irreversibility}} \quad (8.36)$$

Here \hat{T}_m and \hat{C}_m are mean temperature and concentration respectively and ∇T , ∇C , Φ and J are defined as

$$\nabla \hat{T} = \left[\frac{\partial \hat{T}}{\partial r} \hat{e}_r + \frac{1}{r} \frac{\partial \hat{T}}{\partial \vartheta} \hat{e}_\vartheta + \frac{\partial \hat{T}}{\partial z} \hat{e}_z \right], \quad (8.37)$$

$$\nabla \hat{C} = \left[\frac{\partial \hat{C}}{\partial r} \hat{e}_r + \frac{1}{r} \frac{\partial \hat{C}}{\partial \vartheta} \hat{e}_\vartheta + \frac{\partial \hat{C}}{\partial z} \hat{e}_z \right], \quad (8.38)$$

$$\Phi = 2 \left\{ \left[\left(\frac{\partial \hat{u}}{\partial r} \right)^2 + \frac{1}{r^2} (\hat{u})^2 + \left(\frac{\partial \hat{w}}{\partial z} \right)^2 \right] + \left[\frac{\partial \hat{v}}{\partial z} \right]^2 + \left[\frac{\partial \hat{w}}{\partial r} + \frac{\partial \hat{u}}{\partial z} \right]^2 + \left[r \frac{\partial}{\partial r} \left(\frac{\hat{v}}{r} \right) \right]^2 \right\}, \quad (8.39)$$

$$J = \sigma(V \times B), \quad (8.40)$$

After substituting Eqs. (8.37-8.40) in Eq. 8.36 we have

$$\left. \begin{aligned}
S'''_{gen} &= \frac{k}{\hat{T}_m^2} \left(1 + \frac{16\sigma^* \hat{T}_2^3}{3kk^*} \right) \left(\left(\frac{\partial \hat{T}}{\partial r} \right)^2 + \left(\frac{\partial \hat{T}}{\partial z} \right)^2 \right) + \frac{\sigma B_0^2}{\hat{T}_m} (\hat{u}^2 + \hat{v}^2) \\
&+ \frac{\mu}{\hat{T}_m} \left(2 \left[\left(\frac{\partial \hat{u}}{\partial r} \right)^2 + \frac{1}{r^2} (\hat{u})^2 + \left(\frac{\partial \hat{u}}{\partial z} \right)^2 \right] + \left[\frac{\partial \hat{v}}{\partial z} \right]^2 + \left[\frac{\partial \hat{w}}{\partial r} + \frac{\partial \hat{u}}{\partial z} \right]^2 + \left[r \frac{\partial}{\partial r} \left(\frac{\hat{v}}{r} \right) \right]^2 \right) \\
&+ \frac{R_g D}{\hat{C}_m} \left(\frac{1}{r} \frac{\partial \hat{C}}{\partial r} + \frac{\partial^2 \hat{C}}{\partial r^2} + \frac{\partial^2 \hat{C}}{\partial z^2} \right) + \frac{R_g D}{\hat{T}_m} \left(\frac{\partial \hat{T}}{\partial r} \frac{\partial \hat{C}}{\partial r} + \frac{\partial \hat{T}}{\partial z} \frac{\partial \hat{C}}{\partial z} \right),
\end{aligned} \right\} \quad (8.41)$$

Here first, second, third and fourth terms represent the heat transfer, viscous dissipation, Joule heating and mass transfer irreversibilities respectively. In dimensionless form the entropy expression becomes

$$\begin{aligned}
N_G &= \tilde{\theta}'^2 \alpha_1 \left[1 + R(\tilde{\theta}(\theta_w - 1) + 1)^3 \right] \frac{1}{\text{Re}} + \frac{Br}{\text{Re}} (12\tilde{f}'^2 + A^* \tilde{g}'^2 + A^* \tilde{f}''^2) \\
&+ MBrA^* (\tilde{f}'^2 + \tilde{g}'^2) + L \frac{\alpha_2}{\alpha_1} \tilde{\phi}'^2 + L\tilde{\theta}' \tilde{\phi}',
\end{aligned} \quad (8.42)$$

$$\begin{aligned}
\hat{T}_m &= \frac{\hat{T}_1 - \hat{T}_2}{2}, \quad \hat{\psi}_m = \frac{\hat{\psi}_1 - \hat{\psi}_2}{2}, \quad \alpha_1 = \frac{\hat{T}_1 - \hat{T}_2}{\hat{T}_m} = \frac{\Delta \hat{T}}{\hat{T}_m}, \quad \alpha_2 = \frac{\hat{\psi}_1 - \hat{\psi}_2}{\hat{\psi}_m} = \frac{\Delta \hat{\psi}}{\hat{\psi}_m}, \\
Br &= \frac{\mu \Omega_1^2 h^2}{k \Delta \hat{T}}, \quad N_G = \frac{\hat{T}_m S_{GV}}{k \Delta \hat{T} \Omega_1}, \quad A^* = \frac{r^2}{h^2}, \quad L = \frac{R_g D (\hat{C}_1 - \hat{C}_2)}{k}.
\end{aligned} \quad (8.43)$$

8.4 Convergence analysis

HAM provides us opportunity to tackle the nonlinear system of equations. We have $\hbar_{\tilde{f}}$, $\hbar_{\tilde{g}}$, $\hbar_{\tilde{\theta}}$ and $\hbar_{\tilde{\phi}}$ as convergence control parameters which help us to control the convergence region. We draw the \hbar -curves for $\tilde{f}''(0)$, $\tilde{g}'(0)$, $\tilde{\theta}'(0)$ and $\tilde{\phi}'(0)$ at 22nd order of approximations. Straight regions for auxiliary parameters are noted as $-1.1 \leq \hbar_{\tilde{f}} \leq -0.1$, $-1.3 \leq \hbar_{\tilde{g}} \leq -0.2$, $-1.0 \leq \hbar_{\tilde{\theta}} \leq -0.4$ and $-1.0 \leq \hbar_{\tilde{\phi}} \leq -0.4$. Solution converges for whole region of ξ ($0 \leq \xi \leq \infty$). Table 1 is constructed to show the numerical values of velocity, temperature and concentration for convergence. One can see that 23rd, 16th, 45th and 33rd iterations are enough for stable solutions of $\tilde{f}''(0)$, $\tilde{g}'(0)$, $\tilde{\theta}'(0)$ and $\tilde{\phi}'(0)$ respectively. We can calculate the residual errors for

$\tilde{f}, \tilde{g}, \tilde{\theta}$ and $\tilde{\phi}$ by using formulae:

$$\left. \begin{aligned} \Delta_{\tilde{f}} &= \int_0^1 [R_m^{\tilde{f}}(\xi, \tilde{h}_{\tilde{f}})]^2 d\xi, \\ \Delta_{\tilde{g}} &= \int_0^1 [R_m^{\tilde{g}}(\xi, \tilde{h}_{\tilde{g}})]^2 d\xi, \\ \Delta_{\tilde{\theta}} &= \int_0^1 [R_m^{\tilde{\theta}}(\xi, \tilde{h}_{\tilde{\theta}})]^2 d\xi, \\ \Delta_{\tilde{\phi}} &= \int_0^1 [R_m^{\tilde{\phi}}(\xi, \tilde{h}_{\tilde{\phi}})]^2 d\xi, \end{aligned} \right\} \quad (38)$$

In Figs. (8.2(a – d)) the \tilde{h} -curves for residual error of $\tilde{f}, \tilde{g}, \tilde{\theta}$ and $\tilde{\phi}$ are displayed for admissible ranges of \tilde{h} .

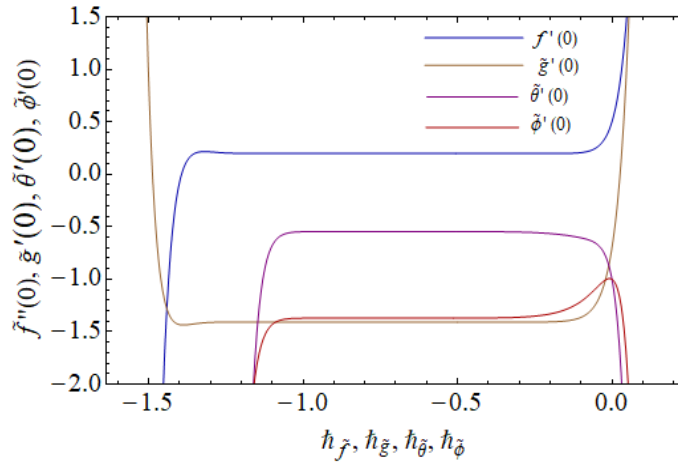


Fig. 8.2a: \tilde{h} -curves for $\tilde{f}''(0), \tilde{g}'(0), \tilde{\theta}'(0)$ and $\tilde{\phi}'(0)$.

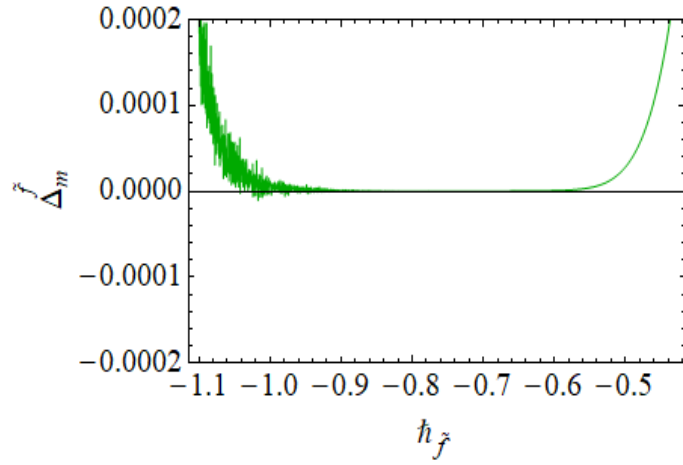


Fig. 8.2b: Residual error for \tilde{f} .

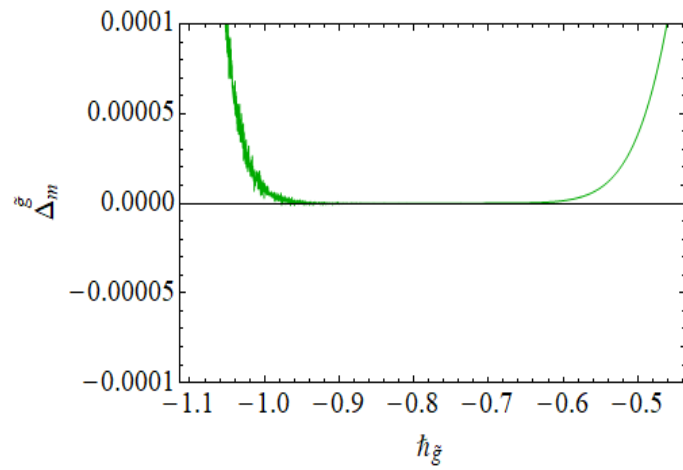


Fig. 8.2c: Residual error for \tilde{g} .

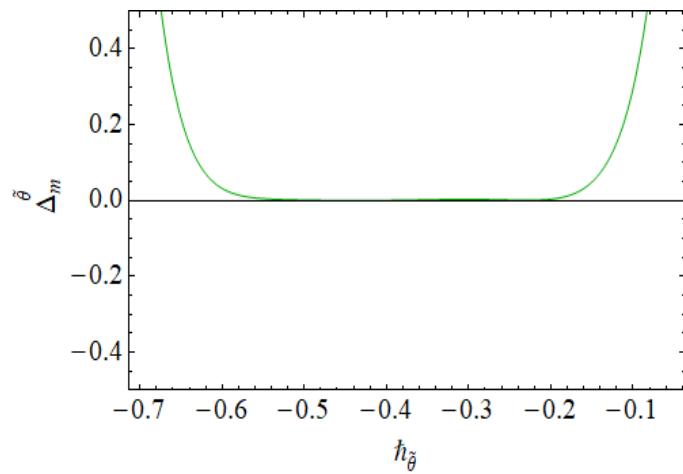


Fig. 8.2d: Residual error for $\tilde{\theta}$.

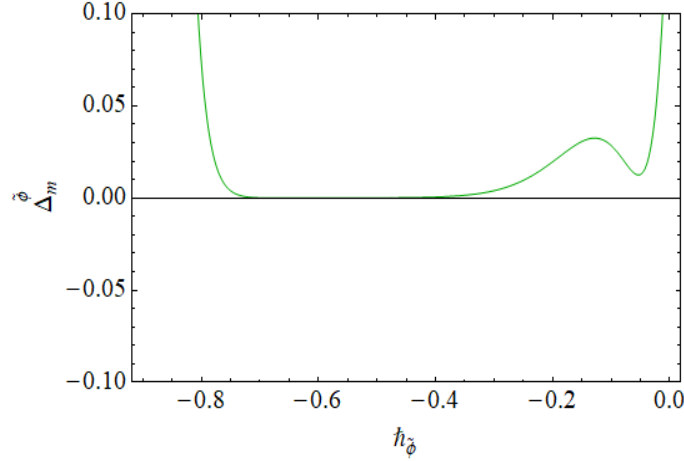


Fig. 8.2e: Residual error for $\tilde{\phi}$.

Table 8.1: Numerical values for convergence of series solution.

Order of approximation	$\tilde{f}'(0)$	$-\tilde{g}'(0)$	$-\tilde{\theta}'(0)$	$-\tilde{\phi}'(0)$
1	0.0616667	1.55333	0.169042	0.950000
16	0.197796	1.40890	0.505364	1.38873
21	0.197792	1.40890	0.501088	1.38763
23	0.197793	1.40890	0.501430	1.38768
33	0.197793	1.40890	0.501795	1.38775
45	0.197793	1.40890	0.501810	1.38775
50	0.197793	1.40890	0.501810	1.38775
60	0.197793	1.40890	0.501810	1.38775

8.5 Physical results

In this portion we discussed the impact of involved variables on the temperature, velocity, concentration, entropy generation, Bejan number, skin friction, Nusselt and Sherwood numbers through different graphs and tables.

8.5.1 Velocity components

Figs. (8.3 – 8.8) are sketched for influence of Hartmann number (M) and porosity parameter (β) on velocities profiles $(\tilde{f}, \tilde{f}', \tilde{g})$ for upper and lower disks. Behaviors of axial, radial and tangential velocities $(\tilde{f}, \tilde{f}', \tilde{g})$ at lower and upper disk against Hartmann number ($M =$

0, 0.5, 1, 1.5, 2) are shown in Figs. (8.3 – 8.5). Magnitude of $(\tilde{f}, \tilde{f}', \tilde{g})$ decline with increasing Hartmann number (M). Physically for magnetic variable the Lorentz force creates resistance between the fluid particles. Due to this resistance motion of the fluid particles slows down throughout the system. Figs. (8.6 – 8.7) portrayed the influence of permeability parameter (β^*) on velocities $(\tilde{f}, \tilde{f}', \tilde{g})$ at both disks. It is noted that velocities are decreasing functions of ($\beta^* = 0.1, 0.5, 0.9, 1.3, 1.7$). Actually for larger permeability parameter (β^*) resistance for fluid particles to flow increases due to porosity and consequently magnitude of $(\tilde{f}, \tilde{f}', \tilde{g})$ decreases.

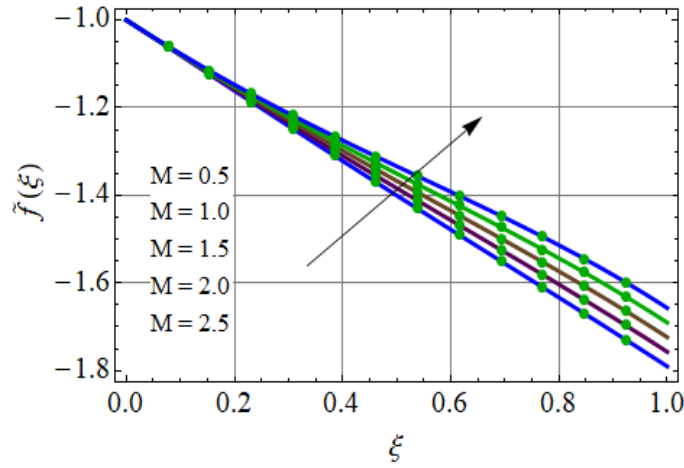


Fig. 8.3: Axial velocity via M .

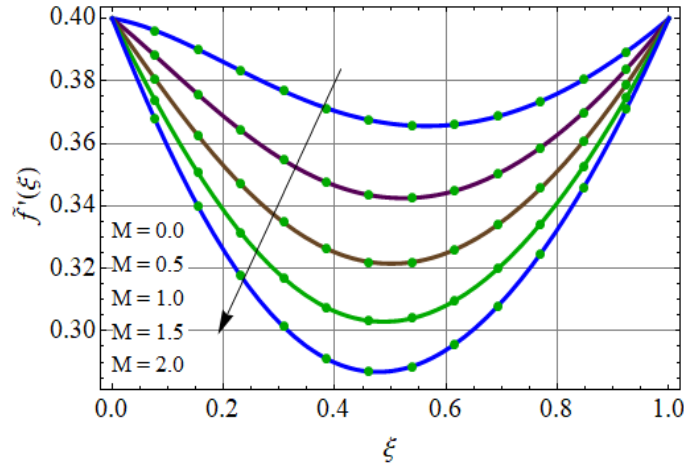


Fig. 8.4: Radial velocity via M .

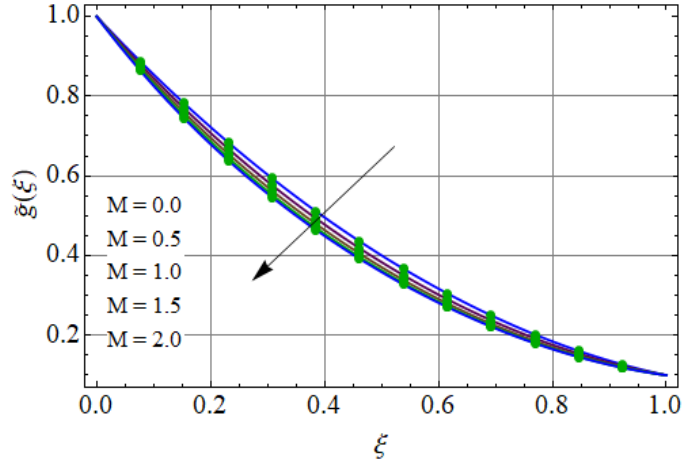


Fig. 8.5: Tangential velocity via M .

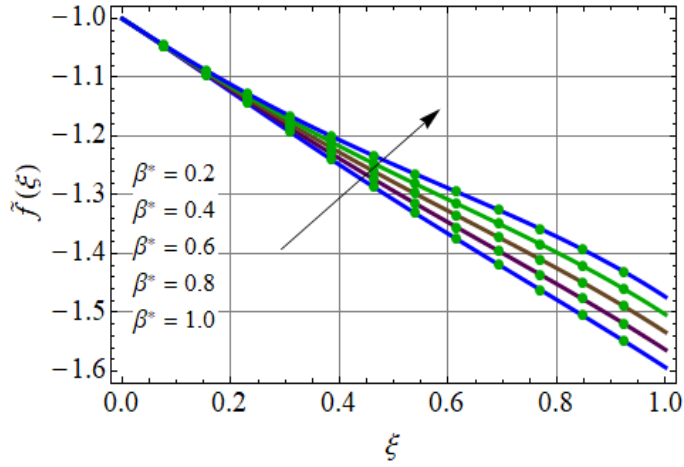


Fig. 8.6: Axial velocity via β^* .

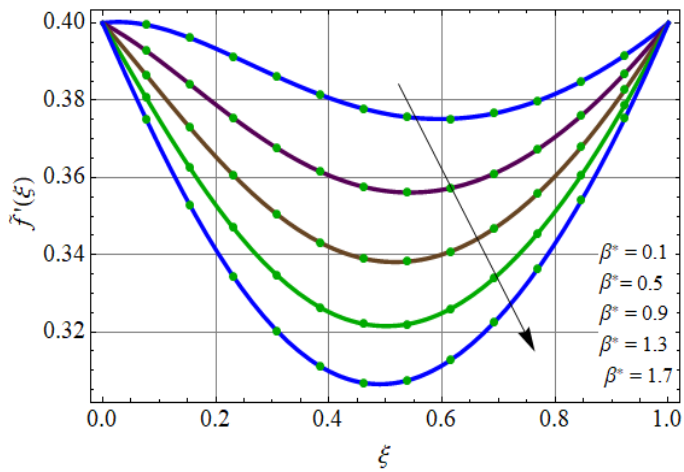


Fig. 8.7: Radial velocity via β^* .

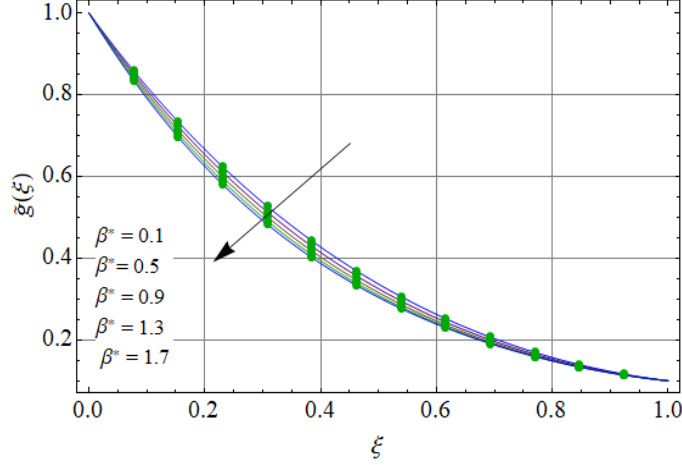


Fig. 8.8: Tangential velocity via β^* .

8.5.2 Temperature

Figs. (8.9 – 8.14) highlight the trend of $\left(\tilde{\theta}(\xi)\right)$ at both disks for radiation parameter, Prandtl number, Hartmann number, Eckert number, heat generation/absorption parameter, and Dufour number. Fig. 8.9 delineates the trend of temperature $\left(\tilde{\theta}(\xi)\right)$ against Pr. For rising estimations of Pr $\left(\tilde{\theta}(\xi)\right)$ shows decreasing trend. Since (Pr) is ratio of momentum diffusivity to thermal diffusivity therefore for larger (Pr) decrease in thermal diffusivity occurs which causes reduction in $\left(\tilde{\theta}(\xi)\right)$ (at both disks). Influence of R on $\left(\tilde{\theta}(\xi)\right)$ is revealed in Fig. 8.10. For increasing values of ($R = 0.5, 1, 1.5, 2.0, 2.5$) fluid temperature enhances. Due to higher values of (R) mean absorption coefficient decreases because it is in inverse relation with (R) so $\left(\tilde{\theta}(\xi)\right)$ increases. Fig. 8.11 reveals the impact of Hartmann number on thermal field. With increasing values of ($M = 0.5, 1, 1.5, 2, 2.5$) increment in Lorentz force is noticed which produces resistance between the liquid particles. This resistance produces more heat which is accountable for increase in $\left(\tilde{\theta}(\xi)\right)$. For higher estimation of Eckert number (Ec) behavior of temperature field at lower and upper disks is noticed in Fig. 8.12. Eckert number shows the relation between kinetic energy and enthalpy difference which is used to show the heat dissipation in the system. For larger ($Ec = 0.5, 1, 1.5, 2.0$) due to increase in kinetic energy the friction inside the fluid enhances which converts the mechanical energy to thermal energy. Therefore temperature is enhanced. Fig. 8.13 discloses impact of heat generation parameter (Q^*) on $\left(\tilde{\theta}(\xi)\right)$ at lower and upper disks. As we increase the values of ($Q^* = 0.3, 0.6, 0.9, 1.2, 1.5$) more heat generated in the sys-

tem and $\left(\tilde{\theta}(\xi)\right)$ enhances. Fig. 8.14 delineates impact of Dufour number (Du) on temperature distribution $\left(\tilde{\theta}(\xi)\right)$. For higher estimation of Dufour number ($Du = 0.4, 0.8, 1.2, 1.6, 2.0$) temperature of the fluid enhances. An increase in energy flux is noticed for larger Dufour number due to increase in concentration gradient which is responsible about temperature enhancement. On can see that temperature near the lower disk is more when compared with upper disk. Physically it is due to reason that temperature of lower disk is higher than upper disk i.e. $(\hat{T}_1 > \hat{T}_2)$.

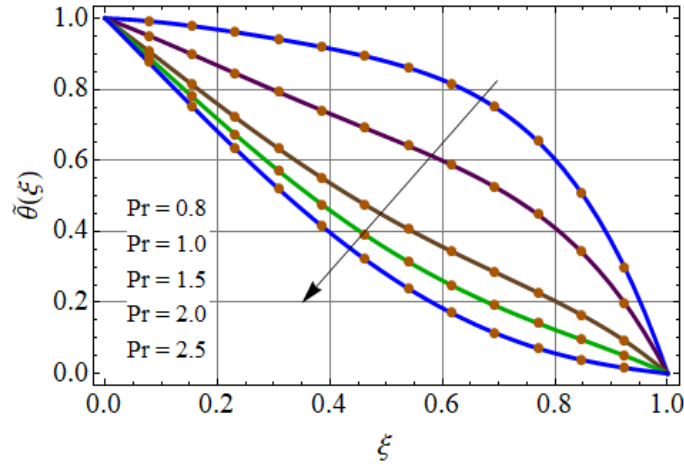


Fig. 8.9: Temperature via Pr .

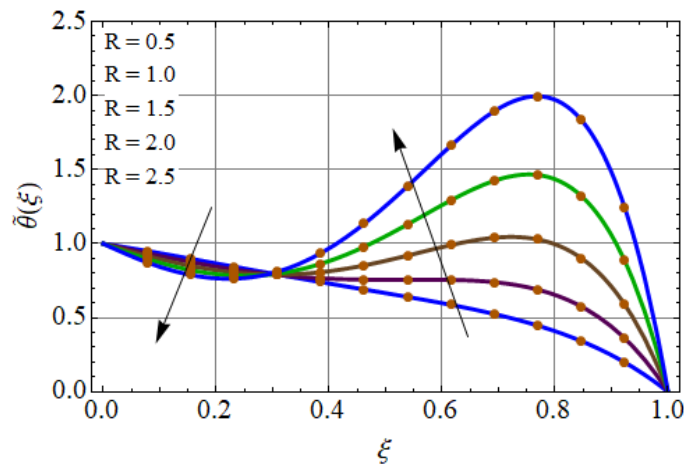


Fig. 8.10: Temperature via R .

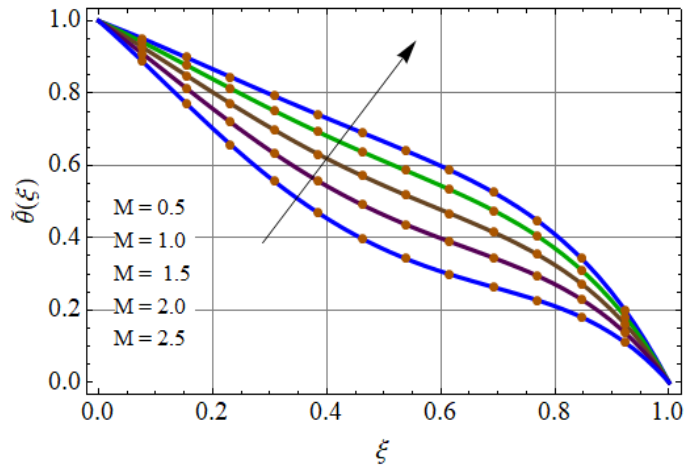


Fig. 8.11: Temperature via M .

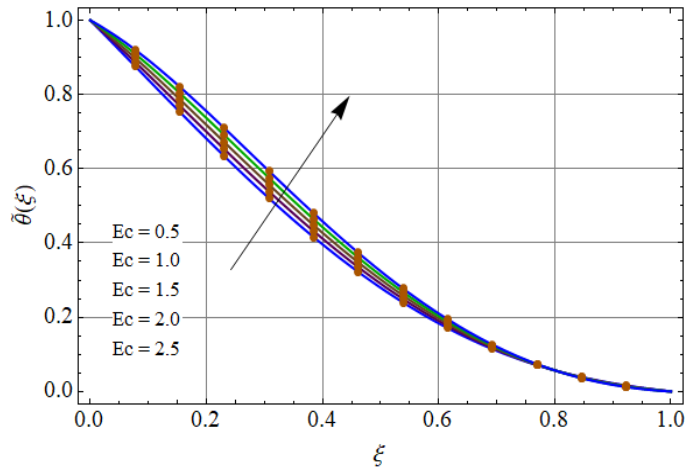


Fig. 8.12: Temperature via Ec .

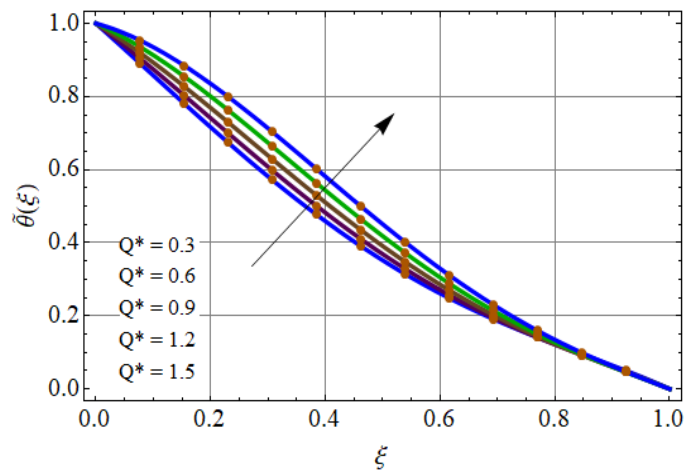


Fig. 8.13: Temperature via Q^* .

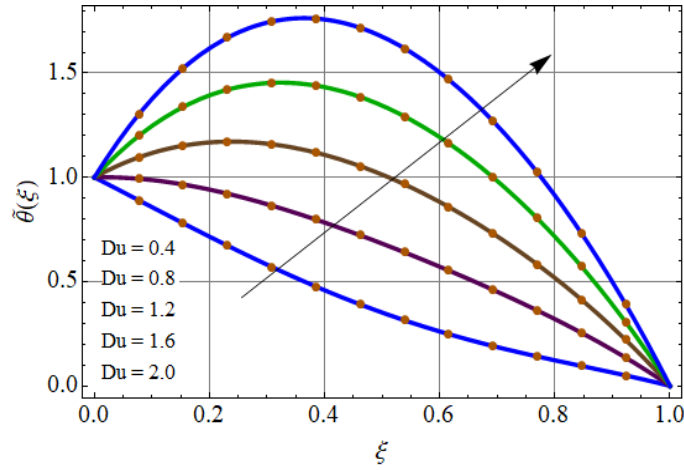


Fig. 8.14: Temperature via Du .

8.5.3 Concentration profile

Figs. (8.15–8.17) are portrayed to show the behavior of chemical reaction parameter (R^*), Soret number (Sr) and Schmidt number (Sc) on concentration ($\tilde{\phi}(\xi)$). Fig. 8.15 displays the outcome of Schmidt number on ($\tilde{\phi}(\xi)$). Concentration is decreased for higher ($Sc = 1.2, 1.5, 1.8, 2.1, 2.4$). Clearly mass diffusivity decays for higher Sc and this leads to reduction of concentration. ($\tilde{\phi}(\xi)$) via Soret number Sr is shown in Fig. 8.16. An enhancement in concentration and layer thickness is observed for higher ($Sr = 0.5, 1.0, 1.5, 2.0, 2.5$). Here higher convective flow for more temperature gradient occurs in view of larger (Sr). Fig. 8.17 displays the outcome of chemical reaction parameter (R^*) on concentration ($\tilde{\phi}(\xi)$). For rising values of (R^*) fluid concentration

$(\tilde{\phi}(\xi))$ enhances.

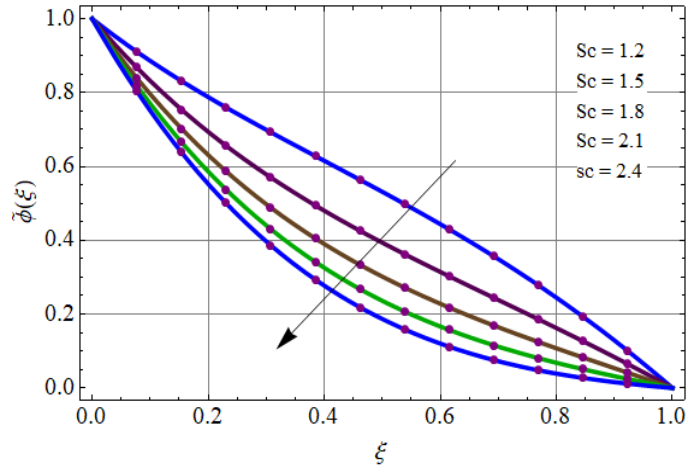


Fig. 8.15: Concentration profile via Sc .

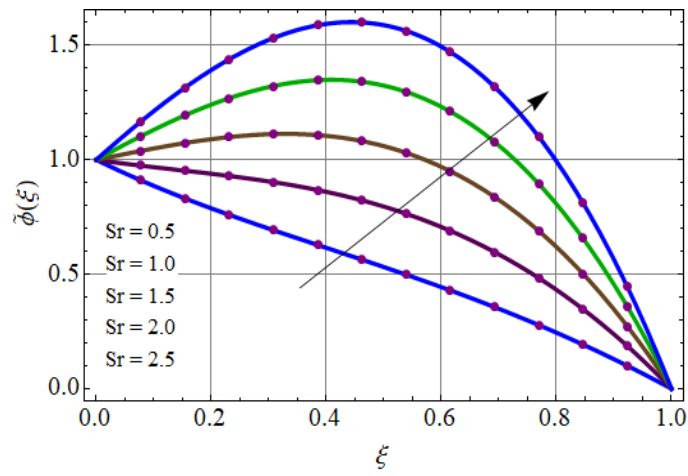


Fig. 8.16: Concentration via Sr .

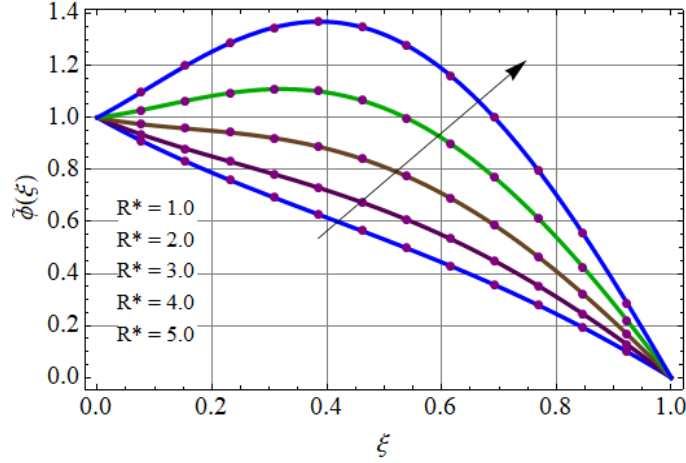


Fig. 8.17: Concentration via R^* .

8.5.4 Entropy generation

Figs. (8.18 – 8.27) show the trend of (N_G) and (Be) at lower and upper disks for variation of radiation parameter (R), Brinkman number (Br), temperature ratio parameter (θ_w) and diffusion parameter (L^*). Influence of Hartmann number (M) on (N_G) and (Be) is displayed in Figs. 8.18 and 8.19. It is noted that disorderedness in the flow system increases due to increase in Lorentz force (which is resistive force) for larger (M) that is why entropy of the fluid also enhances (see Fig. 8.18). Fig. 8.19 shows that for larger (M) the Bejan number enhances due to dominant heat and mass transfer effects. Figs. 8.20 and 8.21 show the influence of radiation parameter (R) on (N_G) and (Be) . For larger values of radiation parameter (R) entropy generation enhances (see Fig. 8.20). Physically for larger (R) increase in internal energy of the system is noticed and thus N_G enhances. For larger Be heat and mass transfer effects are more prominent than viscous effects. That is why (Be) enhances near both disks (see Fig. 8.21). Impact of (Br) on (N_G) and (Be) is elucidated in Figs. 8.22 and 8.23. For larger values of (Br) disorderedness of the system enhances (see Fig. 8.22) while opposite trend is noticed for Bejan number (Be) (see Fig. 8.23). Physically for larger (Br) the conduction rate is less by dissipation and thus (N_G) enhances. Figs. 8.24 and 8.25 are sketched to show the impact of temperature ratio parameter (θ_w) on (N_G) and (Be) . It is worth mentioning that for larger (θ_w) total entropy of the system increases near the lower and upper disks due to heated disks while between the disks (N_G) reduces (see Fig. 8.24). As we know that disks are heated

so for larger (θ_w) disorderedness near the disks is more and consequently entropy rate increases. For larger (θ_w) Bejan number (Be) also rises at both disks due to dominant heat transfer effects near the disks (see Fig. 8.25). Figs. 8.26 and 8.27 delineate the influence of L on (N_G) and (Be). It is noted that both entropy generation and Bejan number are increasing functions of diffusion parameter (L). For larger values of (L) diffusion rate of nanoparticles increases and thus total entropy of the system and Bejan number increase.

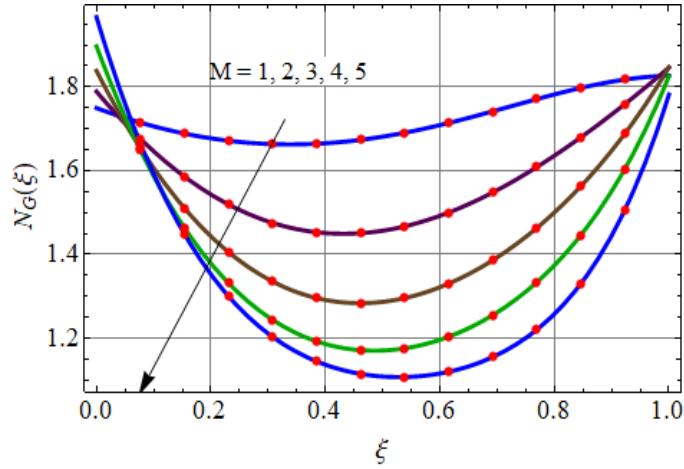


Fig. 8.18: Entropy generation via M .

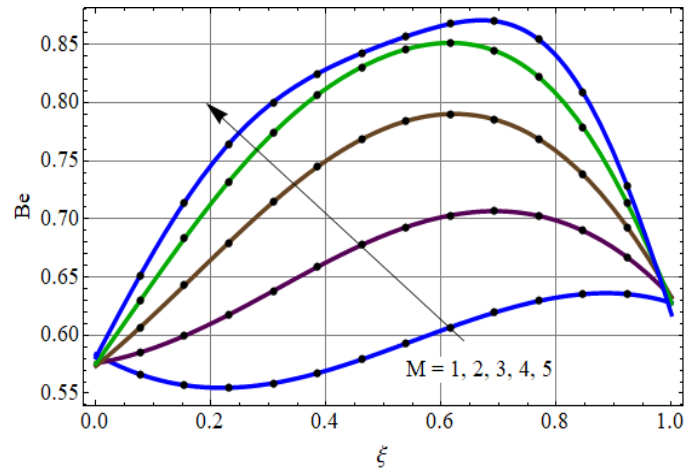


Fig. 8.19: Bejan number via M .

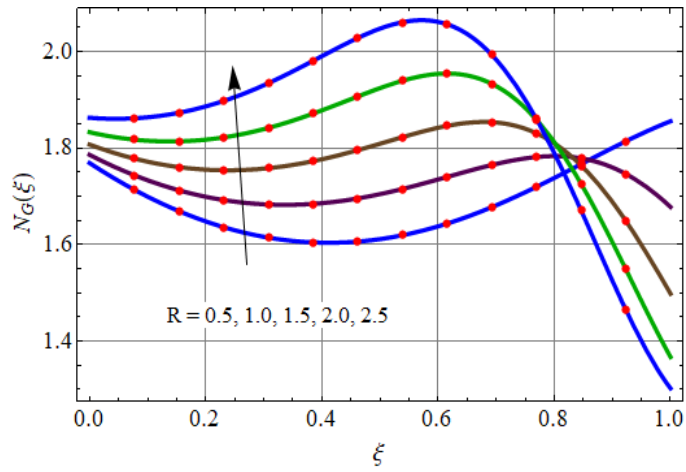


Fig. 8.20: Entropy generation via R .

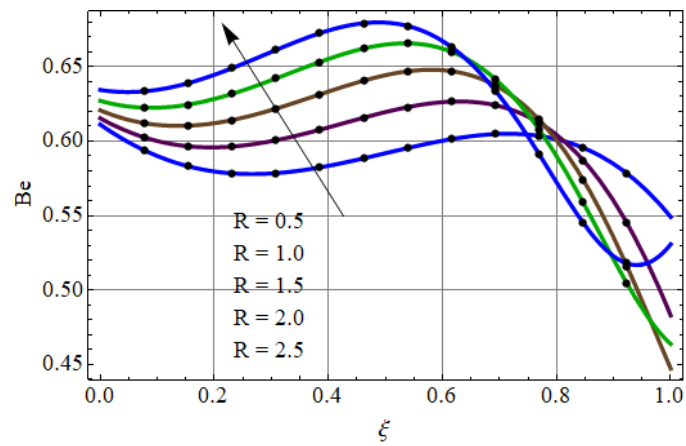


Fig. 8.21: Bejan number via R .

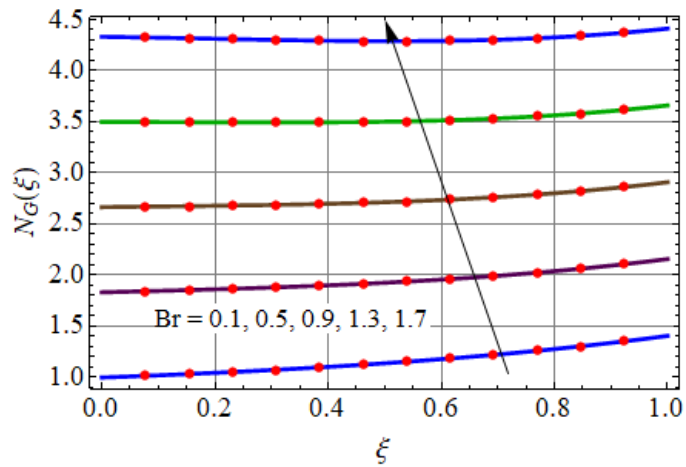


Fig. 8.22: Entropy generation via Br .

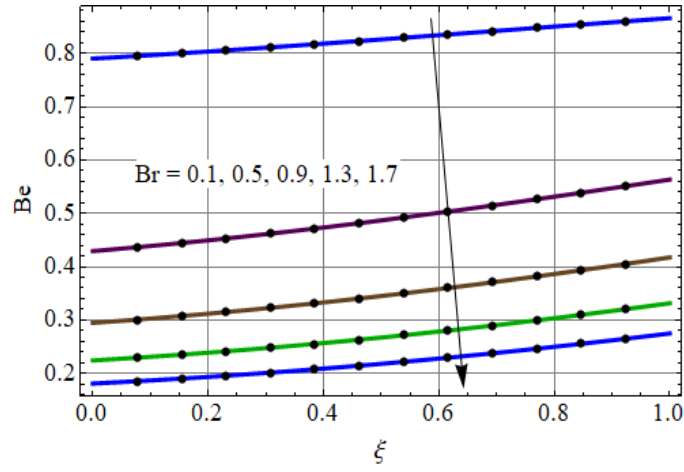


Fig. 8.23: Bejan number via Br .

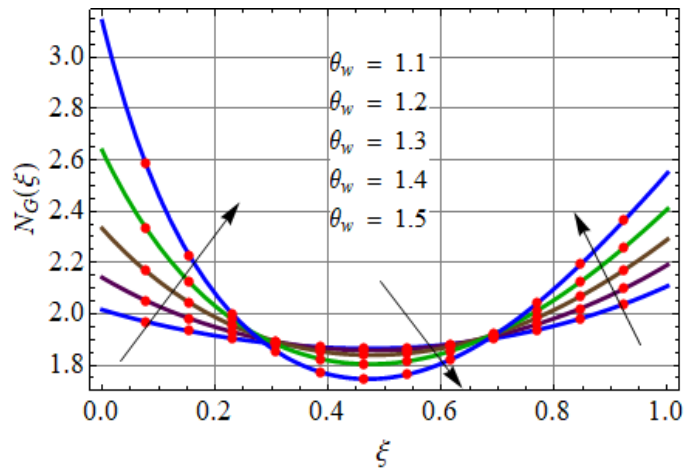


Fig. 8.24: Entropy generation via θ_w .

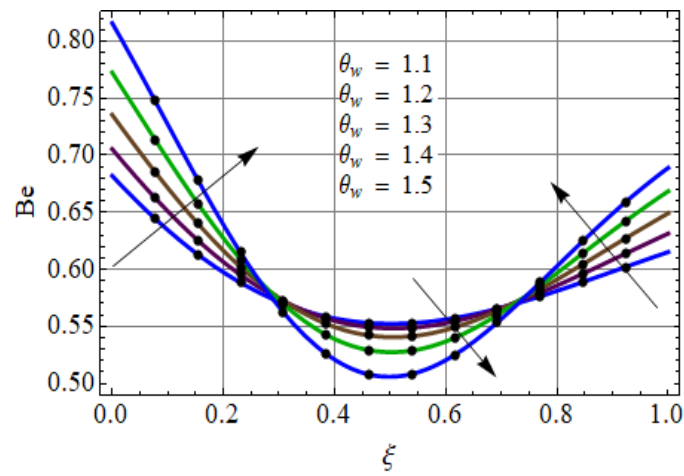


Fig. 8.25: Bejan number via θ_w .

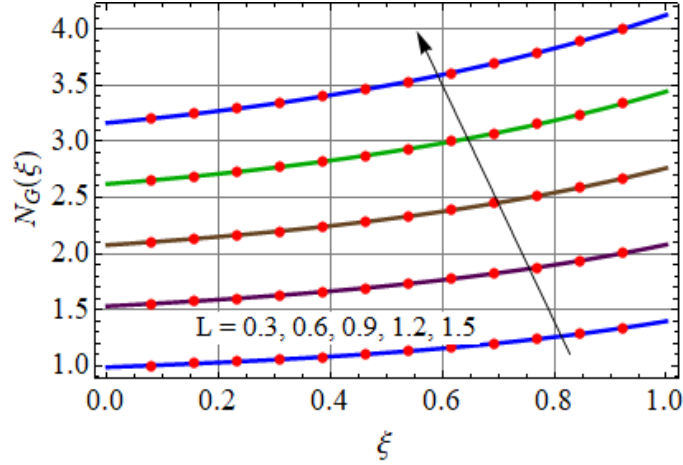


Fig. 8.26: Entropy generation via L .

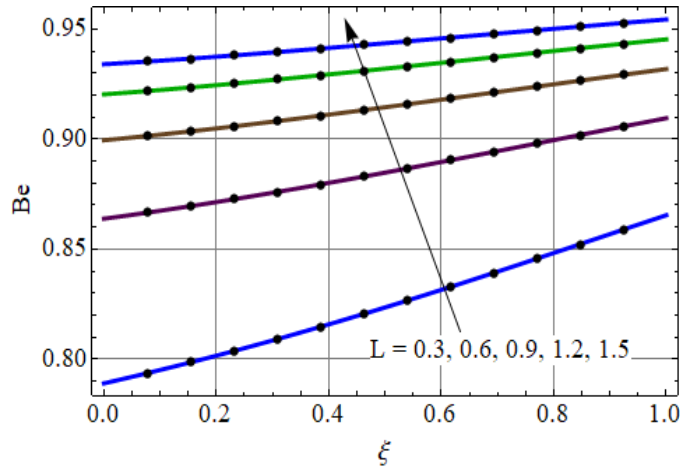


Fig. 8.27: Bejan number via L .

8.5.5 Physical quantities

Tables (8.2-8.4) are computed to analyze the effects of Hartmann number, permeability parameter, Eckert number, Prandtl number, Dufour number, temperature ratio parameter, Soret number and chemical reaction parameter on surface drag force (skin friction), heat transfer (Nusselt number) and mass transfer (Sherwood number) at lower and upper disks. Drag force at surface of lower and upper disk rises for larger (M) and (β) (see Table 8.2). Table 8.3 shows that rate of heat transfer decreases near the lower disk while opposite trend is witnessed at upper disk for higher (Ec), (Pr) and (Du). For larger (θ_w) the Nusselt number displays increasing effect at both disks. With rising (Sr) and (R^*), the mass transfer increases near the lower disk

while it diminishes near the upper disk (see Table 8.4).

Table 8.2: Skin frictions at lower and upper disks.

M	β	$C_{f0} \text{Re}_r^{-0.5}$	$C_{f1} \text{Re}_r^{-0.5}$
0.7	0.9	1.42272	1.05696
0.8		1.44408	1.08356
0.9		1.46568	1.11012
1.0		1.48748	1.13665
0.7	1.0	1.44408	1.08356
	1.1	1.46568	1.11012
	1.2	1.48748	1.13665

Table 8.3: Computational values of (Nu_{x0}, Nu_{x1}) at lower and upper disks.

Ec	Pr	Du	θ_w	Nu_{x0}	Nu_{x1}
0.5	1.0	0.5	1.5	1.17924	3.72640
0.6				1.15043	3.77438
0.7				1.12160	3.82236
0.5	1.1			1.10673	3.81243
	1.2			1.03229	3.90258
	1.0	0.6		1.13481	3.85760
		0.7		1.08795	4.00633
		0.5	1.55	1.23203	4.07194
			1.6	1.23852	4.45414

Table 8.4: Computational values of $(Sh_{x0} \text{Re}_r^{-0.5}, Sh_{x1} \text{Re}_r^{-0.5})$ at lower and upper disks.

Sr	R^*	$Sh_{x0} \text{Re}_r^{-0.5}$	$Sh_{x1} \text{Re}_r^{-0.5}$
0.5	0.5	1.38775	0.413537
0.6		1.45912	0.315432
0.7		1.53454	0.204621
0.5	0.6	1.43133	0.396412
	0.7	1.47417	0.379942
	0.8	1.51631	0.364102

8.6 Conclusions

Main results of present flow situation are as follows:

- Velocity profiles $(\tilde{f}, \tilde{f}', \tilde{g})$ at both disks are decreasing functions of (M) and (β^*) .
- Temperature distribution $(\tilde{\theta}(\xi))$ shows decreasing trend for larger (Pr) while reverse is remarked for (R) , (Ec) , (Q^*) and (Du) .
- Temperature $(\tilde{\theta}(\xi))$ is more near the lower disk than upper disk due to higher temperature i.e. $(T_1 > T_2)$.
- Soret number (Sr) and Schmidt number (Sc) have opposite behavior on concentration distribution $(\tilde{\phi}(\xi))$.
- For larger (Br) , (Rd) and (M) the entropy rate increases.
- Be decays for larger (Br) while opposite impact is noticed for (R) , (M) and (L) .
- N_G and Be is more near the disks while between the disks both quantities show decreasing trend for larger (θ_w) .
- Surface drag force is an increasing function of (β^*) and (M) at lower and upper disks.
- Heat transfer rate has opposite impact at lower and upper disks for larger (Ec) and (Pr) .

Chapter 9

Nonlinear radiated flow of Jeffrey fluid with heat source/sink and thermal stratification

Abstract: MHD nonlinear radiated flow of viscoelastic liquid (Jeffrey fluid) is considered in this chapter. The flow behavior is examined between stretchable surfaces of rotating disks. Electrically conducting liquid is considered. The modeling of energy equation is developed subject to nonlinear radiative heat flux and thermal stratification. Furthermore, homogeneous and heterogeneous reactions are considered. The nonlinear flow expressions are solved for series solutions via homotopy method. The characteristics of various parameters are examined and discussed graphically on the skin friction, velocity, Nusselt number, temperature and concentration. Our obtained outcomes remark that the velocity components are increased versus Deborah number. Velocity in axial direction is less near the lower disk surface for larger ratio of relaxation to retardation times constant. Temperature field is boosted against higher temperature ratio variable. Mass concentration shows contrast impact against Schmidt number and homogeneous reaction variable. Heat transfer rate (Nusselt number) and skin friction (drag force) enhances and decreases versus higher temperature ratio variable and ratio of relaxation to retardation times respectively.

9.1 Modeling

We examine flow of viscoelastic liquid by two stretchable rotating disks. Lower disk is at $z = 0$ upper disk is at distant h apart. Angular velocities of lower and upper disks are Ω_1 and Ω_2 respectively and a_1 and a_2 are their respective stretching rates. Temperatures at lower and upper disks are $T_1(r) = T_0 + A_s r$ and $T_2(r) = T_0 + B_s r$ (see Fig. 9.1).

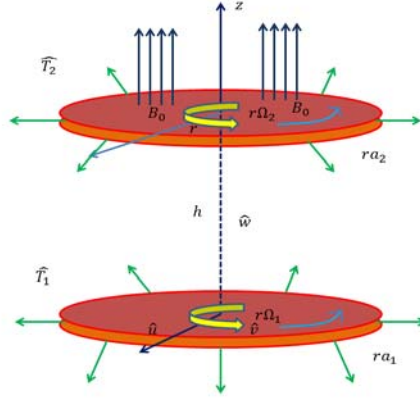
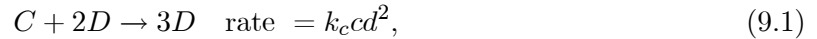


Fig. 9.1: Flow geometry.

Effects of nonlinear thermal radiation and heat source/sink are considered. Homogeneous-heterogeneous reactions are also taken into account. Homogeneous reaction for cubic auto-catalysis is



and on the surface of catalyst the first order isothermal reaction is



Here k_c and k_s are the rate constants and C and D are chemical species with concentrations c and d . We have used the cylindrical coordinates (r, ϑ, z) with velocity components $(\hat{u}, \hat{v}, \hat{w})$.

The relevant equations are

$$\frac{\partial \hat{u}}{\partial r} + \frac{\hat{u}}{r} + \frac{\partial \hat{w}}{\partial z} = 0, \quad (9.3)$$

$$\begin{aligned}
\hat{u} \frac{\partial \hat{u}}{\partial r} + \hat{w} \frac{\partial \hat{u}}{\partial z} - \frac{\hat{v}^2}{r} &= -\frac{\partial p}{\partial r} + \frac{\nu}{1 + \lambda_1^*} \left(\frac{\partial^2 \hat{u}}{\partial r^2} + \frac{1}{r} \frac{\partial \hat{u}}{\partial r} - \frac{\hat{u}}{r^2} + \frac{\partial^2 \hat{u}}{\partial z^2} \right) + \frac{\lambda_2^* \nu}{1 + \lambda_1^*} \left(2\hat{u} \frac{\partial^3 \hat{u}}{\partial r^3} + 2\hat{w} \frac{\partial^3 \hat{u}}{\partial r^2 \partial z} \right. \\
&+ 2\frac{\partial \hat{u}}{\partial r} \frac{\partial^2 \hat{u}}{\partial r^2} + 2\frac{\partial \hat{w}}{\partial r} \frac{\partial^2 \hat{u}}{\partial r \partial z} - \frac{2\hat{u}}{r^2} \frac{\partial \hat{u}}{\partial r} - \frac{2\hat{w}}{r^2} \frac{\partial \hat{u}}{\partial z} - \frac{2\hat{u}^2}{r^3} + \frac{\partial \hat{u}}{\partial z} \frac{\partial^2 \hat{w}}{\partial r^2} + \frac{\partial \hat{w}}{\partial z} \frac{\partial^2 \hat{w}}{\partial r \partial z} \\
&\left. + 2\hat{u} \frac{\partial^3 \hat{u}}{\partial r \partial z^2} + 2\hat{w} \frac{\partial^3 \hat{u}}{\partial z^3} + \frac{\partial \hat{u}}{\partial z} \frac{\partial^2 \hat{u}}{\partial r \partial z} + \frac{\partial \hat{w}}{\partial z} \frac{\partial^2 \hat{u}}{\partial z^2} \right) - \frac{\sigma}{\rho} B_0^2 \hat{u}, \quad (9.4)
\end{aligned}$$

$$\begin{aligned}
\hat{u} \frac{\partial \hat{v}}{\partial r} + \hat{w} \frac{\partial \hat{v}}{\partial z} + \frac{\hat{u} \hat{v}}{r} &= \frac{\nu}{1 + \lambda_1^*} \left(\frac{\partial^2 \hat{v}}{\partial r^2} + \frac{1}{r} \frac{\partial \hat{v}}{\partial r} - \frac{\hat{v}}{r^2} + \frac{\partial^2 \hat{v}}{\partial z^2} \right) + \frac{\lambda_2^* \nu}{1 + \lambda_1^*} \left(2\hat{u} \frac{\partial^3 \hat{v}}{\partial r^3} + 2\hat{w} \frac{\partial^3 \hat{v}}{\partial r^2 \partial z} \right. \\
&- \frac{\hat{w}}{r^2} \frac{\partial \hat{v}}{\partial z} + \frac{\partial \hat{u}}{\partial r} \frac{\partial^2 \hat{v}}{\partial r^2} + \frac{\partial \hat{w}}{\partial r} \frac{\partial^2 \hat{v}}{\partial r \partial z} - \frac{1}{r} \frac{\partial \hat{u}}{\partial r} \frac{\partial \hat{v}}{\partial r} + \frac{\hat{v}}{r^2} \frac{\partial \hat{u}}{\partial r} - \frac{2\hat{u} \hat{v}}{r^3} - \frac{1}{r} \frac{\partial \hat{w}}{\partial r} \frac{\partial \hat{v}}{\partial z} \\
&\left. + 2\hat{u} \frac{\partial^3 \hat{v}}{\partial r \partial z^2} + 2\hat{w} \frac{\partial^3 \hat{v}}{\partial z^3} + \frac{\partial \hat{u}}{\partial z} \frac{\partial^2 \hat{v}}{\partial r \partial z} + \frac{\partial \hat{w}}{\partial z} \frac{\partial^2 \hat{v}}{\partial z^2} \right) - \frac{\sigma}{\rho} B_0^2 \hat{v}, \quad (9.5)
\end{aligned}$$

$$\begin{aligned}
\hat{u} \frac{\partial \hat{w}}{\partial r} + \hat{w} \frac{\partial \hat{w}}{\partial z} &= -\frac{\partial p}{\partial z} + \frac{\nu}{1 + \lambda_1^*} \left(\frac{\partial^2 \hat{w}}{\partial r^2} + \frac{1}{r} \frac{\partial \hat{w}}{\partial r} + \frac{\partial^2 \hat{w}}{\partial z^2} \right) + \frac{\lambda_2^* \nu}{1 + \lambda_1^*} \left(\hat{u} \frac{\partial^3 \hat{w}}{\partial r^2 \partial z} + 2\hat{u} \frac{\partial^3 \hat{w}}{\partial r^3} \right. \\
&+ \hat{w} \frac{\partial^3 \hat{u}}{\partial r \partial z^2} + 2\hat{w} \frac{\partial^3 \hat{w}}{\partial r^2 \partial z} + \frac{\partial \hat{u}}{\partial r} \frac{\partial^2 \hat{u}}{\partial r \partial z} + \frac{\partial \hat{w}}{\partial r} \frac{\partial^2 \hat{u}}{\partial z^2} + \frac{\partial \hat{u}}{\partial r} \frac{\partial^2 \hat{w}}{\partial r^2} + \frac{\partial \hat{w}}{\partial r} \frac{\partial^2 \hat{w}}{\partial r \partial z} \\
&\left. + \frac{\hat{u}}{r} \frac{\partial^2 \hat{w}}{\partial r^2} + \frac{\hat{w}}{r} \frac{\partial^2 \hat{w}}{\partial r \partial z} + 3\hat{u} \frac{\partial^3 \hat{w}}{\partial r \partial z^2} + 3\hat{w} \frac{\partial^3 \hat{w}}{\partial z^3} + 2\frac{\partial \hat{u}}{\partial z} \frac{\partial^2 \hat{w}}{\partial r \partial z} + 2\frac{\partial \hat{w}}{\partial z} \frac{\partial^2 \hat{w}}{\partial z^2} \right), \quad (9.6)
\end{aligned}$$

$$(\rho c_p) \left(\hat{u} \frac{\partial \hat{T}}{\partial r} + \hat{w} \frac{\partial \hat{T}}{\partial z} \right) = k \frac{\partial^2 \hat{T}}{\partial z^2} - \nabla \cdot q_r + Q_0 (\hat{T} - \hat{T}_2), \quad (9.7)$$

$$\hat{u} \frac{\partial c}{\partial r} + \hat{w} \frac{\partial c}{\partial z} = D_C^* \left(\frac{\partial^2 c}{\partial r^2} + \frac{1}{r} \frac{\partial c}{\partial r} + \frac{\partial^2 c}{\partial z^2} \right) - k_c c d^2, \quad (9.8)$$

$$\hat{u} \frac{\partial d}{\partial r} + \hat{w} \frac{\partial d}{\partial z} = D_D^* \left(\frac{\partial^2 d}{\partial r^2} + \frac{1}{r} \frac{\partial d}{\partial r} + \frac{\partial^2 d}{\partial z^2} \right) + k_c c d^2, \quad (9.9)$$

with boundary conditions

$$\begin{aligned}
\hat{u} &= r a_1, \quad \hat{v} = r \Omega_1, \quad \hat{w} = 0, \quad \hat{T} = \hat{T}_1(r) = \hat{T}_0 + A_s r, \quad D_C \frac{\partial c}{\partial z} = k_s c, \quad D_D \frac{\partial d}{\partial z} = -k_s c \quad \text{at } z = 0, \\
\hat{u} &= r a_2, \quad \hat{v} = r \Omega_2, \quad \hat{w} = 0, \quad \hat{T} = \hat{T}_2(r) = \hat{T}_0 + B_s r, \quad c \rightarrow c_0, \quad d \rightarrow 0 \quad \text{at } z = h, \quad (9.10)
\end{aligned}$$

where λ_1^* denotes ratio of relaxation to retardation times, λ_2^* retardation time, σ electrical conductivity, k thermal conductivity, ν kinematic viscosity, c_p specific heat, ρ the density, Q_0

heat generation absorption coefficient and q_r radiative heat flux defined by

$$q_r = \frac{-16\sigma^* \hat{T}^3}{3k^*} \frac{\partial \hat{T}}{\partial z}, \quad (9.11)$$

in which σ^* and k^* denote Stefan-Boltzmann constant and mean absorption coefficients respectively. Letting [11]:

$$\begin{aligned} \hat{u} &= r\Omega_1 \tilde{f}'(\xi), \quad \hat{v} = r\Omega_1 \tilde{g}(\xi), \quad \hat{w} = -2h\Omega_1 \tilde{f}(\xi), \quad \tilde{\theta} = \frac{\hat{T} - \hat{T}_2}{\hat{T}_1 - \hat{T}_0}, \\ \hat{p} &= \rho_f \Omega_1 \nu_f \left(P(\xi) + \frac{1}{2} \frac{r^2}{h^2} \epsilon \right), \quad c = c_0 \tilde{\phi}, \quad d = c_0 \tilde{l}, \quad \xi = \frac{z}{h}. \end{aligned} \quad (9.12)$$

Mass conservation is satisfied and Eqs. (9.4 – 9.10) are reduced to

$$\tilde{f}''' + \beta \operatorname{Re}(\tilde{f}'^2 - 4\tilde{f}\tilde{f}'''' - 4A^* \tilde{f}'^2 + 4A^* \tilde{f}\tilde{f}'') - \operatorname{Re}(1 + \lambda_1^*)(\tilde{f}'^2 - 2\tilde{f}\tilde{f}'' - \tilde{g}^2 - M\tilde{f}') - (1 + \lambda_1^*)\epsilon = 0, \quad (9.13)$$

$$g'' + \beta \operatorname{Re} \left(2A^* f g' - 2A^* f' g - 4f g''' + f'' g' \right) - \operatorname{Re}(1 + \lambda_1^*)(2f' g - 2f g' + M g) = 0, \quad (9.14)$$

$$P' + \frac{2}{1 + \lambda_1^*} f'' + 4 \operatorname{Re} f f' - \frac{\beta}{1 + \lambda_1^*} \left(9f' f'' + 10f f''' \right) - 2\beta \operatorname{Re} f = 0, \quad (9.15)$$

$$\tilde{\theta}'' + R(\tilde{\theta}\alpha_1 + 1)^2(3\tilde{\theta}'^2\alpha_1 + (\tilde{\theta}\alpha_1 + 1)\tilde{\theta}'') - \operatorname{Pr} \operatorname{Re}(\tilde{f}'\tilde{\theta} + \tilde{f}'S - 2\tilde{f}\tilde{\theta}' + Q^*\tilde{\theta}) = 0, \quad (9.16)$$

$$\frac{1}{\operatorname{Re}} \frac{1}{Sc} \tilde{\phi}'' + 2\tilde{f}\tilde{\phi}' - k_1 \tilde{\phi}\tilde{l}^2 = 0, \quad (9.17)$$

$$\frac{\delta}{Sc} \frac{1}{\operatorname{Re}} \tilde{l}'' + 2\tilde{f}\tilde{l}' + k_1 \tilde{\phi}\tilde{l}^2 = 0, \quad (9.18)$$

with

$$\begin{aligned} \tilde{f}(0) &= 0, \quad \tilde{f}(1) = 0, \quad \tilde{f}'(0) = A_1, \quad \tilde{f}'(1) = A_2, \quad \tilde{g}(0) = 1, \\ \tilde{g}(1) &= \Omega, \quad \tilde{\theta}(0) = 1 - S, \quad \tilde{\theta}(1) = 0, \quad \tilde{\phi}'(0) = k_2 \tilde{\phi}(0), \quad \tilde{\phi}(1) = 1, \\ \delta \tilde{l}'(0) &= -k_2 \tilde{\phi}(0), \quad \tilde{l}(1) = 0, \quad P(0) = 0, \end{aligned} \quad (9.19)$$

$$\begin{aligned}
\text{Re} &= \frac{\Omega_1 h^2}{\nu}, \quad M = \frac{\sigma B_0^2}{\rho \Omega_1}, \quad \beta = \lambda_2^* \Omega_1, \quad A_1 = \frac{a_1}{\Omega_1}, \quad A_2 = \frac{a_2}{\Omega_1}, \\
\Omega &= \frac{\Omega_2}{\Omega_1}, \quad \text{Pr} = \frac{\rho c_p \nu}{k}, \quad S = \frac{B_s}{A_s}, \quad Q^* = \frac{Q_0}{\rho c_p \Omega_1}, \quad \alpha_1 = \frac{\hat{T}_1 - \hat{T}_0}{\hat{T}_2} \\
k_1 &= \frac{k_c c_0^2}{\Omega_1}, \quad k_2 = \frac{k_s h}{D_C^*}, \quad \delta = \frac{D_D}{D_C}, \quad Sc = \frac{\nu}{D_C^*}, \quad A^* = \frac{h^2}{r^2}.
\end{aligned} \tag{9.20}$$

Here Re denotes Reynolds number, M Hartmann number, β Deborah number, A_1 and A_2 stretching parameters of lower and upper disks respectively, Ω ratio of angular velocities, Pr Prandtl number, S thermal stratification parameter, Q^* heat generation/absorption parameter, α_1 temperature ratio parameter, k_1 and k_2 homogeneous and heterogeneous reaction parameters respectively, δ ratio of diffusion coefficient and Sc Schmidt number. For eliminating the pressure constant ϵ and to get more simplified form of Eq. (9.13) we have taken the derivative with respect to ξ and get

$$f^{(iv)} + \beta \text{Re} \left(2f'' f''' - 4f f^{(v)} - 4f' f^{(iv)} + 4A^* f f''' - 4A^* f' f'' \right) + \text{Re}(1 + \lambda_1^*) (2f f''' + 2gg' - M f'') = 0. \tag{9.21}$$

When diffusion coefficients D_C and D_D are equal for both chemical species i.e. $\delta = 1$ then

$$\tilde{\phi}(\xi) + \tilde{l}(\xi) = 1. \tag{9.22}$$

Now Eqs. (9.17) and (9.18) yield

$$\frac{1}{\text{Re}} \frac{1}{Sc} \tilde{\phi}'' + 2\tilde{f}\tilde{\phi}' - k_1 \tilde{\phi}(1 - \tilde{\phi})^2 = 0, \tag{9.23}$$

with boundary conditions

$$\tilde{\phi}'(0) = k_2 \tilde{\phi}(0), \quad \tilde{\phi}(1) = 1. \tag{9.24}$$

Shear stresses τ_{zr} and $\tau_{z\theta}$ are defined as

$$\tau_{zr} = \frac{\mu}{1 + \lambda_1^*} \left(\frac{\partial \hat{u}}{\partial z} + \frac{\partial \hat{w}}{\partial r} \right) + \lambda_2^* \left(\hat{u} \frac{\partial}{\partial r} + \hat{w} \frac{\partial}{\partial z} \right) \left(\frac{\partial \hat{u}}{\partial z} + \frac{\partial \hat{w}}{\partial r} \right), \tag{9.25}$$

$$\tau_{z\theta} = \frac{\mu}{1 + \lambda_1^*} \frac{\partial \hat{v}}{\partial z} + \lambda_2^* \left(\hat{u} \frac{\partial}{\partial r} + \hat{w} \frac{\partial}{\partial z} \right) \frac{\partial \hat{v}}{\partial z}, \tag{9.26}$$

where total shear stress τ_w is

$$\tau_w = \sqrt{\tau_{zr}^2 + \tau_{z\theta}^2}. \quad (9.27)$$

Skin friction coefficients C_{f1} and C_{f2} for lower and upper disks are

$$\text{Re}_r^{0.5} C_{f1} = \frac{\tau_w|_{z=0}}{\rho(r\Omega_1)^2} = \frac{1}{(1 + \lambda_1^*)} \left[\frac{\left(\tilde{f}''(0) - \left(2\tilde{f}(0)\tilde{f}'''(0) - \tilde{f}'(0)\tilde{f}''(0) \right) \beta \right)^2}{\left(\tilde{g}'(0) - \left(2\tilde{f}(0)\tilde{g}''(0) - \tilde{f}'(0)\tilde{g}'(0) \right) \beta \right)^2} \right]^{1/2}, \quad (9.28)$$

$$\text{Re}_r^{0.5} C_{f2} = \frac{\tau_w|_{z=h}}{\rho(r\Omega_1)^2} = \frac{1}{(1 + \lambda_1^*)} \left[\frac{\left(\tilde{f}''(1) - \left(2\tilde{f}(1)\tilde{f}'''(1) - \tilde{f}'(1)\tilde{f}''(1) \right) \beta \right)^2}{\left(\tilde{g}'(1) - \left(2\tilde{f}(1)\tilde{g}''(1) - \tilde{f}'(1)\tilde{g}'(1) \right) \beta \right)^2} \right], \quad (9.29)$$

where local Reynolds number is $Re_r = \frac{r\Omega_1 h}{\nu}$.

Heat transfer rate is defined as

$$Nu_{x1} = \frac{hq_w}{k(\hat{T}_1 - \hat{T}_0)} \Big|_{z=0}, \quad Nu_{x2} = \frac{hq_w}{k(\hat{T}_1 - \hat{T}_0)} \Big|_{z=h}, \quad (9.30)$$

where q_w is wall heat flux given by

$$q_w|_{z=0} = -k \frac{\partial \hat{T}}{\partial z} + q_r \Big|_{z=0}, \quad (9.31)$$

$$q_w|_{z=h} = -k \frac{\partial \hat{T}}{\partial z} + q_r \Big|_{z=h}. \quad (9.32)$$

Nusselt numbers can be written as follows:

$$Nu_{x1} = - \left(1 + R(\tilde{\theta}(0)\alpha_1 + 1) \right) \tilde{\theta}'(0), \quad (9.33)$$

$$Nu_{x2} = - \left(1 + R(\tilde{\theta}(1)\alpha_1 + 1) \right) \tilde{\theta}'(1). \quad (9.34)$$

9.2 Solutions methodology and convergence

Homotopy analysis method (HAM) leads to the solutions development. Thus initial guesses and auxiliary linear operators are

$$\tilde{f}_0(\xi) = A_1\xi - 2A_1\xi^2 - A_2\xi^2 + A_1\xi^3 + A_2\xi^3, \quad (9.35)$$

$$\tilde{g}_0(\xi) = 1 + (\Omega - 1)\xi, \quad (9.36)$$

$$\tilde{\theta}_0(\xi) = (1 - S)(1 - \xi), \quad (9.37)$$

$$\tilde{\phi}_0(\xi) = \frac{1}{1 + k_2}(1 + k_2\xi), \quad (9.38)$$

$$\mathcal{L}_{\tilde{f}} = \tilde{f}''''', \quad \mathcal{L}_{\tilde{g}} = \tilde{g}''', \quad \mathcal{L}_{\tilde{\theta}} = \tilde{\theta}''', \quad \mathcal{L}_{\tilde{\phi}} = \tilde{\phi}''', \quad (9.39)$$

with

$$\mathcal{L}_{\tilde{f}} [e_1 + e_2\xi + e_3\xi^2 + e_4\xi^3] = 0, \quad (9.40)$$

$$\mathcal{L}_{\tilde{g}} [e_5 + e_6\xi] = 0, \quad (9.41)$$

$$\mathcal{L}_{\tilde{\theta}} [e_7 + e_8\xi] = 0, \quad (9.42)$$

$$\mathcal{L}_{\tilde{\phi}} [e_9 + e_{10}\xi] = 0, \quad (9.43)$$

where e_i ($i = 1 - 10$) are the constants. There is no doubt that series solutions involve auxiliary parameters $\hbar_{\tilde{f}}$, $\hbar_{\tilde{g}}$, $\hbar_{\tilde{\theta}}$ and $\hbar_{\tilde{\phi}}$. To acquire the admissible ranges we have drawn \hbar -curves at 17th order of approximations. Convergence regions are $0.1 \leq \hbar_{\tilde{f}} \leq 1$, $-1 \leq \hbar_{\tilde{g}} \leq -0.1$, $-0.8 \leq \hbar_{\tilde{\theta}} \leq -0.1$ and $-1.5 \leq \hbar_{\tilde{\phi}} \leq -0.1$. Solution is convergent for entire region of ξ ($0 \leq \xi \leq \infty$) when $\hbar_{\tilde{f}} = 0.5$, $\hbar_{\tilde{g}} = -0.5 = \hbar_{\tilde{\theta}} = \hbar_{\tilde{\phi}}$ (see Fig. 9.1). Table 9.1 is constructed to show the order of convergence. Here $\tilde{f}''(0)$, $\tilde{g}'(0)$, $\tilde{\theta}'(0)$ and $\tilde{\phi}'(0)$ converge at 10th, 12th, 7th

and 7th order of approximations respectively.

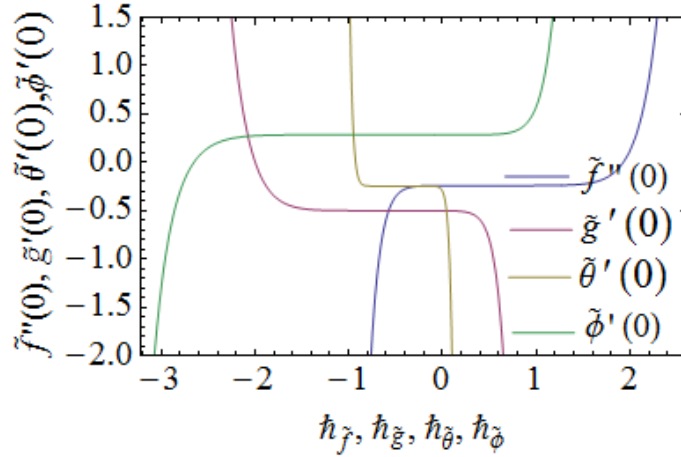


Fig. 9.2: h -curves for $\tilde{f}''(0)$, $\tilde{g}'(0)$, $\tilde{\theta}'(0)$ and $\tilde{\phi}'(0)$.

Table 9.1: Solutions convergence when $\beta = 0.3$, $\text{Re} = 0.001$, $A_1 = 0.01$, $A_2 = 0.1$, $A^* = 0.04$, $\Omega = R = 0.5$, $\alpha_1 = 1.2$, $k_1 = M = k_2 = 0.4$, $Sc = 1$ and $\lambda_1^* = S = Q^* = \text{Pr} = 0.7$.

Order of approximations	$-\tilde{f}''(0)$	$-\tilde{g}'(0)$	$-\tilde{\theta}'(0)$	$\tilde{\phi}'(0)$
1	0.239942	0.4998439	0.2374571	0.2857132
7	0.239885	0.4996902	0.2445976	0.2857120
10	0.239884	0.4996881	0.2445976	0.2857120
12	0.239884	0.4996878	0.2445976	0.2857120
25	0.239884	0.4996878	0.2445976	0.2857120
30	0.239884	0.4996878	0.2445976	0.2857120
35	0.239884	0.4996878	0.2445976	0.2857120
40	0.239884	0.4996878	0.2445976	0.2857120
45	0.239884	0.4996878	0.2445976	0.2857120

9.3 Discussion

This section examines the behaviors of velocity, temperature, concentration, skin friction coefficient and Nusselt number for the different involved variables.

9.3.1 Axial, radial and tangential velocity components

Influence of magnetic parameter M on axial $\tilde{f}(\xi)$ and tangential $\tilde{g}(\xi)$ velocities are shown in Figs. 9.3 and 9.4. For larger value of M both velocity profiles decay. In fact the magnetic parameter is associated with the Lorentz force which provides resistive force and thus velocity reduces. Figs. (9.5 – 9.7) describe the behavior of axial, radial and tangential velocity profiles for larger Reynolds number Re . Magnitude of radial and axial velocity profiles decay for larger Re near both disks (see Figs. 9.5 and 9.6). There is increment in $\tilde{g}(\xi)$ with rise in Re because for larger Reynolds number the inertial forces are dominant (see Fig. 9.7). Figs. (9.8 – 9.10) are portrayed to show the behavior of axial $\tilde{f}(\xi)$, radial $\tilde{f}'(\xi)$ and tangential $\tilde{g}(\xi)$ velocities for larger Deborah number β . At lower disk $\tilde{f}(\xi)$ increases and magnitude of axial velocity at upper disk decays for larger β (see Fig. 9.8). Magnitude of radial and tangential velocities at both disks is increasing for larger β (see Figs. 9.9 and 9.10). Figs. (9.11 – 9.13) are sketched to explain the impact of A_1 on axial, radial and tangential velocities. Magnitude of $\tilde{f}(\xi)$ enhances at lower disk while it shows decreasing impact at upper disk. With an increase in A_1 the stretching rate of lower disk enhances. That is why velocity is more at lower disk than upper disk (see Fig. 9.11). Magnitudes of $\tilde{f}'(\xi)$ and $\tilde{g}(\xi)$ are increasing for higher A_1 at both disks but velocity near lower disk is more than upper disk. It is due to higher rate of stretching of lower disk (see Figs. 9.12 and 9.13). Impact of A_2 on axial, radial and tangential velocities is shown in Figs. (9.14 – 9.16). Magnitude of $\tilde{f}(\xi)$ and $\tilde{f}'(\xi)$ enhance at upper disk while it decays at lower disk for larger stretching parameter of upper disk A_2 . Larger A_2 lead to an enhancement of stretching rate of upper disk (see Figs. 9.14 and 9.15). For larger A_2 the tangential velocity also increases (see Fig. 9.16). Influence of ratio of relaxation to retardation times λ_1^* is shown in Figs. 9.17 and 9.18. Magnitude of axial velocity near both disks decreases with an increase in λ_1^* . For larger λ_1^* the relaxation time increases which means particles need more time to come back from perturbed system to equilibrium system and so velocity reduces (see Fig. 9.17). Tangential velocity is increasing function of λ_1^* (see Fig. 9.18). Behavior of axial and tangential velocities for larger Ω is shown in Figs. 9.19 and 9.20. For larger Ω both $\tilde{f}(\xi)$ and $\tilde{g}(\xi)$ are

increased.

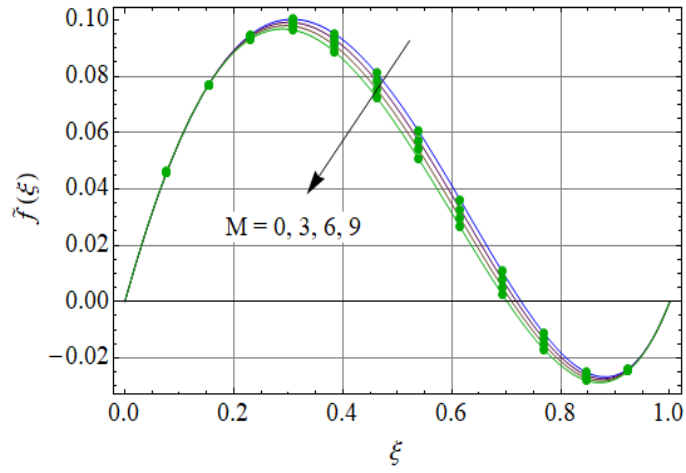


Fig. 9.3: Impact of M for $\tilde{f}(\xi)$.

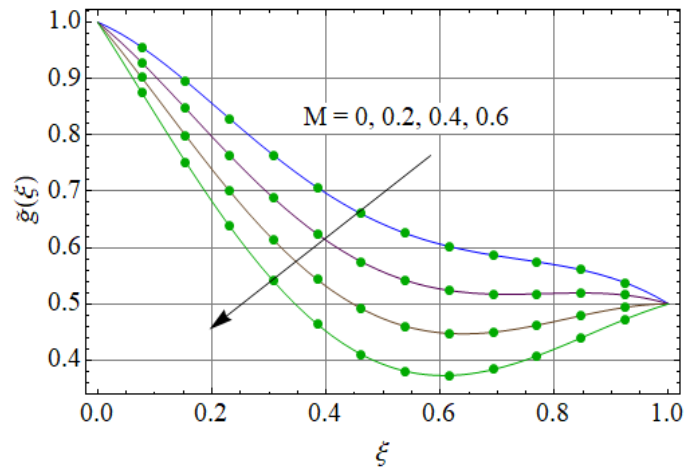


Fig. 9.4: Impact of M for $\tilde{g}(\xi)$.

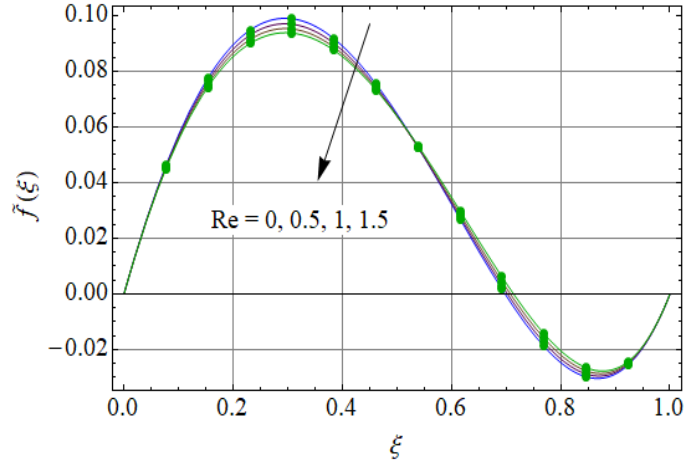


Fig. 9.5: Impact of Re for $\tilde{f}(\xi)$.

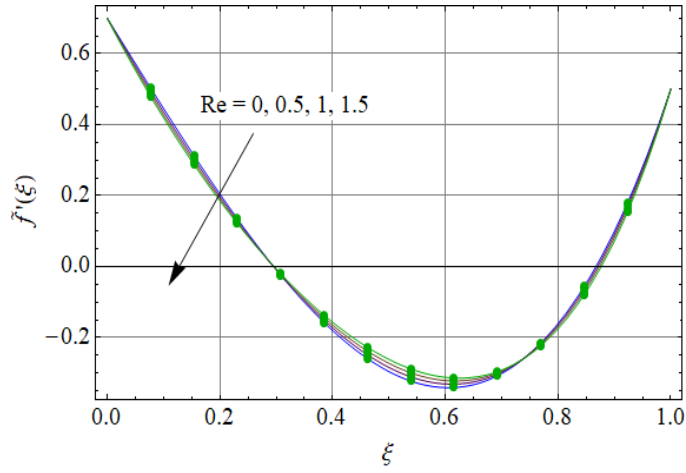


Fig. 9.6: Impact of Re for $\tilde{f}'(\xi)$.

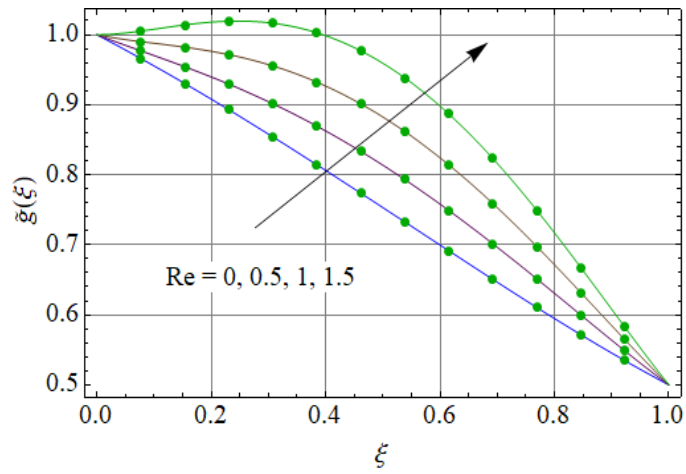


Fig. 9.7: Impact of Re for $\tilde{g}(\xi)$.

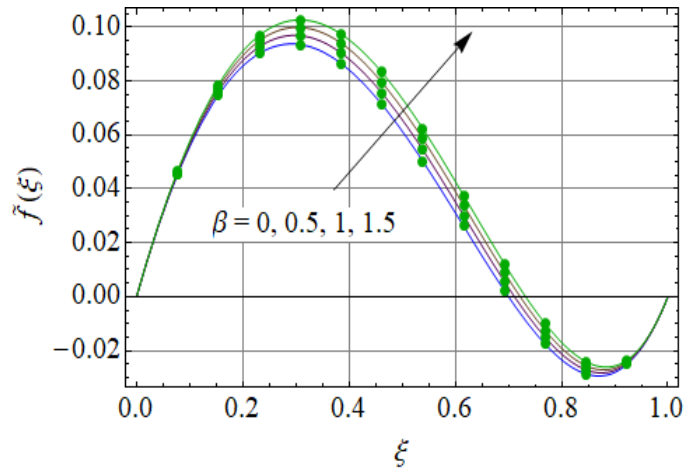


Fig. 9.8: Impact of β for $\tilde{f}(\xi)$.

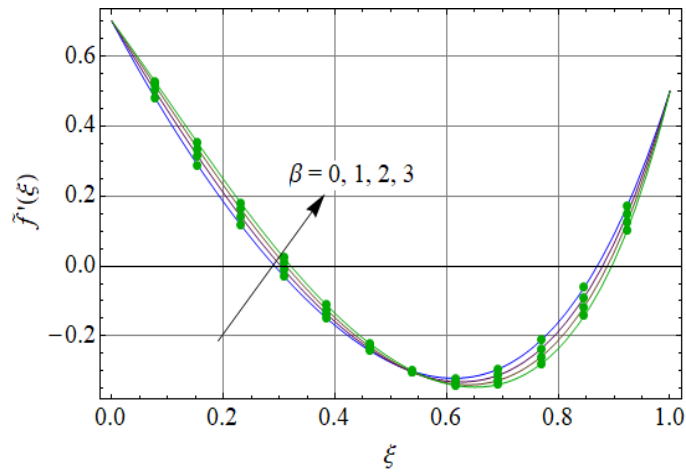


Fig. 9.9: Impact of β for $\tilde{f}'(\xi)$.

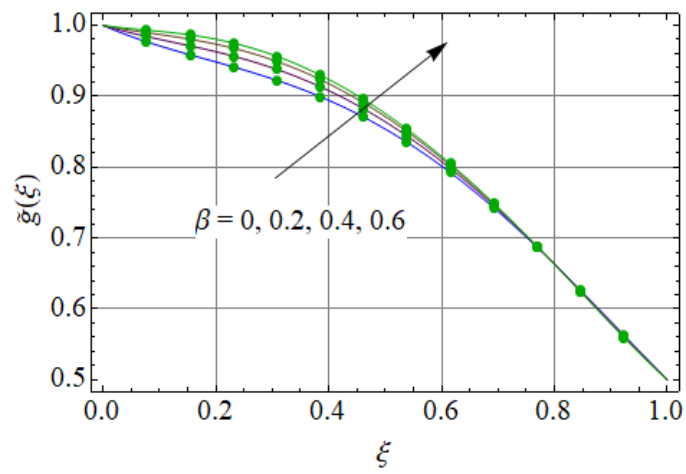


Fig. 9.10: Impact of β for $\tilde{g}(\xi)$.

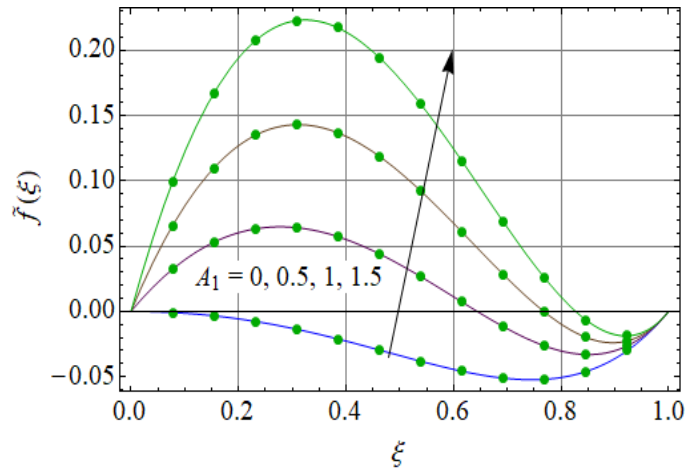


Fig. 9.11: Impact of A_1 for $\tilde{f}(\xi)$.

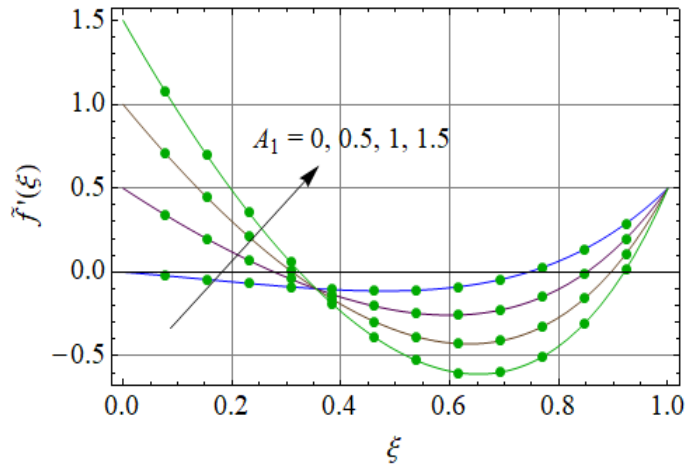


Fig. 9.12: Impact of A_1 for $\tilde{f}'(\xi)$.

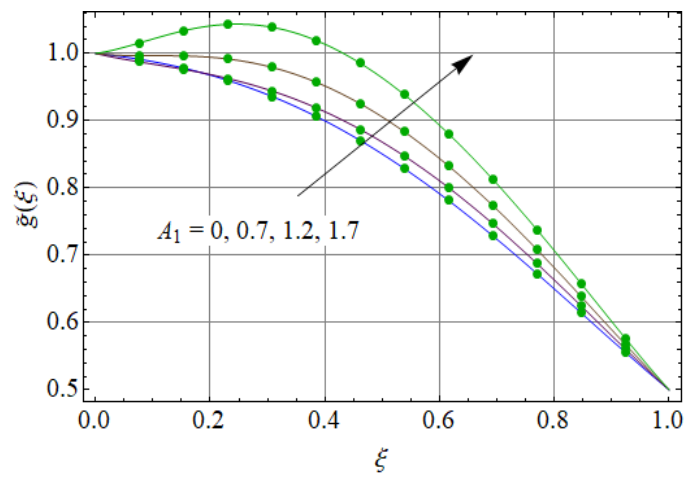


Fig. 9.13: Impact of A_1 for $\tilde{g}(\xi)$.

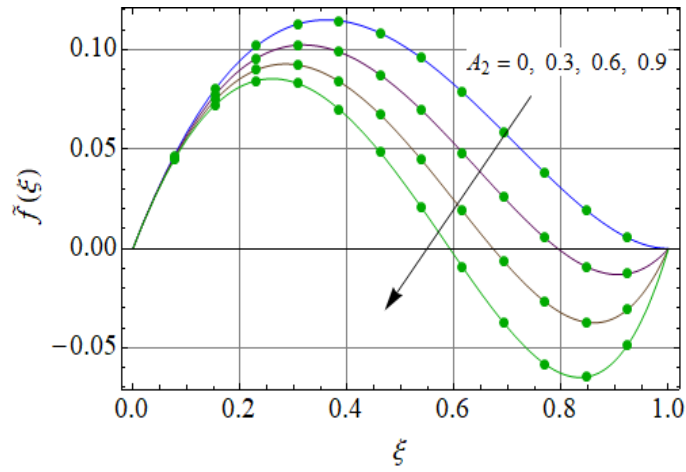


Fig. 9.14: Impact of A_2 for $\tilde{f}(\xi)$.

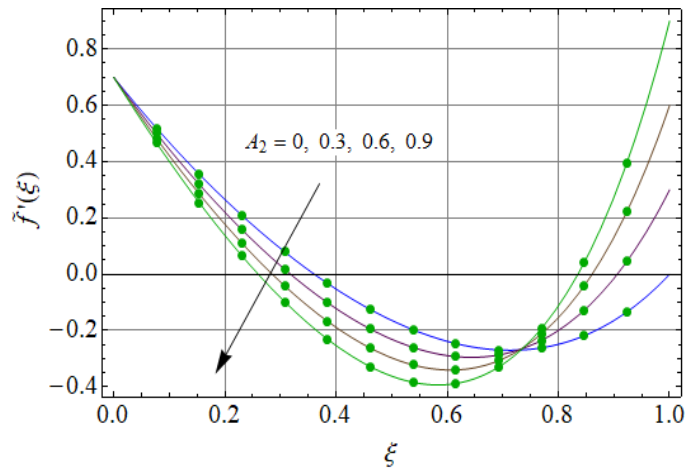


Fig. 9.15: Impact of A_2 for $\tilde{f}'(\xi)$.

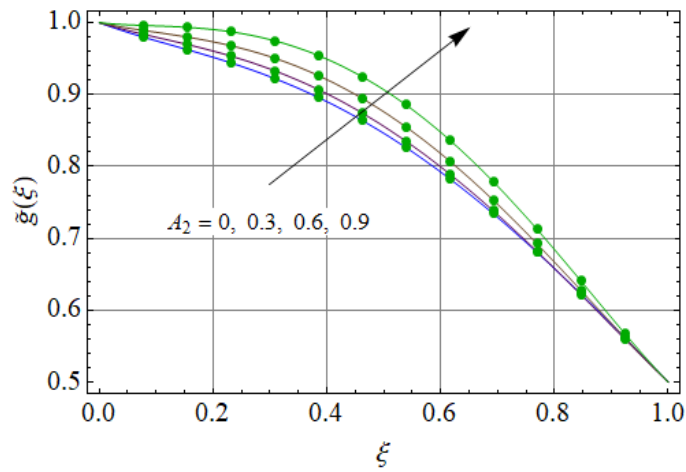


Fig. 9.16: Impact of A_2 for $\tilde{g}(\xi)$.

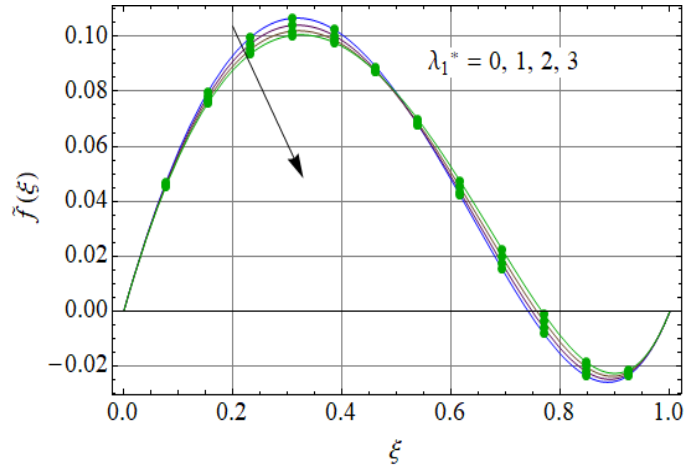


Fig. 9.17: Impact of λ_1^* for $\tilde{f}(\xi)$.

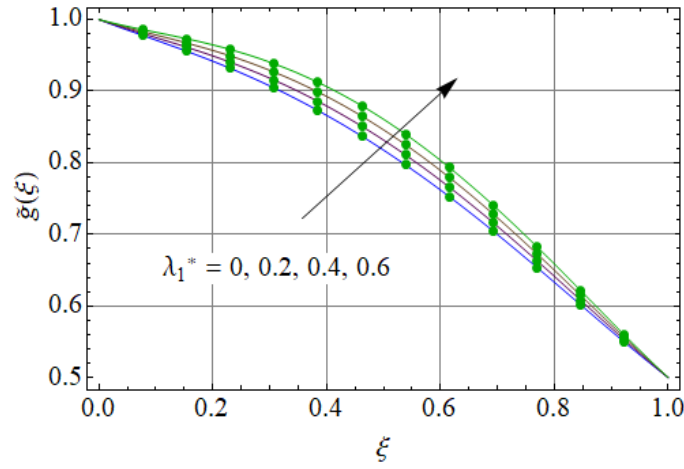


Fig. 9.18: Impact of λ_1^* for $\tilde{g}(\xi)$.

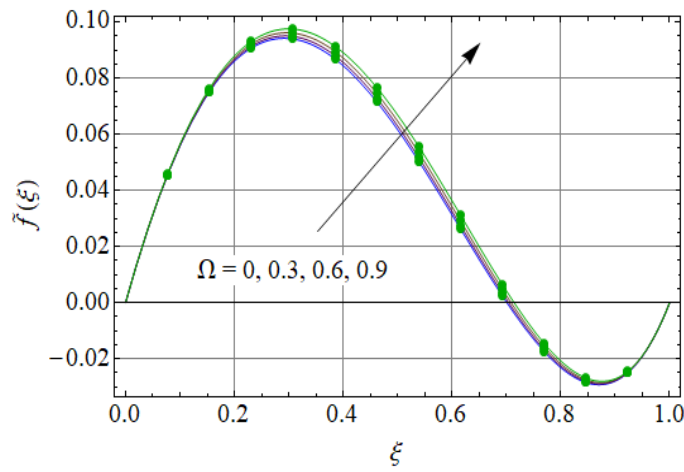


Fig. 9.19: Impact of Ω for $\tilde{f}(\xi)$.

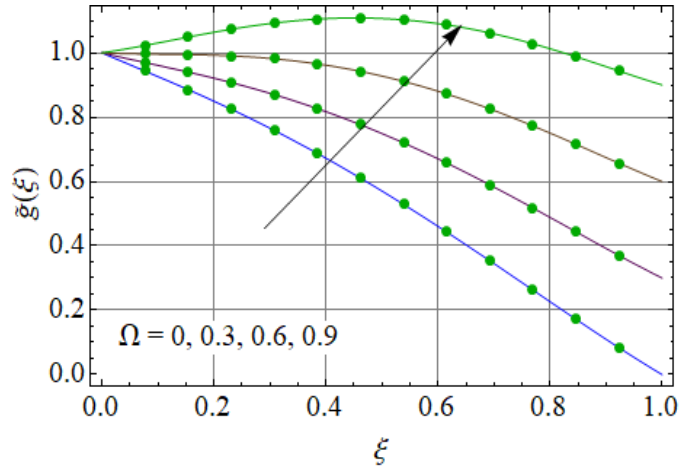


Fig. 9.20: Impact of Ω for $\tilde{g}(\xi)$.

9.3.2 Temperature

Figs. (9.21-9.25) illustrate the temperature. Temperature for thermal stratification parameter S is shown in Fig. 9.21. Larger S gradually decreases the temperature difference between two disks. For larger Prandtl number Pr there is reduction in temperature. Here thermal diffusivity decays for larger Pr (see Fig. 9.22). Impact of radiation R on $\tilde{\theta}(\xi)$ is depicted in Fig. 9.23. Rate of radiative heat transfer reduces for larger R . It is for decrease in mean absorption coefficient and so fluid temperature increases. Temperature ratio parameter impact on $\tilde{\theta}(\xi)$ is sketched in Fig. 9.24. Fluid temperature rises for higher α_1 . Fig. 9.25 shows influence of heat source/sink parameter Q^* on $\tilde{\theta}(\xi)$. It shows that $\tilde{\theta}(\xi)$ is increasing function of Q^* .

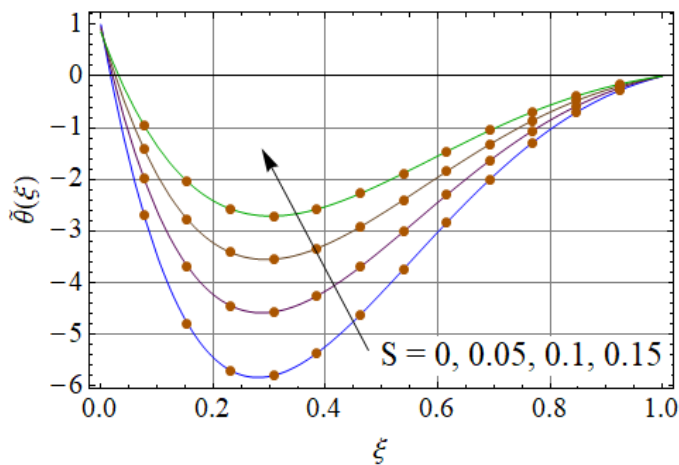


Fig. 9.21: Impact of S for $\tilde{\theta}(\xi)$.

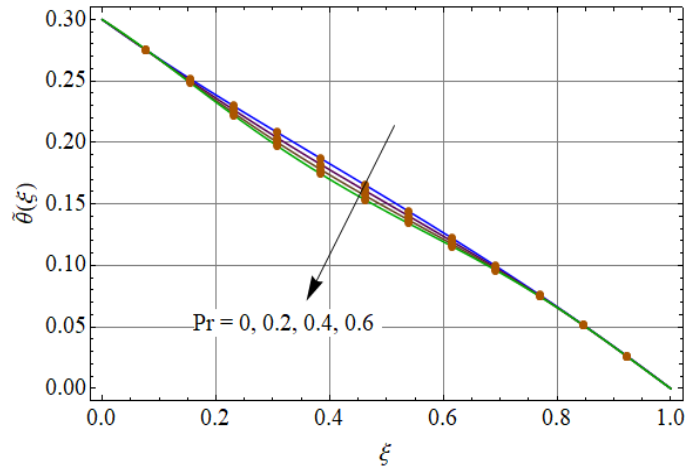


Fig. 9.22: Impact of Pr for $\tilde{\theta}(\xi)$.

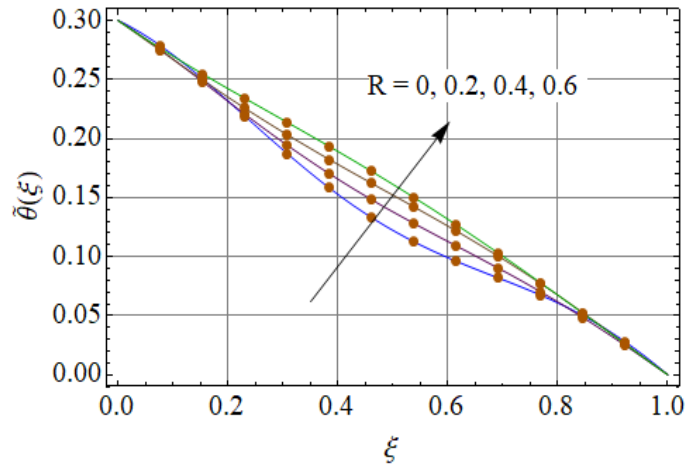


Fig. 9.23: Impact of R for $\tilde{\theta}(\xi)$.

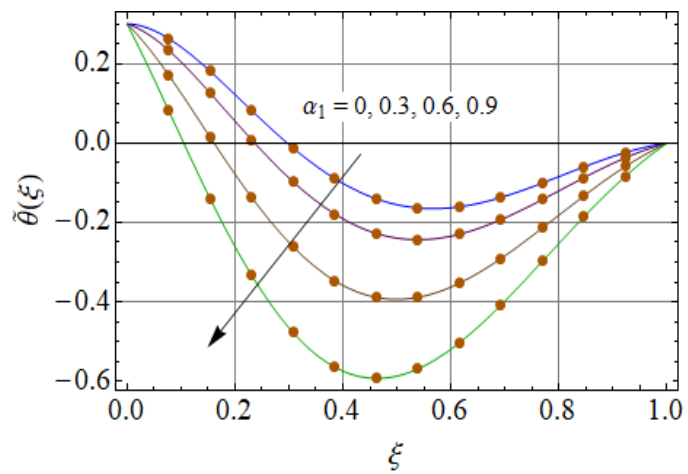


Fig. 9.24: Impact of α_1 for $\tilde{\theta}(\xi)$.

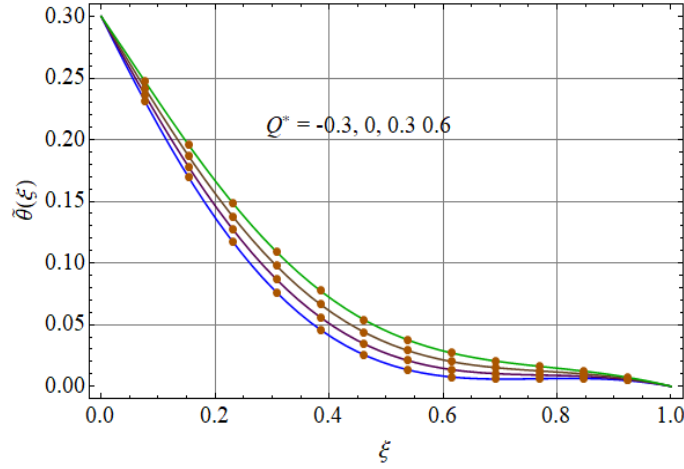


Fig. 9.25: Impact of Q^* for $\tilde{\theta}(\xi)$.

9.3.3 Concentration

Figs. (9.26 – 9.30) are portrayed to show the influence of involved parameters on concentration. Fig. 9.26 shows that for larger Re the concentration of fluid increases because inertial forces are enhanced for larger Re which is in direct relation with mass. Figs. 9.27 and 9.28 depict the effect of stretching parameters A_1 and A_2 on concentration. It is noted that fluid concentration enhances with rise in A_1 while it shows decreasing behavior for larger A_2 . Impact of homogeneous reaction parameter k_1 is shown in Fig. 9.29. Concentration of fluid decays with an increase in k_1 because reactants are consumed during the homogeneous reaction. Fig. 9.30 shows outcome of Sc on concentration of fluid. Here fluid concentration enhances for larger Sc .

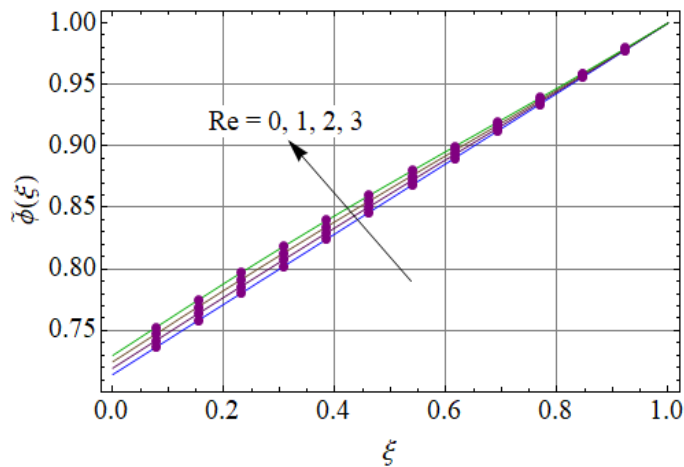


Fig. 9.26: Impact of Re for $\tilde{\phi}(\xi)$.

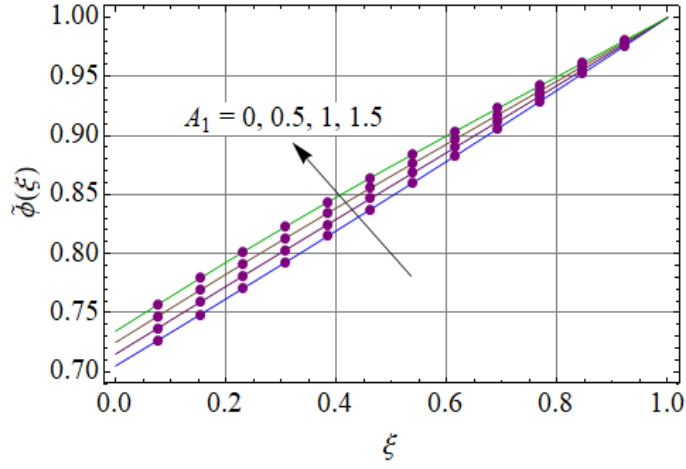


Fig. 9.27: Impact of A_1 for $\tilde{\phi}(\xi)$.

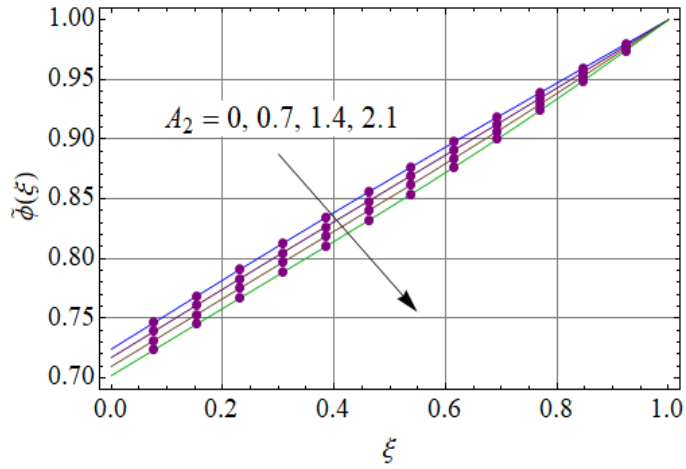


Fig. 9.28: Impact of A_2 for $\tilde{\phi}(\xi)$.

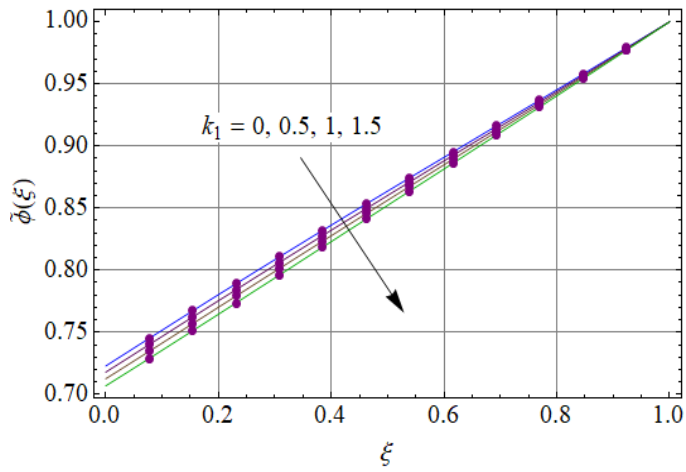


Fig. 9.29: Impact of k_1 for $\tilde{\phi}(\xi)$.

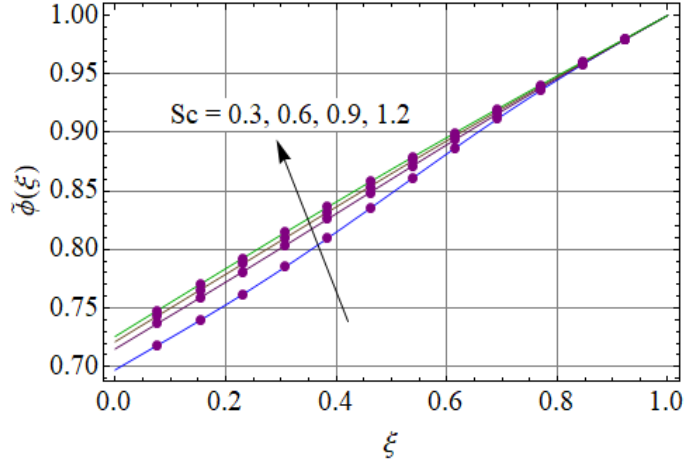


Fig. 9.30: Impact of Sc for $\tilde{\phi}(\xi)$.

9.3.4 Surface drag force

Influence of Reynolds number Re , ratio of relaxation to retardation times constant λ_1^* , Deborah number β and stretching parameter A_1 on skin frictions of lower and upper disks is presented in Figs. (9.31 – 9.34). Fig. 9.31 analyzes that for larger Re the surface drag force rises at both disks. For larger values of λ_1^* the skin friction coefficient decays at both disks. Surface drag force is decreasing function of β at lower disk but it has increasing behavior near upper disk (see Fig. 9.33). Fig. 9.34 is plotted to show the impact of A_1 on skin friction coefficient. Enhancement in surface drag force is noticed for larger A_1 .

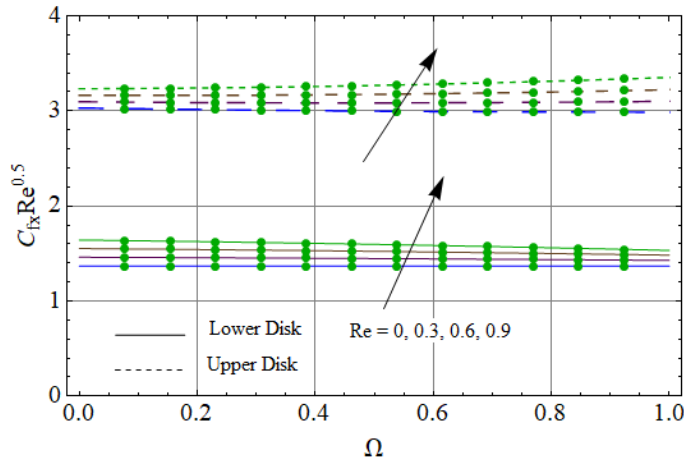


Fig. 9.31: Outcome of Re on $C_{fx} Re^{0.5}$.

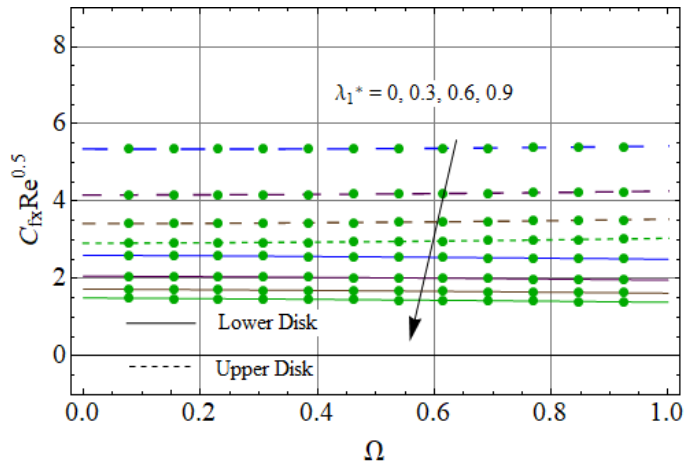


Fig. 9.32: Outcome of λ_1^* on $C_{fx} \text{Re}^{0.5}$.

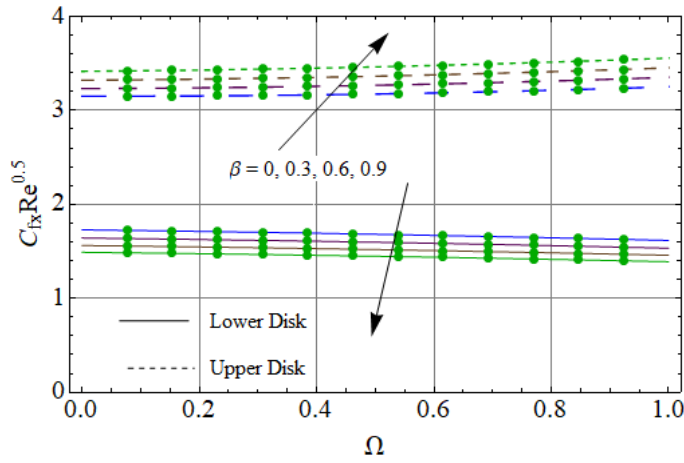


Fig. 9.33: Impact of β on $C_{fx} \text{Re}^{0.5}$.

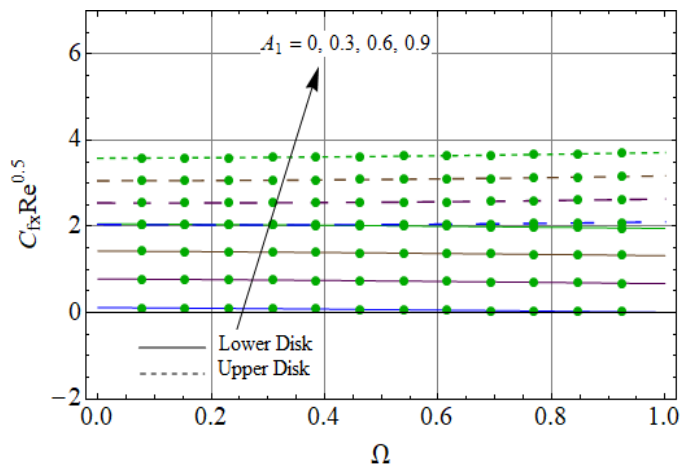


Fig. 9.34: Impact of A_1 on $C_{fx} \text{Re}^{0.5}$.

9.3.5 Nusselt number

Table 9.2 is constructed to show the behavior of involved parameters on Nusselt number. Heat transfer rate enhances for larger R and α_1 while decrease in Nusselt number is observed for increasing stratification parameter S at both disks. Enhancement in Nusselt number is observed for increasing Pr at lower disk but it decreases near the upper disk. For larger Prandtl number the heat transfer rate enhances at lower disk while at upper disk it shows decreasing behavior.

Table 9.2: Computations for Nusselt number.

R	α_1	S	Pr	Nu_{x0}	Nu_{x1}
0.0	1.2	0.7	0.7	0.3000442	0.2999780
0.1				0.350484	0.350411
0.2				0.400922	0.400850
0.5	0.0			0.450044	0.449978
		0.2		0.464093	0.464025
		0.4		0.479270	0.479201
		0.7	0.0	2.31304	2.31278
			0.1	1.98213	1.98189
			0.2	1.67913	1.67893
			0.3	1.40158	1.40158
			0.3	1.40163	1.40154
			0.6	1.40167	1.40152
			0.9	1.40172	1.40150

9.4 Closing remarks

Here we studied the radiative flow of Jeffrey fluid in presence of homogeneous-heterogeneous reaction and heat source/sink effects. The main points are:

- For larger Deborah number β the axial, radial and tangential velocity components are enhanced at lower disk.
- With an increase in λ_1^* the magnitude of axial velocity reduces.

- Temperature $\tilde{\theta}(\xi)$ is increasing function of α_1 , R and Q^* .
- Fluid concentration becomes less for larger k_1 while increasing behavior is observed for larger Re .
- Opposite impact for surface drag force is noticed at lower and upper disks for larger β .
- Heat transfer rate at both disks is an increasing function of α_1 .
- Jeffrey fluid model reduces to viscous fluid when $\lambda_1 = \lambda_2 = 0$.

Chapter 10

Second grade fluid flow by rotating disk with heat generation/absorption and homogeneous/heterogeneous reactions

Abstract: Rotating flow is addressed of second grade liquid in this chapter. Heat and mass transport are discussed. Heat generation/absorption is accounted. At the stretchable surface homogeneous and heterogeneous reactions are considered. Series solutions are computed of the nonlinear flow expressions subject to auxiliary variables through homotopy method. Main consideration in this chapter is given to the graphical representation of the flow variables on the velocity components, concentration, temperature, Nusselt number and skin friction coefficient. The graphical outcomes remark that the velocity components (axial,radial,tangential) are increased against viscoelastic variable. Thermal field is opposite impact versus heat source/sink and viscoelastic variables. The concentration profile is more versus viscoelastic parameter, Schmidt number and heterogeneous reaction variable. Magnitude of Nusselt number as well as skin friction are upsurged via viscoelastic variable.

10.1 Modeling

Consider the steady axisymmetric flow of second grade fluid by a rotating disk. Disk at $z = 0$ rotates with angular velocity Ω_1 . Stretching rate of disk is a_1 . Disk and ambient temperatures are maintained at \hat{T}_w and \hat{T}_∞ respectively (see Fig. 10.1).

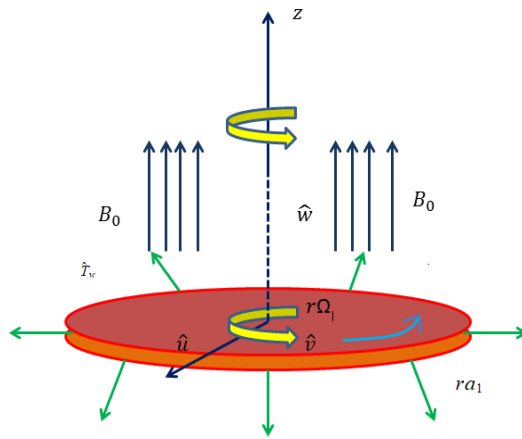
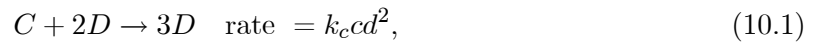


Fig. 10.1: Flow geometry.

Effects of heat generation/absorption are considered. Homogeneous-heterogeneous reactions are also present. Homogeneous reaction for cubic autocatalysis is



and on the surface of catalyst the first order isothermal reaction is



Here k_c and k_s are the rate constants and C and D are chemical species with concentrations c and d . We have used the cylindrical coordinates (r, ϑ, z) with velocity components $(\hat{u}, \hat{v}, \hat{w})$.

The relevant equations are

$$\frac{\partial \hat{u}}{\partial r} + \frac{\hat{u}}{r} + \frac{\partial \hat{w}}{\partial z} = 0, \quad (10.3)$$

$$\begin{aligned} \hat{u} \frac{\partial \hat{u}}{\partial r} + \hat{w} \frac{\partial \hat{u}}{\partial z} - \frac{\hat{v}^2}{r} &= \nu \frac{\partial^2 \hat{u}}{\partial z^2} + \frac{\alpha_1^*}{\rho} \left(\hat{u} \frac{\partial^3 \hat{u}}{\partial r \partial z^2} + \hat{w} \frac{\partial^3 \hat{u}}{\partial z^3} + \frac{\partial \hat{v}}{\partial r} \frac{\partial^2 \hat{v}}{\partial z^2} - \frac{1}{r} \left(\frac{\partial \hat{u}}{\partial z} \right)^2 \right. \\ &\quad \left. - \frac{\partial^2 \hat{v}}{\partial z^2} \frac{\hat{v}}{r} + \frac{\partial \hat{v}}{\partial z} \frac{\partial^2 \hat{v}}{\partial r \partial z} + \frac{\partial \hat{w}}{\partial z} \frac{\partial^2 \hat{u}}{\partial z^2} + 3 \frac{\partial \hat{u}}{\partial z} \frac{\partial^2 \hat{u}}{\partial r \partial z} + 2 \frac{\partial \hat{u}}{\partial r} \frac{\partial^2 \hat{u}}{\partial z^2} \right) \end{aligned} \quad (10.4)$$

$$\hat{u} \frac{\partial \hat{v}}{\partial r} + \hat{w} \frac{\partial \hat{v}}{\partial z} + \frac{\hat{u} \hat{v}}{r} = \nu \frac{\partial^2 \hat{v}}{\partial z^2} + \frac{\alpha_1^*}{\rho} \left(\hat{u} \frac{\partial^3 \hat{v}}{\partial r \partial z^2} + \hat{w} \frac{\partial^3 \hat{v}}{\partial z^3} - 2 \frac{\partial \hat{v}}{\partial z} \frac{\partial^2 \hat{u}}{\partial r \partial z} + \frac{\partial^2 \hat{v}}{\partial z^2} \frac{\hat{u}}{r} - \frac{1}{r} \frac{\partial \hat{u}}{\partial z} \frac{\partial \hat{v}}{\partial z} \right) \quad (10.5)$$

$$(\rho c_p) \left(\hat{u} \frac{\partial \hat{T}}{\partial r} + \hat{w} \frac{\partial \hat{T}}{\partial z} \right) = k \frac{\partial^2 \hat{T}}{\partial z^2} + Q_0 (\hat{T} - \hat{T}_\infty), \quad (10.6)$$

$$\hat{u} \frac{\partial c}{\partial r} + \hat{w} \frac{\partial c}{\partial z} = D_C \left(\frac{\partial^2 c}{\partial r^2} + \frac{1}{r} \frac{\partial c}{\partial r} + \frac{\partial^2 c}{\partial z^2} \right) - k_c c d^2, \quad (10.7)$$

$$\hat{u} \frac{\partial d}{\partial r} + \hat{w} \frac{\partial d}{\partial z} = D_D \left(\frac{\partial^2 d}{\partial r^2} + \frac{1}{r} \frac{\partial d}{\partial r} + \frac{\partial^2 d}{\partial z^2} \right) + k_c c d^2, \quad (10.8)$$

with boundary conditions

$$\begin{aligned} \hat{u} &= r a, \quad \hat{v} = r \Omega, \quad \hat{w} = 0, \quad \hat{T} = \hat{T}_w, \quad D_C \frac{\partial c}{\partial z} = k_s c, \quad D_D \frac{\partial d}{\partial z} = -k_s c \quad \text{at } z = 0, \\ \hat{u} &= 0, \quad \hat{v} = 0, \quad \hat{T} = \hat{T}_\infty, \quad c \rightarrow c_0, \quad d \rightarrow 0 \quad \text{at } z \rightarrow \infty, \end{aligned} \quad (10.9)$$

where α_1^* is material parameter of second grade fluid, ρ density, c_p specific heat, k thermal conductivity, ν kinematic viscosity, Q_0 heat generation absorption coefficient and D_C and D_D are diffusion species coefficients. Considering

$$\begin{aligned} \hat{u} &= r \Omega_1 \tilde{f}'(\xi), \quad \hat{v} = r \Omega_1 \tilde{g}(\xi), \quad \hat{w} = -2h \Omega_1 \tilde{f}(\xi), \quad \tilde{\theta} = \frac{\hat{T} - \hat{T}_\infty}{\hat{T}_w - \hat{T}_\infty}, \\ \hat{p} &= \rho_f \Omega_1 \nu_f \left(P(\xi) + \frac{1}{2} \frac{r^2}{h^2} \epsilon \right), \quad c = c_0 \tilde{\phi}, \quad d = c_0 \tilde{l}, \quad \xi = \frac{z}{h}, \end{aligned} \quad (10.10)$$

equation (10.3) is trivially satisfied while Eqs. (10.4 – 10.9) are reduced to

$$\tilde{f}''' + We \operatorname{Re} (2\tilde{f}''^2 + \tilde{g}'^2 - 2\tilde{f}\tilde{f}^{iv} + \tilde{f}'\tilde{f}''') - \operatorname{Re}(\tilde{f}'^2 - 2\tilde{f}\tilde{f}'' - \tilde{g}'^2) = 0, \quad (10.11)$$

$$\tilde{g}'' + We \operatorname{Re} \left(2\tilde{f}'\tilde{g}'' - 2\tilde{f}\tilde{g}''' - 3\tilde{f}''\tilde{g}' \right) - \operatorname{Re}(2\tilde{f}'\tilde{g} - 2\tilde{f}\tilde{g}') = 0, \quad (10.12)$$

$$\tilde{\theta}'' + \operatorname{Pr} \operatorname{Re}(\tilde{f}'\tilde{\theta} - 2\tilde{f}\tilde{\theta}') + Q^*\tilde{\theta} = 0, \quad (10.13)$$

$$\frac{1}{\text{Re}} \frac{1}{Sc} \tilde{\phi}'' + 2\tilde{f}\tilde{\phi}' - k_1\tilde{\phi}\tilde{l}^2 = 0, \quad (10.14)$$

$$\frac{\delta}{Sc} \frac{1}{\text{Re}} \tilde{l}'' + 2\tilde{f}\tilde{l}' + k_1\tilde{\phi}\tilde{l}^2 = 0, \quad (10.15)$$

with

$$\begin{aligned} \tilde{f}(0) &= 0, \tilde{f}(\infty) = 0, \tilde{f}'(0) = A_1, \tilde{f}'(\infty) = 0, \tilde{g}(0) = 1, \\ \tilde{g}(\infty) &= 0, \tilde{\theta}(0) = 1, \tilde{\theta}(\infty) = 0, \tilde{\phi}'(0) = k_2\tilde{\phi}(0), \tilde{\phi}(\infty) = 1, \\ \delta\tilde{l}'(0) &= -k_2\tilde{\phi}(0), \tilde{l}(\infty) = 0, P(0) = 0, \end{aligned} \quad (10.16)$$

$$\begin{aligned} \text{Re} &= \frac{\Omega_1 h^2}{\nu}, A_1 = \frac{a_1}{\Omega_1}, We = \frac{\alpha_1^*}{\rho h^2} \\ \text{Pr} &= \frac{\rho c_p \nu}{k}, Q^* = \frac{Q_0}{\rho c_p \Omega_1}, k_1 = \frac{k_c c_0^2}{\Omega_1} \\ k_2 &= \frac{k_s h}{D_C}, \delta = \frac{D_D}{D_C}, Sc = \frac{\nu}{D_C}, \end{aligned} \quad (10.17)$$

Here Re denotes Reynolds number, A_1 stretching parameter, We Weissenberg number, Pr Prandtl number, Q^* heat generation/absorption parameter, k_1 and k_2 the homogeneous and heterogeneous reaction parameters respectively, δ ratio of diffusion coefficient and Sc Schmidt number. When diffusion coefficients D_C and D_D are equal for both chemical species i.e. $\delta = 1$ then

$$\tilde{\phi}(\xi) + \tilde{l}(\xi) = 1. \quad (10.18)$$

Now Eqs. (10.14) and (10.15) yield

$$\frac{1}{\text{Re}} \frac{1}{Sc} \tilde{\phi}'' + 2\tilde{f}\tilde{\phi}' - k_1\tilde{\phi}(1 - \tilde{\phi})^2 = 0, \quad (10.19)$$

with boundary conditions

$$\tilde{\phi}'(0) = k_2\tilde{\phi}(0), \tilde{\phi}(1) = 1. \quad (10.20)$$

Skin friction coefficients in radial and tangential directions are C_{f_r} and C_{f_θ} respectively

$$C_{f_r} = \frac{\tau_{zr}}{\rho(r\Omega_1)^2}, \quad (10.21)$$

$$C_{f_\theta} = \frac{\tau_{z\theta}}{\rho(r\Omega_1)^2}, \quad (10.22)$$

Shear stresses τ_{zr} and $\tau_{z\theta}$ are defined by

$$\begin{aligned} \tau_{zr} = & \mu \left(\frac{\partial \hat{u}}{\partial z} + \frac{\partial \hat{w}}{\partial r} \right) + \alpha_1^* \left(\hat{u} \frac{\partial}{\partial r} + \hat{w} \frac{\partial}{\partial z} \right) \left(\frac{\partial \hat{u}}{\partial z} + \frac{\partial \hat{w}}{\partial r} \right) + 2 \frac{\partial \hat{v}}{\partial z} \left(\frac{\partial \hat{v}}{\partial r} - \frac{\hat{v}}{r} \right) + \frac{\partial \hat{u}}{\partial r} \frac{\partial \hat{w}}{\partial r} + \frac{\partial \hat{u}}{\partial z} \frac{\partial \hat{w}}{\partial z} \\ & + 3 \left(\frac{\partial \hat{u}}{\partial r} \frac{\partial \hat{u}}{\partial z} + \frac{\partial \hat{w}}{\partial r} \frac{\partial \hat{w}}{\partial z} \right) - \alpha_1^* \left(\left(\frac{\partial \hat{u}}{\partial r} + \frac{\partial \hat{w}}{\partial z} \right) \left(\frac{\partial \hat{u}}{\partial z} + \frac{\partial \hat{w}}{\partial r} \right) + \frac{\partial \hat{v}}{\partial z} \left(\frac{\partial \hat{v}}{\partial r} - \frac{\hat{v}}{r} \right) \right), \end{aligned} \quad (10.23)$$

$$\begin{aligned} \tau_{z\theta} = & \mu \frac{\partial \hat{v}}{\partial z} + \alpha_1^* \left(\hat{u} \frac{\partial^2 \hat{v}}{\partial r \partial z} + \hat{w} \frac{\partial^2 \hat{v}}{\partial z^2} + \frac{\partial \hat{u}}{\partial z} \frac{\partial \hat{v}}{\partial r} - \frac{\hat{v}}{r} \frac{\partial \hat{u}}{\partial z} + 3 \frac{\hat{u}}{r} \frac{\partial \hat{v}}{\partial z} + \frac{\partial \hat{v}}{\partial z} \frac{\partial \hat{w}}{\partial z} \right) \\ & - \alpha_1^* \left(\frac{\partial \hat{u}}{\partial z} \frac{\partial \hat{v}}{\partial r} - \frac{\hat{v}}{r} \frac{\partial \hat{u}}{\partial z} + \frac{\partial \hat{w}}{\partial r} \frac{\partial \hat{v}}{\partial r} - \frac{\hat{v}}{r} \frac{\partial \hat{w}}{\partial r} + 2 \frac{\hat{u}}{r} \frac{\partial \hat{v}}{\partial z} + 2 \frac{\partial \hat{v}}{\partial z} \frac{\partial \hat{w}}{\partial z} \right), \end{aligned} \quad (10.24)$$

Skin friction coefficients C_{f_r} and C_{f_θ} in dimensionless forms are

$$\text{Re}_r C_{f_r} = \tilde{f}''(0) + \beta \text{Re}[3\tilde{f}'(0)\tilde{f}''(0) - 2\tilde{f}(0)\tilde{f}'''(0) + \tilde{g}(0)\tilde{g}'(0)], \quad (10.25)$$

$$\text{Re}_r C_{f_\theta} = \tilde{g}'(0) + \beta \text{Re}[4\tilde{f}'(0)\tilde{g}'(0) - 2\tilde{f}(0)\tilde{g}''(0)], \quad (10.26)$$

where local Reynolds number is $\text{Re}_r = \frac{r\Omega_1 h}{\nu}$.

Heat transfer rate is defined as

$$Nu_x = \frac{hq_w}{k(\hat{T}_w - \hat{T}_\infty)} \Big|_{z=0}, \quad (10.27)$$

in which wall heat flux q_w is given by

$$q_w|_{z=0} = -k \frac{\partial \hat{T}}{\partial z} \Big|_{z=0}. \quad (10.28)$$

Nusselt number is

$$Nu_x = -\tilde{\theta}'(0). \quad (10.29)$$

10.2 Solutions methodology and convergence

Homotopy analysis method (HAM) leads to the solutions development. Thus initial guesses and auxiliary linear operators are

$$\tilde{f}_0(\xi) = A_1(1 - \exp(-\xi)), \quad (10.30)$$

$$\tilde{g}_0(\xi) = \exp(-\xi), \quad (10.31)$$

$$\tilde{\theta}_0(\xi) = \exp(-\xi), \quad (10.32)$$

$$\tilde{\phi}_0(\xi) = 1 - \frac{1}{2} \exp(-k_2\xi), \quad (10.33)$$

$$\mathcal{L}_{\tilde{f}} = \tilde{f}''' - \tilde{f}', \quad \mathcal{L}_{\tilde{g}} = \tilde{g}'' - \tilde{g}, \quad \mathcal{L}_{\tilde{\theta}} = \tilde{\theta}'' - \tilde{\theta}, \quad \mathcal{L}_{\tilde{\phi}} = \tilde{\phi}'' - \tilde{\phi}, \quad (10.34)$$

with

$$\mathcal{L}_{\tilde{f}} [A_1 + A_2 e^\xi + A_3 e^{-\xi}] = 0, \quad (10.35)$$

$$\mathcal{L}_{\tilde{g}} [A_4 e^\xi + A_5 e^{-\xi}] = 0, \quad (10.36)$$

$$\mathcal{L}_{\tilde{\theta}} [A_6 e^\xi + A_7 e^{-\xi}] = 0, \quad (10.37)$$

$$\mathcal{L}_{\tilde{\phi}} [A_8 e^\xi + A_9 e^{-\xi}] = 0, \quad (10.38)$$

where A_i ($i = 1 - 9$) are the constants. There is no doubt that series solutions involve auxiliary parameters $\hbar_{\tilde{f}}$, $\hbar_{\tilde{g}}$, $\hbar_{\tilde{\theta}}$ and $\hbar_{\tilde{\phi}}$. To acquire the admissible ranges we have drawn the \hbar -curves at 16th order of approximations. Convergence regions are $-1.9 \leq \hbar_{\tilde{f}} \leq -0.9$, $-1.8 \leq \hbar_{\tilde{g}} \leq -0.6$, $-1.5 \leq \hbar_{\tilde{\theta}} \leq -0.9$ and $-2.3 \leq \hbar_{\tilde{\phi}} \leq -1.3$. Solution is convergent for entire region of ξ ($0 \leq \xi \leq \infty$) when $\hbar_{\tilde{f}} = \hbar_{\tilde{g}} = -1.5 = \hbar_{\tilde{\phi}}$ and $\hbar_{\tilde{\theta}} = -1.3$. Table 1 is constructed to show the order of convergence. $\tilde{f}''(0)$, $\tilde{g}'(0)$, $\tilde{\theta}'(0)$ and $\tilde{\phi}'(0)$ converge at 10th, 23th, 26th and 24th order

of approximations respectively.

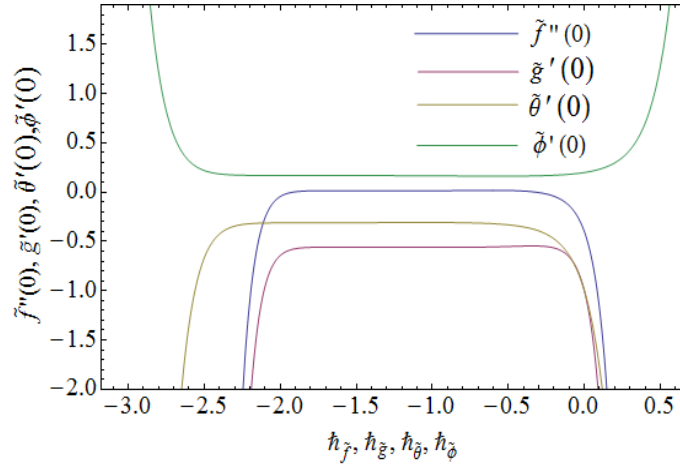


Fig. 10.2: h -curves for $\tilde{f}''(0)$, $\tilde{g}'(0)$, $\tilde{\theta}'(0)$ and $\tilde{\phi}'(0)$.

Table 10.1: Solutions convergence when $Re = 0.3$, $A_1 = 0.4$, $We = 0.01$, $Pr = 1.5$, $k_1 = k_2 = 0.4$, $Sc = 1$ and $Q^* = 0.2$.

Order of approximations	$\tilde{f}''(0)$	$-\tilde{g}'(0)$	$-\tilde{\theta}'(0)$	$\tilde{\phi}'(0)$
1	0.0044	0.4300	0.6120	0.17741
5	0.0259	0.5479	0.3467	0.16148
10	0.0150	0.5599	0.3158	0.16483
22	0.0150	0.5573	0.3095	0.16958
23	0.0150	0.5572	0.3096	0.16959
24	0.0150	0.5572	0.3097	0.16961
26	0.0150	0.5572	0.3099	0.16961
30	0.0150	0.5572	0.3099	0.16961
40	0.0150	0.5572	0.3099	0.16961

10.3 Discussion

Present section is prepared just to investigate the effects of involved dimensionless variables on velocity (axial, radial, tangential), temperature, concentration, skin friction coefficient and Nusselt number.

10.3.1 Axial, radial and tangential velocity components

Impact of viscoelastic parameter We on axial, radial and tangential velocity profiles is shown in Figs. (10.3 – 10.5). For larger values of We fluid viscosity decreases because We is inversely proportional to the viscosity and hence fluid velocity (axial, radial and tangential) enhances. Influence of Re on axial, radial and tangential velocities is shown in Figs. (10.6 – 10.8). It is clear from these figures that for larger Reynolds number Re the axial, radial and tangential velocities are reducing. In fact Re is directly proportional to the density of fluid. When density enhances then velocities in radial, axial and tangential directions decay. Figs. (10.9 – 10.11) are portrayed to show the behavior of axial $\tilde{f}(\xi)$, radial $\tilde{f}'(\xi)$ and tangential $\tilde{g}(\xi)$ velocities for stretching parameter A_1 . Magnitude of $\tilde{f}(\xi)$ and $\tilde{f}'(\xi)$ enhances for larger A_1 because stretching rate of disk is increasing through A_1 (see Figs. 10.9 and 10.10). Decreasing behavior is observed for tangential velocity $\tilde{g}(\xi)$ with an increase in stretching parameter A_1 . With increase in A_1 the rotational velocity Ω_1 is reduced. It causes decrease in tangential velocity (see Fig. 10.11).

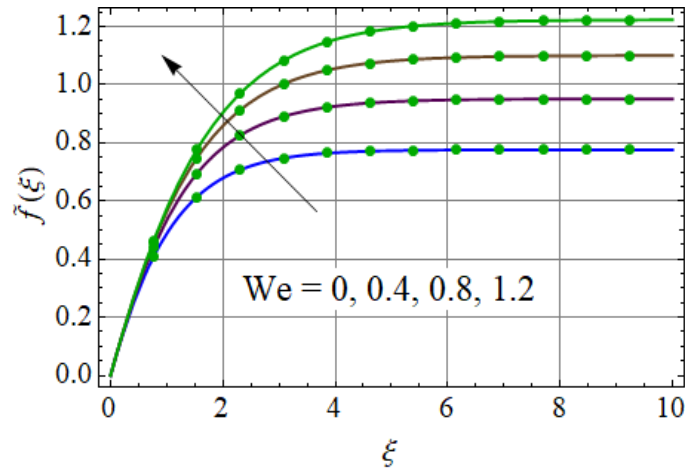


Fig. 10.3: Impact of We for $\tilde{f}(\xi)$.

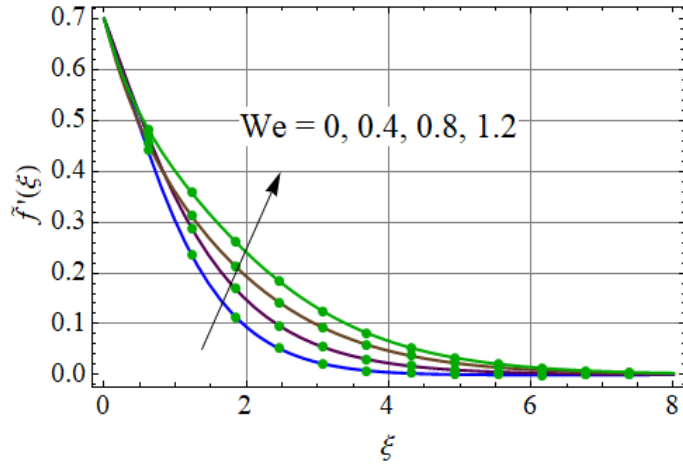


Fig. 10.4: Impact of We for $\tilde{f}'(\xi)$.

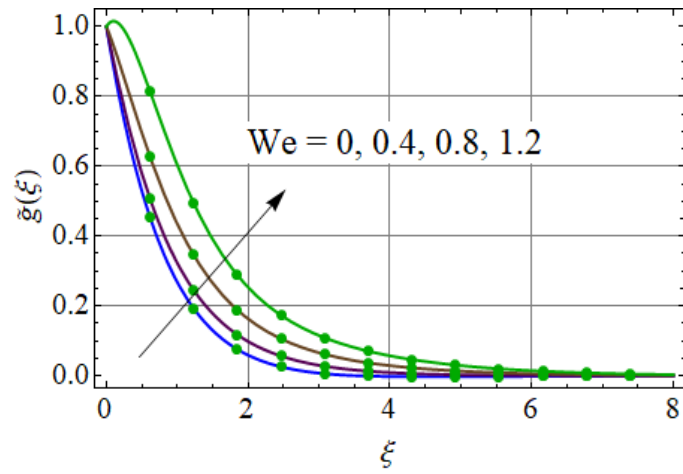


Fig. 10.5: Impact of We for $\tilde{g}(\xi)$.

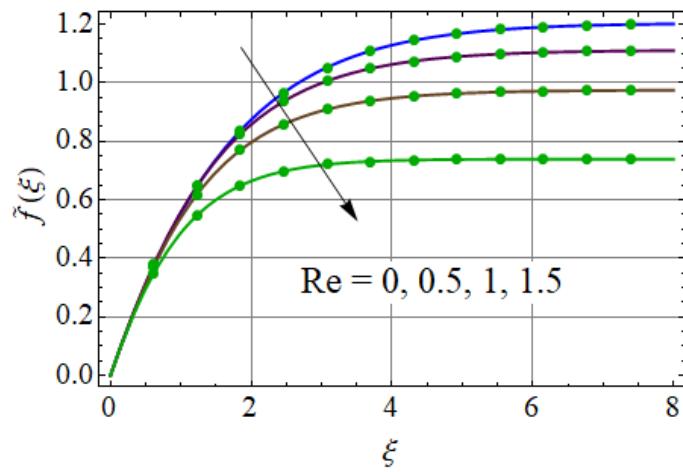


Fig. 10.6: Impact of Re for $\tilde{f}(\xi)$.

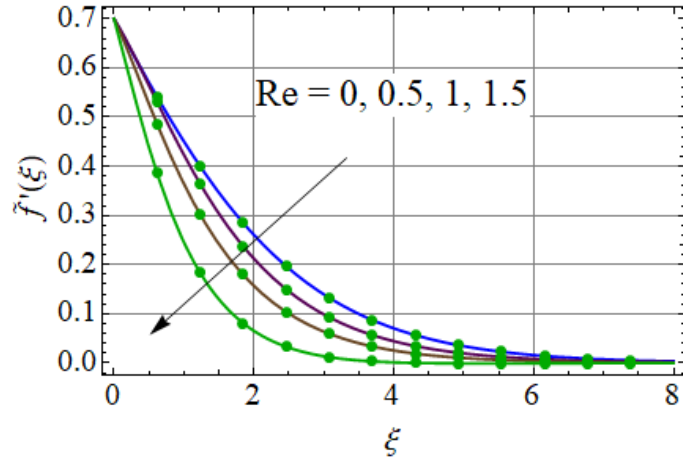


Fig. 10.7: Impact of Re for $\tilde{f}'(\xi)$.

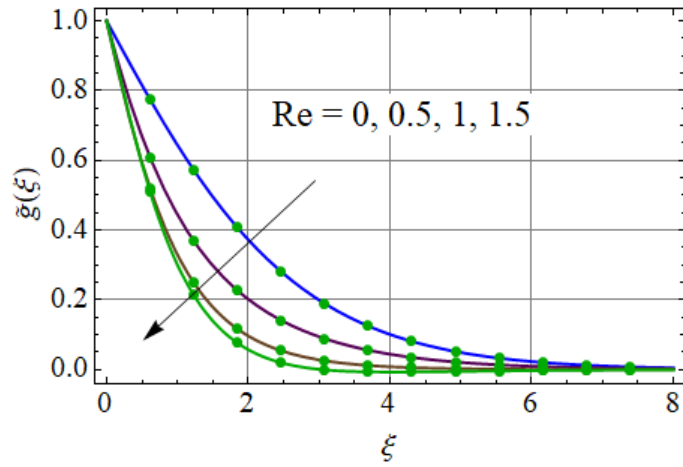


Fig. 10.8: Impact of Re for $\tilde{g}(\xi)$.

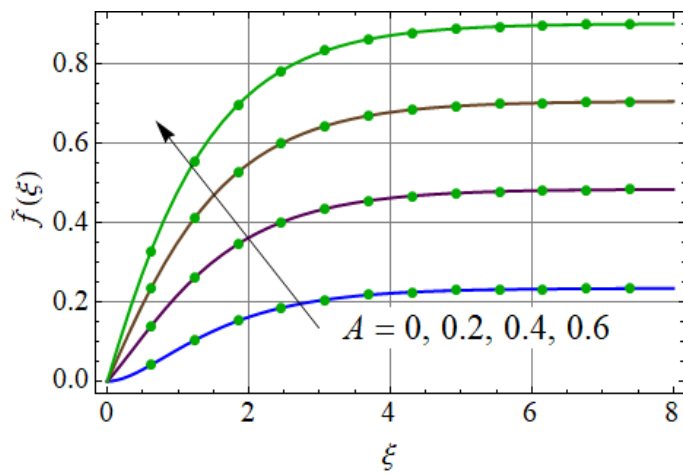


Fig. 10.9: Impact of A_1 for $\tilde{f}(\xi)$.

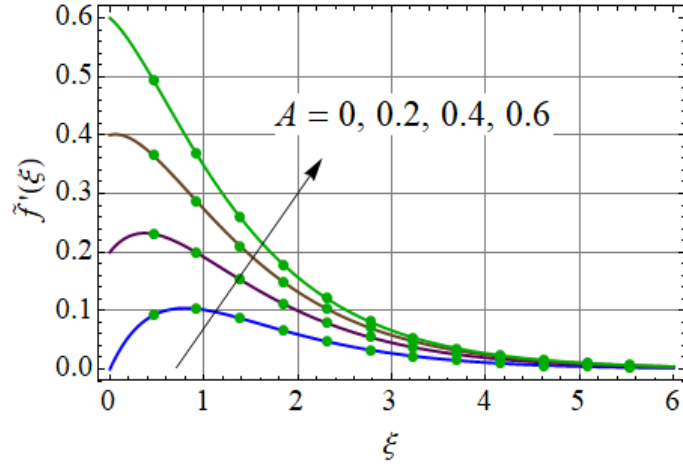


Fig. 10.10: Impact of A_1 for $\tilde{f}'(\xi)$.

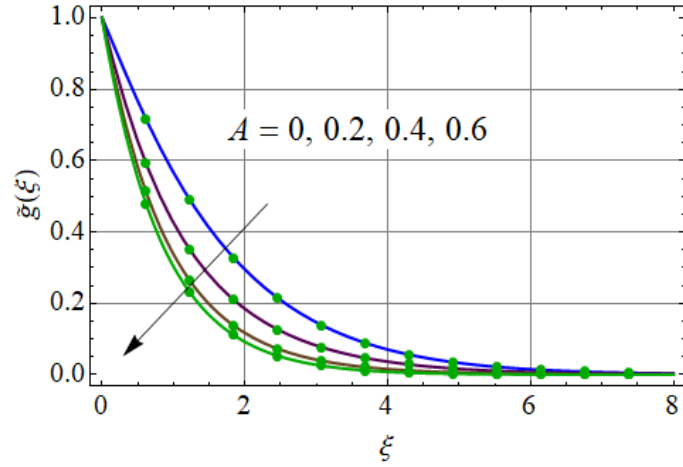


Fig. 10.11: Impact of A_1 for $\tilde{g}(\xi)$.

10.3.2 Temperature

Figs. (10.12–10.15) are made to examine the temperature. Temperature for Prandtl number Pr is shown in Fig. 10.12. Larger Pr gradually decreases the temperature of fluid because thermal diffusivity decays for larger Pr . Fig. 10.13 shows influence of heat source/sink parameter Q^* on $\tilde{\theta}(\xi)$. It shows that $\tilde{\theta}(\xi)$ is increasing function of Q^* . Impact of viscoelastic parameter We on temperature is depicted in Fig. 10.14. Here decreasing effects are captured for larger We .

For larger Reynolds number Re there is decreasing impact of temperature (see Fig. 10.15).

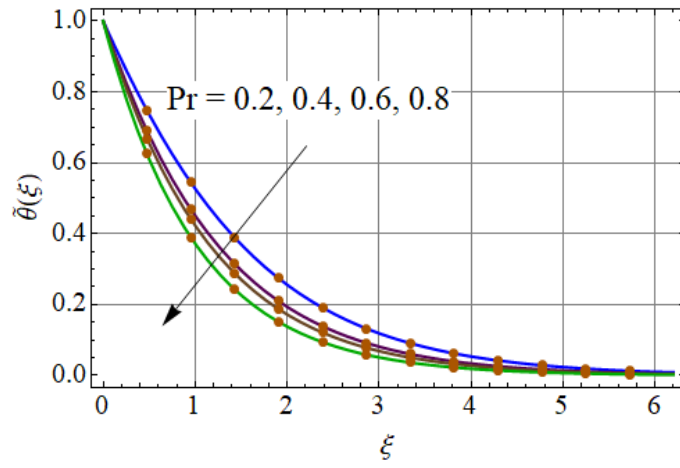


Fig. 10.12: Impact of Pr for $\tilde{\theta}(\xi)$.

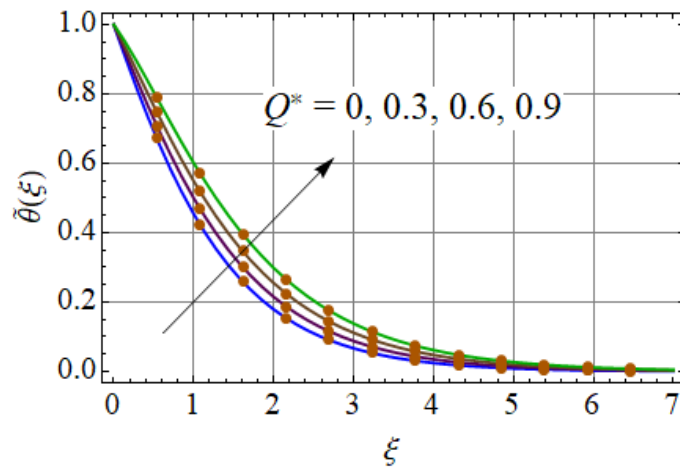


Fig. 10.13: Impact of Q^* for $\tilde{\theta}(\xi)$.

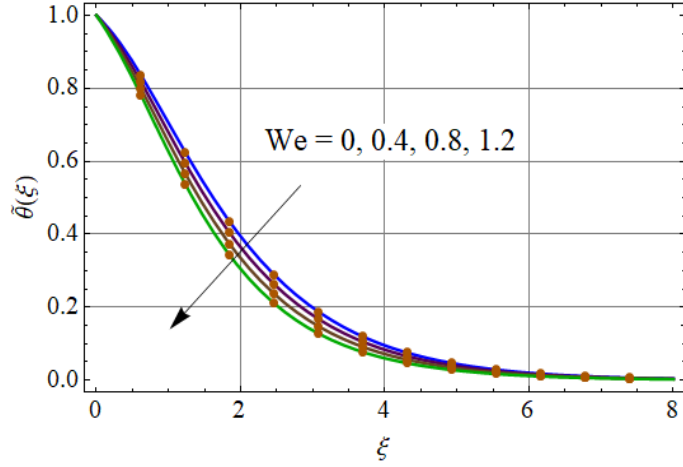


Fig. 10.14: Impact of We for $\tilde{\theta}(\xi)$.

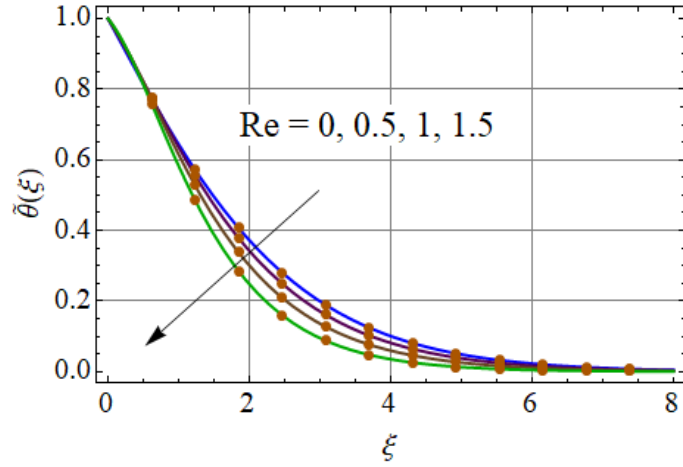


Fig. 10.15: Impact of Re for $\tilde{\theta}(\xi)$.

10.3.3 Concentration

Figs. (10.16 – 10.20) are portrayed to show the influence of involved parameters on concentration. Impact of homogeneous reaction parameter k_1 is depicted in Fig. 10.16. As expected the concentration of fluid decreases for higher k_1 . It is through the fact that reactants are consumed during the homogeneous reaction. While opposite behavior of $\tilde{\phi}(\xi)$ is captured for larger heterogeneous reaction parameter k_2 (see Fig. 10.17). For increasing value of k_2 the diffusion coefficient reduces and less diffused particles enhance the concentration. Increment in concentration is noticed for larger Sc (see Fig. 10.18). As Sc is the ratio of momentum to mass diffusivity. Therefore momentum diffusivity increases for larger Sc which in turn enhances the

concentration. Fig. 10.19 shows that for larger We the concentration of fluid increases. Fig. 10.20 portrayed the influence of Re on concentration. It shows that $\tilde{\phi}(\xi)$ enhances with increase in Re .

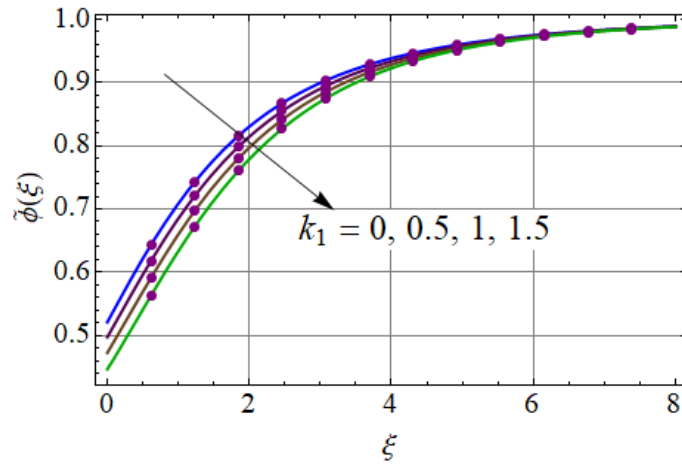


Fig. 10.16: Impact of k_1 for $\tilde{\phi}(\xi)$.

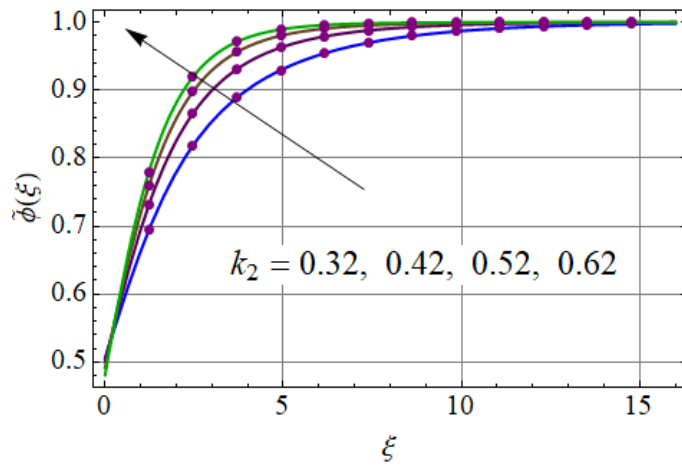


Fig. 10.17: Impact of k_2 for $\tilde{\phi}(\xi)$.

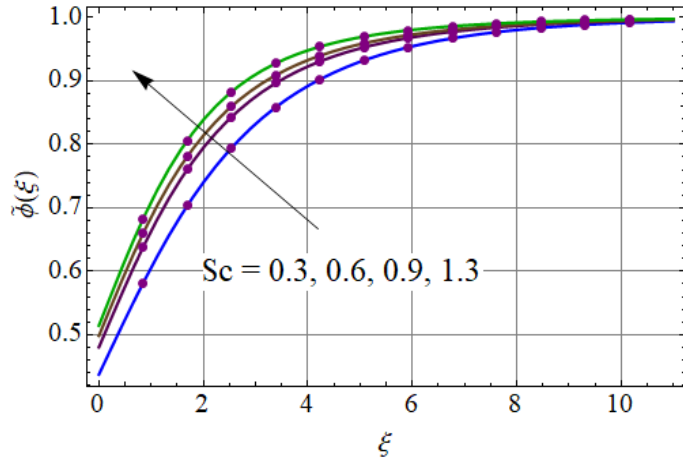


Fig. 10.18: Impact of Sc for $\tilde{\phi}(\xi)$.

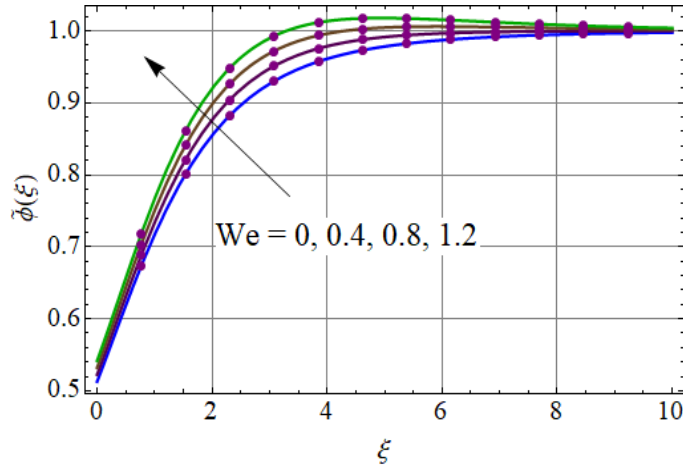


Fig. 10.19: Impact of We for $\tilde{\phi}(\xi)$.

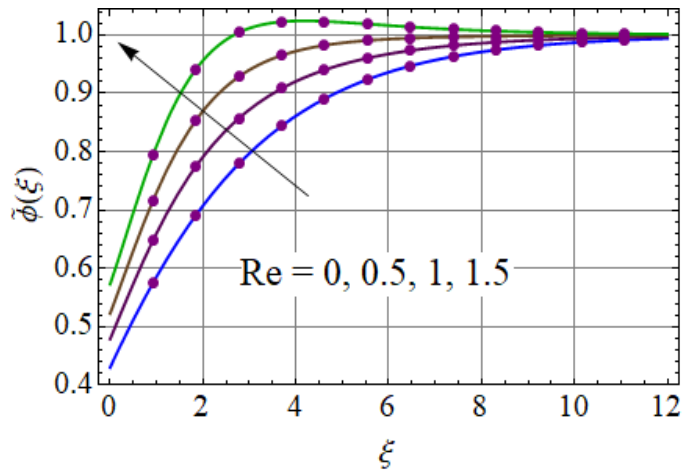


Fig. 10.20: Impact of Re for $\tilde{\phi}(\xi)$.

10.3.4 Surface drag force

Impacts of viscoelastic parameter We , stretching parameter A_1 and Reynolds number Re on skin friction coefficient are shown in Figs. (10.21 – 10.23). It is clear from the Figs. that magnitude of skin friction coefficient in radial and tangential directions enhances for larger We , A_1 and Re .

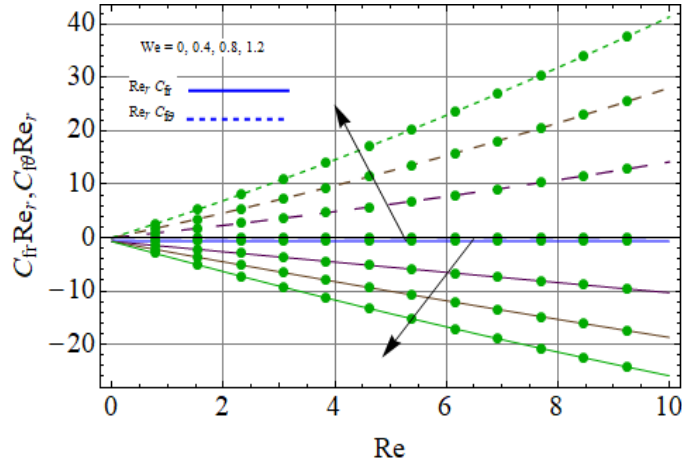


Fig. 10.21: Impact of We for $C_{fr} Re_r$ and $C_{f\theta} Re_r$.

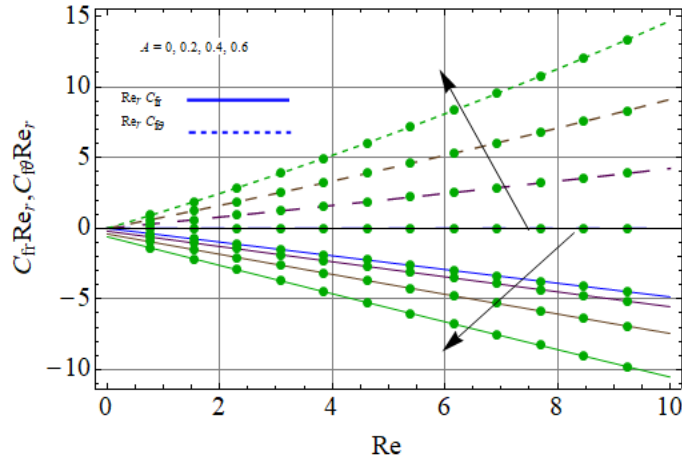


Fig. 10.22: Impact of A_1 for $C_{fr} Re_r$ and $C_{f\theta} Re_r$.

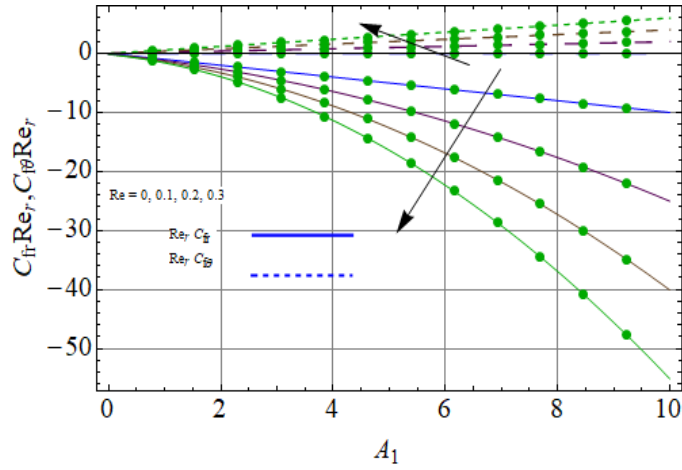


Fig. 10.23: Impact of Re for $C_{fr} Re_r$ and $C_{f\theta} Re_r$.

10.3.5 Nusselt number

Figs. (10.24 – 10.26) are sketched to analyze the effect of viscoelastic parameter We , Prandtl number Pr and heat generation/absorption parameter Q^* on Nusselt number. Fig. 10.24 shows that Nusselt number is increasing function of We while reduction in heat transfer rate is noticed for larger Pr and Q^* (see Figs. 10.25 and 10.26).

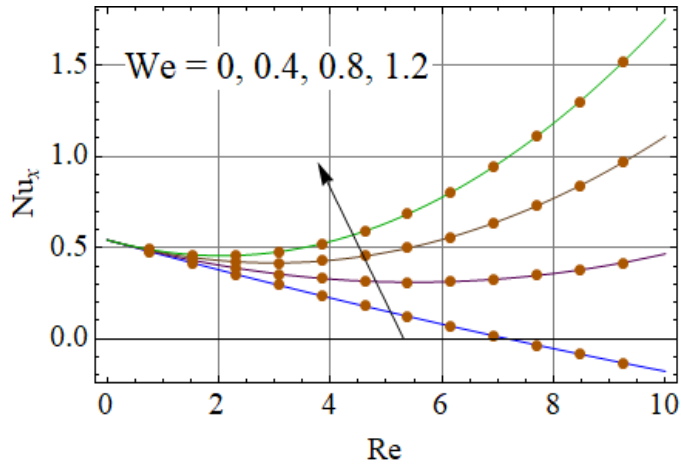


Fig. 10.24: Nu_x via We

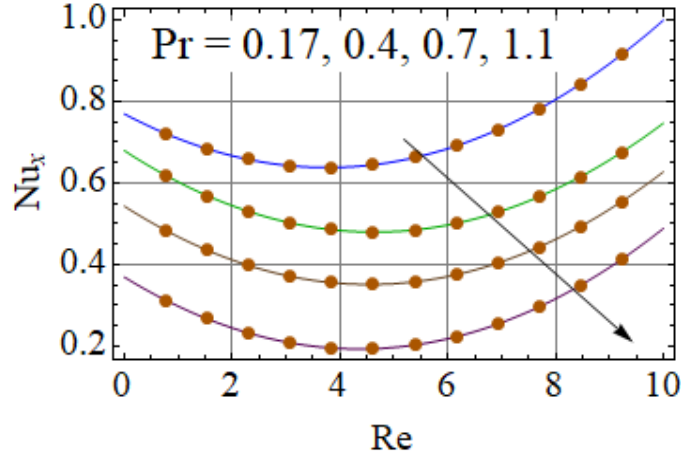


Fig. 10.25: Nu_x via Pr.

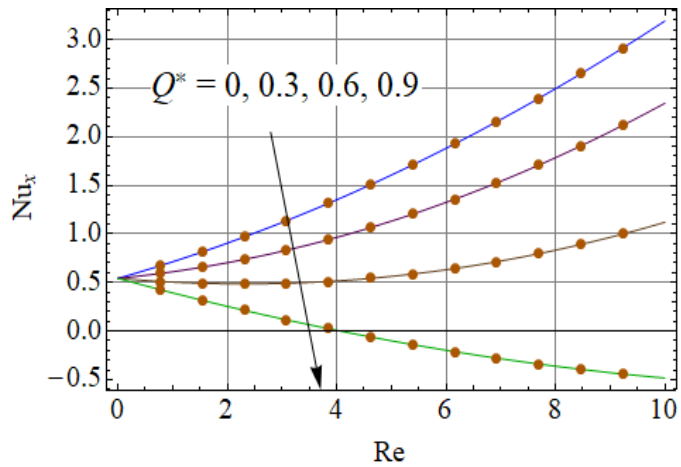


Fig. 10.26: Nu_x via Q^* .

10.4 Closing remarks

Here we consider the flow of second grade fluid accounting heat source/sink and homogeneous-heterogeneous reactions. The main findings are:

- Increasing behavior of axial, radial and tangential velocities is captured for larger viscoelastic parameter We .
- Temperature decreases for larger Prandtl number Pr while opposite behavior is noticed for increasing heat source parameter Q^* .
- Temperature is decreasing function of viscoelastic parameter We .

- Concentration decays for larger k_1 while opposite behavior is examined for increasing k_2 .
- Concentration shows similar behavior for larger Schmidt number Sc and viscoelastic parameter We .
- Viscoelastic parameter We gives rise to surface drag force and Nusselt number.
- Heat transfer rate decays for larger Prandtl number Pr .

Chapter 11

Dissipative flow of Williamson fluid with entropy generation

Abstract: This study is made to predict entropy generation in dissipative flow between two rotating disks. Relations for Williamson fluid are adopted. Dissipation, heat source/sink and radiation are considered. Convergent series solutions to nonlinear system is established. Outcomes of sundry variables on physical quantities are arranged.

11.1 Constitutive equations

Here we are analyze steady and incompressible flow of Williamson fluid between two rotating disks. Flow is taken axisymmetric. Entropy generation is examined for additional effects of heat source/sink and thermal radiation. Stretching rate, angular velocity and temperature of lower disk are a_1 , Ω_1 and \hat{T}_1 while for upper disk the stretching rate, angular velocity and temperature are denoted by a_2 , Ω_2 and \hat{T}_2 respectively. We denote B_0 as the magnetic strength

applied in z -direction (see Fig. 11.1).

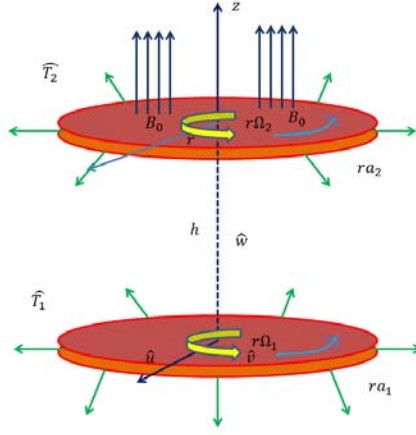


Fig. 11.1: Flow geometry.

Governing equations for velocity and temperature are [11]:

$$\frac{\partial \hat{u}}{\partial r} + \frac{\hat{u}}{r} + \frac{\partial \hat{w}}{\partial z} = 0, \quad (11.1)$$

$$\rho \left(\hat{u} \frac{\partial \hat{u}}{\partial r} + \hat{w} \frac{\partial \hat{u}}{\partial z} - \frac{\hat{v}^2}{r} \right) + \frac{\partial \hat{p}}{\partial r} = \frac{\partial \tau_{rr}}{\partial r} + \frac{\partial \tau_{zr}}{\partial z} + \frac{\tau_{rr} - \tau_{\vartheta\vartheta}}{r} - \frac{\sigma}{\rho} B_0^2 \hat{u}, \quad (11.2)$$

$$\rho \left(\hat{u} \frac{\partial \hat{v}}{\partial r} + \hat{w} \frac{\partial \hat{v}}{\partial z} + \frac{\hat{v} \hat{u}}{r} \right) = \frac{\partial \tau_{r\vartheta}}{\partial r} + \frac{\partial \tau_{z\vartheta}}{\partial z} + \frac{2\tau_{r\vartheta}}{r} - \frac{\sigma}{\rho} B_0^2 \hat{v}, \quad (11.3)$$

$$\rho \left(\hat{u} \frac{\partial \hat{w}}{\partial r} + \hat{w} \frac{\partial \hat{w}}{\partial z} \right) + \frac{\partial \hat{p}}{\partial z} = \frac{\partial \tau_{rz}}{\partial r} + \frac{\partial \tau_{zz}}{\partial z} + \frac{\tau_{rz}}{r}, \quad (11.4)$$

$$\rho c_p \left(\hat{u} \frac{\partial \hat{T}}{\partial r} + \hat{w} \frac{\partial \hat{T}}{\partial z} \right) = k \left(\frac{1}{r} \frac{\partial \hat{T}}{\partial r} + \frac{\partial^2 \hat{T}}{\partial r^2} + \frac{\partial^2 \hat{T}}{\partial z^2} \right) - \nabla \cdot q_r + \tau \cdot L + Q_0 (\hat{T} - \hat{T}_2), \quad (11.5)$$

with boundary conditions

$$\left. \begin{aligned} u = ra_1, \quad v = r\Omega_1, \quad w = 0, \quad \hat{T} = \hat{T}_1 \quad \text{at } z = 0, \\ u = ra_2, \quad v = r\Omega_2, \quad P = P_2, \quad \hat{T} = \hat{T}_2 \quad \text{at } z = h, \end{aligned} \right\} \quad (11.6)$$

where

$$\left. \begin{aligned} \tau_{rr} &= \left(2\frac{\partial\hat{u}}{\partial r}\right) (\mu_0 + (\mu_0 - \mu_\infty)\Gamma\dot{\gamma}), \quad \tau_{\psi\psi} = \left(2\frac{\hat{u}}{r}\right) (\mu_0 + (\mu_0 - \mu_\infty)\Gamma\dot{\gamma}), \\ \tau_{zz} &= \left(2\frac{\partial\hat{w}}{\partial z}\right) (\mu_0 + (\mu_0 - \mu_\infty)\Gamma\dot{\gamma}), \quad \tau_{r\psi} = \tau_{\psi r} = \left(\frac{\partial\hat{v}}{\partial r} - \frac{\hat{v}}{r}\right) (\mu_0 + (\mu_0 - \mu_\infty)\Gamma\dot{\gamma}), \\ \tau_{zr} = \tau_{rz} &= \left(\frac{\partial\hat{u}}{\partial z} + \frac{\partial\hat{w}}{\partial r}\right) (\mu_0 + (\mu_0 - \mu_\infty)\Gamma\dot{\gamma}), \quad \tau_{z\psi} = \tau_{\psi z} = \left(\frac{\partial\hat{v}}{\partial z}\right) (\mu_0 + (\mu_0 - \mu_\infty)\Gamma\dot{\gamma}), \end{aligned} \right\} \quad (11.7)$$

$$\dot{\gamma} = \sqrt{2\left(\frac{\partial\hat{u}}{\partial r}\right)^2 + \left(\frac{\partial\hat{v}}{\partial r} - \frac{\hat{v}}{r}\right)^2 + \left(\frac{\partial\hat{u}}{\partial z} + \frac{\partial\hat{w}}{\partial r}\right)^2 + 2\left(\frac{\hat{u}}{r}\right)^2 + \left(\frac{\partial\hat{v}}{\partial z}\right)^2 + 2\left(\frac{\partial\hat{w}}{\partial z}\right)^2}, \quad (11.8)$$

$$\tau.L = (\mu_0 + (\mu_0 - \mu_\infty)\Gamma\dot{\gamma}) \left[\begin{aligned} &2\left(\frac{\partial\hat{u}}{\partial r}\right)^2 + \left(\frac{\partial\hat{v}}{\partial r} - \frac{\hat{v}}{r}\right)^2 + \left(\frac{\partial\hat{u}}{\partial z} + \frac{\partial\hat{w}}{\partial r}\right)^2 \\ &+ 2\left(\frac{\hat{u}}{r}\right)^2 + \left(\frac{\partial\hat{v}}{\partial z}\right)^2 + 2\left(\frac{\partial\hat{w}}{\partial z}\right)^2 \end{aligned} \right]. \quad (11.9)$$

Radiative heat flux q_r is defined as

$$q_r = -\frac{16\sigma^* \hat{T}_2^3}{3k^*} \frac{\partial\hat{T}}{\partial z}, \quad (11.10)$$

After substituting Eqs. (11.7 – 11.10) in Eqs. (11.1 – 11.5) we get

$$\left. \begin{aligned} \rho \left(\hat{u} \frac{\partial\hat{u}}{\partial r} + \hat{w} \frac{\partial\hat{u}}{\partial z} - \frac{\hat{v}^2}{r} \right) + \frac{\partial\hat{p}}{\partial r} &= \frac{\partial}{\partial r} \left[\left(2\frac{\partial\hat{u}}{\partial r}\right) (\mu_0 + (\mu_0 - \mu_\infty)\Gamma\dot{\gamma}) \right] \\ + \frac{\partial}{\partial z} \left[\left(\frac{\partial\hat{u}}{\partial z} + \frac{\partial\hat{w}}{\partial r}\right) (\mu_0 + (\mu_0 - \mu_\infty)\Gamma\dot{\gamma}) \right] &+ \left[\left(2\frac{\partial\hat{u}}{\partial r}\right) - \left(2\frac{\hat{u}}{r}\right) \right] \frac{(\mu_0 + (\mu_0 - \mu_\infty)\Gamma\dot{\gamma})}{r} - \frac{\sigma}{\rho} B_0^2 \hat{u}, \end{aligned} \right\} \quad (11.11)$$

$$\begin{aligned} \rho \left(\hat{u} \frac{\partial\hat{v}}{\partial r} + \hat{w} \frac{\partial\hat{v}}{\partial z} + \frac{\hat{v}\hat{u}}{r} \right) &= \frac{\partial}{\partial r} \left[\left(\frac{\partial\hat{v}}{\partial r} - \frac{\hat{v}}{r}\right) (\mu_0 + (\mu_0 - \mu_\infty)\Gamma\dot{\gamma}) \right] + \frac{\partial}{\partial z} \left[\left(\frac{\partial\hat{v}}{\partial z}\right) (\mu_0 + (\mu_0 - \mu_\infty)\Gamma\dot{\gamma}) \right] \\ &+ \frac{2}{r} \left[\left(\frac{\partial\hat{v}}{\partial r} - \frac{\hat{v}}{r}\right) (\mu_0 + (\mu_0 - \mu_\infty)\Gamma\dot{\gamma}) \right] - \frac{\sigma}{\rho} B_0^2 \hat{v}, \end{aligned} \quad (11.12)$$

$$\begin{aligned} \rho \left(\hat{u} \frac{\partial\hat{w}}{\partial r} + \hat{w} \frac{\partial\hat{w}}{\partial z} \right) + \frac{\partial\hat{p}}{\partial z} &= \frac{\partial}{\partial r} \left[\left(\frac{\partial\hat{u}}{\partial z} + \frac{\partial\hat{w}}{\partial r}\right) (\mu_0 + (\mu_0 - \mu_\infty)\Gamma\dot{\gamma}) \right] + \frac{\partial}{\partial z} \left[\left(2\frac{\partial\hat{w}}{\partial z}\right) (\mu_0 + (\mu_0 - \mu_\infty)\Gamma\dot{\gamma}) \right] \\ &+ \frac{(\partial\hat{u}}{\partial z} + \frac{\partial\hat{w}}{\partial r}) (\mu_0 + (\mu_0 - \mu_\infty)\Gamma\dot{\gamma})}{r}, \end{aligned} \quad (11.13)$$

$$\begin{aligned} \rho c_p \left(\hat{u} \frac{\partial \hat{T}}{\partial r} + \hat{w} \frac{\partial \hat{T}}{\partial z} \right) &= k \left(\frac{1}{r} \frac{\partial \hat{T}}{\partial r} + \frac{\partial^2 \hat{T}}{\partial r^2} + \frac{\partial^2 \hat{T}}{\partial z^2} \right) - \frac{1}{\rho c_p} \nabla \cdot q_r + \frac{Q_0}{\rho c_p} (\hat{T} - \hat{T}_2) \\ &+ (\mu_0 + (\mu_0 - \mu_\infty) \Gamma \dot{\gamma}) \left[\begin{aligned} &2 \left(\frac{\partial \hat{u}}{\partial r} \right)^2 + \left(\frac{\partial \hat{v}}{\partial r} - \frac{\hat{v}}{r} \right)^2 + \left(\frac{\partial \hat{u}}{\partial z} + \frac{\partial \hat{w}}{\partial r} \right)^2 \\ &+ 2 \left(\frac{\hat{u}}{r} \right)^2 + \left(\frac{\partial \hat{v}}{\partial z} \right)^2 + 2 \left(\frac{\partial \hat{w}}{\partial z} \right)^2 \end{aligned} \right] \quad (11.14) \end{aligned}$$

Letting [2, 7, 8]:

$$\hat{u} = r\Omega_1 \tilde{f}(\xi), \quad \hat{v} = r\Omega_1 \tilde{g}(\xi), \quad \hat{w} = h\Omega_1 \tilde{h}(\xi), \quad \tilde{\theta} = \frac{\hat{T} - \hat{T}_2}{\hat{T}_1 - \hat{T}_2}, \quad \hat{p} = \rho\Omega_1 \nu P(\xi), \quad \xi = \frac{z}{h}, \quad (11.15)$$

we obtain

$$2\tilde{f} + \tilde{h}' = 0, \quad (11.16)$$

$$(1 + We\dot{\gamma})\tilde{f}'' + \text{Re}(\tilde{g}^2 - \tilde{f}^2 - \tilde{h}\tilde{f}' - M\tilde{f}) + \frac{WeA^{*2}}{\dot{\gamma}}(\tilde{f}''\tilde{f}'^2 + \tilde{f}'\tilde{g}'\tilde{g}'') + \frac{2We}{\dot{\gamma}}(3\tilde{f}\tilde{f}'^2 + \tilde{f}\tilde{g}'^2 + \tilde{f}\tilde{h}'\tilde{h}'') = 0, \quad (11.17)$$

$$(1 + We\dot{\gamma})\tilde{g}'' - \text{Re}(2\tilde{f}\tilde{g} + \tilde{h}\tilde{g}' + M\tilde{g}) + \frac{WeA^{*2}}{\dot{\gamma}}(\tilde{f}''\tilde{f}'\tilde{g}' + \tilde{g}'^2\tilde{g}'') + \frac{2We}{\dot{\gamma}}(2\tilde{f}\tilde{f}'\tilde{g}' + \tilde{g}'\tilde{h}'\tilde{h}'') = 0, \quad (11.18)$$

$$\text{Re}(P' + \tilde{h}\tilde{h}') - (1 + We\dot{\gamma})(\tilde{f}' + 2\tilde{h}'') - \frac{WeA^{*2}}{\dot{\gamma}}(\tilde{f}'^3 + \tilde{f}'\tilde{g}'^2 + 2\tilde{f}'\tilde{h}'\tilde{f}'' + 2\tilde{h}'\tilde{g}'\tilde{g}'') - \frac{4We}{\dot{\gamma}}(2\tilde{f}\tilde{f}'\tilde{h}' + \tilde{h}'^2\tilde{h}'') = 0, \quad (11.19)$$

$$\frac{\tilde{\theta}''}{\text{Pr Re}}(1 + R) - \tilde{h}\tilde{\theta}' + \frac{Ec}{A^{*2}\text{Re}}(1 + We\dot{\gamma})(4\tilde{f}^2 + A^2(\tilde{f}'^2 + \tilde{g}'^2) + 2\tilde{h}'^2) + Q^*\tilde{\theta} = 0, \quad (11.20)$$

$$\tilde{h}(0) = 0, \quad \tilde{f}(0) = A_1, \quad \tilde{f}(1) = A_2, \quad \tilde{g}(0) = 1, \quad \tilde{g}(1) = \Omega,$$

$$\tilde{\theta}(0) = 1, \quad \tilde{\theta}(1) = 1, \quad P(1) = 0, \quad (11.21)$$

$$\dot{\gamma} = \sqrt{4\tilde{f}^2 + A^{*2}(\tilde{f}'^2 + \tilde{g}'^2) + 2\tilde{h}'^2}, \quad (11.22)$$

$$\begin{aligned} M &= \frac{\sigma B_0^2}{\rho\Omega_1}, \quad We = \frac{(\mu_0 - \mu_\infty)\Gamma\Omega_1}{\mu_0}, \quad \text{Pr} = \frac{\rho c_p \nu}{k}, \quad R = \frac{16\sigma^* T_2^3}{3kk^*}, \\ Q^* &= \frac{Q_0}{\rho c_p \Omega_1}, \quad A_1 = \frac{a_1}{\Omega_1}, \quad A_2 = \frac{a_2}{\Omega_1}, \quad \Omega = \frac{\Omega_2}{\Omega_1}, \quad \text{Re} = \frac{r^2 \Omega_1}{\nu}. \end{aligned} \quad (11.23)$$

11.1.1 Physical quantities

Surface drag force for radial and tangential directions at lower disk are

$$\left. \begin{aligned} C_{f0} &= \frac{\tau_{rz}|_{z=0}}{\mu_0 \Omega_1}, \\ C_{g0} &= \frac{\tau_{\psi z}|_{z=0}}{\mu_0 \Omega_1}, \end{aligned} \right\} \quad (11.24)$$

In dimensionless form one obtains

$$\begin{aligned} \frac{C_{f0}}{\sqrt{\text{Re}}} &= \left(1 + We \sqrt{4 \left(\tilde{f}(0) \right)^2 + \text{Re} \left(\left(\tilde{f}'(0) \right)^2 + \left(\tilde{g}'(0) \right)^2 \right) + 2 \left(\tilde{h}'(0) \right)^2} \right) \tilde{f}'(0), \\ \frac{C_{g0}}{\sqrt{\text{Re}}} &= \left(1 + We \sqrt{4 \left(\tilde{f}(0) \right)^2 + \text{Re} \left(\left(\tilde{f}'(0) \right)^2 + \left(\tilde{g}'(0) \right)^2 \right) + 2 \left(\tilde{h}'(0) \right)^2} \right) \tilde{g}'(0), \end{aligned} \quad (11.25)$$

where $\text{Re} = \frac{r^2 \Omega_1}{\nu}$ denotes Reynolds number.

At upper and lower disks the heat transfer rates are

$$Nu_{x0} = \frac{q_w}{k(\hat{T}_1 - \hat{T}_2)} \Big|_{z=0}, \quad Nu_{x1} = \frac{q_w}{k(\hat{T}_1 - \hat{T}_2)} \Big|_{z=h}, \quad (11.26)$$

where q_w satisfies [10]:

$$\left. \begin{aligned} q_w|_{z=0} &= -k \frac{\partial \hat{T}}{\partial z} + q_r \Big|_{z=0}, \\ q_w|_{z=(\nu/\Omega_1)^{0.5}} &= -k \frac{\partial \hat{T}}{\partial z} + q_r \Big|_{z=h}, \end{aligned} \right\} \quad (11.27)$$

Nusselt numbers in dimensionless form are

$$Nu_{x0} = -(1 + R) \tilde{\theta}'(0), \quad Nu_{x1} = -(1 + R) \tilde{\theta}'(1). \quad (11.28)$$

11.2 Solution technique

Initial approximations (\tilde{h}_0 , \tilde{f}_0 , \tilde{g}_0 and $\tilde{\theta}_0$) and linear operators ($\mathcal{L}_{\tilde{h}}$, $\mathcal{L}_{\tilde{f}}$, $\mathcal{L}_{\tilde{g}}$ and $\mathcal{L}_{\tilde{\theta}}$) can be put into the forms:

$$\tilde{h}_0 = 0, \quad \tilde{f}_0 = A_1(1 - \xi) + A_2\xi, \quad \tilde{g}_0 = 1 + \xi(\Omega - 1), \quad \tilde{\theta}_0 = 1 - \xi, \quad (11.29)$$

$$\mathcal{L}_{\tilde{h}} = \tilde{h}', \quad \mathcal{L}_{\tilde{f}} = \tilde{f}'', \quad \mathcal{L}_{\tilde{g}} = \tilde{g}'', \quad \mathcal{L}_{\tilde{\theta}} = \tilde{\theta}'', \quad (11.30)$$

$$\left. \begin{aligned} \mathcal{L}_{\hat{h}}[Z_1] &= 0, \\ \mathcal{L}_{\hat{f}}[Z_2 + Z_3\xi] &= 0, \\ \mathcal{L}_{\hat{g}}[Z_4 + Z_5\xi] &= 0, \\ \mathcal{L}_{\hat{\theta}}[Z_6 + Z_7\xi] &= 0, \end{aligned} \right\} \quad (11.31)$$

where $Z_i (i = 1 - 9)$ are constants.

11.3 Determination of entropy generation

In thermo-fluidic irreversibility occurs by heat transfer and viscous effects of fluid. In present analysis entropy generation is effected by heat transfer, viscous dissipation and Joule heating. Equation for entropy generation in dimensional form is [15,18]:

$$S_{gen}''' = \underbrace{\frac{k}{\hat{T}_m^2} \left(1 + \frac{16\sigma^* \hat{T}_2^3}{3kk^*} \right) [\nabla \hat{T}]^2}_{\text{heat transfer irreversibility}} + \underbrace{\frac{\mu}{\hat{T}_m} \Phi}_{\text{viscous dissipation irreversibility}} + \underbrace{\frac{1}{\hat{T}_m} [(\mathbf{J} - Q\mathbf{V}) \cdot (\mathbf{V} \times \mathbf{B})]}_{\text{Joule heating irreversibility}}, \quad (11.32)$$

where \hat{T}_m is mean temperature and $\nabla \hat{T}$, $\nabla \hat{C}$, Φ and \mathbf{J} are defined as

$$\nabla \hat{T} = \left[\frac{1}{r} \frac{\partial \hat{T}}{\partial \vartheta} \hat{e}_\vartheta + \frac{\partial \hat{T}}{\partial r} \hat{e}_r + \frac{\partial \hat{T}}{\partial z} \hat{e}_z \right], \quad (11.33)$$

$$\nabla \hat{C} = \left[\frac{1}{r} \frac{\partial \hat{C}}{\partial \vartheta} \hat{e}_\vartheta + \frac{\partial \hat{C}}{\partial r} \hat{e}_r + \frac{\partial \hat{C}}{\partial z} \hat{e}_z \right], \quad (11.34)$$

$$\Phi = (\mu_0 + (\mu_0 - \mu_\infty)\Gamma\dot{\gamma}) \left[\begin{aligned} & \left(\frac{\partial \hat{u}}{\partial r} - \frac{\hat{u}}{r} \right)^2 + 2 \left(\frac{\partial \hat{u}}{\partial r} \right)^2 + \left(\frac{\partial \hat{u}}{\partial z} + \frac{\partial \hat{w}}{\partial r} \right)^2 \\ & + 2 \left(\frac{\partial \hat{w}}{\partial z} \right)^2 + 2 \left(\frac{\hat{u}}{r} \right)^2 + \left(\frac{\partial \hat{v}}{\partial z} \right)^2 \end{aligned} \right], \quad (11.35)$$

$$J = \sigma(\mathbf{V} \times \mathbf{B}), \quad (11.36)$$

Note that electric field effects are omitted. By putting Eqs. (11.31 – 11.34) in Eq. (11.30) we get

$$S'''_{gen} = \frac{k}{\hat{T}_m^2} \left(1 + \frac{16\sigma^* \hat{T}_2^3}{3kk^*} \right) \left(\left(\frac{\partial \hat{T}}{\partial r} \right)^2 + \left(\frac{\partial \hat{T}}{\partial z} \right)^2 \right) + \frac{\sigma B_0^2}{\hat{T}_m} (\hat{u}^2 + \hat{v}^2) \left. \vphantom{S'''_{gen}} \right\} \\ + \frac{1}{\hat{T}_m} (\mu_0 + (\mu_0 - \mu_\infty) \Gamma \dot{\gamma}) \left[\begin{array}{l} 2 \left(\frac{\partial \hat{u}}{\partial r} \right)^2 + \left(\frac{\partial \hat{v}}{\partial r} - \frac{\hat{v}}{r} \right)^2 + \left(\frac{\partial \hat{u}}{\partial z} + \frac{\partial \hat{w}}{\partial r} \right)^2 \\ + 2 \left(\frac{\hat{u}}{r} \right)^2 + \left(\frac{\partial \hat{v}}{\partial z} \right)^2 + 2 \left(\frac{\partial \hat{w}}{\partial z} \right)^2 \end{array} \right]. \quad (11.37)$$

In Eq. (11.35) first, second and third terms are due to heat transfer irreversibility with radiation effect, Joule heating irreversibility and viscous dissipation irreversibility respectively. After applying transformations dimensionless one arrives at

$$N_G = [1 + R] \theta'^2 \alpha_1 + MBr(\tilde{f}^2 + \tilde{g}^2) + \frac{Br}{A^{*2}} (1 + We\dot{\gamma})(4\tilde{f}'^2 + A^{*2}(\tilde{f}'^2 + \tilde{g}'^2) + 2\tilde{h}'^2), \quad (11.38)$$

with

$$\alpha_1 = \frac{\Delta \hat{T}}{\hat{T}_m}, \quad Br = \frac{\mu r^2 \Omega_1^2}{k \Delta \hat{T}}, \\ N_G = \frac{S'''_{gen} \hat{T}_m h^2}{k \Delta \hat{T}}. \quad (11.39)$$

Bejan number is

$$Be = \frac{[1 + R] \theta'^2 \alpha_1}{[1 + R] \theta'^2 \alpha_1 + MBr(\tilde{f}^2 + \tilde{g}^2) + \frac{Br}{A^{*2}} (1 + We\dot{\gamma})(4\tilde{f}'^2 + A^{*2}(\tilde{f}'^2 + \tilde{g}'^2) + 2\tilde{h}'^2)} \quad (11.40)$$

11.4 Convergence analysis

HAM technique is applied for convergence of our solutions. There are auxiliary parameters $\tilde{h}_{\tilde{h}}$, $\tilde{h}_{\tilde{f}}$, $\tilde{h}_{\tilde{g}}$ and $\tilde{h}_{\tilde{\theta}}$ which gave us freedom for controlling our convergence region. The regions of \tilde{h} for velocities and temperature where our solutions is convergent include $-0.4 \leq \tilde{h}_{\tilde{h}} \leq -1.3$,

$-1.2 \leq \tilde{h}_{\tilde{f}} \leq -0.2$, $-1.2 \leq \tilde{h}_{\tilde{g}} \leq -0.3$ and $-1.2 \leq \tilde{h}_{\tilde{\theta}} \leq -0.6$.

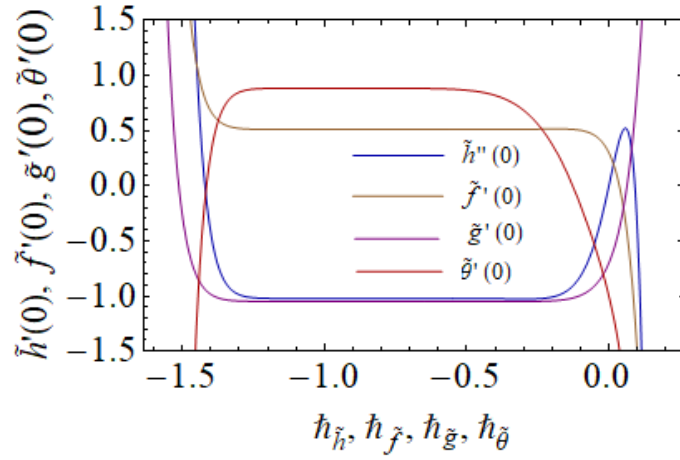


Fig. 11.2: \tilde{h} -curves of velocities ($\tilde{h}''(0)$, $\tilde{f}'(0)$, $\tilde{g}'(0)$) and temperature ($\tilde{\theta}'(0)$).

Table 11.1: Numerical values for convergence of series solutions.

Order of approximation	$-\tilde{h}''(0)$	$\tilde{f}'(0)$	$-\tilde{g}'(0)$	$-\tilde{\theta}'(0)$
1	0.4200000	0.4853426	0.9141499	0.4634267
20	1.022671	0.5113370	1.049157	0.8852918
22	1.022674	0.5113378	1.049155	0.8852522
23	1.022675	0.5113379	1.049155	0.8852446
24	1.022676	0.5113379	1.049155	0.8852409
26	1.022676	0.5113379	1.049155	0.8852388
30	1.022676	0.5113379	1.049155	0.8852388
40	1.022676	0.5113379	1.049155	0.8852388
50	1.022676	0.5113379	1.049155	0.8852388

11.5 Physical results

Behaviors of velocity, temperature, skin friction, Bejan number, entropy generation and Nusselt number are analyzed in this section.

11.5.1 Velocity components

Figs. (11.3 – 11.5) witness the influence of magnetic parameter (M) on axial, radial and tangential velocities (\tilde{h} , \tilde{f} , \tilde{g}). For larger values of ($M = 0, 0.4, 0.8, 1.2, 1.6$) motion of the fluid reduces. It is observed that for higher (M) the Lorentz force which is in direct relation with (M) enhances so it produces resistance for fluid particles and consequently (\tilde{h} , \tilde{f} , \tilde{g}) reduces. Similar behavior is noted near lower and upper disk. Figs. (11.6-11.11) are sketched to examine the effect of stretching parameters of lower and upper disks ($A_1 = 0, 0.2, 0.4, 0.6, 0.8$ and $A_2 = 0, 0.2, 0.4, 0.6, 0.8$) on (\tilde{h} , \tilde{f} , \tilde{g}). It is noted that axial and radial velocities are increasing functions of (A_1 and A_2) while opposite impact is seen for tangential velocity ($\tilde{g}(\xi)$). Physically for larger (A_1 and A_2) the stretching rates of respective disks become greater. That is why the axial and radial velocities increase. Also rotational velocity is in inverse relation with tangential velocity so ($\tilde{g}(\xi)$) decays for larger (A_1 and A_2). Impact of Weissenberg number (We) on axial, radial and tangential velocities is displayed in Figs. (11.12 – 11.14). It is analyzed that axial and tangential velocities are increasing functions of ($We = 0, 0.5, 1, 1.5, 2$) while radial velocity decays for (We). It is due to an increase in viscosity. Fig. 11.15 shows impact of rotational parameter (Ω) on ($\tilde{g}(\xi)$). Increasing trend of ($\tilde{g}(\xi)$) is noticed for larger ($\Omega = 0, 0.3, 0.6, 0.9, 1.2$).

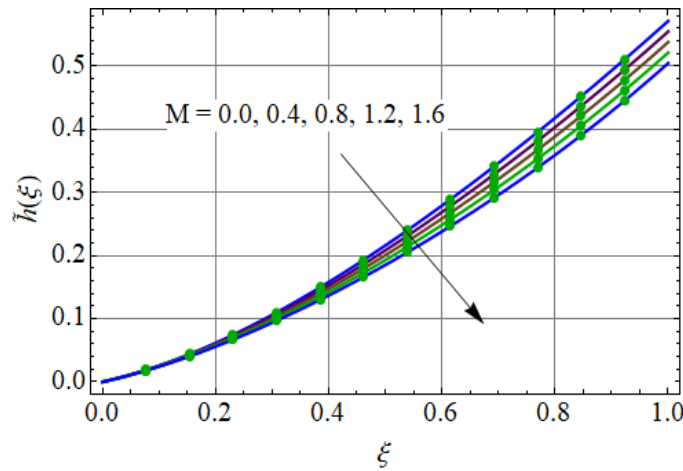


Fig. 11.3: \tilde{h} via M .

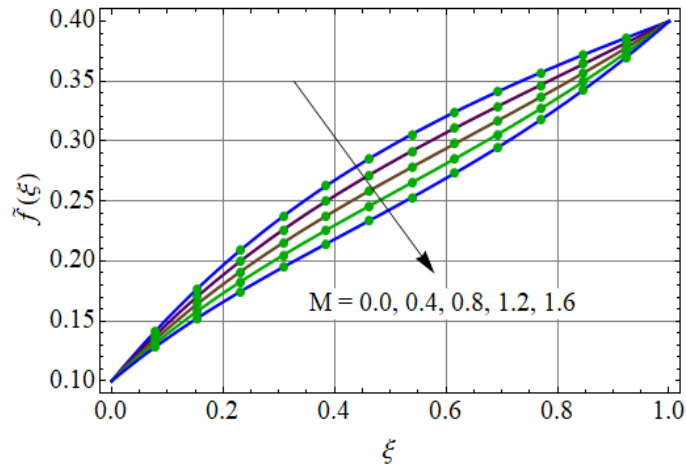


Fig. 11.4: \tilde{f} via M .

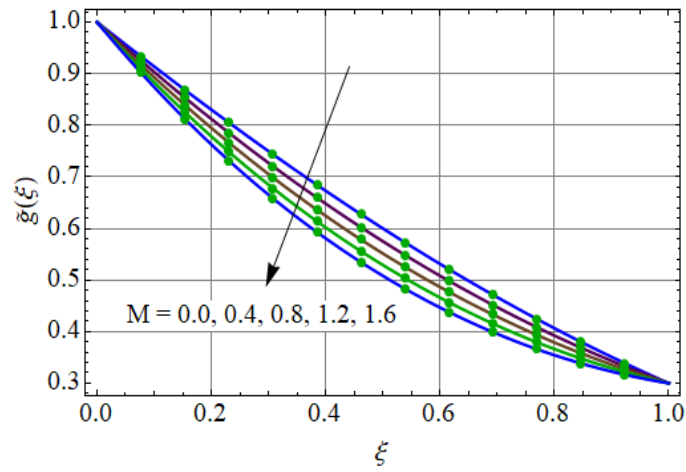


Fig. 11.5: \tilde{g} via M .

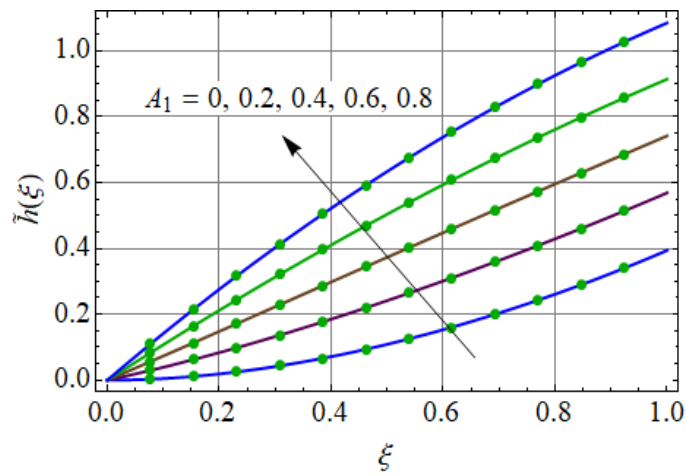


Fig. 11.6: \tilde{h} via A_1 .

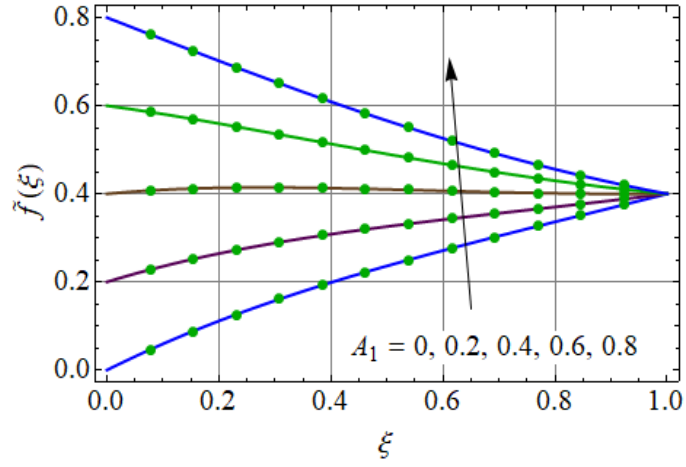


Fig. 11.7: \tilde{f} via A_1 .

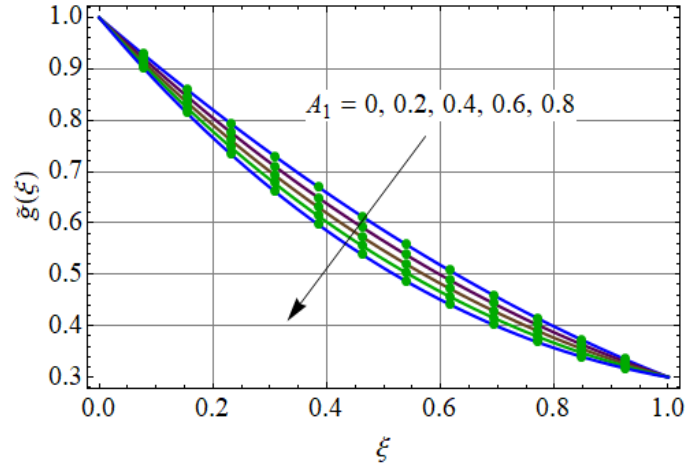


Fig. 11.8: \tilde{g} via A_1 .

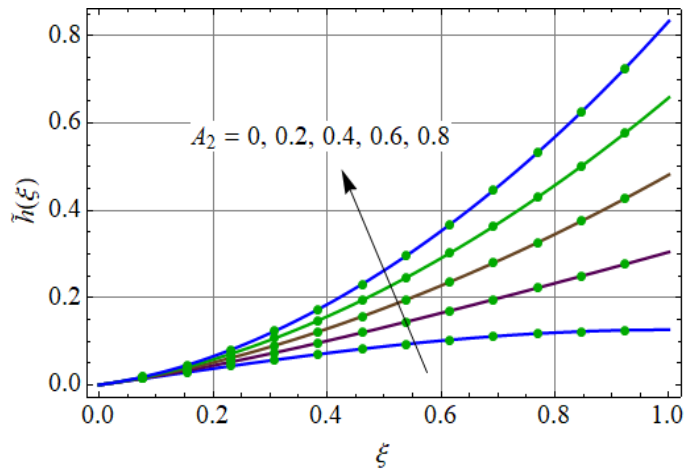


Fig. 11.9: \tilde{h} via A_2 .

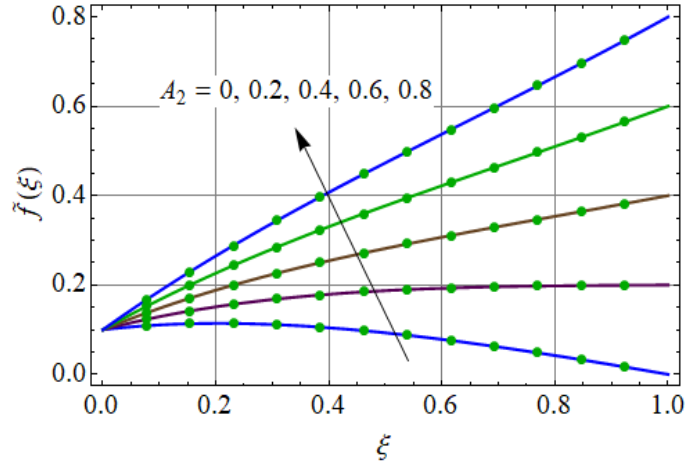


Fig. 11.10: \tilde{f} via A_2 .

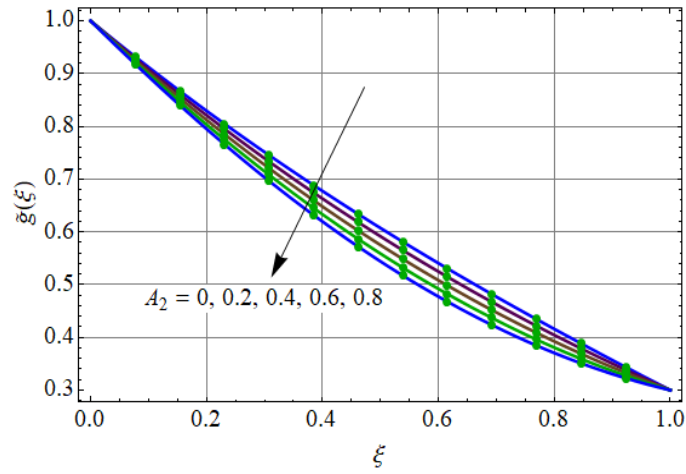


Fig. 11.11: \tilde{g} via A_2 .

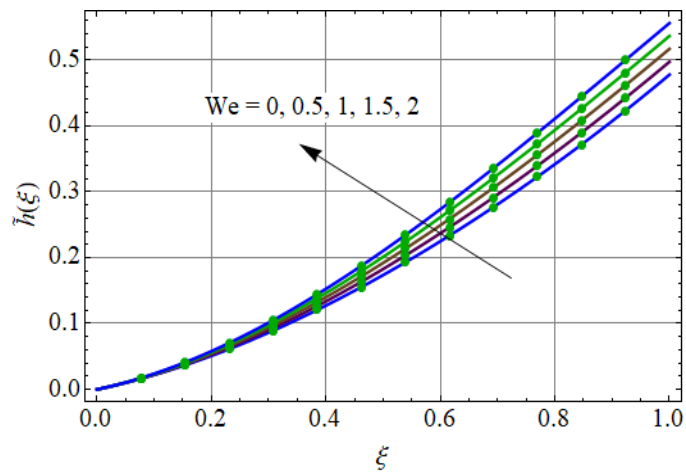


Fig. 11.12: \tilde{h} via We .

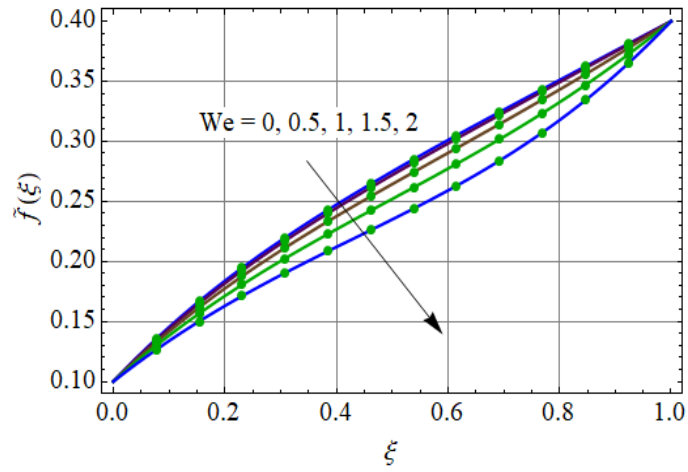


Fig. 11.13: \tilde{f} via We .

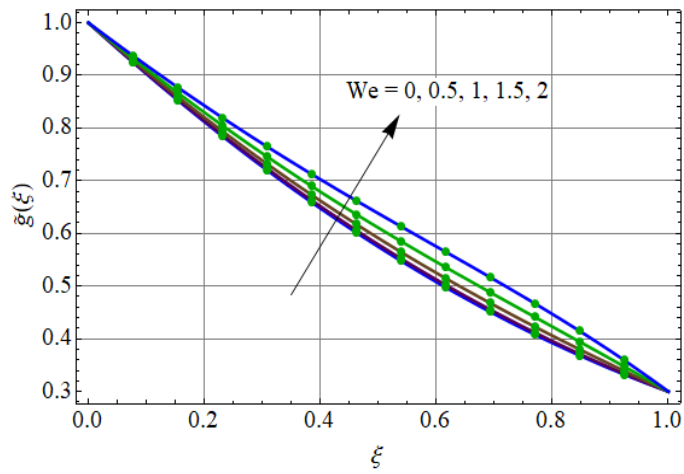


Fig. 11.14: \tilde{g} via We .

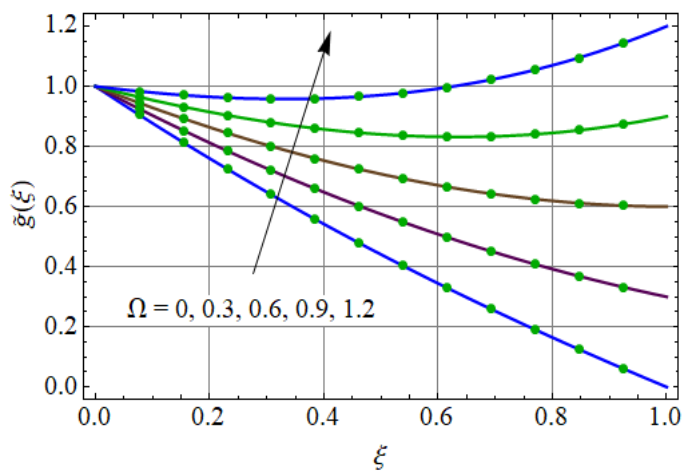


Fig. 11.15: \tilde{g} via Ω .

11.5.2 Temperature

Figs. (11.16–11.19) are displayed for outcomes of Weissenberg number (We), heat source parameter (Q^*), Eckert number (Ec) and radiation parameter (R). Fig. 11.16 elucidates the effect of Weissenberg number (We) on temperature ($\tilde{\theta}(\xi)$). It is worth mentioning that temperature of the fluid rises for larger ($We = 0, 0.5, 1, 1.5, 2$). It is due to an increase in resistance for more viscosity. For larger values of heat source parameter ($Q^* = 0, 0.3, 0.6, 0.9, 1.2$) temperature ($\tilde{\theta}(\xi)$) enhances (see Fig. 11.17). For rising (Q^*) more heat is provided to the system and so temperature enhances. Behaviors of ($\tilde{\theta}(\xi)$) for larger Eckert number ($Ec = 0, 0.2, 0.4, 0.6, 0.8$) and radiation parameter ($R = 0, 0.3, 0.6, 0.9, 1.2$) are mentioned in Figs. 11.18 and 11.19. It is noticed that both parameters are used to boost up the temperature ($\tilde{\theta}(\xi)$). Eckert number actually witnesses the heat dissipation in the system because it is relation between enthalpy difference and kinetic energy. Hence for larger (Ec) the kinetic energy enhances which increases the friction inside the fluid and consequently temperature of fluid (see Fig. 11.18). Mean absorption coefficient reduces for larger (R) which is responsible for an increase in temperature ($\tilde{\theta}(\xi)$) (see Fig. 11.19).

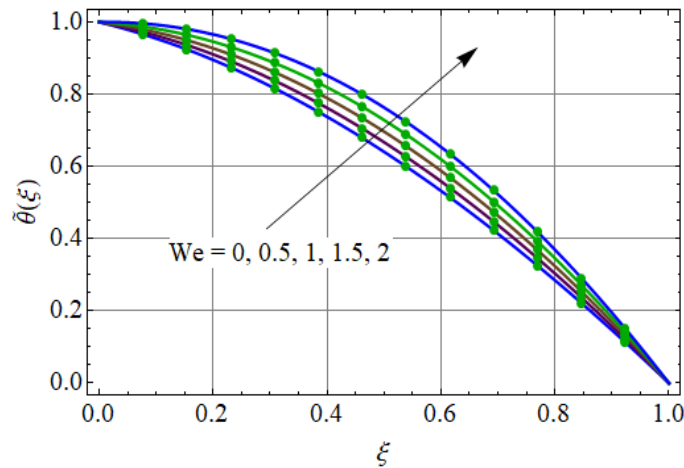


Fig. 11.16: $\tilde{\theta}$ via We .

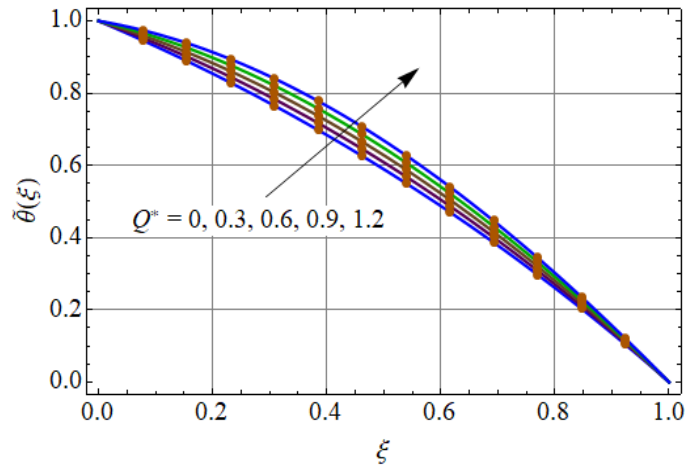


Fig. 11.17: $\tilde{\theta}$ via Q^* .

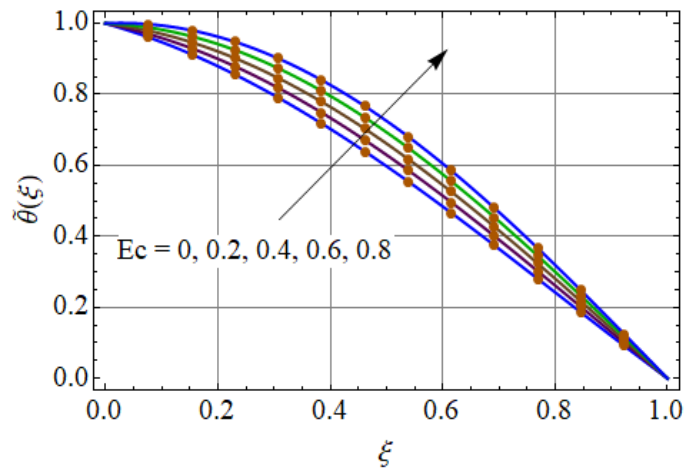


Fig. 11.18: $\tilde{\theta}$ via Ec .

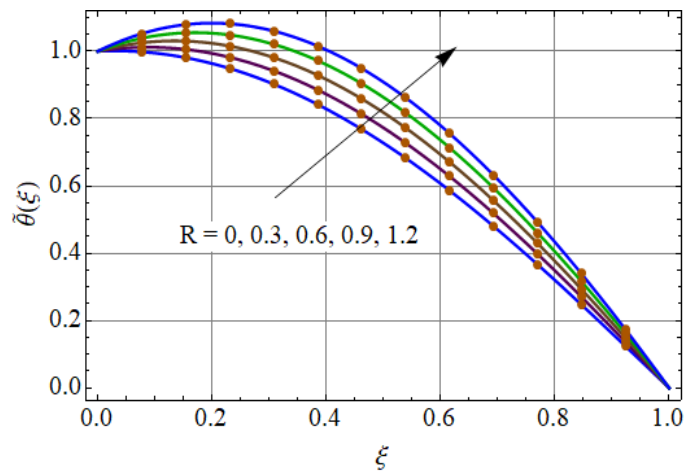


Fig. 11.19: $\tilde{\theta}$ via R .

11.5.3 Bejan number and entropy generation

Figs. (11.20 – 11.29) analyze the impacts of Hartmann number (M), Brinkman number (Br), Weissenberg number (We), stretching parameter of lower disk (A_1) and radiation parameter (R) on Bejan number (Be) and entropy generation (N_G) at lower and upper disks. One can easily examine that entropy rate enhances for larger (M) while Bejan number behaves oppositely for higher (M). As we increase the values of ($M = 0, 0.4, 0.8, 1.2, 1.6$) the Lorentz force enhances which produces resistance in the system and consequently disorderedness also increases (see Fig. 11.20). With increasing values of (M) the viscous dissipation irreversibility dominant over than heat transfer irreversibility so Bejan number reduces (see Fig. 11.21). Effect of (Br) on entropy generation and Bejan number (Be) is delineated in Figs. 11.22 and 11.23. For larger ($Br = 0, 0.2, 0.4, 0.6, 0.8$) entropy generation (N_G) enhances (see Fig. 11.22). In fact when we increase (Br) dissipation produces less conduction rate and thus enhances entropy generation increases. We can see that Bejan number is equals to 1 when ($Br = 0$). In fact for ($Br = 0$) the viscous dissipation irreversibility vanishes and only heat transfer irreversibility retains. Hence for ($Br = 0$) Bejan number is maximum and when we increase Br from 0.2 to 0.8 then it starts decreasing (see Fig. 11.23). Figs. 11.24 and 11.25 disclose the behavior of Bejan number (Be) and entropy generation (N_G) for variation of Weissenberg number (We) at lower and upper disks. It is worthmentioning that for larger ($We = 0, 0.2, 0.4, 0.6, 0.8$) the entropy generation increases and Bejan number reduces. Viscosity difference enhances for larger (We) which increases the resistance and ultimately disorderedness (entropy generation N_G) in the system (see Fig. 11.24). Bejan number reduces via (We) (see Fig. 11.25). Entropy generation (N_G) and Bejan number (Be) trend for rising stretching parameter (A_1) is shown in Figs. (11.26 and 11.27). Here Bejan number and entropy generation have opposite impacts for variation of ($A_1 = 0, 0.1, 0.2, 0.3, 0.4$). It is analyzed that entropy generation (N_G) and Bejan number (Be) are increased via larger radiation parameter (R). Increase in internal energy of the system is noticed for higher ($R = 0, 0.2, 0.4, 0.6, 0.8$). That is why disorderedness in the system enhances (see Fig. 11.26). With higher radiation (R) the heat transfer irreversibility

becomes more prominent than viscous dissipation irreversibility therefore (Be) rises.

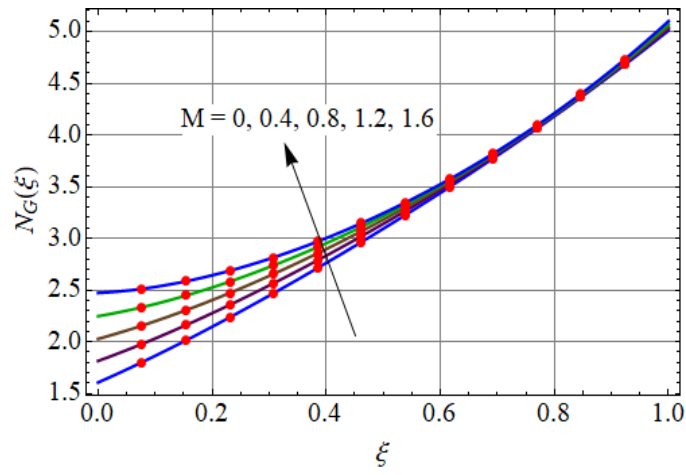


Fig. 11.20: N_G via M .

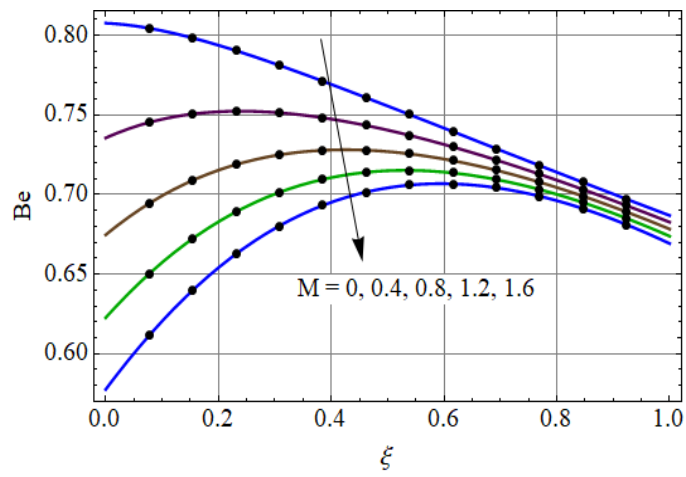


Fig. 11.21: Be via M .

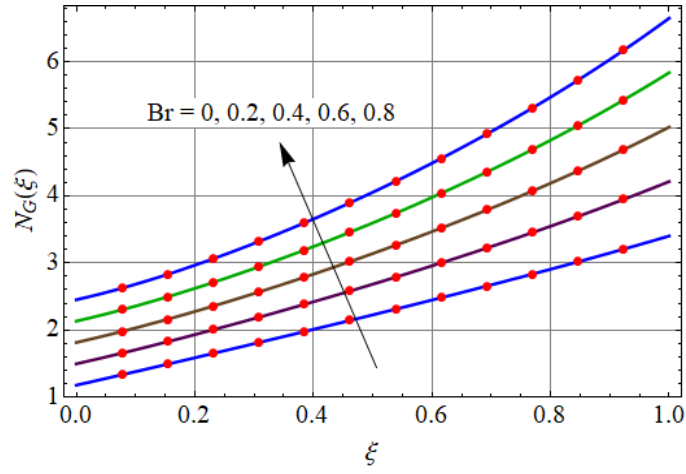


Fig. 11.22: N_G via Br .

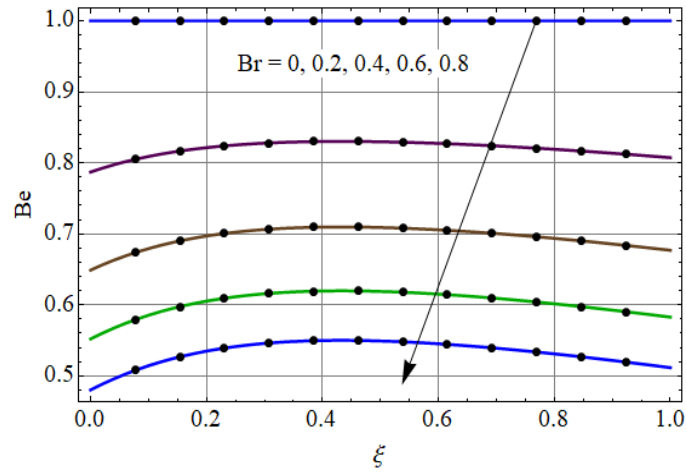


Fig. 11.23: Be via Br .

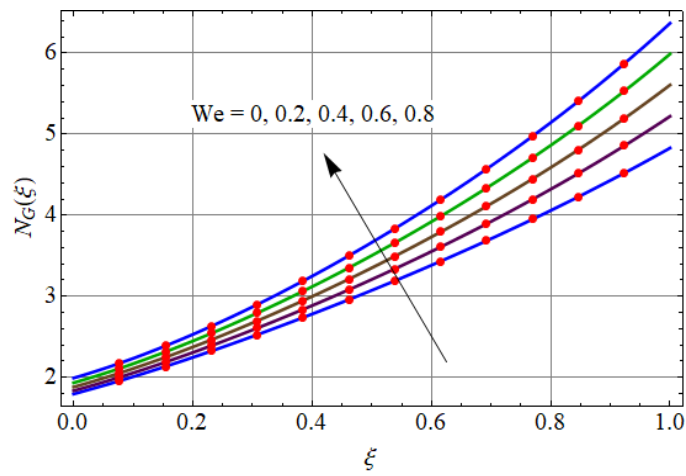


Fig. 11.24: N_G via We .

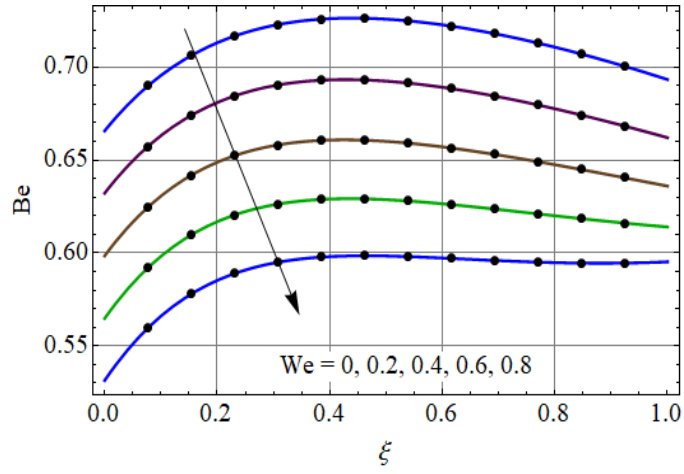


Fig. 11.25: Be via We .

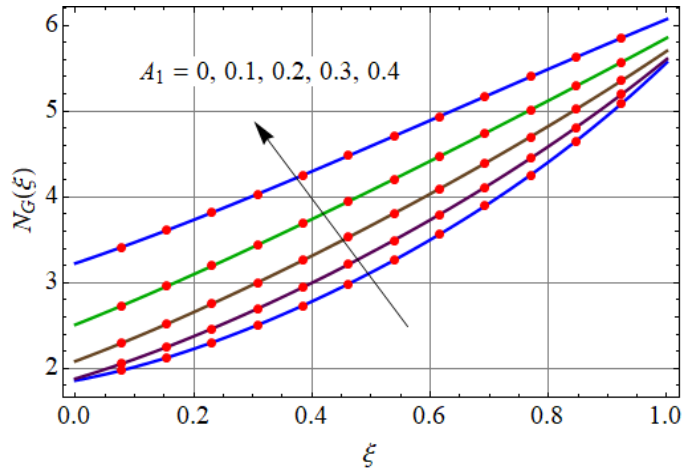


Fig. 11.26: N_G via A_1 .

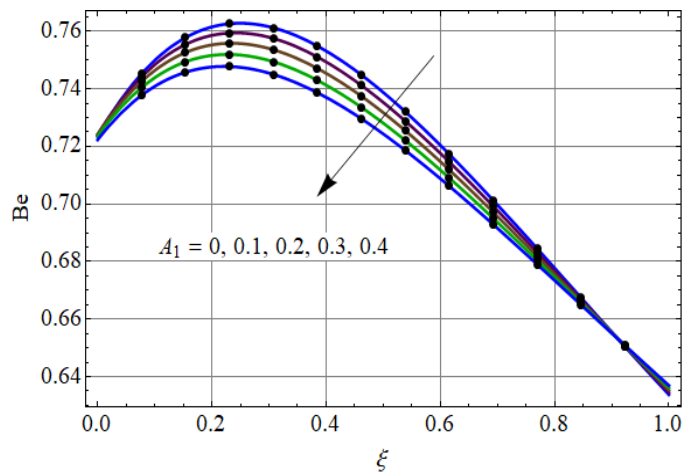


Fig. 11.27: Be via A_1 .

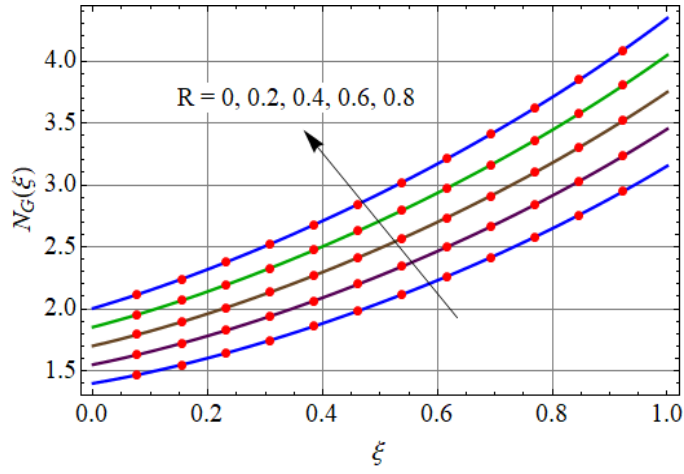


Fig. 11.28: N_G via R .

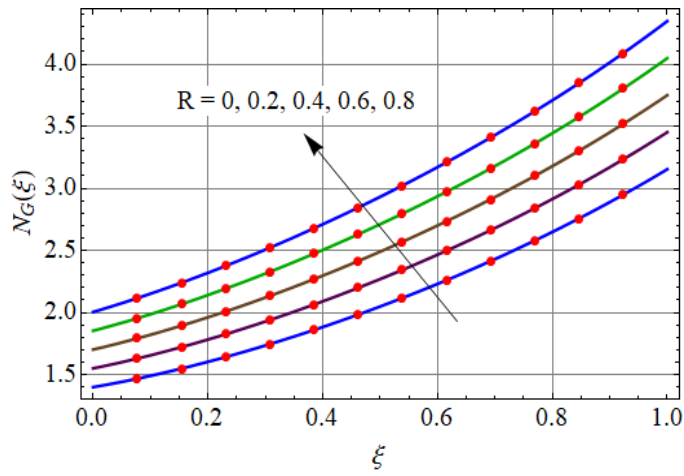


Fig. 11.28: N_G via R .

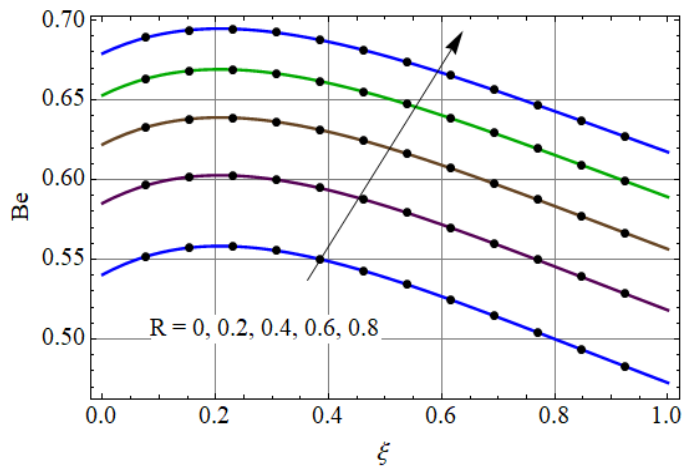


Fig. 11.29: Be via R .

11.5.4 Skin friction and Nusselt number

Tables 11.2 and 11.3 depict behaviors of skin friction coefficient and heat transfer rates at lower and upper disks respectively for larger Weissenberg number (We), Hartmann number (M) and radiation parameter (R). It is shown that at lower disk the magnitude of surface drag force in radial and transverse directions increases for larger ($We = 0.1, 0.2, 0.3$). Furthermore opposite impacts of C_{f0} and C_{g0} are noticed for larger (M) (see Table 11.2). Table 11.3 delineates that heat transfer rate enhances at lower and upper disks with increasing (R) while for larger (We) the Nusselt number reduces.

Table 11.2: Surface drag force at lower disk for different values of We and M .

We	M	C_{f0}	$-C_{g0}$
0.1	0.4	0.550420	1.12934
0.2		0.590397	1.20342
0.3		0.630044	1.27751
0.1	0.5	0.538203	1.15981
	0.6	0.526205	1.19000

Table 11.3: Heat transfer rate at lower and upper disks for larger values of R and We .

R	We	$-\tilde{\theta}(0)$	$-\tilde{\theta}(1)$
1.0	0.1	0.88524	3.2134
1.1		0.78022	3.0975
1.2		0.68606	2.9933
1.0	0.2	0.94264	3.3089
	0.3	0.99978	3.4040

11.6 Conclusions

Main results are mentioned below:

- Axial and tangential velocities increase for larger (We).
- Impacts of Q^* , We and Ec on temperature are increasing.

- Entropy generation (disorderedness) in the system is more for larger (Br) , (M) , (R) and (We) .
- Bejan number is equals to 1 (maximum) when $(Br = 0)$ and it starts decreasing with increasing (Br) .
- Surface drag force (C_{f0}, C_{g0}) rises for larger (We) .
- Opposite impacts of (R) and (We) are noticed for heat transfer rate.

Chapter 12

Novel aspects of Soret and Dufour in entropy generation minimization for Williamson fluid flow

Abstract: MHD flow of Williamson fluid between two rotating disks is discussed. Soret and Dufour effects are analyzed. Impacts of stratification, viscous dissipation and activation energy are also considered. Bejan number and entropy generation for stratified flow is discussed. Von-Karman relations lead to ordinary differential equations (ODEs). Convergent solution of complicated ODE's is found by homotopic procedure. The results of physical quantities are discussed through plots and numerical values.

12.1 Formulation

Steady flow of Williamson fluid between two rotating stretchable disks is studied. Our aim is to scrutinize the entropy generation minimization (*EGM*) in flow with effects of Dufour/Soret, stratification and viscous dissipation. Chemical reaction with activation energy is also investigated. Flow is initiated due to stretching of disks. The lower at ($z = 0$) and upper at ($z = h$) disks have respective angular velocities Ω_1 and Ω_2 . Flow is caused by stretching of lower disk. Lower and upper disks correspond to temperatures (\hat{T}_1, \hat{T}_2) and concentration (\hat{C}_1, \hat{C}_2) . A

uniform magnetic field of strength (B_0) is exerted in the z -direction (see Fig. 12.1).

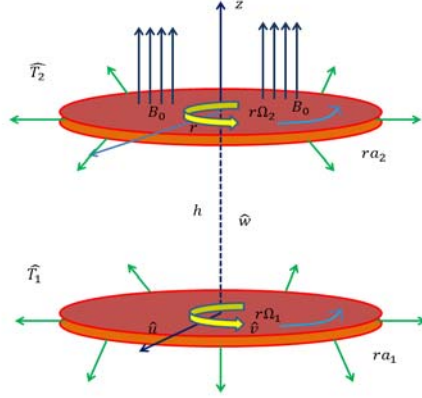


Fig. 12.1. Flow geometry.

An extra stress tensor (τ) of Williamson fluid is

$$\tau = \left[\mu_\infty + \frac{(\mu_0 - \mu_\infty)}{1 - \Gamma \dot{\gamma}} \right] \mathbf{A}, \quad (12.1)$$

where (\mathbf{A}) denotes first Rivlin-Erickson tensor, (μ_0) the zero shear rate viscosity and (μ_∞) infinite shear rate viscosity and ($\Gamma > 0$) a time constant. Here ($\dot{\gamma}$) is defined by

$$\dot{\gamma} = \sqrt{\frac{1}{2} (tr \mathbf{A}^2)}. \quad (12.2)$$

Through Eq. (12.1) one obtains

$$\tau = (\mu_0 + (\mu_0 - \mu_\infty) \Gamma \dot{\gamma}) \mathbf{A}, \quad (12.3)$$

which further yields

$$\begin{aligned} \tau_{rr} &= 2((\mu_0 - \mu_\infty) \Gamma \dot{\gamma} + \mu_0) \left(\frac{\partial \hat{u}}{\partial r} \right), \quad \tau_{\vartheta\vartheta} = 2((\mu_0 - \mu_\infty) \Gamma \dot{\gamma} + \mu_0) \left(\frac{1}{r} \frac{\partial \hat{v}}{\partial \vartheta} + \frac{\hat{u}}{r} \right), \\ \tau_{zz} &= 2((\tilde{\mu}_0 - \tilde{\mu}_\infty) \Gamma \dot{\gamma} + \tilde{\mu}_0) \left(\frac{\partial \hat{w}}{\partial z} \right), \quad \tau_{\vartheta r} = \tau_{r\vartheta} = ((\mu_0 - \mu_\infty) \Gamma \dot{\gamma} + \mu_0) \left(\frac{1}{r} \frac{\partial \hat{u}}{\partial \vartheta} + \frac{\partial \hat{v}}{\partial r} - \frac{\hat{v}}{r} \right), \\ \tau_{rz} &= \tau_{zr} = ((\mu_0 - \mu_\infty) \Gamma \dot{\gamma} + \mu_0) \left(\frac{\partial \hat{w}}{\partial r} + \frac{\partial \hat{u}}{\partial z} \right), \quad \tau_{z\vartheta} = \tau_{\vartheta z} = ((\mu_0 - \mu_\infty) \Gamma \dot{\gamma} + \mu_0) \left(\frac{1}{r} \frac{\partial \hat{w}}{\partial \vartheta} + \frac{\partial \hat{v}}{\partial z} \right) \end{aligned}$$

$$\dot{\gamma} = \sqrt{\frac{2 \left[\left(\frac{\partial \hat{u}}{\partial r} \right)^2 + \left(\frac{\partial \hat{w}}{\partial z} \right)^2 + \left(\frac{\hat{u}}{r} + \frac{1}{r} \frac{\partial \hat{v}}{\partial \vartheta} \right)^2 \right] + \left(\frac{1}{r} \frac{\partial \hat{u}}{\partial \vartheta} + \frac{\partial \hat{v}}{\partial r} - \frac{\hat{v}}{r} \right)^2 + \left(\frac{\partial \hat{v}}{\partial z} + \frac{1}{r} \frac{\partial \hat{w}}{\partial \vartheta} \right)^2}{\left(\frac{\partial \hat{w}}{\partial r} + \frac{\partial \hat{u}}{\partial z} \right)^2}}. \quad (12.5)$$

Mathematical statements for problem under consideration satisfy

$$\frac{\partial \hat{u}}{\partial r} + \frac{\hat{u}}{r} + \frac{\partial \hat{w}}{\partial z} = 0, \quad (12.6)$$

$$\rho \left(\hat{w} \frac{\partial \hat{u}}{\partial z} + \hat{u} \frac{\partial \hat{u}}{\partial r} - \frac{\hat{v}^2}{r} \right) = -\frac{\partial \hat{p}}{\partial r} + \frac{\partial \tau_{rr}}{\partial r} + \frac{\partial \tau_{zr}}{\partial z} + \frac{\tau_{rr} - \tau_{\vartheta\vartheta}}{r} - \sigma B_0^2 \hat{u}, \quad (12.7)$$

$$\rho \left(\hat{u} \frac{\partial \hat{v}}{\partial r} + \hat{w} \frac{\partial \hat{v}}{\partial z} + \frac{\hat{v} \hat{u}}{r} \right) = \frac{\partial \tau_{r\vartheta}}{\partial r} + \frac{\partial \tau_{z\vartheta}}{\partial z} + 2 \frac{\tau_{r\vartheta}}{r} - \sigma B_0^2 \hat{v}, \quad (12.8)$$

$$\rho \left(\hat{u} \frac{\partial \hat{w}}{\partial r} + \hat{w} \frac{\partial \hat{w}}{\partial z} \right) = -\frac{\partial \hat{p}}{\partial z} + \frac{\partial \tau_{rz}}{\partial r} + \frac{\partial \tau_{zz}}{\partial z} + \frac{\tau_{rz}}{r}, \quad (12.9)$$

$$\left[\hat{u} \frac{\partial \hat{T}}{\partial r} + \hat{w} \frac{\partial \hat{T}}{\partial z} \right] = \frac{k}{\rho c_p} \left(\frac{\partial^2 \hat{T}}{\partial z^2} + \frac{\partial^2 \hat{T}}{\partial r^2} + \frac{1}{r} \frac{\partial \hat{T}}{\partial r} \right) + \tau.L + \frac{D_m K_T}{c_p C_s} \left(\frac{\partial^2 \hat{C}}{\partial r^2} + \frac{\partial^2 \hat{C}}{\partial z^2} + \frac{1}{r} \frac{\partial \hat{C}}{\partial r} \right), \quad (12.10)$$

$$\begin{aligned} \hat{u} \frac{\partial \hat{C}}{\partial r} + \hat{w} \frac{\partial \hat{C}}{\partial z} &= D \left(\frac{\partial^2 \hat{C}}{\partial r^2} + \frac{\partial^2 \hat{C}}{\partial z^2} + \frac{1}{r} \frac{\partial \hat{C}}{\partial r} \right) + \frac{D_m K_T}{\hat{T}_m} \left(\frac{1}{r} \frac{\partial \hat{T}}{\partial r} + \frac{\partial^2 \hat{T}}{\partial r^2} + \frac{\partial^2 \hat{T}}{\partial z^2} \right) \\ &\quad - k_r^2 (\hat{C} - \hat{C}_2) \left(\frac{\hat{T}}{\hat{T}_2} \right)^n \exp \left(\frac{-E_a}{\kappa \hat{T}} \right), \end{aligned} \quad (12.11)$$

$$\tau.L = [(\mu_0 - \mu_\infty) \Gamma \dot{\gamma} + \mu_0] \left[2 \left(\frac{\partial \hat{u}}{\partial r} \right)^2 + 2 \left(\frac{\partial \hat{w}}{\partial z} \right)^2 - 2 \frac{\hat{v}}{r} \frac{\partial \hat{v}}{\partial r} + \left(\frac{\partial \hat{v}}{\partial r} \right)^2 + \frac{\hat{v}^2}{r^2} + 2 \frac{\hat{u}^2}{r^2} + \left(\frac{\partial \hat{u}}{\partial z} \right)^2 + \left(\frac{\partial \hat{v}}{\partial z} \right)^2 \right] \quad (12.12)$$

$$\begin{aligned} \hat{u} &= a_1 r, \quad \hat{v} = \Omega_1 r, \quad \hat{w} = 0, \quad \hat{T} = \hat{T}_1 = A_s r + \hat{T}_0, \quad \hat{C} = \hat{C}_1 = C_s r + \hat{C}_0, \quad \text{at } z = 0, \\ \hat{u} &= a_2 r, \quad \hat{v} = \Omega_2 r, \quad \hat{p} = 0, \quad \hat{C} = \hat{C}_2 = D_s r + \hat{C}_0, \quad \hat{T} = \hat{T}_2 = B_s r + \hat{T}_0 \quad \text{at } z = h, \end{aligned} \quad (12.13)$$

where in (r, ϑ, z) directions the velocity components are $(\check{u}, \check{v}, \check{w})$ respectively, (\hat{p}) the hydrostatic pressure, (C_p) specific heat, (ρ) density of fluid, (k) thermal conductivity, (D_m) the effective diffusivity rate of mass, (C_s) the Susceptibility of concentration, (K_T) thermal-diffusion ratio, (k_r) the reaction rate, (σ) electrical conductivity, (E_α) activation energy where $(\kappa = 8.61 \times 10^{-5} eV/K)$ the Boltzmann constant, (n) the fitted rate constant and (T_m) mean

temperature of fluid.

Suitable transformations for this analysis are

$$\begin{aligned}\hat{u} &= r\Omega_1 \tilde{f}(\xi), \quad \hat{v} = r\Omega_1 \tilde{g}(\xi), \quad \hat{w} = h\Omega_1 \tilde{h}(\xi), \\ \tilde{\phi}(\xi) &= \frac{\hat{C} - \hat{C}_2}{\hat{C}_1 - \hat{C}_0}, \quad \tilde{P}(\xi) = \frac{\hat{p}}{\rho h^2 \Omega_1^2}, \quad \tilde{\theta}(\xi) = \frac{\hat{T} - \hat{T}_2}{\hat{T}_1 - \hat{T}_0}, \quad \xi = \frac{z}{h},\end{aligned}\quad (12.14)$$

Eq. (12.1) is satisfied and Eqs. (12.7 – 12.13) take the forms

$$\tilde{h}' + 2\tilde{f} = 0 \quad (12.15)$$

$$(1 + We\dot{\gamma}) \tilde{f}'' + \text{Re}(-\tilde{f} + \tilde{g}^2 - \tilde{h}\tilde{f}' - M\tilde{f}) + \frac{WeA^{*2}}{\dot{\gamma}} (\tilde{f}''\tilde{f}'^2 + \tilde{g}''\tilde{g}'\tilde{f}') + \frac{2We}{\dot{\gamma}} (\tilde{h}''\tilde{h}'\tilde{f}' + 3\tilde{f}'^2\tilde{f} + \tilde{g}'^2\tilde{f}) = 0, \quad (12.16)$$

$$(1 + We\dot{\gamma}) \tilde{g}'' - M\tilde{g} + \frac{WeA^{*2}}{\dot{\gamma}} (\tilde{g}''\tilde{g}'^2 + \tilde{g}''\tilde{g}'\tilde{f}') - \tilde{h}\tilde{g}' + \frac{2We}{\dot{\gamma}} (\tilde{g}'\tilde{h}'\tilde{h}'' + 2\tilde{g}'\tilde{f}\tilde{f}') - 2\tilde{g}\tilde{f} = 0, \quad (12.17)$$

$$\begin{aligned}\text{Re}(P' + \hat{h}'\hat{h}) - \frac{WeA^{*2}}{\dot{\gamma}} (\tilde{f}'^3 + \tilde{f}'\tilde{g}'^2 + \tilde{f}''\tilde{f}'\tilde{h}' + \tilde{g}''\tilde{g}'\tilde{h}') - 2(1 + We\dot{\gamma}) (\tilde{f}' + \tilde{h}'') \\ - \frac{4We}{\dot{\gamma}} (2\tilde{f}\tilde{f}'\tilde{h}' + \tilde{h}''\tilde{h}'^2) = 0\end{aligned}\quad (12.18)$$

$$\begin{aligned}\text{Re}\tilde{\theta}'' + (\tilde{\theta} + S) - (\text{Re})(\text{Pr}) (\tilde{h}\tilde{\theta}' + S\tilde{f} + \tilde{\theta}\tilde{f}) + Du (\text{Re}\tilde{\phi}'' + \tilde{\phi} + Z) \\ + (Ec)(\text{Pr})(1 + We\dot{\gamma}) (4\tilde{f}'^2 + \text{Re}\tilde{f}'^2 + \text{Re}\tilde{g}'^2 + 2\tilde{h}'^2) = 0,\end{aligned}\quad (12.19)$$

$$\begin{aligned}\text{Re}\tilde{\phi}'' - \text{Re}Sc\tilde{f} (Z + \tilde{\phi}) - \text{Re}(Sc)\tilde{\phi}'\tilde{h} + Sr (\text{Re}\tilde{\theta}'' + S + \tilde{\theta}) + (\tilde{\phi} + Z) \\ - R^* (\text{Re}) Sc (1 + \alpha_1\tilde{\theta})^n \exp\left(\frac{-E_1}{1 + \alpha_1\tilde{\theta}}\right) \tilde{\phi} = 0,\end{aligned}\quad (12.20)$$

with boundary conditions

$$\begin{aligned}\tilde{f}(0) &= A_1, \quad \tilde{h}(0) = 0, \quad \tilde{g}(0) = 1, \quad \tilde{\phi}(0) = 1 - Z, \quad \tilde{\theta}(0) = 1 - S, \quad \text{at } \xi = 0, \\ \tilde{f}(1) &= A_2, \quad \tilde{g}(1) = \Omega, \quad \tilde{\theta}(1) = 0, \quad P(1) = 0, \quad \tilde{\phi}(1) = 0, \quad \text{at } \xi = 1.\end{aligned}\quad (12.21)$$

$$\tilde{\gamma} = \sqrt{4\tilde{f}^2 + \text{Re}(\tilde{f}'^2 + \tilde{g}'^2)} + 2\tilde{h}'^2 \quad (12.22)$$

where

$$\begin{aligned} M &= \frac{\sigma B_0^2}{\rho \Omega_1}, \quad \text{Re} = \frac{\Omega_1 r^2}{\nu}, \quad R^* = \frac{k_r^2}{\Omega_1}, \quad E_1 = \frac{E_a}{\kappa \hat{T}_2}, \quad Sr = \frac{D_m K_T}{D \bar{T}_m} \frac{\hat{T}_1 - \hat{T}_0}{\hat{C}_1 - \hat{C}_0}, \quad \alpha_1 = \frac{\hat{T}_1 - \hat{T}_0}{\hat{T}_2}, \\ \text{Pr} &= \frac{\mu_0 c_p}{k}, \quad Z = \frac{\hat{C}_2 - \hat{C}_0}{\hat{C}_1 - \hat{C}_0}, \quad Du = \frac{\rho D_m K_T}{k C_s} \frac{\hat{C}_1 - \hat{C}_0}{\hat{T}_1 - \hat{T}_0}, \quad A_1 = \frac{a_1}{\Omega_1}, \quad A_2 = \frac{a_2}{\Omega_1} \\ We &= \frac{\Omega_1 \Gamma (\mu_0 - \mu_\infty)}{\mu_0}, \quad Sc = \frac{\nu}{D}, \quad S = \frac{\hat{T}_2 - \hat{T}_0}{\hat{T}_1 - \hat{T}_0}, \quad Ec = \frac{\Omega^2 r^2}{c_p (\hat{T}_1 - \hat{T}_0)}. \end{aligned} \quad (12.23)$$

Here (Re) represents local Reynold number, (Ec) Eckert number, (Pr) Prandtl number, (We) Weissenberg number, (M) magnetic field parameter, (Sc) Schmidt number, (Du) Dufour number, (Sr) Soret number, (S) thermal stratification parameter, (Z) solutal stratification parameter, (E_1) dimensionless activation energy, (R^*) dimensionless reaction rate and (δ) temperature difference parameter.

Radial and tangential shear stresses and heat transfer rate at lower disk are

$$C_{\hat{f}_{r1}} = \frac{\tau_{rz}|_{z=0}}{\mu_0 \Omega_1}, \quad C_{\hat{f}_{\theta 1}} = \frac{\tau_{\theta z}|_{z=0}}{\mu_0 \Omega_1}, \quad Nu_{r1} = \frac{r q_w|_{z=0}}{k (\hat{T}_1 - \hat{T}_0)} \quad (12.24)$$

where (q_w) is

$$q_w = -k \frac{\partial \hat{T}}{\partial z}, \quad (12.25)$$

Definitions of Nusselt number and skin friction coefficients at lower disk are

$$\left. \begin{aligned} Nu_{r1} &= -\sqrt{\text{Re}} \tilde{\theta}'(0), \\ \frac{C_{\hat{f}_{r1}}}{\sqrt{\text{Re}}} &= \left[1 + (We) \tilde{f}'(0) \sqrt{4\tilde{f}^2(0) + \text{Re}(\tilde{g}'^2(0) + \tilde{f}'^2(0)) + 2\tilde{h}'^2(0)} \right], \\ \frac{C_{\hat{f}_{\theta 1}}}{\sqrt{\text{Re}}} &= \left[1 + (We) \tilde{g}'(0) \sqrt{4\tilde{f}^2(0) + \text{Re}(\tilde{g}'^2(0) + \tilde{f}'^2(0)) + 2\tilde{h}'^2(0)} \right], \end{aligned} \right\} \quad (12.26)$$

At upper disk (radial, tangential) the shear stresses and Nusselt number are

$$C_{\hat{f}_{r2}} = \frac{\tau_{rz}|_{z=h}}{\mu_0 \Omega_1}, \quad C_{\hat{f}_{\theta 2}} = \frac{\tau_{\theta z}|_{z=h}}{\mu_0 \Omega_1}, \quad Nu_{r1} = \frac{r q_w|_{z=h}}{k (\hat{T}_1 - \hat{T}_0)} \quad (12.27)$$

Thus Nusselt number and skin friction for upper disk are obtained as:

$$\left. \begin{aligned} Nu_{r2} &= -\sqrt{\text{Re}}\tilde{\theta}'(1), \\ \frac{C_{f_{r2}}}{\sqrt{\text{Re}}} &= \left[1 + (We)\tilde{f}'(1) \sqrt{4\tilde{f}^2(1) + 2\hat{h}'^2(1) + \text{Re}(\tilde{g}'^2(1) + \tilde{f}'^2(1))} \right], \\ \frac{C_{f_{\theta 2}}}{\sqrt{\text{Re}}} &= \left[1 + (We)\tilde{g}'(1) \sqrt{4\tilde{f}^2(1) + \text{Re}(\tilde{g}'^2(1) + \tilde{f}'^2(1)) + 2\hat{h}'^2(1)} \right], \end{aligned} \right\} \quad (12.28)$$

For lower and upper disks the Sherwood numbers are

$$Sh = \frac{rJ_w}{D(\hat{C}_1 - \hat{C}_0)} \Big|_{z=0}, \quad Sh = \frac{rJ_w}{D(\hat{C}_1 - \hat{C}_0)} \Big|_{z=h}, \quad (12.29)$$

where (J_w) is

$$J_w = - \left[D \frac{\partial \hat{C}}{\partial z} \right], \quad (12.30)$$

Thus after using transformations the Sherwood numbers are

$$\left. \begin{aligned} \frac{Sh_{x0}}{\sqrt{\text{Re}}} &= -\tilde{\phi}'(0), \\ \frac{Sh_{x1}}{\sqrt{\text{Re}}} &= -\tilde{\phi}'(1). \end{aligned} \right\} \quad (12.31)$$

12.2 Solution technique

Auxiliary linear operators and initial approximations are:

$$\mathcal{L}_{\tilde{h}} = \tilde{h}', \quad \mathcal{L}_{\tilde{f}} = \tilde{f}'', \quad \mathcal{L}_{\tilde{g}} = \tilde{g}'', \quad \mathcal{L}_{\tilde{\theta}} = \tilde{\theta}'', \quad \mathcal{L}_{\tilde{\phi}} = \tilde{\phi}'', \quad (12.32)$$

$$\begin{aligned} \tilde{h}_0 &= 0, \quad \tilde{f}_0 = A_1 - A_1 \exp(-\xi) + A_2(\xi), \quad \tilde{g}_0 = 1 + \xi(\Omega - 1), \\ \tilde{\theta}_0 &= (1 - \xi)(1 - S_1), \quad \tilde{\phi}_0 = (1 - \xi)(1 - S_2). \end{aligned} \quad (12.33)$$

with

$$\left. \begin{aligned} \mathcal{L}_{\tilde{h}}[Z_1] &= 0, \\ \mathcal{L}_{\tilde{f}}[Z_2 + Z_3\xi] &= 0, \\ \mathcal{L}_{\tilde{g}}[Z_4 + Z_5\xi] &= 0, \\ \mathcal{L}_{\tilde{\theta}}[Z_6 + Z_7\xi] &= 0, \\ \mathcal{L}_{\tilde{\phi}}[Z_8 + Z_9\xi] &= 0, \end{aligned} \right\} \quad (12.34)$$

where the constants are Z_i ($i = 1 - 5$).

12.3 Convergence

Auxiliary variables ($\tilde{h}_{\tilde{g}}, \tilde{h}_{\tilde{\phi}}, \tilde{h}_{\tilde{\theta}}, \tilde{h}_{\tilde{h}}, \tilde{h}_{\tilde{f}}$) have prominent role in convergence analysis. Fig. 12.2 displayed \tilde{h} -curves for m th order of approximation. The solutions are found convergent for the regions $-1.7 \leq \tilde{h}_{\tilde{h}} \leq -0.3$, $-1.2 \leq \tilde{h}_{\tilde{f}} \leq -0.3$, $-1.0 \leq \tilde{h}_{\tilde{g}} \leq -0.4$, $-0.9 \leq \tilde{h}_{\tilde{\theta}} \leq -0.6$ and $-1.0 \leq \tilde{h}_{\tilde{\phi}} \leq -0.7$. Table 1 consists of numerical values of velocity, temperature and concentration. To show the numerical values of velocity, concentration and temperature distribution Table 12.1 is constructed. Clearly the meaningful solutions of $\tilde{h}'(0)$, $\tilde{f}'(0)$, $\tilde{g}'(0)$, $\tilde{\theta}'(0)$, $\tilde{\phi}'(0)$ started from 20th order of approximations.

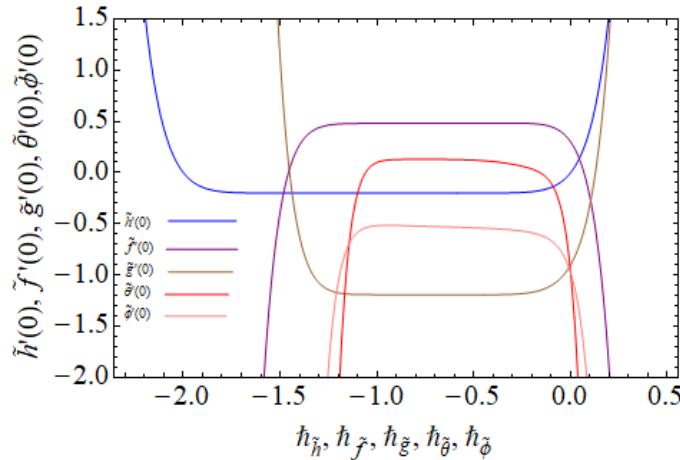


Fig. 12.1: \tilde{h} - curves.

Table 12.1: Series solutions convergence for $\Omega = 0.2$, $A_1 = 0.1$, $A_2 = 0.4$, $E_1 = 0.5$, $R^* = 0.5$, $\alpha_1 = 0.5$, $S_1 = S_2 = 0.02$, $D_f = 0.5$, $Ec = 0.1$, $M = 0.7$, $Sc = 1$, $Re = 0.7$,

$$We = 0.2, Pr = 0.6, Sr = 0.3, \tilde{h}_{\tilde{h}} =, \tilde{h}_{\tilde{f}} =, \tilde{h}_{\tilde{g}} = \tilde{h}_{\tilde{\theta}} = \tilde{h}_{\tilde{\phi}} = -0.8,$$

Order of approximation	$-\tilde{h}(0)$	$\tilde{f}'(0)$	$-\tilde{g}'(0)$	$\tilde{\theta}'(0)$	$-\tilde{\phi}'(0)$
1	0.20000	0.5272	1.0380	-0.1108	0.6884
5	0.20000	0.4809	1.192	-0.09493	0.6863
11	0.20000	0.4812	1.192	0.09682	0.5462
16	0.20000	0.4812	1.192	0.2655	0.4127
20	0.20000	0.4812	1.192	0.2655	0.3554
25	0.20000	0.4812	1.192	0.2655	0.3554
30	0.20000	0.4812	1.192	0.2655	0.3554
40	0.20000	0.4812	1.192	0.2655	0.3554

12.4 Entropy

In presence of thermal irreversibility, Joule heating irreversibility, viscous dissipation irreversibility and mass transfer irreversibility, the formulation of entropy generation is presented.

Its dimensional form is represented by

$$S_G'' = \underbrace{\frac{1}{\hat{T}_m} \Phi}_{\text{Viscous dissipation irreversibility}} + \underbrace{\frac{k}{\hat{T}_m^2} (\nabla \hat{T})^2}_{\text{Thermal irreversibility}} + \underbrace{\frac{\sigma}{\hat{T}_m} B_0^2 (\hat{u}^2 + \hat{v}^2)}_{\text{Joule dissipation irreversibility}} + \underbrace{\frac{R_g D}{\hat{C}_m} [\nabla \hat{C}]^2 + \frac{R_g D}{\hat{T}_m} [\nabla \hat{C} \cdot \nabla \hat{T}]}_{\text{mass transfer irreversibility}} \quad (12.35)$$

where (\hat{C}_m) and (\hat{T}_m) are mean concentration and temperature respectively and $(\nabla \hat{T})$, $(\nabla \hat{C})$ and (Φ) are defined as

$$\nabla \hat{T} = \left(\frac{\partial \hat{T}}{\partial r} \right) \hat{e}_r + \left(\frac{1}{r} \frac{\partial \hat{T}}{\partial \vartheta} \right) \hat{e}_\vartheta + \left(\frac{\partial \hat{T}}{\partial z} \right) \hat{e}_z, \quad (11.36)$$

$$\nabla \hat{C} = \left(\frac{\partial \hat{C}}{\partial r} \right) \hat{e}_r + \left(\frac{1}{r} \frac{\partial \hat{C}}{\partial \vartheta} \right) \hat{e}_\vartheta + \left(\frac{\partial \hat{C}}{\partial z} \right) \hat{e}_z, \quad (11.37)$$

$$\Phi = (\mu_0 + (\mu_0 - \mu_\infty) \Gamma \ddot{\gamma}) \left[2 \left[\left(\frac{\partial \hat{u}}{\partial r} \right)^2 + \frac{\partial \hat{u}}{\partial z} \frac{\partial \hat{w}}{\partial r} - \frac{\hat{v}}{r} \frac{\partial \hat{v}}{\partial r} + \frac{\hat{u}^2}{r^2} + \left(\frac{\partial \hat{w}}{\partial z} \right)^2 \right] + \left(\frac{\partial \hat{v}}{\partial r} \right)^2 + \left[\left(\frac{\partial \hat{w}}{\partial r} \right)^2 + \frac{\hat{v}^2}{r^2} + \left(\frac{\partial \hat{u}}{\partial z} \right)^2 + \left(\frac{\partial \hat{v}}{\partial z} \right)^2 \right] \right], \quad (12.38)$$

After applying transformation one has

$$\begin{aligned}
N_G = & \alpha_1 \left[\text{Re} \tilde{\theta}'^2 + (S_1 + \tilde{\theta})^2 \right] + M(\text{Re})(Br) (\tilde{f}^2 + \tilde{g}^2) + (Br)(1 + We\ddot{\gamma}) \left[4\tilde{f}^2 + \text{Re} \tilde{f}'^2 + \text{Re} \tilde{g}'^2 + 2\tilde{h}'^2 \right] \\
& + L \left[\frac{\alpha_2}{\alpha_1} \right] \left[\text{Re} \tilde{\phi}'^2 + (\tilde{\phi} + S_1)^2 \right] + L \left[(\tilde{\theta} + S_1) (S_2 + \tilde{\phi}) + \text{Re} \tilde{\phi}'\tilde{\theta}' \right]. \tag{12.39}
\end{aligned}$$

Dimensionless parameters are

$$\begin{aligned}
\alpha_1 = & \frac{\hat{T}_1 - \hat{T}_0}{\hat{T}_m}, \quad L = \frac{R_g D (\hat{C}_1 - \hat{C}_0)}{k}, \quad Br = \frac{\mu_0 r^2 \Omega_1^2}{k (\hat{T}_1 - \hat{T}_0)}, \\
N_G = & \frac{r^2 \hat{T}_m S_G''}{k (\hat{T}_1 - \hat{T}_0)}, \quad \alpha_2 = \frac{\hat{C}_1 - \hat{C}_0}{\hat{C}_m}. \tag{12.40}
\end{aligned}$$

Here (Br) and (N_G) are Brinkman number and local entropy generation respectively, (α_1) and (α_2) are temperature and concentration ratio parameters and (L) diffusion parameter.

Here the dimensionless form of Bejan number (Be) is

$$Be = \frac{\text{Entropy generation due to heat and mass transfer}}{\text{Total entropy generation}}, \tag{12.41}$$

or

$$\begin{aligned}
Be = & \frac{\alpha_1 \left[\text{Re} \tilde{\theta}'^2 + (S_1 + \tilde{\theta})^2 \right] + L \left[\frac{\alpha_2}{\alpha_1} \right] \left[\text{Re} \tilde{\phi}'^2 + (S_1 + \tilde{\phi})^2 \right] + L \left[(S_1 + \tilde{\theta}) (S_2 + \tilde{\phi}) + \text{Re} \tilde{\phi}'\tilde{\theta}' \right]}{L \left[(S_1 + \tilde{\theta}) (S_2 + \tilde{\phi}) + \text{Re} \tilde{\phi}'\tilde{\theta}' \right] + M(\text{Re})(Br) (\tilde{f}^2 + \tilde{g}^2) + \alpha_1 \left[\text{Re} \tilde{\theta}'^2 + (S_1 + \tilde{\theta})^2 \right] + L \frac{\alpha_2}{\alpha_1} \left[\text{Re} \tilde{\phi}'^2 + (S_1 + \tilde{\phi})^2 \right] + (Br)(1 + We\ddot{\gamma}) \left[4\tilde{f}^2 + \text{Re} \tilde{f}'^2 + \text{Re} \tilde{g}'^2 + 2\tilde{h}'^2 \right]}, \tag{12.42}
\end{aligned}$$

12.5 Discussion

This section emphasis on the discussion of graphical interpretation of various physical parameters for velocity, temperature, entropy generation, Bejan number, skin friction, Nusselt number and Sherwood number.

Figs. (12.3 – 12.8) are designed to analyze the behavior of Hartmann number (M) and Weissenberg number (We) on $(\tilde{h}(\xi))$, $(\tilde{f}(\xi))$ and $(\tilde{g}(\xi))$ in axial, radial and transverse directions. These quantities are discussed for both upper and lower disks. Figs. (12.3 – 12.5) analyzed behavior of (M) for axial $(\tilde{h}(\xi))$, radial $(\tilde{f}(\xi))$ and tangential $(\tilde{g}(\xi))$ velocities at both disks. It is noticed that magnitude of velocities $(\tilde{h}(\xi))$, $(\tilde{f}(\xi))$, $(\tilde{g}(\xi))$ decays with the increment in Hartmann number (M). A resistive force is produced when transverse magnetic field acts. Such force acting as Lorentz force generates resistance and it decreases the velocity. Influence of Weissenberg number (We) on $(\tilde{h}(\xi))$, $(\tilde{f}(\xi))$ and $(\tilde{g}(\xi))$ is shown in Figs (12.6 – 12.8). The axial and radial velocities $(\tilde{h}(\xi))$ and $(\tilde{f}(\xi))$ rise with larger Weissenberg number (We) while tangential velocity $(\tilde{g}(\xi))$ reduces. For higher (We) the angular velocity (Ω_1) enhances and so $(\tilde{h}(\xi))$ and $(\tilde{f}(\xi))$ increase (see Figs. 12.6 and 12.7).

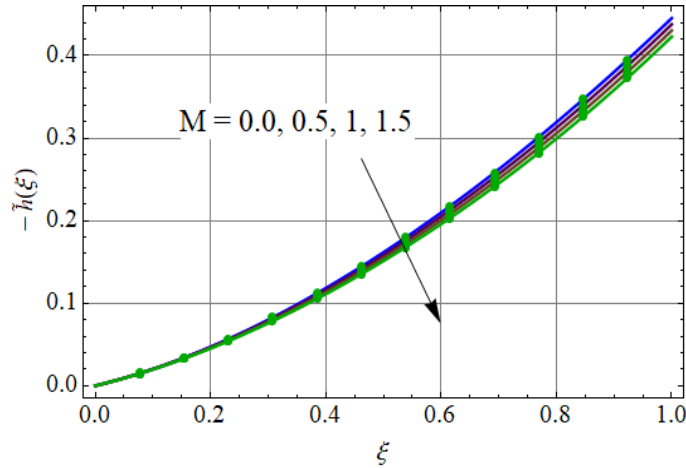


Fig. 12.3. Axial velocity $\tilde{h}(\xi)$ via M .

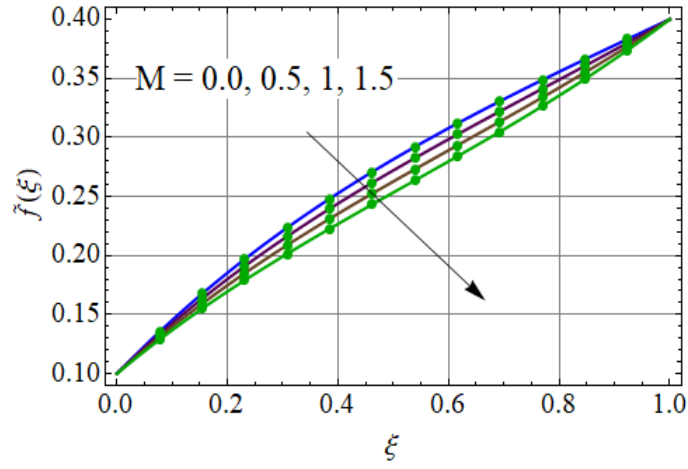


Fig. 12.4. Radial velocity $\tilde{f}(\xi)$ via M .

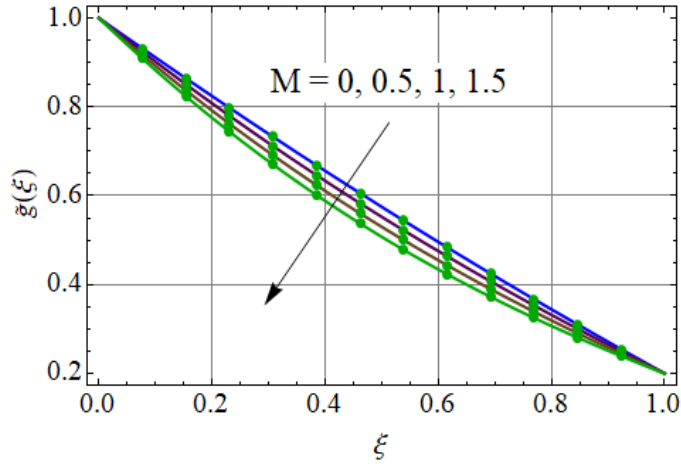


Fig. 12.5. Tangential velocity $\tilde{g}(\xi)$ via M .

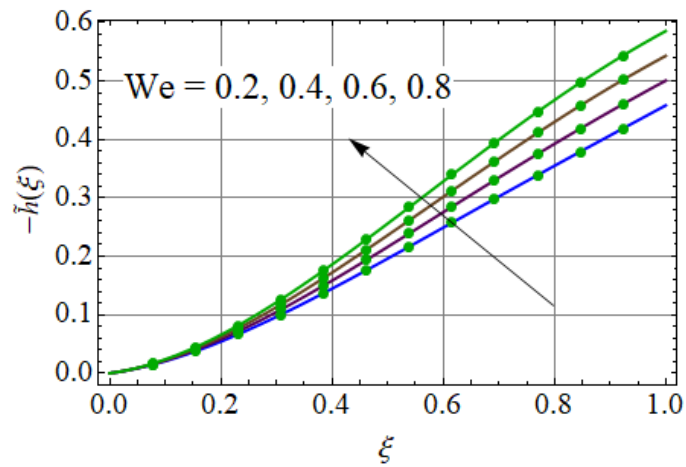


Fig. 12.6. Axial velocity $\tilde{h}(\xi)$ via We .

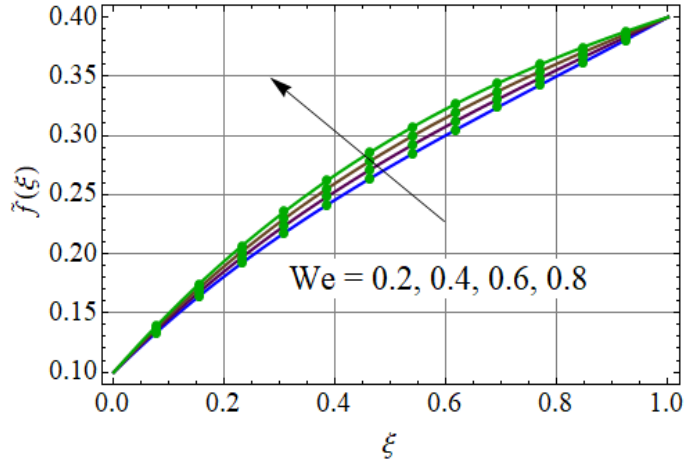


Fig. 12.7. Radial velocity $\tilde{f}(\xi)$ via We .

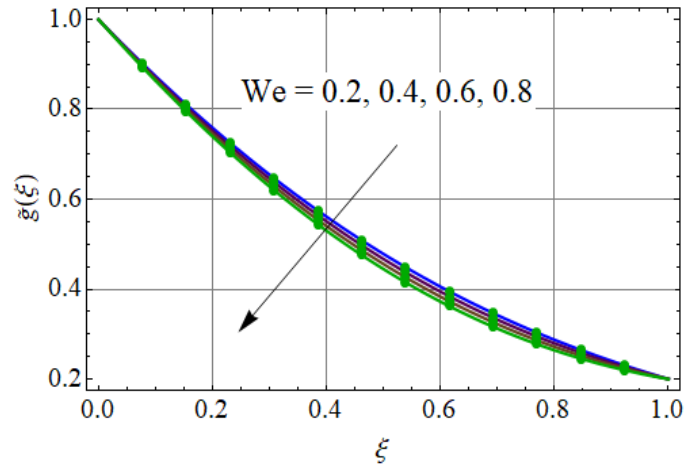


Fig. 12.8. Tangential velocity $\tilde{g}(\xi)$ via We .

12.5.1 Temperature

Figs. (12.9 – 12.12) illustrate the trend of temperature ($\tilde{\theta}(\xi)$) against Dufour number (Du), thermal stratification parameter (S_1), Weissenberg number (We) and Prandtl number (Pr). Fig. 12.9 discloses impact of (Du) on ($\tilde{\theta}(\xi)$) at lower and upper disks. Fluid temperature via (Du) enhances. Energy flux is enhanced due to rise in concentration gradient for varying (Du) and it leads to enhance the fluid temperature. Temperature near lower disk is more when compared with upper disk. Physically it is because of higher temperature of lower disk than upper disk i.e. ($\hat{T}_1 \succ \hat{T}_2$). Fig. 12.10 delineates the impact of thermal stratification parameter (S_1) on ($\tilde{\theta}(\xi)$). For larger estimation of (S_1) the temperature decreases due to occurrence of

potential drop between ambient fluid temperature and surface condition. Fig. 12.11 shows role of Weissenberg number (We) on $\tilde{\theta}(\xi)$. Temperature increases for higher estimation of (We). Behavior of Prandtl number (Pr) on $\tilde{\theta}(\xi)$ is identified in Fig. 12.12. For larger (Pr) thermal diffusivity has smaller value which causes reduction in temperature $\tilde{\theta}(\xi)$.

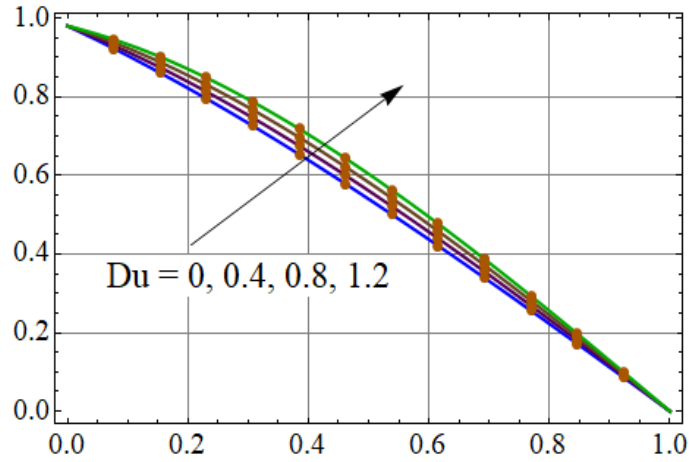


Fig. 12.9. $\tilde{\theta}(\xi)$ via Du .

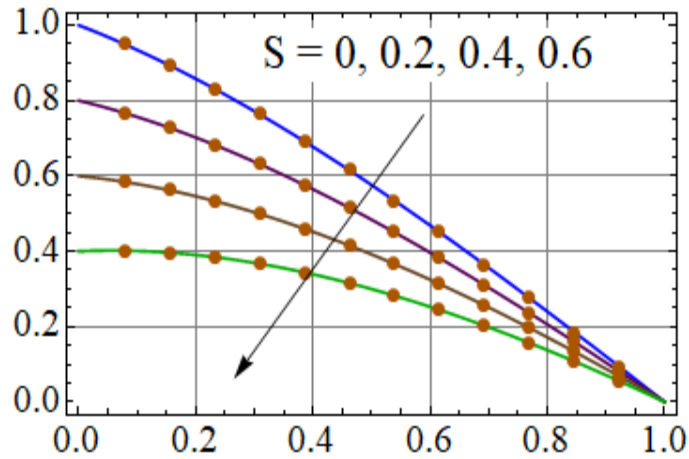


Fig. 12.10. $\tilde{\theta}(\xi)$ via S .

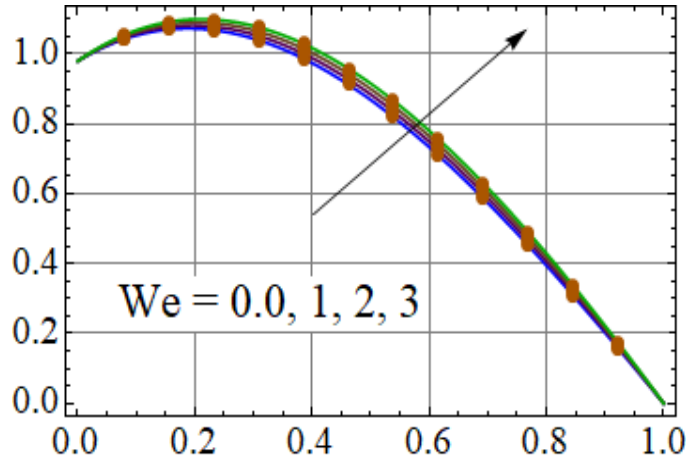


Fig. 12.11. $\tilde{\theta}(\xi)$ via We .

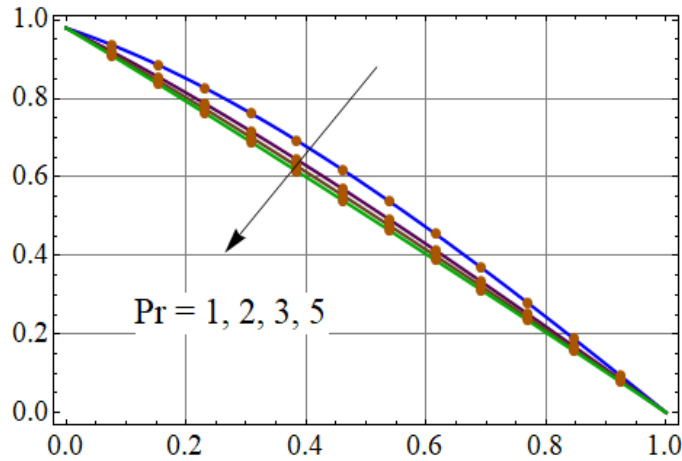


Fig. 12.12. $\tilde{\theta}(\xi)$ via Pr .

12.5.2 Concentration

Figs (12.13 – 12.18) are sketched to show the trend of concentration $\left(\tilde{\phi}(\xi)\right)$ for variations of Schmidt number (Sc), Soret number (Sr), dimensionless activation energy parameter (E_1), dimensionless reaction rate (σ), temperature difference parameter (δ) and solutal stratification parameter (S_2). For growing values of (Sc) the concentration $\left(\tilde{\phi}(\xi)\right)$ decays. It is due to fact that mass diffusivity reduces for higher (Sc) due to which concentration $\left(\tilde{\phi}(\xi)\right)$ decreases (see Figs. 12.13).. Effect of Soret number (Sr) on $\left(\tilde{\phi}(\xi)\right)$ is displayed in Fig. 12.14. It is observed that concentration $\left(\tilde{\phi}(\xi)\right)$ increases for larger (Sr). Temperature gradient enhances for larger (Sr) which tends to more convective flow. Hence concentration distribution $\left(\tilde{\phi}(\xi)\right)$ enhances.

Fig. 12.15. reveals that concentration $\left(\tilde{\phi}(\xi)\right)$ increases for larger dimensionless activation energy parameter (E_1) . Generative chemical reaction is promoted due to decrease in Arrhenius function $\left(\frac{\hat{T}}{\hat{T}_\infty}\right) \exp\left(\frac{-E_a}{\kappa\hat{T}}\right)$. When (E_a) increases then concentration $\left(\tilde{\phi}(\xi)\right)$ enhances. Fig. 12.16 is portrayed to discuss chemical reaction parameter (R^*) on $\left(\tilde{\phi}(\xi)\right)$. For larger (σ) the reduction in concentration $\left(\tilde{\phi}(\xi)\right)$ is noticed. Due to concentration gradient this behavior shows weak buoyancy effect thus reduction occurs for $\left(\tilde{\phi}(\xi)\right)$. Fig. 12.17 reveals that concentration $\left(\tilde{\phi}(\xi)\right)$ reduces for larger temperature difference parameter (δ) . From Fig. 12.18 it can be seen that concentration $\left(\tilde{\phi}(\xi)\right)$ is decreasing function of larger solutal stratification parameter (S_2) .

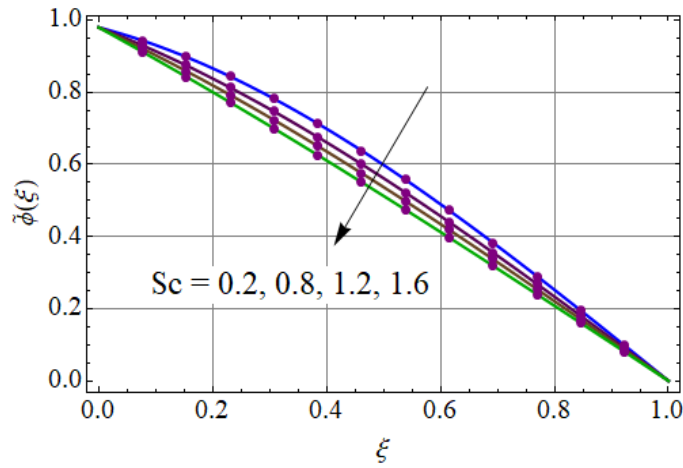


Fig. 12.13. $\tilde{\phi}(\xi)$ via Sc .

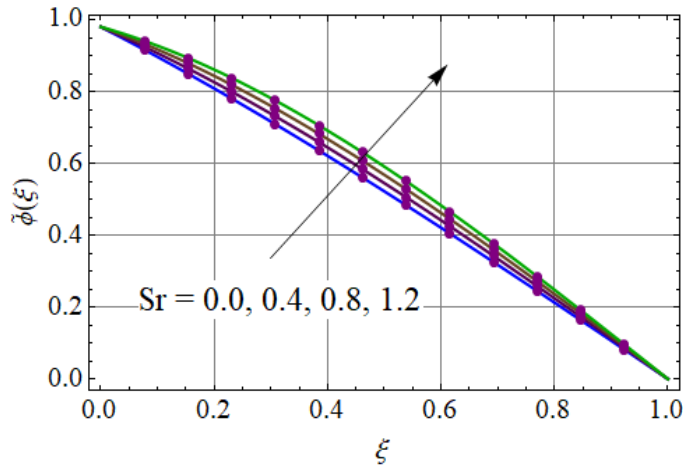


Fig. 12.14. $\tilde{\phi}(\xi)$ via Sr .

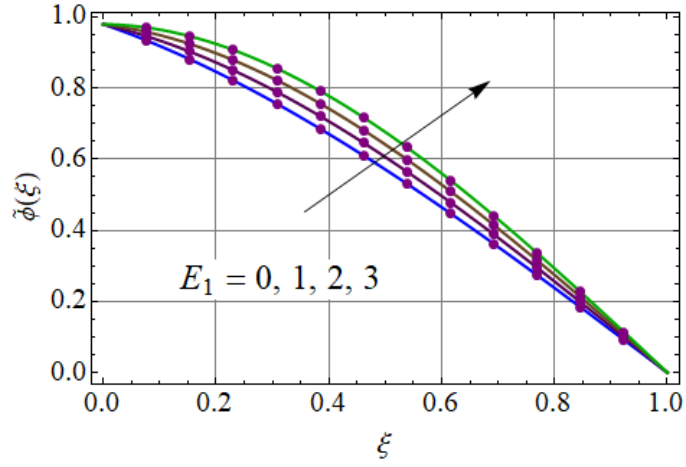


Fig. 12.15. $\tilde{\phi}(\xi)$ via E_1 .

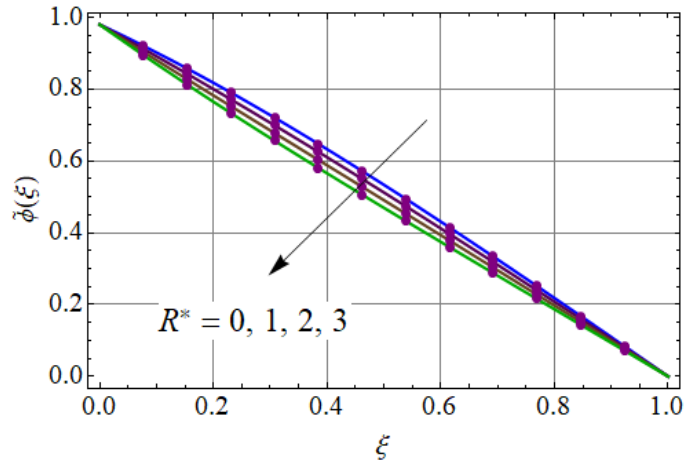


Fig. 12.16. $\tilde{\phi}(\xi)$ via R^* .

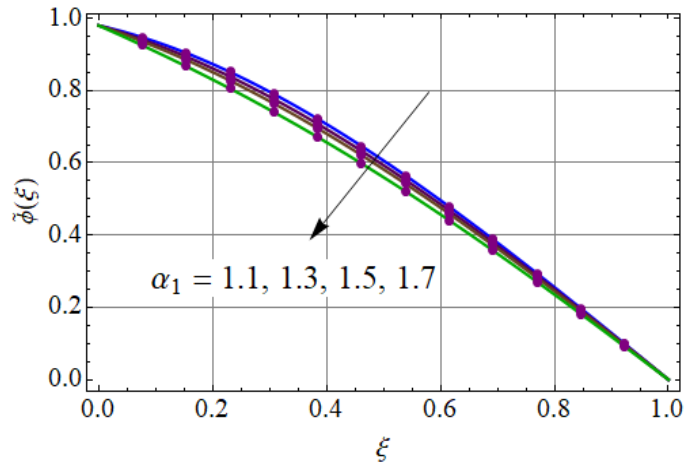


Fig. 12.17. $\tilde{\phi}(\xi)$ via α_1 .

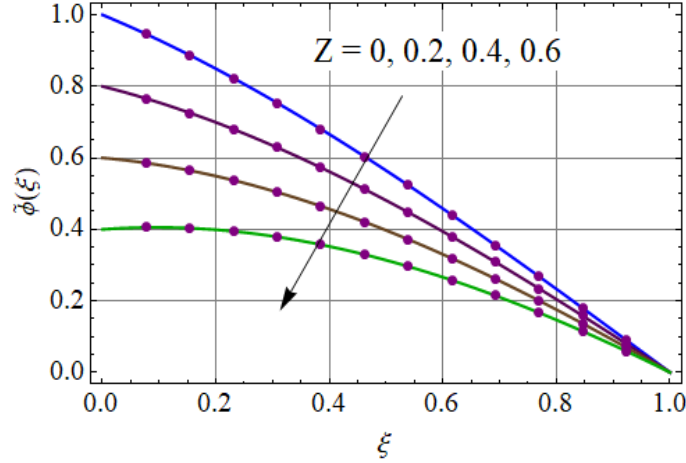


Fig. 12.18. $\tilde{\phi}(\xi)$ via Z .

12.5.3 Entropy generation minimization

This section emphasis on graphical interpretation of pertinent variables of entropy generation (N_G) and Bejan number (Be). Br effects on (N_G) and (Be) are shown in Fig. 12.19 and 12.20. Opposite trend is witnessed for (Be) due to increment in disorderedness of system for larger (Br). For larger estimation of (Br) due to dissipation the less conduction rate is produced and thus entropy generation (N_G) enhances. Impacts of diffusion (L) on (N_G) and (Be) are portrayed in Figs. 12.21 and 12.22. Both (N_G) and (Be) are increased for larger (L). For increasing (L) the nanoparticles diffusion rate enhances and so Bejan number and total entropy of the system rise. We effect on (N_G) and (Be) is discussed by Figs. 12.23 and 12.24. For larger (We) the entropy generation increases while Bejan number reduces. Figs. (12.25 – 12.28) show impacts of solutal and thermal stratification parameters (S_2) and (S_1) on (N_G) and (Be). Both (N_G) and (Be) are reduced for larger estimation of (S_1) and (S_2). Figs. 12.29 and 12.30 clearly reveals influence of (M) on (N_G) and (Be). Enhancement is witnessed in (N_G) with an increment of magnetic parameter (M). For growing (M) the fluid resistance rises due to rise in Lorentz force and consequently (N_G) increases. Bejan number (Be) reduces for larger (M).

Here irreversibility of fluid friction prevailed over the heat and mass transfer irreversibilities.

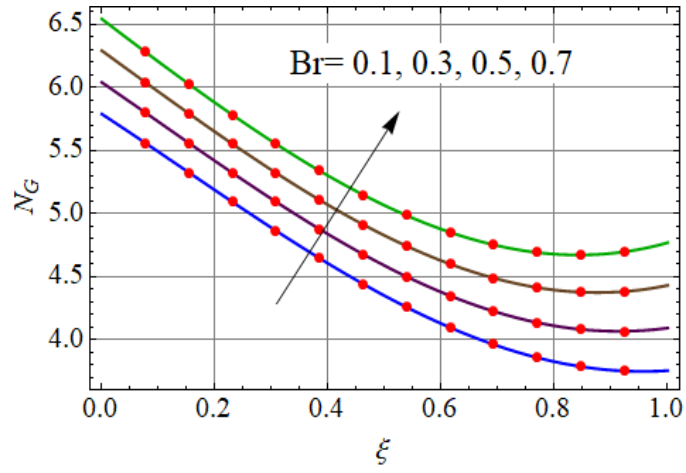


Fig. 12.19. Entropy generation $N_G(\xi)$ via Br .

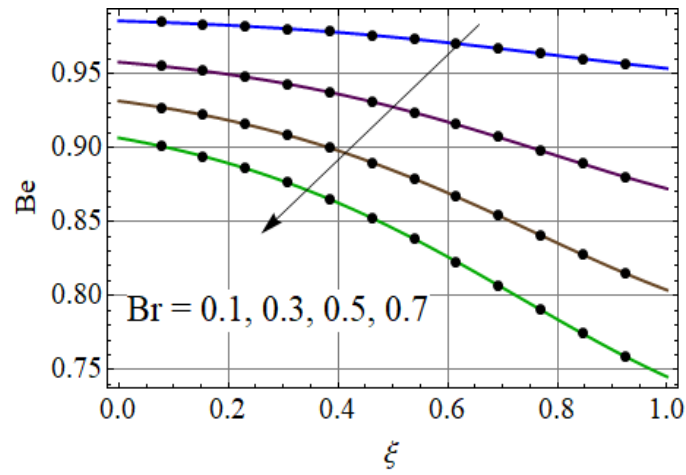


Fig. 12.20. Bejan number Be via Br .

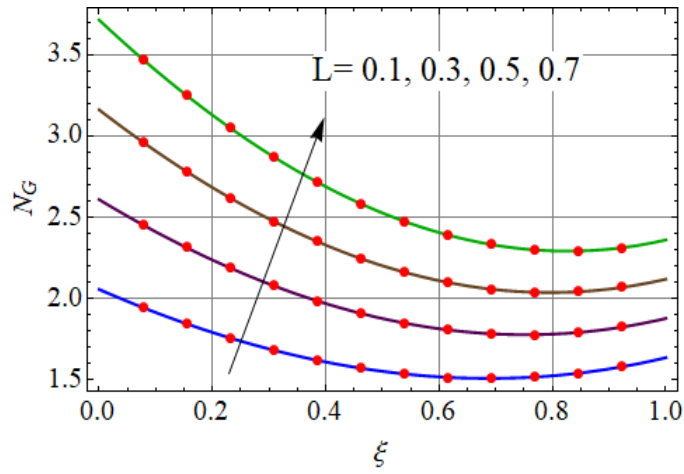


Fig. 12.21. Entropy generation $N_G(\xi)$ via L .

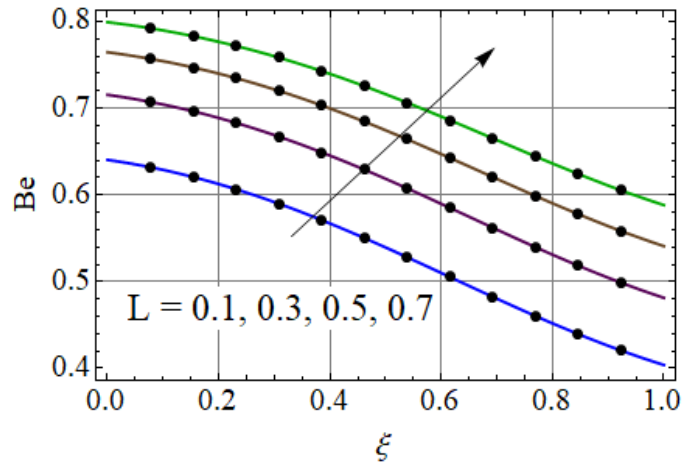


Fig. 12.22. Bejan number Be via L .

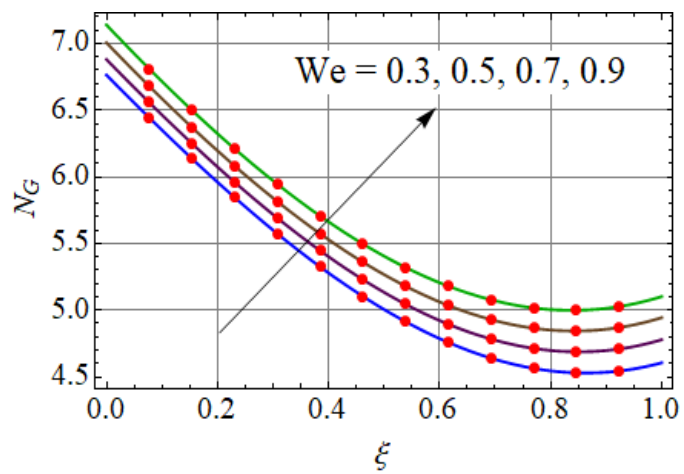


Fig. 12.23. Entropy generation $N_G(\xi)$ via We .

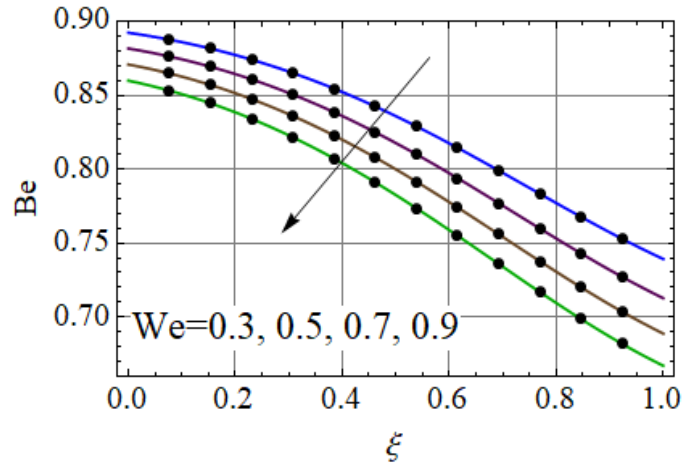


Fig. 12.24. Bejan number Be via We .

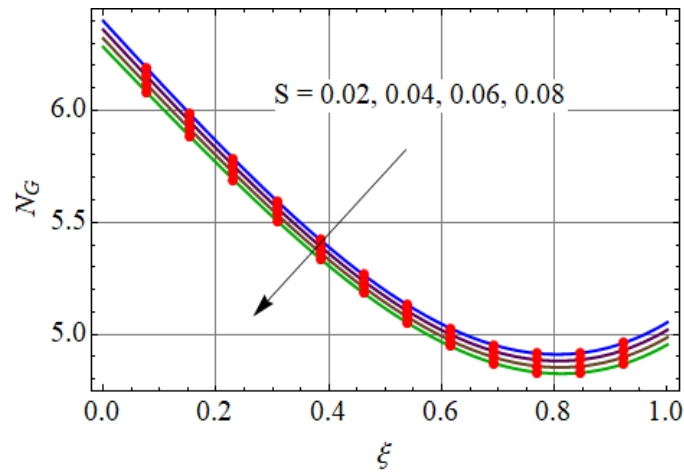


Fig. 12.25. Entropy generation $N_G(\xi)$ via S .

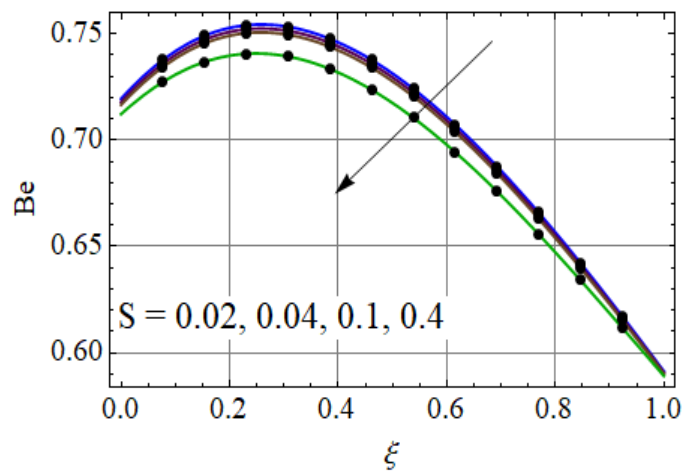


Fig. 12.26. Bejan number Be via S .

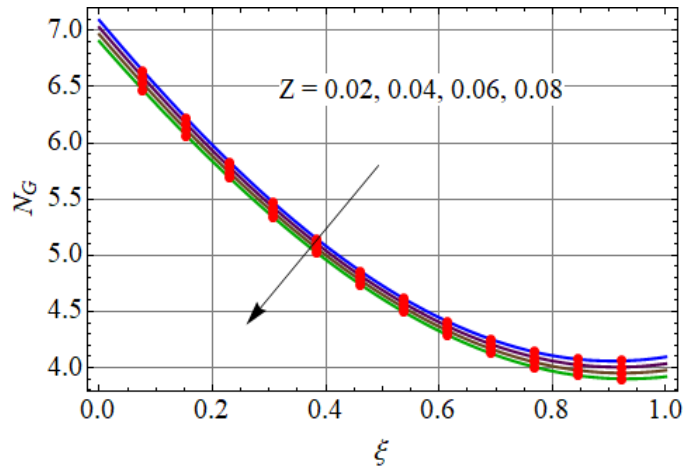


Fig. 12.27. Entropy generation $N_G(\xi)$ via Z .

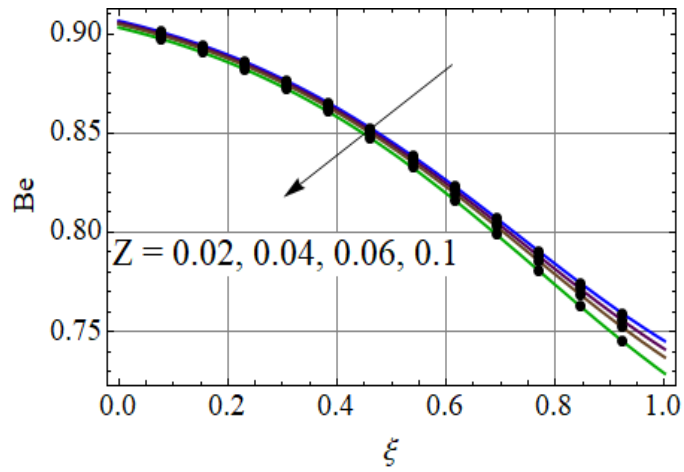


Fig. 12.28. Bejan number Be via Z .

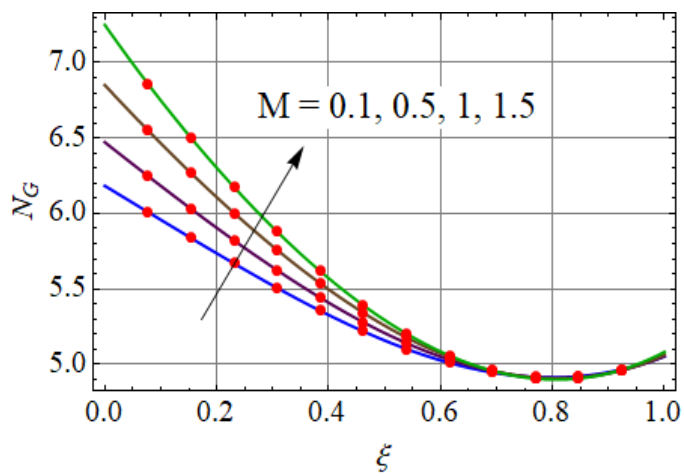


Fig. 12.29. Entropy generation $N_G(\xi)$ via M .

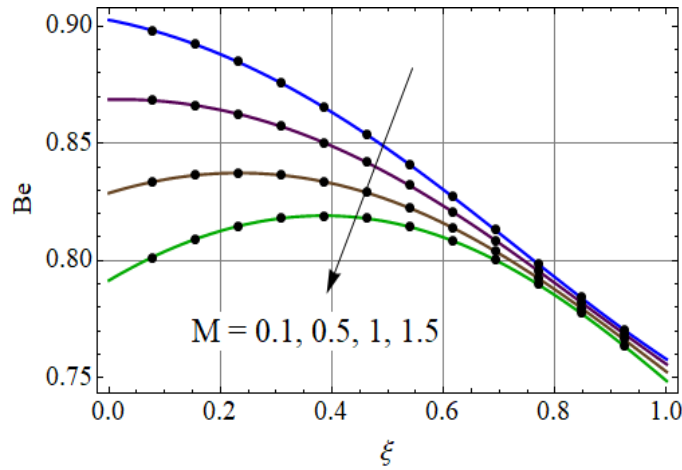


Fig. 12.30. Bejan number Be via M .

12.5.4 Skin friction and Nusselt and Sherwood numbers

Influence of Reynold number (Re) and (We) on skin friction coefficient at lower and upper disks is analyzed in Figs. 12.31 and 12.32. There is an increase in skin friction at both disks for larger Re while for higher (We) drag force at lower disk increases and it decays at upper disk. From Figs. 12.33 and 12.34 it can be seen that for increasing Eckert number (Ec) and Weissenberg number (We) the heat transfer rate decay near surface of lower and upper disks. Figs. 12.35 and 12.36 are drawn to analyze stratification variable (S) on Sherwood number. For varying (S) the Sherwood number near the surface of lower disk reduces. However near upper disk the Sherwood number has reverse behavior.

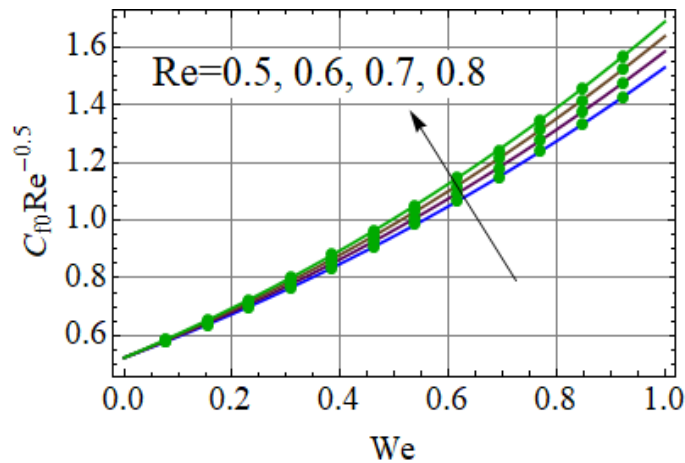


Fig. 12.31. Skin friction via Re and We .

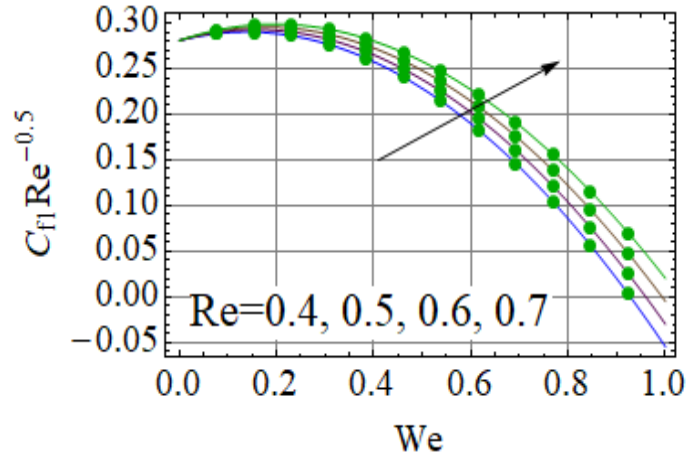


Fig. 12.32. Skin friction via Re and We .

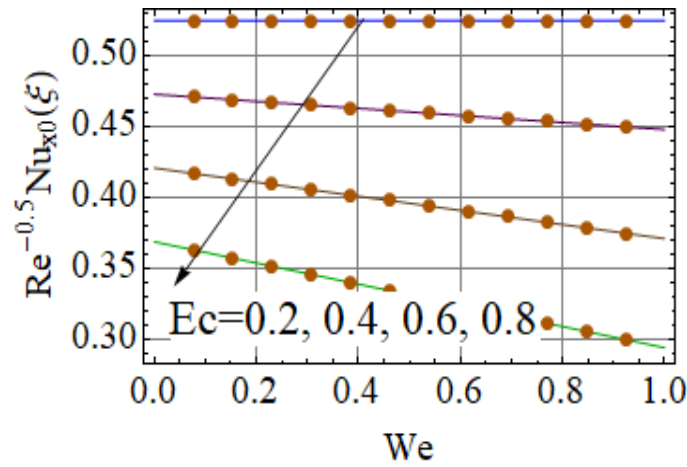


Fig. 12.33. Nusselt number via Ec and We .

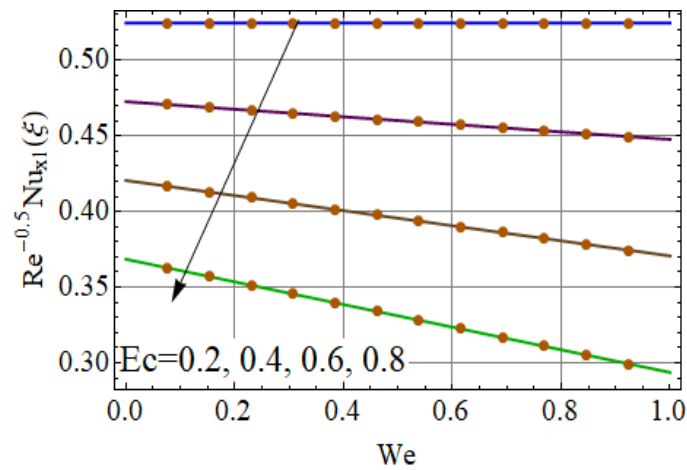


Fig. 12.34. Nusselt number via Ec and We .

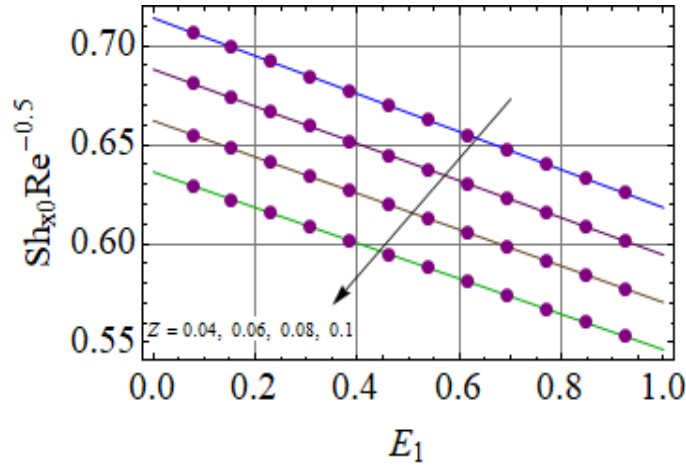


Fig. 12.35. Sherwood number via S and E_1 .

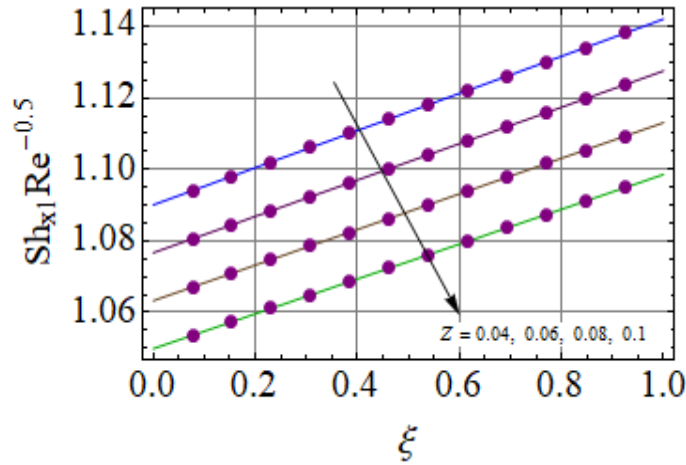


Fig. 12.36. Sherwood number via S and E_1 .

12.6 Conclusions

The following observations are worth mentioning.

- Velocities $(\tilde{h}(\xi))$, $(\tilde{f}(\xi))$ and $(\tilde{g}(\xi))$ reduce for (M) at both disks while $(\tilde{h}(\xi))$ and $(\tilde{f}(\xi))$ are increasing functions of (We) .
- For larger (S) and (Pr) the temperature $(\tilde{\theta}(\xi))$ decays while increasing trend is noticed for (We) and (Du) .
- Opposite trend of concentration $(\tilde{\phi}(\xi))$ is noticed for (Z) and (Sc) .
- Increasing behavior of (Re) for skin friction is observed.

- Entropy rate through (Br) , (L) and (We) enhances while it decreases for thermal and solutal stratification parameters (S) and (Z) .
- Bejan number has decreasing behavior for larger (S) , (Z) , (We) , and (Br) while it increases for larger (L) .

Chapter 13

Thesis Conclusion

This thesis addresses in particular the nonlinear flows of both viscous and non-Newtonian liquids. Modeling for rotating disk problems is designed. Three non-Newtonian fluid models under discussion are second grade, Williamson and Jeffrey. In these problems formulation, the two types of nanoliquids are considered. The novel aspects of Brownian motion, thermophoresis and thermophysical properties of nanoliquids are addressed. Analysis for thermal radiation, microorganism bioconvection, mixed convection, magnetohydrodynamics, dissipation and Ohmic heating are considered. Entropy concept is modeled employing second thermodynamic relation. Applied magnetic field effects in flows by rotating disk with variable thickness is investigated. The velocity and thermal slip conditions are considered. Porous medium, homogeneous and heterogeneous reactions and Soret and Dufour effects are also investigated. Stratification is analyzed. The velocity, temperature and concentration are discussed. Nusselt and Sherwood numbers and entropy generation are advanced with respect to considered flows.

This thesis is organized in the form of twelve chapters. The first chapter has introductory material. Bioconvection flow with microorganism and nanoparticles is considered in chapter two. Nonlinear stretching to rotating disk is modeled in chapter three. Partial slip is featured in chapter four. Ferrofluid flow between two axially rotating disks is investigated in chapter five. Statistical declaration and probable error in the presence of homogeneous and heterogeneous reactions are presented in chapter six. Chapters seven and eight investigate the entropy generation and thermos effects in non-radiated flow for rotating disk. Chapters nine to twelve are for flows of Jeffrey, second grade and Williamson liquids in the presence

of homogeneous-heterogeneous reactions and radiation. Viscous dissipation, activation energy and heat source/sink are considered.

Key findings of whole thesis are mentioned below:

- Axial velocity profile $\left(\tilde{h}(\xi)\right)$ is decaying by greater values of M, ς, ϵ^* and γ_1 . Opposite trend is noticed for rising A, n, λ and ϕ .
- Radial velocity $\left(\tilde{f}(\xi)\right)$ is increasing function of $Re, \gamma_1, A_1, \beta, We$ and λ on the other side it decays for β^*, M, γ_1 and γ_2 .
- Tangential velocity enhances for higher estimation of $n, \varsigma, \phi, \epsilon^*, Re, \Omega, \beta, \lambda_1^*$ and We and decreases for $M, A_1, \lambda, \gamma_2$ and β^* .
- Density profile $\left(\tilde{\chi}(\xi)\right)$ decays for increasing Pe, Lb, Pr and Ld however it shows opposite impact for greater Le, Nt and R^* .
- Temperature impact against $Nb, Nt, R, M, \lambda, \phi, Ec, Q^*$ and Du is increasing and temperature shows decreasing behavior for Pr, γ_3, S and We .
- It is observed that concentration field $\left(\tilde{\phi}(\xi)\right)$ rises for Nt, Sr, R^*, k_2, We and E_1 and decays for Le, Nb, Pr, Sc, k_1 and Z .
- Entropy generation enhances for greater $\alpha_1, R, Br, \phi, M, \alpha_2, L$ and We while opposite trend is seen for greater Re, γ_3, S and Z .
- Bejan number boosts for higher α_1, R, α_2, L and Nt however it show decaying behavior for Br, ϕ, M, γ_3 and Z .
- Surface drag force decays for increasing γ_2, γ_1 and λ_1^* and it depicts increasing behavior for M, ϕ, λ and β .
- Nusselt number increases for ϕ, α, We and Ec .

Bibliography

- [1] T. V. Karman, Uber laminare and turbulente Reibung, *Zeit. Angew. Math. Mech.* 1 (1921) 233 – 252.
- [2] W. G. Cochran, The flow due to a rotating disk, *Proc. Camb. Philo. Soc.* 30 (1934) 365 – 375.
- [3] K. Stewartson, On the flow between two rotating coaxial disks, *Proc. Comb. Phil. Soc.* 49 (1953) 333 – 341.
- [4] P. J. Chapple and V. K. Stokes, On the flow between a rotating and a stationary disk, Report No. FLD 8. Dept. Mech. Eng. Princeton University (1962).
- [5] G. L. Mellor, P. J. Chapple and V. K. Stokes, On the flow between a rotating and a stationary disk, *J. Fluid Mech.* 31 (1968) 95 – 112.
- [6] R. C. Arora and V. K. Stokes, On the heat transfer between two rotating disks, *Int. J. Heat Mass Transf.* 15 (1972) 2119 – 2132.
- [7] S. K. Kumar, W. I. Tacher and L. T. Watson, Magneto hydrodynamic flow between a solid rotating disk and a porous stationary disk, *Appl. Math. Model.* 13 (1989) 494 – 500
- [8] T. Hayat, S. Qayyum, M. Imtiaz and A. Alsaedi, MHD flow and heat transfer between coaxial rotating stretchable disks in a thermally stratified medium, *Plos One* 11 (5) (2016) e0155899.
- [9] M. Imtiaz, T. Hayat, A. Alsaedi and B. Ahmad, Convective flow of carbon nanotubes between rotating stretchable disks with thermal radiation effects, *Int. J. Mas Transf.* 101 (2016) 948-957.(Chapter 6 52)

- [10] T. Hayat, S. Qayyum, M. I. Khan and A. Alsaedi, Entropy generation in magnetohydrodynamic radiative flow due to rotating disk in presence of viscous dissipation and Joule heating, *Physics of Fluids* 30 (2018) 017101.
- [11] T. Hayat, S. Qayyum, M. Imtiaz and A. Alsaedi, Flow between two stretchable rotating disks with Cattaneo-Christov heat flux model, *Results Phys.* 7 (2017) 126-133.
- [12] S. Xun, J. Zhao, L. Zheng, X. Chen, X. Zhang, Flow and heat transfer of Ostwald-de Waele fluid over a variable thickness rotating disk with index decreasing, *Int. J. Heat Mass Transf.* 103 (2016) 1214-1224.
- [13] P. M. Kumar and A. Kavitha, Three-dimensional flow of Jeffrey fluid between a rotating and stationary disks with suction, *Ain Shams Eng. J.* 9 (2018) 2351-2356.
- [14] M. Turkyilmazoglu, MHD fluid flow and heat transfer due to a shrinking rotating disk, *Computers & Fluids*, 90 (2014) 51-56.
- [15] M. Turkyilmazoglu, Nanofluid flow and heat transfer due to a rotating disk, *Computers & Fluids*, 94 (2014) 139-146.
- [16] S. U. S. Choi, Enhancing thermal conductivity of fluids with nanoparticles developments and applications of non-Newtonian fluid flow, *ASME FED* 66 (1995) 99 – 105.
- [17] X. Si, H. Li, L. Zheng, Y. Shen and X. Zhang, A mixed convection flow and heat transfer of pseudo-plastic power law nanofluids past a stretching vertical plate, *Int. J. Heat Mass Transf.* 105 (2017) 350 – 358.
- [18] T. Hayat, S. Qayyum, M. Imtiaz and A. Alsaedi, Comparative study of silver and copper water nanofluids with mixed convection and nonlinear thermal radiation, *Int. J. Heat Mass Transf.* 102 (2016) 723 – 732.
- [19] M. Sheikholeslami, D. D. Ganji, M. Y. Javed and R. Ellahi, Effect of thermal radiation on MHD nanofluid flow and heat transfer by means of two phase model, *J. Magn. Magn. Mater.* 374 (2015) 36 – 43.

- [20] T. Hayat, S. Qayyum, A. Alsaedi and A. Shafiq, Inclined magnetic field and heat source/sink aspects in flow of nanofluid with nonlinear thermal radiation, *Int. J. Heat Mass Transf.* 103 (2016) 99 – 107.
- [21] W. A. Khan, M. J. Uddin and A. I. M. Ismail, Hydrodynamic and thermal slip effect on double-diffusive free convective boundary layer flow of a nanofluid past a flat vertical plate in the moving free stream, *Plos One*, 8, (3) (2013) e54024.
- [22] S. A. Shehzad, Z. Abdullah, F. M. Abbasi, T. Hayat and A. Alsaedi, Magnetic field effect in three-dimensional flow of an Oldroyd-B nanofluid over a radiative surface, *J. Magn. Magn. Mater.* 399 (2016) 97 – 108.
- [23] T. Hayat, M. I. Khan, M. Waqas and A. Alsaedi, Newtonian heating effect in nanofluid flow by a permeable cylinder, *Results Phys.* 7 (2017) 256-262.
- [24] T. Hayat, M. I. Khan, S. Qayyum and A. Alsaedi, Entropy generation in flow with silver and copper nanoparticles, *Colloids Surfaces A: Physicochemical Eng. Aspects* 539 (2018) 335-346.
- [25] T. Hayat, S. Qayyum, M. I. Khan and A. Alsaedi, Current progresses about probable error and statistical declaration for radiative two phase flow using Ag H₂O and Cu H₂O nanomaterials, *Int. J. Hydrogen Energy*, 42 (2017) 29107-29120.
- [26] T. Hayat, M. I. Khan, S. Qayyum and A. Alsaedi, Modern developments about statistical declaration and probable error for skin friction and Nusselt number with copper and silver nanoparticles, *Chinese J. Phys.* 55 (2017) 2501-2513.
- [27] S. Qayyum, T. Hayat, M. I. Khan, and A. Alsaedi, A framework for nonlinear thermal radiation and homogeneous-heterogeneous reactions flow based on silver-water and copper-water nanoparticles: A numerical model for probable error, *Results Phys.* 7 (2017) 1907-1914.
- [28] M. Turkyilmazoglu, Free and circular jets cooled by single phase nanofluids, *European J. Mech. - B/Fluids*, 76 (2019) 1-6.

- [29] M. I. Khan, A. Kumar, T. Hayat, M. Waqas and Ramayan Singh, Entropy generation in flow of Carreau nanofluid, *J. Mol. Liq.* 278 (2019) 677-687.
- [30] T. Hayat, M. Rashid, A. Alsaedi and B. Ahmad, Flow of nanofluid by nonlinear stretching velocity, *Results Phys.* 8 (2018) 1104-1109.
- [31] T. Hayat, S. Qayyum, A. Alsaedi and S. A. Shehzad, Nonlinear thermal radiation aspects in stagnation point flow of tangent hyperbolic nanofluid with double diffusive convection, *J. Mol. Liq.* 223 (2016) 969 – 978.
- [32] M. Turkyilmazoglu, Flow of a micropolar fluid due to a porous stretching sheet and heat transfer, *Int. J. Non-Linear Mech.* 83 (2016) 59 – 64.
- [33] T. Hayat, S. Qayyum, M. Imtiaz and A. Alsaedi, Three-dimensional rotating flow of Jeffrey fluid for Cattaneo-Christov heat flux model, *AIP Adv.* 6(2) (2016) 025012.
- [34] S. U. Rahman, R. Ellahi, S. Nadeem and Q. M. Z. Zia, Simultaneous effects of nanoparticles and slip on Jeffrey fluid through tapered artery with mild stenosis, *J. Mol. Liq.* 218 (2016) 484 – 493.
- [35] T. Hayat, M. Waqas, M. I. Khan and A. Alsaedi, Impacts of constructive and destructive chemical reactions in magnetohydrodynamic (MHD) flow of Jeffrey liquid due to nonlinear radially stretched surface, *J. Mol. Liq.* 225 (2016) 302 – 310.
- [36] K. Das, R. P. Sharma and A. Sarkar, Heat and mass transfer of a second grade magnetohydrodynamic fluid over a convectively heated stretching sheet, *J. Comp. Design Eng.* 3 (2016) 330 – 336.
- [37] T. Hayat, S. Jabeen, A. Shafiq and A. Alsaedi, Radiative squeezing flow of second grade fluid with convective boundary conditions, *Plos One* 11 (4) (2016) e0152555.
- [38] A. Majeed, T. Javed and A. Ghaffari, Numerical investigation on flow of second grade fluid due to stretching cylinder with Soret and Dufour effects, *J. Mol. Liq.* 221 (2016) 878 – 884.

- [39] T. Hayat, M. Zubair, M. Waqas, A. Alsaedi and M. Ayub, Application of non-Fourier heat flux theory in thermally stratified flow of second grade liquid with variable properties, *Chinese J. Phy.* 55 (2017) 230 – 241.
- [40] P. D. Ariel, Computation of flow of a second grade fluid near a rotating disk, *Int. J. Engng. Sci.* 35 (1997) 1335 – 1357.
- [41] T. Hayat, S. Ayub, A. Tanveer and A. Alsaedi, Numerical simulation for MHD Williamson fluid utilizing modified Darcy's law, *Results Phys.* 10 (2018) 751-759.
- [42] T. P. Lyubimova, A. V. Perminov and M. G. Kazimardanov, Stability of quasi-equilibrium states and supercritical regimes of thermal vibrational convection of a Williamson fluid in zero gravity conditions, *Int. J. Heat Mass Transf.* 129 (2019) 406-414.
- [43] T. Hayat, S. Ahmad, M. I. Khan and A. Alsaedi, Exploring magnetic dipole contribution on radiative flow of ferromagnetic Williamson fluid, *Results Phys.* 8 (2018) 545-551.
- [44] Z. Shah, E. Bonyah, S. Islam, W. Khan and M. Ishaq, Radiative MHD thin film flow of Williamson fluid over an unsteady permeable stretching sheet, *Heliyon*, 4 (10) (2018) e00825
- [45] M. Ramzan, M. Bilal and J. D. Chung, MHD stagnation point Cattaneo–Christov heat flux in Williamson fluid flow with homogeneous–heterogeneous reactions and convective boundary condition-A numerical approach, *J. Mol. Liq.* 225 (2017) 856-862.
- [46] D. Viju, R. Gautam and R. Vinu, Application of the distributed activation energy model to the kinetic study of pyrolysis of *Nannochloropsis oculata*, *Algal Research* 35 (2018) 168-177.
- [47] M. I. Khan, S. Qayyum, T. Hayat, M. Waqas, M. I. Khan and A. Alsaedi, Entropy generation minimization and binary chemical reaction with Arrhenius activation energy in MHD radiative flow of nanomaterial. *J. Mol. Liq.* 259 (2018) 274-283.
- [48] T. Hayat, A. A. Khan, F. Bibi and S. Farooq, Activation energy and non-Darcy resistance in magneto peristalsis of Jeffrey material, *J. Phys. Chem. Solids*, 129 (2019) 155-161.

- [49] L. Kramer, V. Maier-Kiener, Y. Champion, B. Sarac and R. Pippan, Activation volume and energy of bulk metallic glasses determined by nanoindentation, *Material Design*, 155 (2018) 116-124.
- [50] T. Hayat, L. Sajjad, M. I. Khan, M. I. Khan and A. Alsaedi, Salient aspects of thermofusion and diffusion thermo on unsteady dissipative flow with entropy generation, *J. Mol. Liq.* 282 (2019) 557-565.
- [51] T. Hayat, S. Ahmad, M. I. Khan, A. Alsaedi and M. Waqas, Investigation of second grade fluid through temperature dependent thermal conductivity and non-Fourier heat flux, *Results Phys.* 9 (2018) 871-878.
- [52] M. I. Khan, A. Alsaedi, S. Qayyum, T. Hayat and M. I. Khan, Entropy generation optimization in flow of Prandtl–Eyring nanofluid with binary chemical reaction and Arrhenius activation energy, *Colloid. Surfaces A.* 570 (2019) 117-126.
- [53] A. Ambekar and J. J. Yoh, Chemical kinetics of multi-component pyrotechnics and mechanistic deconvolution of variable activation energy, *Proceedings Combustion Inst.* 37 (2019) 3193-3201.
- [54] M. Irfan, W. A. Khan, M. Khan, M. M. Gulzar, Influence of Arrhenius activation energy in chemically reactive radiative flow of 3D Carreau nanofluid with nonlinear mixed convection, *J. Phys. Chemistry Solids*, 125 (2019) 141-152.
- [55] L. Ahmad and M. Khan, Importance of activation energy in development of chemical covalent bonding in flow of Sisko magneto-nanofluids over a porous moving curved surface, *Int. J. Hydrogen Energy*, 44 (2019) 10197-10206.
- [56] M. A. Chaudhary and J. H. Merkin, A simple isothermal model for homogeneous-heterogeneous reactions in boundary-layer flow. I Equal diffusivities, *Fluid Dyn*, 16 (1995) 311-333.
- [57] Z. Abbas, M. Sheikh and I. Pop, Stagnation-point flow of a hydromagnetic viscous fluid over stretching/shrinking sheet with generalized slip condition in the presence of homogeneous–heterogeneous reactions, *J. Taiwan Inst. Chem. Eng.* 55 (2015) 69 – 75.

- [58] P. K. Kameswarana, S. Shawa, P. Sibanda and P. V. S. N. Murthy, Homogeneous–heterogeneous reactions in a nanofluid flow due to a porous stretching sheet, *Int. J. Heat Mass Transf.* 57 (2013) 465 – 472.
- [59] M. Sheikh and Z. Abbas, Homogeneous–heterogeneous reactions in stagnation point flow of Casson fluid due to a stretching/shrinking sheet with uniform suction and slip effects, *Ain Shams Eng. J. In Press* 8 (2017) 467-474.
- [60] T. Hayat, S. Qayyum, M. Imtiaz and A. Alsaedi, Impact of Cattaneo-Christov heat flux in Jeffrey fluid flow with homogeneous-heterogeneous reactions, *Plos One* 11(2) (2016) e0148662.
- [61] A. Mahdy, Aspects of homogeneous-heterogeneous reactions on natural convection flow of micropolar fluid past a permeable cone, *Appl. Math. Computation*, 352 (2019) 59-67.
- [62] Nai-Li Xu and H. Xu and A. Raees, Homogeneous-heterogeneous reactions in flow of nanofluids near the stagnation region of a plane surface: The Buongiorno’s model, *Int. J. Heat Mass Transf.* 125 (2018) 604-609.
- [63] F. A. Soomro, Z. H. Khan, R. Haq and Q. Zhang, Heat transfer analysis of Prandtl liquid nanofluid in the presence of homogeneous-heterogeneous reactions, *Results Phys.* 10 (2018) 379-384.
- [64] M. Imtiaz, T. Hayat and A. Alsaedi, MHD convective flow of Jeffrey fluid due to a curved stretching surface with homogeneous-heterogeneous reactions, *Plos One* 11(9) (2016) e0161641.
- [65] M. I. Khan, M. Waqas, T. Hayat and A. Alsaedi, A comparative study of Casson fluid with homogeneous-heterogeneous reactions, *J. Colloid Interface Sci.* 498 (2017) 85-90.
- [66] M. Ramzan, M. Bilal and J. D. Chung, MHD stagnation point Cattaneo-Christov heat flux in Williamson fluid flow with homogenous-heterogeneous reactions and convective boundary condition-a numerical approach, *J. Mol. Liq.* 225 (2017) 856-862.

- [67] I. Khan, M.Y. Malik, A. Hussain, T. Salahuddin, Effect of homogenous-heterogeneous reactions on MHD Prandtl fluid flow over a stretching sheet, *Results Phys.* 7 (2017) 4226-4231.
- [68] Z. Abbas and M. Sheikh, Numerical study of homogeneous-heterogeneous reactions on stagnation point flow of ferrofluid with non-linear slip condition, *Chin. J. Chem. Eng.* 25 (2017) 11-17.
- [69] T. Hayat, M.I. Khan, A. Alsaedi and M.I. Khan, Homogeneous-heterogeneous reactions and melting heat transfer effects in the MHD flow by a stretching surface with variable thickness, *J. Mol. Liq.* 223 (2016) 960-968.
- [70] A. K. Alzahrani, Darcy–Forchheimer 3D flow of carbon nanotubes with homogeneous and heterogeneous reactions, *Phys. Letters A*, 382 (38) (2018) 2787-2793.
- [71] T. Hayat, M. I. Khan, M. Farooq, A. Alsaedi, M. Waqas and T. Yasmeen, Impact of Cattaneo-Christov heat flux model in flow of variable thermal conductivity fluid over a variable thicked surface, *Int. J. Heat Mass Transf.* 99 (2016) 702 – 710.
- [72] G. K. Ramesh, B. C. P. Kumara, B. J. Gireesha and M. M. Rashidi, Casson fluid flow near the stagnation point over a stretching sheet with variable thickness and radiation, *J. Appl. Fluid Mech.* 9 (3) (2016) 1115 – 1122.
- [73] S. Xun, J. Zhao, L. Zheng, X. Chen and X. Zhang, Flow and heat transfer of Ostwald-de Waele fluid over a variable thickness rotating disk with index decreasing, *Int. J. Heat Mass Transf.* 103 (2016) 1214 – 1224.
- [74] T. Hayat, Z. Hussain, A. Alsaedi and A. Asghar, Carbon nanotubes effects in the stagnation point flow towards a nonlinear stretching sheet with variable thickness, *Adv. Powder Tech.* 27 (2016) 1677 – 1688.
- [75] T. Fang, J. Zhang and Y. Zhong, Boundary layer flow over a stretching sheet with variable thickness, *Appl. Math. Comp.* 218 (2012) 7241 – 7252.
- [76] A. Bejan, A study of entropy generation in fundamental convective heat transfer, *ASME J. Heat Transf.* 101 (1979) 718-725.

- [77] M. I. Khan, S. Qayyum, T. Hayat, A. Alsaedi and M. I. Khan, Investigation of Sisko fluid through entropy generation, *J. Mol. Liq.* 257 (2018) 155-163.
- [78] M. Vatanmakan, E. Lakzian and M. R. Mahpeykar, Investigating the entropy generation in condensing steam flow in turbine blades with volumetric heating, *Energy*, 147 (2018) 701-714.
- [79] M. I. Khan, S. Qayyum, T. Hayat, M. Waqas, M. I. Khan and A. Alsaedi, Entropy generation minimization and binary chemical reaction with Arrhenius activation energy in MHD radiative flow of nanomaterial, *J. Mol. Liq.* 259 (2018) 274-283.
- [80] A. Gul, I. Khan and S. S. Makhanov, Entropy generation in a mixed convection Poiseuille flow of molybdenum disulphide Jeffrey nanofluid, *Results Phys.* 9 (2018) 947-954.
- [81] Z. Y. Xie and Y. J. Jian, Entropy generation of two-layer magnetohydrodynamic electroosmotic flow through microparallel channels, *Energy*, 139 (2017) 1080-1093.
- [82] M. I. Khan, S. Ullah, T. Hayat, M. I. Khan and A. Alsaedi, Entropy generation minimization (EGM) for convection nanomaterial flow with nonlinear radiative heat flux, *J. Mol. Liq.* 260 (2018) 279-291.
- [83] G. Huminic and A. Huminic, The heat transfer performances and entropy generation analysis of hybrid nanofluids in a flattened tube, *Int. J. Heat Mass Transf.* 119 (2018) 813-827.
- [84] S. Farooq, T. Hayat, A. Alsaedi and S. Asghar, Mixed convection peristalsis of carbon nanotubes with thermal radiation and entropy generation, *J. Mol. Liq.* 250 (2018) 451-467.
- [85] M. Kiyasatfar, Convective heat transfer and entropy generation analysis of non-Newtonian power-law fluid flows in parallel-plate and circular microchannels under slip boundary conditions, *Int. J. Thermal Sci.* 128 (2018) 15-27.
- [86] S. J. Liao, *Homotopy Analysis Method in Nonlinear Differential Equations*, Springer, Heidelberg, Germany, 2012.
- [87] S. J. Liao, Notes on the homotopy analysis method: Some definitions and theorems, *Comm. Nonlinear Sci. Num. Simulation* 14 (2009) 983 - 997.

- [88] S. Abbasbandy, E. Shivanian and K. Vajravelu, Mathematical properties of h-curve in the frame work of the homotopy analysis method, *Comm. Nonlinear Sci. Num. Simulation* 16 (2011) 4268 - 4275.
- [89] M. Turkyilmazoglu and I. Pop, Exact analytical solutions for the flow and heat transfer near the stagnation point on a stretching/shrinking sheet in a Jeffrey fluid, *Int. J. Heat Mass Transf.* 57 (2013) 82 - 88.
- [90] T. Hayat, M. I. Khan, M. Farooq, T. Yasmeen and A. Alsaedi, Stagnation point flow with Cattaneo-Christov heat flux and homogeneous-heterogeneous reactions, *J. Mol. Liq.* 220 (2016) 49 - 55.
- [91] M. Sheikholeslami, M. Hatami and D. D. Ganji, Micropolar fluid flow and heat transfer in a permeable channel using analytical method, *J. Mol. Liq.* 194 (2014) 30 - 36.
- [92] T. Hayat, M.I. Khan, M. Farooq, A. Alsaedi, M. Waqas and T. Yasmeen, Impact of Cattaneo-Christov heat flux model in flow of variable thermal conductivity fluid over a variable thicked surface, *Int. J. Heat Mass Transf.* 99 (2016) 702 - 710.
- [93] J. Sui, L. Zheng, X. Zhang and G. Chen, Mixed convection heat transfer in power law fluids over a moving conveyor along an inclined plate, *International Journal of Heat and Mass Transfer*, 85 (2015) 1023 - 1033.
- [94] T. Hayat, M. I. Khan, S. Qayyum and A. Alsaedi, Modern developments about statistical declaration and probable error for skin friction and Nusselt number with copper and silver nanoparticles, *Chinese Journal of Physics*, 55 (2017) 2501 - 2513.
- [95] M. Turkyilmazoglu, Convergence accelerating in the homotopy analysis method: A new approach, *Adv. Applied Math. Mech.* 17 (2018) in press.
- [96] T. Hayat, S. Qayyum, M. Imtiaz and A. Alsaedi, Impact of Cattaneo-Christov heat flux in Jeffrey fluid flow with homogeneous-heterogeneous reactions, *Plos One*, 11 (2016) e0148662.

- [97] T. Hayat, M. I. Khan, S. Qayyum and A. Alsaedi, Entropy generation in magnetohydrodynamic radiative flow due to rotating disk in presence of viscous dissipation and Joule heating, *Physics Fluids*, 30 (2018) 017101.
- [98] A. Jafarimoghaddam, On the homotopy analysis method (HAM) and homotopy perturbation method (HPM) for a nonlinearly stretching sheet flow of Eyring-Powell fluids, *Eng. Sci. Technol. Int. J.* 22 (2019) 439-451.
- [99] T. Hayat, M. I. Khan, S. Qayyum, M. I. Khan and A. Alsaedi, Entropy generation for flow of Sisko fluid due to rotating disk, *J. Mol. Liq.* 264 (2018) 375-385.
- [100] H. Y. Martínez and J. F. G. Aguilar, A new modified definition of Caputo-Fabrizio fractional-order derivative and their applications to the Multi Step Homotopy Analysis Method (MHAM), *J. Comp. Appl. Math.* 346 (2019) 247-260